

phil
4/6/67
ANL-7290

ANL-7290

MASTER

Argonne National Laboratory

REACTOR ENGINEERING DIVISION ANNUAL REPORT

July 1, 1965 to June 30, 1966

DISCLAIMER

This report was prepared as an account of work sponsored by an agency of the United States Government. Neither the United States Government nor any agency Thereof, nor any of their employees, makes any warranty, express or implied, or assumes any legal liability or responsibility for the accuracy, completeness, or usefulness of any information, apparatus, product, or process disclosed, or represents that its use would not infringe privately owned rights. Reference herein to any specific commercial product, process, or service by trade name, trademark, manufacturer, or otherwise does not necessarily constitute or imply its endorsement, recommendation, or favoring by the United States Government or any agency thereof. The views and opinions of authors expressed herein do not necessarily state or reflect those of the United States Government or any agency thereof.

DISCLAIMER

Portions of this document may be illegible in electronic image products. Images are produced from the best available original document.

The facilities of Argonne National Laboratory are owned by the United States Government. Under the terms of a contract (W-31-109-Eng-38) between the U. S. Atomic Energy Commission, Argonne Universities Association and The University of Chicago, the University employs the staff and operates the Laboratory in accordance with policies and programs formulated, approved and reviewed by the Association.

MEMBERS OF ARGONNE UNIVERSITIES ASSOCIATION

The University of Arizona	The University of Iowa	Northwestern University
Carnegie Institute of Technology	Kansas State University	University of Notre Dame
Case Institute of Technology	The University of Kansas	The Ohio State University
The University of Chicago	Loyola University	Purdue University
University of Cincinnati	Marquette University	Saint Louis University
Illinois Institute of Technology	Michigan State University	Washington University
University of Illinois	The University of Michigan	Wayne State University
Indiana University	University of Minnesota	The University of Wisconsin
Iowa State University	University of Missouri	

LEGAL NOTICE

This report was prepared as an account of Government sponsored work. Neither the United States, nor the Commission, nor any person acting on behalf of the Commission:

A. Makes any warranty or representation, expressed or implied, with respect to the accuracy, completeness, or usefulness of the information contained in this report, or that the use of any information, apparatus, method, or process disclosed in this report may not infringe privately owned rights; or

B. Assumes any liabilities with respect to the use of, or for damages resulting from the use of any information, apparatus, method, or process disclosed in this report.

As used in the above, "person acting on behalf of the Commission" includes any employee or contractor of the Commission, or employee of such contractor, to the extent that such employee or contractor of the Commission, or employee of such contractor prepares, disseminates, or provides access to, any information pursuant to his employment or contract with the Commission, or his employment with such contractor.

Printed in the United States of America

Available from

Clearinghouse for Federal Scientific and Technical Information
National Bureau of Standards, U. S. Department of Commerce
Springfield, Virginia 22151

Price: Printed Copy \$3.00; Microfiche \$0.65

ANL-7290
Reactor Technology
(TID-4500)
AEC Research and
Development Report

ARGONNE NATIONAL LABORATORY
9700 South Cass Avenue
Argonne, Illinois 60439

CONFIDENTIAL

H.C. # 3.00; 65

REACTOR ENGINEERING DIVISION
ANNUAL REPORT

July 1, 1965 to June 30, 1966

L. J. Koch, Division Director

LEGAL NOTICE

This report was prepared as an account of Government sponsored work. Neither the United States, nor the Commission, nor any person acting on behalf of the Commission:

A. Makes any warranty or representation, expressed or implied, with respect to the accuracy, completeness, or usefulness of the information contained in this report, or that the use of any information, apparatus, method, or process disclosed in this report may not infringe privately owned rights; or

B. Assumes any liabilities with respect to the use of, or for damages resulting from the use of any information, apparatus, method, or process disclosed in this report.

As used in the above, "person acting on behalf of the Commission" includes any employee or contractor of the Commission, or employee of such contractor, to the extent that such employee or contractor of the Commission, or employee of such contractor prepares, disseminates, or provides access to, any information pursuant to his employment or contract with the Commission, or his employment with such contractor.

April 1967

CONTRIBUTORS

R. P. Anderson	A. E. Knox
T. T. Anderson	W. L. Kolb
R. H. Armstrong	V. M. Kolba
N. Balai	W. C. Lipinski
J. F. Bartusek (PE) ¹	P. A. Lottes
C. R. Breden	D. E. Lutz
R. C. Brubaker	R. H. Lykken
N. Bulut (PE) ¹	J. F. Matousek
T. R. Bump	J. F. Marchaterre
J. P. Burelbach	A. Marchertas
T. C. Cameron	E. L. Martinec
Y. W. Chang	W. F. Molloy (PE) ¹
I. Charak	J. H. Monaweck
E. J. Ceisla (RO) ²	J. R. Mrozynski
E. J. Croke	T. P. Mulcahey
J. J. Dickson	R. H. Olp
P. Elias	C. V. Pearson
V. J. Elsbergas (EL) ³	M. Petrick
H. K. Fauske	A. W. Pierce (RO) ²
E. C. Filewicz	E. S. Pierson
S. H. Fistedis	G. F. Popper
J. R. Folkrod	R. R. Rhode
L. W. Fromm	G. S. Rosenberg
J. D. Geier	R. W. Seidensticker
G. D. Giorgis	O. S. Seim
G. H. Golden	R. M. Singer
N. R. Grant	R. C. Skaardal
H. Halle	S. B. Skladzien
E. E. Hamer	A. Smaardyk
A. H. Heineman	F. A. Smith
J. B. Heineman	E. S. Sowa
B. M. Hoglund	D. W. Sparks
R. E. Holtz	R. P. Stein
H. H. Hooker	T. E. Sullivan
C. Hsu	J. H. Tessier
K. A. Hub	D. H. Thompson
E. Hutter	W. Thompson (RC) ⁴
W. D. Jackson	J. V. Tokar
A. R. Jamrog	R. A. Valentin
J. R. Janicek	G. C. Vellender (RO) ²
R. A. Jaross	W. R. Ware
R. F. Jones (RO) ²	R. J. Weatherhead
W. J. Kann	J. T. Weills
I. Kliger	E. A. Wimunc

¹On loan from Plant Engineering Division.²On loan from Reactor Operations Division.³On loan from Electronics Division.⁴On loan from Remote Control Division.

TABLE OF CONTENTS

	<u>Page</u>
Section 1. REACTOR PROJECTS AND PROGRAMS	
1.1	EXPERIMENTAL BREEDER REACTOR-II (EBR-II) 9
1.1.1	Summary 9
1.1.2	Plant Improvements 9
1.1.2.1	Modification of Main Primary System Pump Covers 9
1.1.2.2	Removal and Modification of Sodium Surveillance Periscope 10
1.1.2.3	Removal and Repair of Subassembly Transfer Arm. 12
1.1.2.4	Spent Fuel Subassembly Monitor: An Additional Safeguard Against Loading Error 13
1.1.2.5	Redesign of Core Subassembly Blanket Sections . . 15
1.1.2.6	Spare Components for Control Rod Drive Mechanisms 17
1.1.2.7	Digital Control of EBR-II. 17
1.1.3	Experimental Support 18
1.1.3.1	Mark-B and Mark-C Irradiation Test Subassemblies 18
1.1.3.2	Hydraulic Holddown Characteristics of Irradiation Test Subassemblies. 23
1.1.3.3	Mark-II Oscillator System. 24
1.1.3.4	Universal Materials Stressed Test Assembly 26
1.2	ARGONNE ADVANCED RESEARCH REACTOR (AARR)
1.2.1	Summary 27
1.2.2	Title-I Design 33
1.2.2.1	Site, Buildings, and Auxiliary Structures 37
1.2.2.2	Reactor Components 41
1.2.2.3	Fuel Handling 52
1.2.2.4	Experimental Facilities. 55
1.2.2.5	Heat Removal and Auxiliary Systems 63
1.2.2.6	Instrumentation and Control. 67
1.2.3	Supporting Research, Design, and Development 70
1.2.3.1	Mark-I Core Development 70
1.2.3.2	Control Blades and Drive Mechanisms. 96
1.2.3.3	Stress Analysis of Core Support Grid. 98
1.2.3.4	Stress Analysis of Reactor Vessel. 99
1.2.3.5	Factors Involved in Selection of Vessel Material . . 103

TABLE OF CONTENTS

	<u>Page</u>
1.2.3.6 Studies Related to Development of Beam Tube Facilities	104
1.2.3.7 Analytical and Experimental Studies of the Flow-Reversal Problem in Hydraulic Rabbit Facilities . .	107
1.2.3.8 Corrosion and Compatability of Reactor Materials .	111
1.2.3.9 System Dynamics and Transient Analysis	115
1.3 EXPERIMENTAL BOILING WATER REACTOR (EBWR) - Plutonium Recycle Experiment	119
1.3.1 Summary	119
1.3.2 Plant Inspection, Repairs, and Modification.	120
1.3.2.1 System Piping, Welds, and Valving	120
1.3.2.2 Lower Allowable Maximum Operating Steam Pressure	121
1.3.2.3 Feedwater Full-Flow Filters	121
1.3.3 Reactor Kinetics	122
1.3.3.1 Cold-Critical Experiments.	122
1.3.3.2 Zero Power Transfer Function.	122
1.4 ARGONNE NUCLEAR ROCKET PROGRAM.	123
1.4.1 Summary	123
1.4.2 10,000-lb-thrust System	124
1.4.2.1 Description.	124
1.4.2.2 Engine Weight vs. Thrust Characteristics.	124
1.4.3 Argonne Hydrogen Flow Facility.	126
1.4.3.1 Loop-Heater Performance.	128
1.4.4 Structural Mechanics	128
1.4.4.1 Deformation Analysis of a Grid Plate Support Structure	129
1.4.4.2 Experimental Study of Shell Deformation and Stability	130
1.4.4.3 Vibration Exciter Facility	130
1.4.4.4 Transient Thermal Stresses in Fuel Element Coolant Channels	134
1.4.4.5 Possible Influences of Anisotropy on Thermal Stress Solutions.	135
1.4.4.6 Multipurpose High-Temperature Model Testing Furnace Facility	135

TABLE OF CONTENTS

	<u>Page</u>
Section 2. FAST REACTOR RESEARCH AND DEVELOPMENT	
2.1	Advanced Systems and Concepts 139
2.1.1	1000-MW(e) Metal-Fueled Fast Breeder Reactor Concept 139
2.1.2	Engineering Design and Cost Study of Sodium- Heated Steam-Generator and Turbine-Generator Islands for 500-MW(e) and 1000-MW(e) Central Stations 141
2.1.3	1000-MW(e) Fast Breeder Reactor Follow-On Program. 144
2.2	Materials and Components 147
2.2.1	1200°F Component and Materials Evaluation Loop . . 147
2.2.2	High-Temperature (1200°F) Sodium, Long-Term Environmental Test Loop. 149
2.2.3	Material Compatability Test Facility 150
2.2.4	Modified Falex Machine for Wear Tests in High- Temperature Sodium. 152
2.2.5	1200°F Sodium Furnace-Tensile Testing Machine. . . 156
2.3	Sodium Quality Control 159
2.3.1	Sodium Vapor Trap Development. 159
2.3.2	Sodium Sampling Methods 160
2.3.3	Sodium Quality Measurement Loop 160
2.3.4	Sodium Analytical Loop 161
2.3.5	Sodium Quality Control Laboratory 162
2.4	In-Core Instrumentation 163
2.4.1	Thermocouples 163
2.4.2	In-Core Electromagnetic Flowmeter 168
Section 3. LIQUID METAL HEAT TRANSFER RESEARCH PROGRAM	
3.1	Objectives. 170
3.2	Boiling Sodium Studies 170
3.2.1	Objective 170
3.2.2	2100°F Boiling Sodium Test Facility 170
3.2.3	Advanced Heater Development 171

TABLE OF CONTENTS

	<u>Page</u>
3.3 Evaluation of Traditional Liquid-Metal Heat Transfer	
Design Computations.	173
3.3.1 Objectives and Methods of Approach	173
3.3.2 Heat Transfer in Double-Pipe Heat Exchangers	173
3.3.3 Temperatures in Reactor Coolant Channels.	177
Section 4. MAGNETOHYDRODYNAMICS	
4.1 Liquid-Metal MHD Generators for Central Station and Space Power	178
4.1.1 Objectives.	178
4.1.2 D-C Conduction MHD Generator Operations with Two-Phase Liquid-Metal Flows	179
4.1.3 Reduction of End Losses in MHD Channels	182
4.1.4 Materials Constraints on A-C Induction MHD Generators	185
Section 5. REACTOR SAFETY RESEARCH AND DEVELOPMENT	
5.1 Coolant Dynamics.	188
5.1.1 Analytical Model for Predicting Boiling Superheats in Liquid Metals.	188
5.1.2 Sodium Expulsion Studies.	190
5.1.3 A Technique to Study Sodium-Air Reactions	191
5.1.4 Analytical-Experimental Studies of Critical Flow in Steam-Water Mixtures, Sodium, and Water	193
5.2 Reactor Control and Stability	198
5.2.1 A Single Fixed-Position Detector System for Continuously Monitoring Ten Decades of Neutron Flux.	198
5.2.2 Studies of Time- and Space-Dependent Reactor Dynamics	200
5.2.3 Synthesis of Optimal Control System for Nuclear Reactors with Generalized Temperature Feedback.	202
5.3 Fuel Meltdown Studies: Experimental Facilities	203
5.3.1 Large TREAT Loop	203
5.3.2 An In-Pile Loop to Study Fuel Failure Propagation.	208

TABLE OF CONTENTS

	<u>Page</u>
5.4 Containment	209
5.4.1 A New Concept of Primary Containment by Energy Absorption	209

Section 6. STUDIES AND EVALUATIONS

6.1 Feasibility Study of a Nuclear Steam Supply System Using a 10,000-MW Sodium-Cooled Fast Breeder Reactor	216
---	-----

Section 7. PUBLICATIONS

7.1 Methods of Reporting	227
7.2 Recap of Publications	227

BLANK

Section 1

REACTOR PROJECTS AND PROGRAMS

1.1 EXPERIMENTAL BREEDER REACTOR-II (EBR-II)

1.1.1 Summary

On September 13, 1965, principal responsibility for the EBR-II was formally transferred from the Reactor Engineering Division at Argonne, to the Idaho Division. Since that time, personnel from both Divisions have collaborated in effecting system repairs and improvements, and in developing experimental equipment, all designed to increase plant reliability, reduce operational complexities and costs, and enhance the irradiation test capability of the reactor.

In some instances (e.g., primary pump motor covers), this joint effort has resulted in minor modification of accessible drive units to expedite occasional, manual dislodgement of inaccessible drive shafts. In other cases, scheduled shutdowns have been used advantageously to plan and effect removal, modification, and reinstallation of major components (e.g., subassembly transfer arm). This was done to eliminate difficulties that might impair operation or cause unscheduled shutdown of the AEC's sole fast flux irradiation test facility.

In an effort to reduce operational complexities and costs, two revisions have been made in the fertile blanket sections of the core subassemblies, and definitive design of an irradiated fuel subassembly monitor is nearing completion. Proposed for installation in the primary tank, this monitor will safeguard against inadvertent, remote loading of a spent subassembly into the reactor.

In terms of enhancing the irradiation capability of EBR-II, the Reactor Engineering Division has fabricated four models of the Mark-B irradiation test subassembly, established their hydraulic characteristics in an out-of-pile water loop, and is currently engaged in the conceptual design of a Mark-C unit. Also, prototype components of the Mark-II oscillator system have been successfully tested in an air environment, a facility for testing the integrated prototype system in 850° sodium is under construction, and design of the in-reactor control schemes and instrumentation is essentially completed.

1.1.2 Plant Improvements

1.1.2.1 Modification of Main Primary System Pump Covers

As previously reported (see ANL-7190, p. 16), the sticking trouble experienced during start-up of No. 1 pump was attributed to accumulation of

sodium oxide in the running clearance between the pump shaft and the upper and lower labyrinth bushings in the shield plug. Originally specified as 0.030 and 0.033 in. for pumps No. 1 and No. 2, respectively, these clearances were increased to 0.110 and 0.120 in. during reworking of the pump shafts. In addition, the shaft penetrations in the horizontal baffle plates below the shield plug were machined slightly in excess of the bushing clearances. In the case of No. 1 pump, this enlarged annular space provided a path for increased flow of sodium-vapor-contaminated inert gas upward along the pump shaft, with consequent binding after a scheduled reactor shutdown for several weeks. In this instance, the shaft was rotated manually to effect dislodgement.

Although both pump motors are readily accessible from atop the primary tank, they are hermetically sealed. Hence, each unit must be partially dismantled to gain access to the drive shaft for manual rotation. Therefore, to eliminate this time-consuming operation, both pump covers will be modified to accommodate a shaft extension, when necessary, to engage and manually rotate the pump shaft. The shaft extension will operate through an O-ring-sealed, oil-filled section. This section will be pressurized with inert gas to prevent inleakage of air into the sealed motor housing.

Drawings and material specifications for the modified covers have been forwarded to cognizant Idaho Division personnel for their review and/or implementation should the shaft binding recur. To date, no binding has occurred since reactor shutdowns have been limited to very short periods.

1.1.2.2 Removal and Modification of Sodium Surveillance Periscope

The subject periscope is an assembly consisting of a $14\frac{1}{2}$ -ft-long, tubular, optical system housed in a full-length shielded enclosure. This tube can be lowered into the argon blanket region of the primary tank for viewing purposes. When not in use, the tube is raised into the shielded enclosure.

The assembly was installed in a spare nozzle of the EBR-II primary tank, in June, 1962, for viewing certain internal areas during the sodium-fill period and, for a limited time thereafter, during cold-trapping operations. A secondary purpose was to test various materials required in optical systems (e.g., lenses, windows, gaskets, and special light sources) under actual reactor operating conditions of high gamma radiation and corrosive aerosol at $\sim 800^{\circ}\text{F}$. Data from these tests were to provide the basis for further development of remote viewing devices for service in future fast reactors.

The periscope was used successfully for short periods (3-4 min) during initial filling and subsequent cleanup operations. However, after the sodium had been heated to 750°F , an attempt to use the periscope revealed

that the optical system had become obscured and inoperative. At that time, the periscope was raised into its shielded container where it remained throughout the ensuing wet critical experiments and approach-to-power program.

During a scheduled reactor shutdown in January, 1965, the optical system tube was removed from the assembly, checked and found to be non-radioactive, and shipped to Illinois for examination. It was found that excessive heat had melted the pitch-type cement in the achromat lens located at the lower end of the tube, causing it to become opaque. Also, one of the stainless steel, knife-edge-type gaskets at the lower end cap had failed due to thermal cycling. This failure permitted inleakage of sodium which formed a light film of oxide on the two, simple, objective lenses.

The following modifications were made to correct these malfunctions:

- (1) The cemented achromat lens was converted to an air-spaced type.
- (2) The simple, uncoated, objective lenses were replaced with coated types which do not attract sodium particles as readily as did the uncoated type.
- (3) The metallic gaskets were replaced with a new high-temperature, reinforced Teflon gasket material.
- (4) Kovar-type seals were employed as seals for synthetic-sapphire-to-metal frames.
- (5) The screw-type joints were redesigned as bolted flange-type joints.
- (6) The light source window was enlarged to increase the available illumination.
- (7) The periscope argon system was revised to maintain a constant gas pressure (5 in. W.G.) inside the periscope. In addition, the argon flow was increased to enhance cooling and purging.

No laboratory tests of the modifications will be performed. The periscope assembly will be reinstalled in the primary tank and evaluated in service. Reinstallation is scheduled for the next shutdown period.

Further research and development work is contingent upon the performance of this assembly and the funding available for more advanced and improved concepts. Tentatively, there are two areas wherein resolution of unknowns could have a marked influence on the success of future viewing devices:

(1) The sodium "fog" phenomenon, which is suspected to occur in sodium-saturated inert gas at, or above, 700°F.

(2) An optically transparent window material or window coating, which is unaffected by sustained exposure to corrosive sodium vapor in the temperature range 700-1000°F, and high gamma radiation.

1.1.2.3 Removal and Repair of Subassembly Transfer Arm

During routine fuel handling in early February, 1966, operation of the transfer arm sensing and locking device became progressively more difficult. Because of its vital role in effecting transfers of subassemblies between the reactor and storage basket within the primary tank, the decision was made to remove and inspect the transfer arm-plug assembly during a reactor shutdown period scheduled for late February.

After consideration of various removal methods which would ensure leaktight integrity of the primary tank, it was concluded that the most expeditious and economical scheme would be to withdraw the plug assembly into a flexible gastight bag.

Accordingly, Division personnel assumed the responsibility for (1) designing, procuring, and demonstrating the reliability of such an enclosure; (2) devising a method of sealing it to the transfer arm plug nozzle; and (3) preparing a detailed sequence for removal of the plug into the bag and transport to a shielded area for inspection. These responsibilities were fulfilled as follows:

(1) A sample of neoprene rubber-coated nylon fabric was obtained from a local vendor. This sample was successfully tested for 6 hr under conditions simulating those expected during the removal operation: ambient temperature of, and in contact with sodium particles at, 250°F. Sufficient material was then purchased to fabricate a bag 9 ft in diameter and 30 ft long.

(2) Preparatory to removal of the transfer arm plug, the bag was folded around and clamped at the lower end to the plug nozzle. At the upper end, the bag was sealed in similar fashion to the plug-lifting lugs which were engaged by the building crane. During subsequent lifting operations, the bag unfolded, forming a leaktight enclosure around the withdrawn transfer arm-plug assembly.

The degree of success achieved by the foregoing procedure is best measured by the fact that withdrawal of the plug assembly was accomplished in 1 hr without incident and undue radiation hazard to maintenance personnel.

Subsequent disassembly and inspection of the transfer arm revealed a broken bell crank pivot in the sensing and locking pin linkage. The failure was traced to an incomplete weld. This portion of the linkage was redesigned to eliminate the welded pivot. In addition, the material was changed from Type 304 stainless steel to Type 4140 steel.

Upon completion of these modifications, the transfer arm-plug assembly was reinstalled in the primary tank, using the same flexible bag technique. Reinstallation and subsequent check-out tests were performed during the week of March 7, 1966. Since that time, routine fuel handling has been carried out without further difficulty.

Inspection of Rotating Shield Plug Annuli

Removal of the transfer arm-plug assembly presented an opportunity for remote visual inspection of the annuli between the primary tank cover and the large and small indexing shield plugs. The objective here was to determine whether these annuli could, or had, become "bridged" or partially filled with frozen sodium or sodium oxide.

The position of the transfer arm plug relative to the shield plugs precluded inspection of the entire circumference of each shield plug. However, with the aid of a simple periscope arrangement, it was possible to view and photograph large sections of each annuli. Assuming that these sections are representative of the entire circumference of each rotating plug, there is no cause for concern; each section evidenced a very slight amount of sodium condensate and no bridging.

1.1.2.4 Spent Fuel Subassembly Monitor: An Additional Safeguard against Loading Error

Refueling of the EBR-II involves remote-controlled transfers and exchanges between spent fuel subassemblies in the reactor and identically-shaped, fresh or reprocessed units in the primary tank storage rack. Despite the rigorously controlled fueling sequence and inventory-accounting system, which have prevailed without malfunction thus far, a remote possibility exists that, during repeated unloading and loading operations, a spent subassembly might be removed from the storage rack and returned to the reactor. Subsequent irradiation to higher fuel burnup could lead to subassembly failure and possible damage to the reactor. As an additional safeguard against such a loading error, it is proposed to install an Irradiated Fuel Monitoring System in the primary tank to help the operators distinguish between spent and reprocessed fuel subassemblies during refueling operations.

The monitoring system consists of a special high-temperature gamma ionization chamber, drive mechanism, and readout instrumentation

to differentiate between the gamma-radiation levels and patterns of the respective subassemblies. Supporting design calculations indicate that radiation from a reprocessed fuel subassembly is lower by a factor of $\sim 10^4$ than that emitted from a spent unit. Also, that the radiation profile is more uniform, while that of a spent unit is typically cosine in shape.

The gamma chamber and drive mechanism will be installed in a Type 304 stainless steel thimble which measures 12 in. O.D. at the top and 19 ft-10 in. long. This thimble extends through the "X" nozzle of the primary tank, with the lower stepped-down section (3 in. O.D., 12 ft long) tangent to the arc inscribed by the transfer arm. (See Fig. 1-1.)

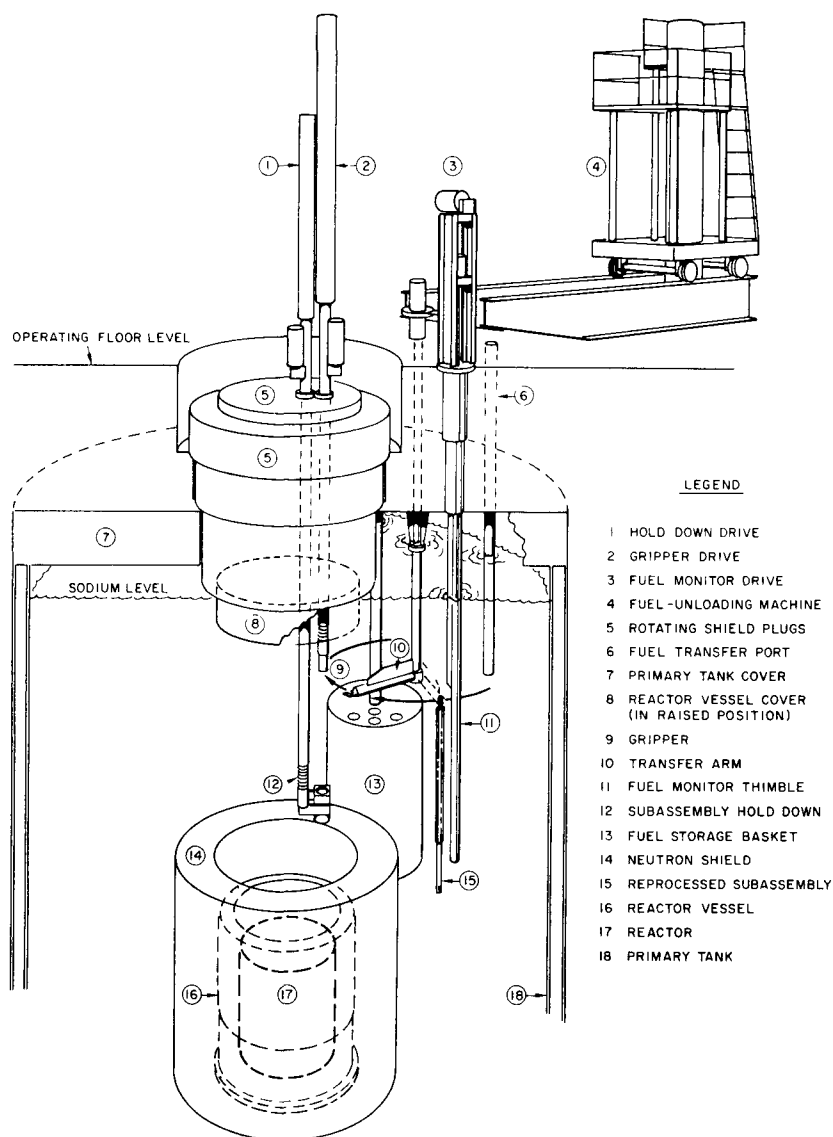


Fig. 1-1. Concept of Irradiated Fuel Subassembly Monitor installation in the EBR-II primary tank. In this view, transfer arm has positioned the suspended fuel subassembly adjacent to the thimble containing the gamma chamber. When properly identified, the subassembly will be transported to and engaged by the gripper for insertion into the reactor.

In operation, the gamma chamber in this section will be raised or lowered a maximum of 60 in. This vertical travel corresponds to the active height of the subassembly when it is supported by the transfer arm while enroute from the storage basket. Finally, the fuel-handling sequence will be modified to incorporate a transfer-arm stop at the Irradiated Fuel Monitor location. At this point, every core subassembly will be scanned and identified prior to its transfer to the gripper mechanism for insertion into the reactor.

The status of the monitoring system is as follows. Conceptual design drawings and purchase specifications have been finalized; definitive design of the prototype system is underway. Construction and initial tests are expected to be completed by January, 1967.

1.1.2.5 Redesign of Core Subassembly Blanket Sections

The original design of the core subassemblies included a blanket section of fertile material above and below the core section for breeding measurements. Unlike the core section, which contained 91, wire-spaced, sodium-bonded, enriched fuel elements (0.144 O.D., 14.22 in. long), each blanket section contained 18 elements (0.375 in. O.D., 18 in. long) of similarly bonded, unalloyed, depleted uranium. These elements were made intentionally thicker to obtain plutonium production distributions; however, even at that time they were considered too thick for optimum economy of plant operation. More recently, a point was reached where the breeding data derived from these elements no longer justified the complexity and cost of their fabrication. As a result of efforts to simplify construction and reduce costs, the original design of these blanket sections has undergone two revisions since April, 1964.

In the first revision (Fig. 1-2(A)), the uranium blanket elements were replaced with solid stainless steel rods of identical dimensions. These rods were positioned between two support grids, with a central spacer rod and a retainer nut. Several of these subassemblies were loaded into the reactor during the latter part of FY-1966.

The latest revision (Fig. 1-2(B)) proposes to replace these parts with a stainless steel triflute section. It will serve as a reflector and shield to protect the structural portions of the reactor above and below the core section. In addition, a flow distributor will be installed in the lower blanket section to direct the sodium coolant into the grid which supports the active fuel elements.

Construction of these subassemblies is pending completion of water loop tests on prototype components. The objective here is to ensure that the hydraulic characteristics match those of the subassembly shown in Fig. 1-2(A).

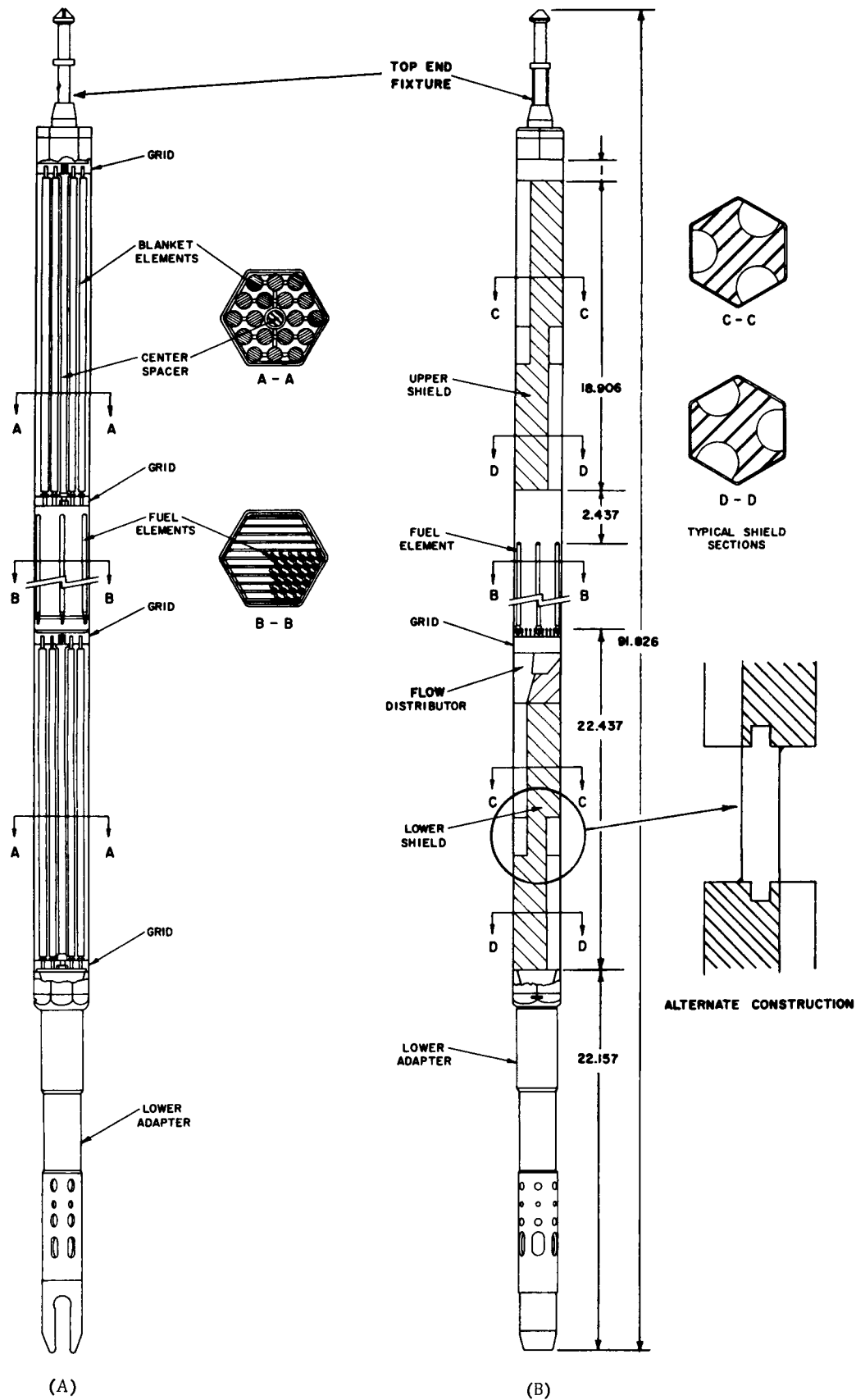


Fig. 1-2. Sectional views of revised core subassemblies containing solid stainless steel (A) blanket rods and (B) triflute reflector and shield section

1.1.2.6 Spare Components for Control Rod Drive Mechanisms

Two 26-ft-long concentric drive, gripper, and sensing shaft assemblies, with gripper mechanisms, were fabricated and shipped to the reactor site. Both assemblies were needed to complete the two spare control rod drive mechanisms that are kept readily available for partial or complete replacement of an inoperable drive unit. As reported in ANL-7190 (p. 21), shaft assemblies in control rod drives No. 7 and No. 9 were damaged by failure of the oscillator drive mechanism. In addition, two spare gripper mechanisms were fabricated, and sufficient raw material, particularly tubular products involving long-delivery times, was procured to expedite construction of two more shaft assemblies at a later date.

With the exception of certain gripper improvements and minor material changes, the new components were fabricated according to the original drawings and specifications. Gripper improvements included: (1) welded cam bars on the jaw-actuating sleeve; (2) one-piece jaw construction; (3) redesign of the jaw cam-bearing surface; (4) a stronger entry guide for the control rod; and (5) jaw revisions that permit an opened gripper to pass through the reactor vessel cover sleeves.

The expeditious manner in which these components were made available is best illustrated by the fact that procurement of the necessary hardware and materials was initiated in October, 1965. One gripper assembly was completed and shipped to the Idaho site in December, 1965. All raw material for future fabrication of spare components was received at Argonne by February, 1966. The second spare gripper and the two shaft assemblies were completed in September, 1966. Some delay in shaft fabrication was experienced due to difficulties in holding dimensional tolerances while extruding the outer tubes.

1.1.2.7 Digital Control of EBR-II

The first phase of the EBR-II improvement program to achieve automatic demand control response ranging from 10 to 100% of full power has been deferred at the procurement stage. This phase provided for the procurement, evaluation, and installation of digital control equipment which would automatically adjust secondary sodium flowrates to match reactor system and steam system requirements. If successful, the control functions of the digital equipment were to be expanded to include primary sodium flow and, ultimately, neutron flux.

Purchase of the digital control equipment has been withheld in response to a request by DRDT to defer procurement until technical justification for such equipment to improve the irradiation test capabilities of EBR-II has been received and concurred with by DRDT.

A letter to this effect has been forwarded. Briefly, it outlines the proposed on-line and off-line applications of digital control to EBR-II, their specific roles in enhancing safety and utility of EBR-II as a fuels irradiation facility and, finally, their contributions to the technology of automated control and instrumentation for future LMFBR plants.

1.1.3 Experimental Support

1.1.3.1 Mark-B and Mark-C Irradiation Test Subassemblies

Four models of the Mark-B subassembly design were completed, the pressure drop characteristics of each model were determined in water loop tests, and conceptual design of a Mark-C unit was started.

Mark-B

Outwardly, the basic features of the Mark-B design are identical to those of the Mark-A unit: both employ the top end fixture, hexagonal can, and lower adapter of a standard core subassembly. Inwardly, the Mark-B subassembly contains several features which identify the respective models and which represent a distinct improvement over the Mark-A design.

Briefly, the Mark-A subassembly provides for simultaneous irradiation of nineteen encapsulated samples. Maximum capsule length is about 40 in. Maximum sample length and diameter that can be accommodated is about 37 and 0.32 in., respectively. Each capsule is positioned within a dimpled shroud tube. Spaces between adjoining shroud tubes are closed off with filler strips so that essentially all of the coolant flows through the shroud tubes.

By comparison, the Mark-B subassembly (Fig. 1-3) offers (1) greater flexibility in the number, diameter, length, and hence, experimental capacity of the test elements that can be accommodated; (2) potential use of unencapsulated fuel specimens; and (3) the potential of remote assembly when facilities become available to allow successive irradiations of given samples.

Table 1-1 lists the number and corresponding diametral tolerances of test elements that can be installed in the respective Mark-B models. Each element measures 61 in. long, with approximately 58 in. interior length available for experiments. If desired, the interior length can be reduced by one of the two alternate methods shown in Fig. 1-4.

Table 1-1. Total Number and Diametral Tolerances of Test Elements Contained in Mark-B Subassemblies

Model No.	No. of Elements	Diameters, in.		Spacer Wire Dia., in.
		O.D.	I.D.*	
B-61	61	0.220 ± .001	0.188 ± .001	0.0515 ± .0005
B-37	37	0.290 ± .001	0.250 ± .001	0.0565 ± .0005
B-19	19	0.375 ± .001	0.325 ± .001	0.0970 ± .0005
B-7	7	0.8055 ± .0005	0.750 ± .003	-

*Size as ordered in Type 304L stainless steel; to be furnished to experimenters.

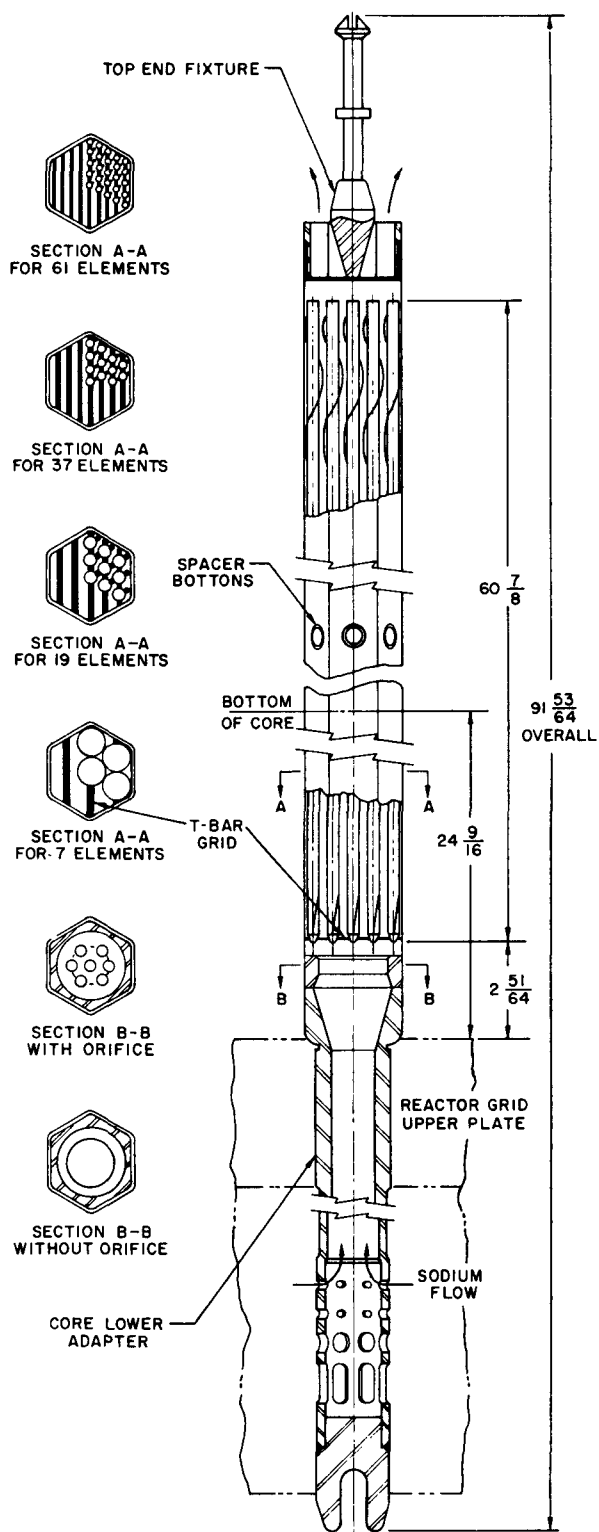


Fig. 1-3. Sectional views of Mark-B irradiation test subassembly

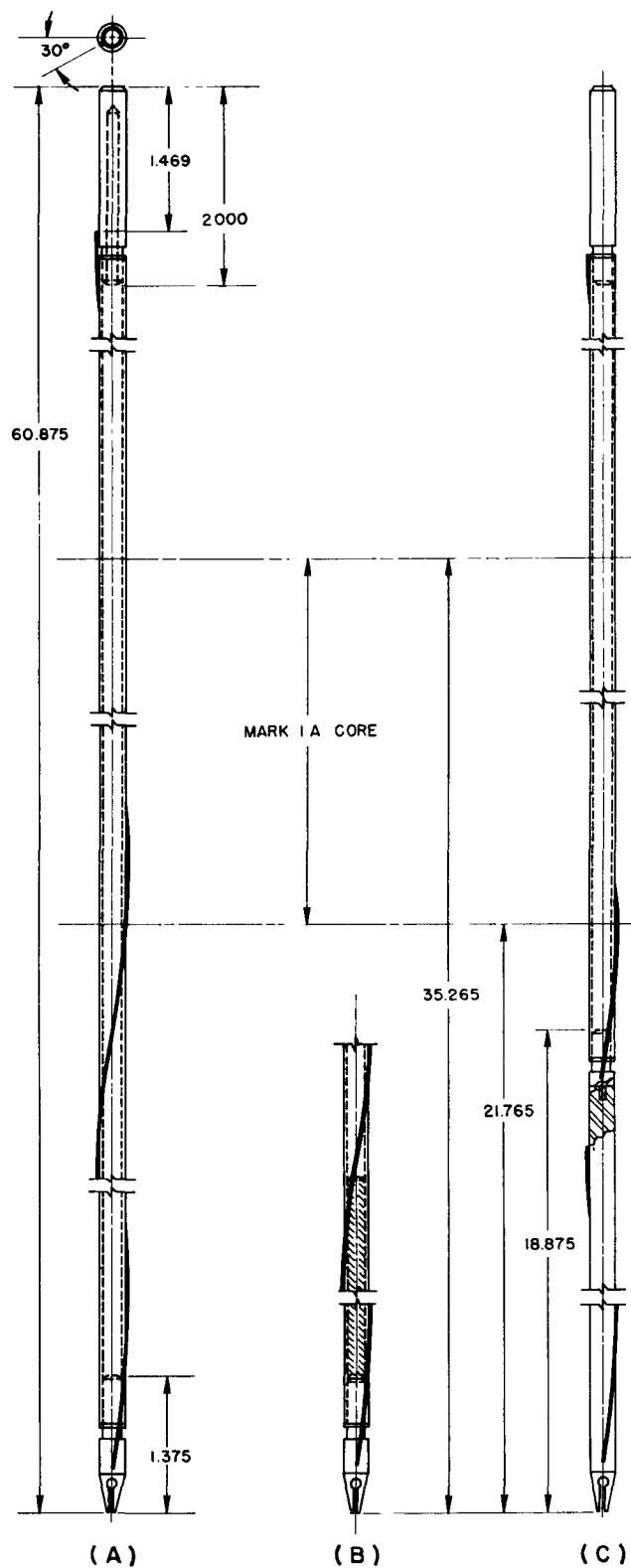


Fig. 1-4. (A) Typical Mark-B test element. Also shown are two methods for reducing capacity of radiation capsule: (B) use of insert of optional length, and (C) longer end fitting. Latter is welded to test element at reactor site and may be severed after irradiation to provide a more convenient shipping length.

Test elements for Models B-61, B-37, and B-19 are spaced by spiral wires which have a 6-in. pitch similar to the standard EBR-II fuel elements. These wires are welded to the elements just prior to loading in the designated subassembly. This procedure allows the off-site experimenter to assemble, test, and ship the elements without interference from the wire. Also, unlike the shroud tube of Mark-A, this mode of spacing allows higher sodium flowrates. If a reduction in flow is desired, an orificed grid support can be substituted. (See Section B-B, Fig. 1-3.)

As evidenced by the test element diameters in Table 1-1, the Model B-7 subassembly has the smallest flow area and is intended primarily for irradiating structural material specimens. The seven elements are devoid of wire spacers. (See appropriate Section A-A, Fig. 1-3.) In addition, the outer length has been shortened to $57\frac{7}{8}$ in. to provide a plenum above the elements for mixing of effluent coolant.

Pressure Drop Characteristics. Figure 1-5 is a composite plot of flowrates vs. pressure drop as a function of reactor row position for prototype Mark-B subassemblies. These tests were conducted in the same water loop that was used to determine flow values for the standard core and Mark-A irradiation subassemblies. In each instance, the subassembly was positioned in a mock-up core support grid located in a vertical section of the loop. Different reactor rows were simulated by the addition of bushings to cover flow holes. Main flow in the loop was measured on the high-pressure side across a standard orifice plate with a mercury manometer and/or pressure gages. Leakage around the outside of the lower adapter was measured in the same manner. Flow was achieved by a centrifugal pump which has a capacity of ~100 gpm against a 230-ft head. Finally, the water test data were converted to sodium flow at 800°F by using appropriate density and viscosity corrections (temperature compensated).

Velocity and Flow Distribution. In the Mark-B design, the flow channels do not have equivalent areas; i.e., the channels between the outer elements and the hexagonal tube are larger than those between any groups of three elements.

Figure 1-6 shows the mathematical models employed and the corresponding calculated velocity and flow distribution in each of the Mark-B models. The calculations were based on methods which were previously verified by flow tests on a scaled-up model of an EBR-II standard core subassembly.^{1*} In these tests, there was a 3% variation in both velocity and flow across the subassembly. With respect to the Mark-B subassemblies, the problem is whether cross-mixing may be a more serious consideration as the space between elements and element size increases. Subject to experimental verification, it is believed that the distribution values in Fig. 1-6 may vary by 7%.

*Superscript numerals correspond to references listed at the end of each subsection throughout this report.

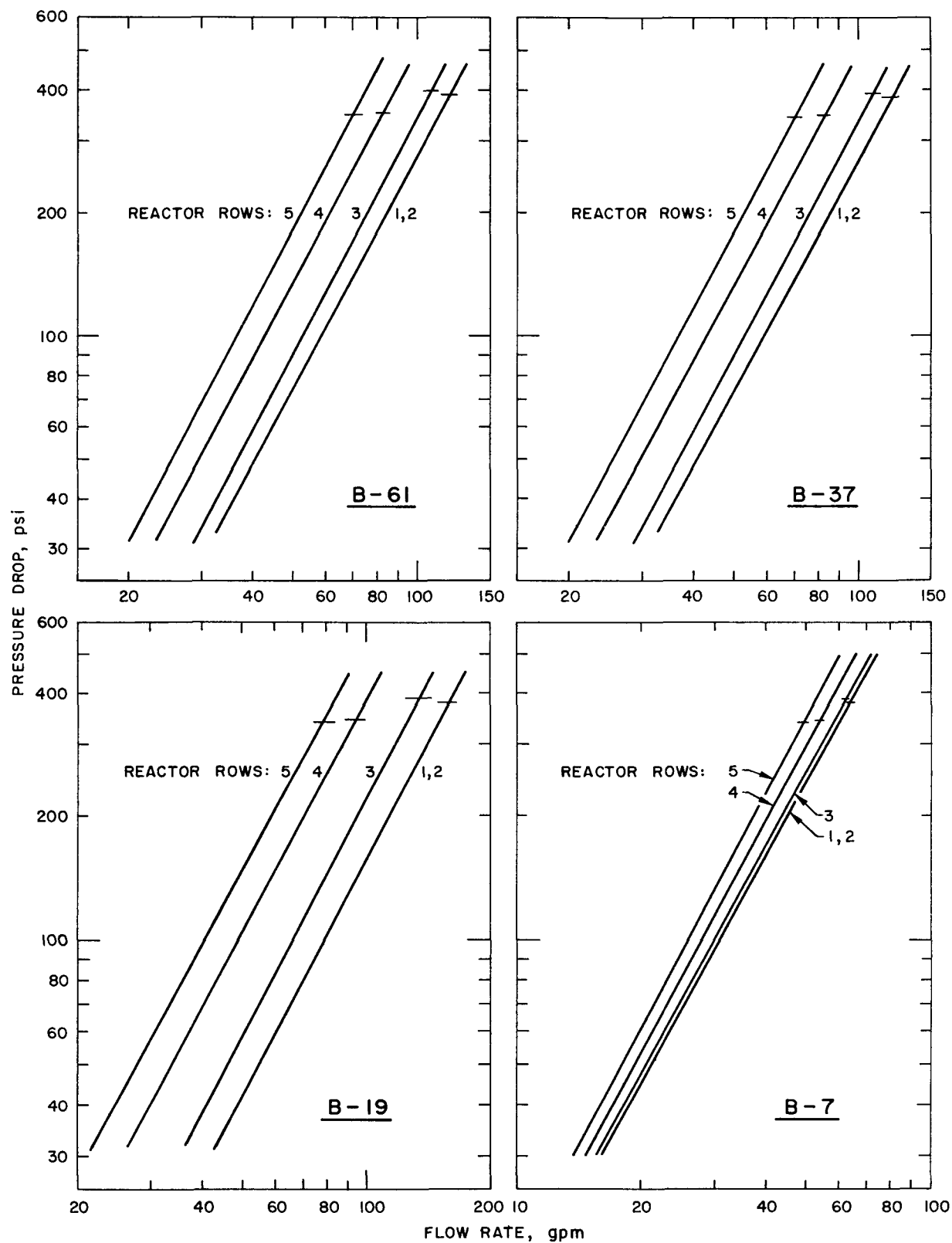


Fig. 1-5. Pressure drop as a function of sodium flow at 800°F through Mark-B irradiation test subassemblies. Horizontal dashes near top of curves are the effective ΔP for the reference 67-subassembly EBR-II core.

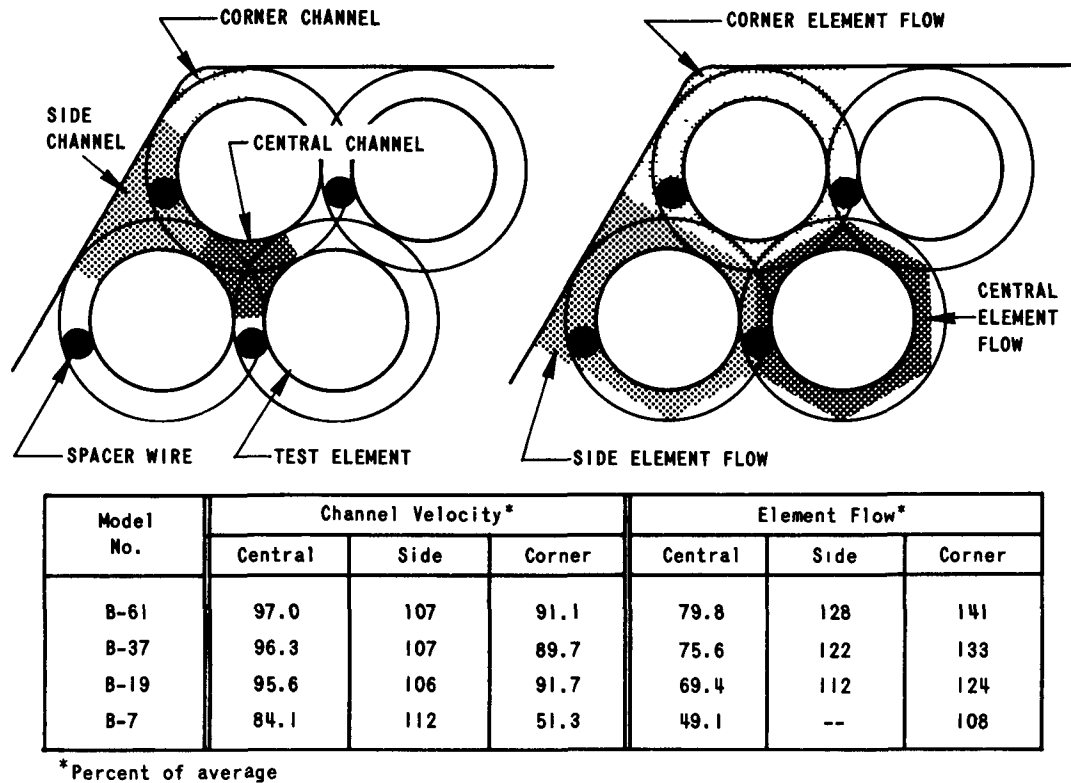


Fig. 1-6. Mathematical models and calculated velocity and flow distribution in Mark-B irradiation test subassemblies

Mark-C

In addition to the advantages cited for the Mark-B subassembly, the proposed Mark-C unit will permit irradiation of fuel elements at higher coolant temperatures than can be attained in either the Mark-A or Mark-B designs

As shown in Fig 1-7, the Mark-C subassembly will accommodate 37 test elements (0 220 in O D , 0 188 in I D.) or 19 elements (0 290 in O.D , 0 250 in I.D) spaced with spiral wires of 0 0515 in and 0 0805 in diameter, respectively. All elements have an irradiation length of 41 in. They are positioned on a support grid which contains orificing for the entire subassembly and for diverting a major portion of the flow through an annulus surrounding the cluster of test elements. This bypass annulus is formed by the outer hexagonal enclosure and the double-walled shroud which encircles the test elements. The double wall is provided to reduce thermal stresses generated by the ΔT across the shroud. Finally, a mixing plenum is located above the enshrouded cluster. The objective here is to ensure an exit coolant temperature that will reasonably match the effluent temperature of adjacent standard core subassemblies. Maximum permissible sodium temperature at the shroud outlet has been calculated to be 1200°F.

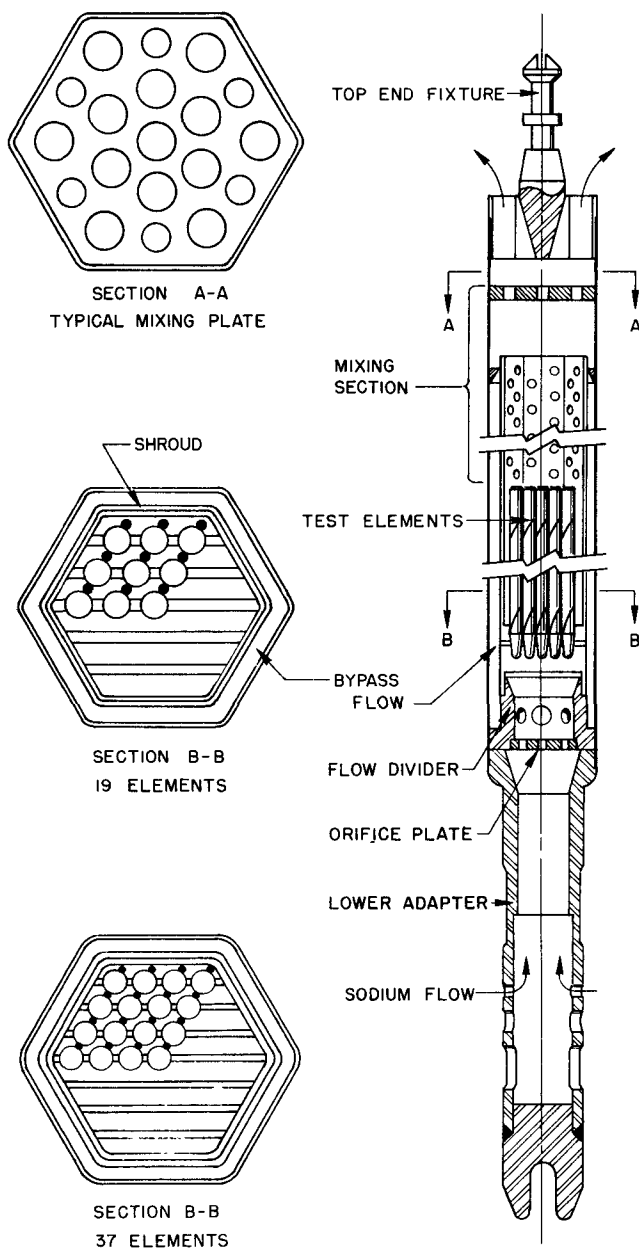


Fig. 1-7. Sectional views of Mark-C irradiation test subassembly

1.1.3.2 Hydraulic Hold-Down Characteristics of Irradiation Test Subassemblies

One safety feature of the standard EBR-II core subassemblies is the downward hydraulic force, which increases with increased upward sodium coolant flow. This force is in addition to the gravitational force (weight) of the subassemblies. In operation, the combined forces prevent these subassemblies from being lifted out of their respective positions in the core support grid.

Since the EBR-II is the principal fast flux test facility, many irradiation test subassemblies also will be installed in the core zone. Moreover the weights of, and the design flow through, these subassemblies will vary, based on the nature of the test materials and the number of test elements. Hence, calculations were performed to determine the hydraulic hold-down or seating force of these subassemblies.

The resultant curves (Fig. 1-8) show that in a core position with normal pressure drops (derived from operating data), the hydraulic hold-down force cannot be more than 2 lb (negative). The total seating

force is then the appropriate curve value plus the weight of the subassembly in sodium. This weight can be obtained by simple displacement computations, using the measured weight of the particular subassembly in air and water. In general, the combined hold-down forces should be adequate for any irradiation test subassembly positioned in the core zone of the EBR-II reactor.

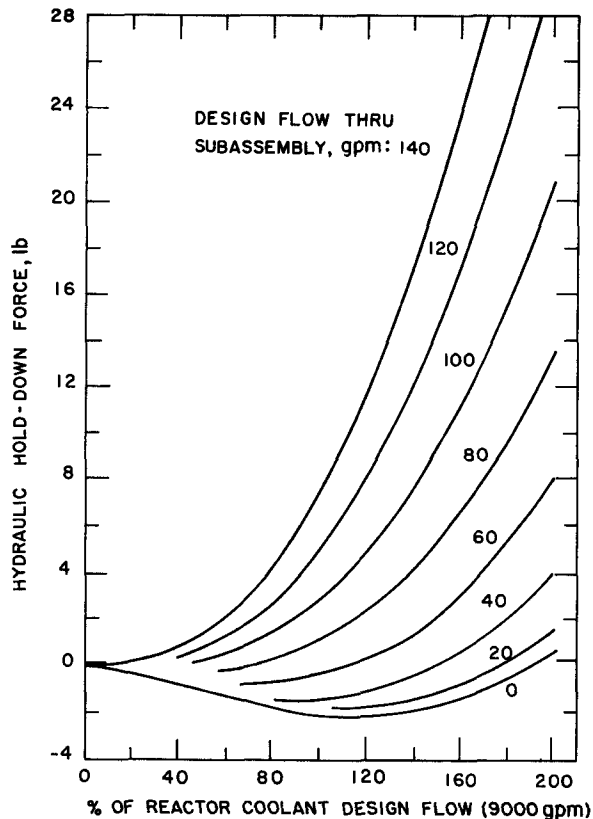


Fig. 1-8. Calculated hydraulic hold-down force for any EBR-II subassembly in the core zone

the gripper assembly revealed no evidence of wear on the gripper jaws or the sensing and jaw-actuating mechanisms.

The final series of tests will be made on the prototype oscillator rod and drive assembly in an induction-heated vessel containing sodium at 850°F. Fabricated from Type 304 stainless steel pipe (10¼ in. I.D., 32½ ft long), the vessel internals include a liner tube with bushings to simulate the drive shaft bearing supports in the primary tank, and a mock-up of the reactor grid and control rod thimble into which the oscillator rod is locked. These tests are pending completion of the temporary operating console. This console also will be used for initial installation check-out tests in the reactor.

Design Control and Instrumentation

Modes of Control. Conceptual design of the control scheme, instrumentation, and electrical system has been completed. Briefly, part of the oscillator drive will be controlled from the EBR-II Fuel-Handling Console, and part from a separate panel in the Reactor Control Room. For example, during fuel-handling operations, the gripper jaws on the oscillator drive and the control rod drives will be operated from the Fuel-Handling Console in

1.1.3.3 Mark-II Oscillator System

Out-of-Pile Tests

A full-scale mock-up of the oscillator rod (see ANL-7190, p. 37) was constructed to facilitate initial testing of the prototype gripper-drive assembly in an air environment. To simplify construction, standard-size tubing was used which closely approximated the 28-ft-long, rotating drive shaft. Finally, the outer bearing guide tube was supported at the same elevations as will be employed in the EBR-II primary tank.

At the outset, the drive shaft and dummy oscillator rod were rotated for short periods (0.5-6 hr) at speeds up to 4 rps. Subsequent tests included shaft rotation at 2 rps for 291 hr, and at 4 rps for 104.5 hr. Throughout these tests, there was a minimum of vibration and no malfunctions. Post-test examination of

the Reactor Building. On the other hand, during reactor operations, when transfer function measurements are desired, rotation of the oscillator rod will be controlled from the Reactor Control Room. The mode of operation is controlled by a manually-operated rotation lock on the drive mechanism; it is positioned by an operator just prior, and subsequent, to fuel handling.

Operating Characteristics. Total rotational speed of the oscillator drive (0.002 to 2 rps), is divided into three ranges, with provisions for a fourth range up to about 10 rps. Within each range, the speed is continuously adjustable from the Control Room panel by energizing a small motor that controls the variable speed transmission. Each range is selected by energizing the appropriate clutch in the gear box. An interlock prevents engagement of any clutch until (1) the transmission speed has been reduced to zero rps; and (2) a prescribed time delay has expired after stopping the rotational drive motor.

Instrumentation. Rotational position of the drive is monitored by (1) a synchro generator for remote position indication; (2) three sine-cosine potentiometers; they are geared to operate at one, two, and three times rotational speed to generate synchronized input position signals and their harmonics; (3) a pulser that generates 180 pulses and one marker pulse per revolution; and, finally, (4) a pulser that effects one switch closure per revolution. Each pulser provides timing signals.

Resistance potentiometers also are used to signal the position of the gripper jaw, sensing rod, and control setting of the variable-speed transmission. In addition, limit switches are employed to indicate the status of certain critical operations, i.e., gripper jaws fully open or closed, sensing rod loaded or empty, angular orientation lock engaged or disengaged, and solenoid-actuated locking pin in or out.

The normal controls, interlocks, and limit switches are backed up (1) by a locking pawl on the jaw drive motor, which prevents jaw operation during rod rotation; and (2) by audible alarm signals. These alarms will be energized by force-sensitive devices upon detection of any significant friction or obstruction during installation or removal of the oscillator rod system.

During subsequent drive rotation, all position-monitoring signals will be displayed on appropriate instrumentation in the Reactor Control Room. Important data will be recorded on magnetic tape. Definitive design and wiring diagrams for the permanent electrical system to be operated from the Reactor Control Room is scheduled for completion in August, 1966.

1.1.3.4 Universal Materials Stressed Test Assembly

The objective of this activity is to develop a practical and economical standard test assembly for evaluating mechanical properties of candidate structural materials exposed to out-of-pile and in-pile environments while under stress. Tentatively, it is assumed that the assembly ultimately would be installed in the EBR-II, with no communication to a point outside the reactor.

On these bases, the most promising concept evolved thus far features a small tube (test specimen), an internal filler bar (to reduce gas volume), with provisions for initially pressurizing the intervening annulus and maintaining a leaktight assembly. Prescribed pressure-induced stresses in the tube wall are generated by raising the temperature of the test medium (coolant) surrounding the assembly. By varying the respective initial charging pressures, several tube assemblies could be tested simultaneously over various stress ranges at a common temperature.

Figure 1-9 shows two variations of the basic concept that are being explored. The intent here is to achieve the simplest stress and strain

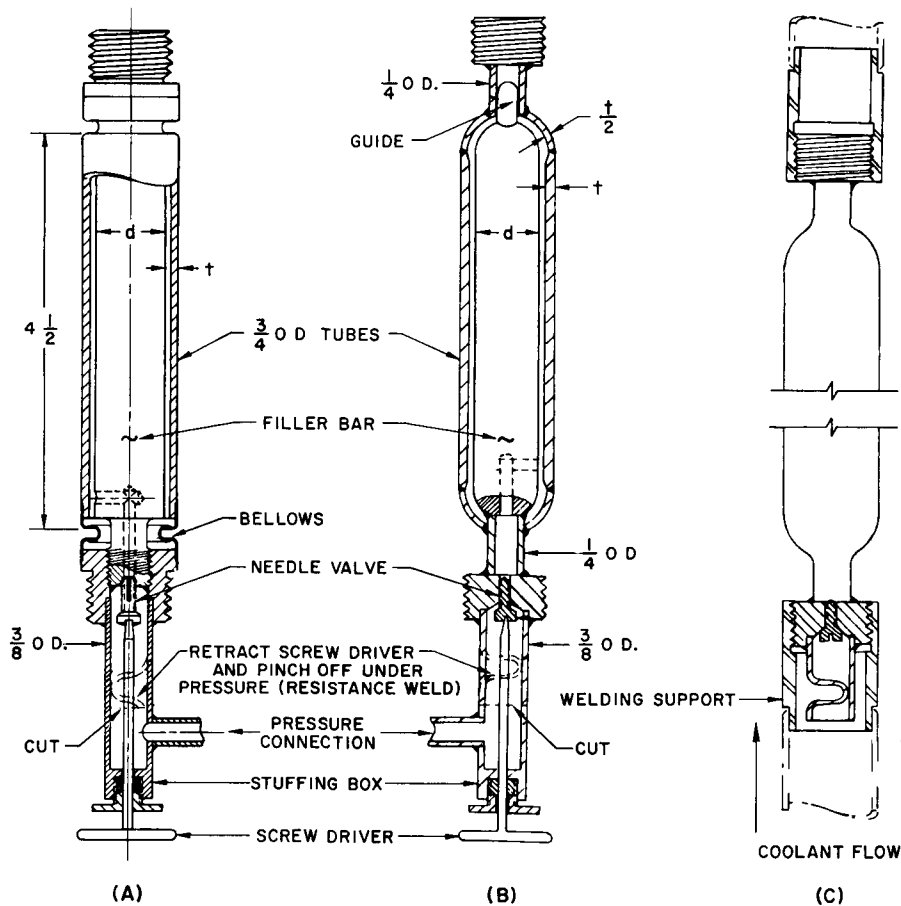


Fig. 1-9. Concepts of (A) uniaxially stressed and (B) biaxially stressed tubular test specimen assemblies. Also shown is method of pressurizing and sealing each unit prior to attachment of welding support end fittings (C). These fittings eliminate welding of dissimilar metal supporting structures. All dimensions are in inches.

patterns in the tube wall and thus to simplify accurate volume-change calculations. Assembly (A) is designed to virtually eliminate longitudinal stress and to produce essentially uniaxial stress in the circumferential direction. An omega bellows is used to effect a seal between the specimen tube and the filler bar shoulder. This mode of construction provides axial freedom for differential thermal expansion between the tube and "insulated" bar in case of rapid thermal transients in the surrounding coolant. Some degree of radial freedom is afforded at the tube ends and should result in a nearly uniform hoop stress from end to end.

In the biaxially-stressed concept (Assembly (B)), the hemispherical end caps of the specimen tube are welded to and supported by 0.25-in. tubes. The filler bar is also welded to the support tube at the valved end, but is free and guided at the opposite end to eliminate axial restraint. This mode of construction probably results in the simplest stress and strain patterns in the tube and ends, as well as the simplest volume-change calculations for materials whose elastic moduli at proposed operating or exposure temperatures are known.

Ultimate selection is contingent upon (1) completion of optimization of design and structural analyses of both concepts; (2) ease of fabricating prototype units; and finally (3) results of out-of-pile proof tests at anticipated pressures and temperatures.

REFERENCE

1. L. J. Koch, W. B. Loewenstein, and H. O. Monson, *Addendum to Hazard Summary Report on Experimental Breeder Reactor-II (EBR-II)*, ANL-5719 (Addendum; June, 1962), Appendix C, pp. 201-213.

✓ 1.2 ARGONNE ADVANCED RESEARCH REACTOR (AARR)

1.2.1 Summary

The Argonne Advanced Research Reactor (AARR) is a multipurpose tool which will enable scientists at Argonne and midwestern universities to extend basic nuclear physics, nuclear chemistry, and solid state research programs beyond the scope of research reactors currently available at the Argonne site. Principal experimental facilities consist of an internal thermal column, or flux trap, having an unperturbed thermal neutron flux approaching $4 \times 10^{15} \text{ n}/(\text{cm}^2)(\text{sec})$, and a multiplicity of horizontal beam tubes having thermal neutron fluxes in excess of $1 \times 10^{15} \text{ n}/(\text{cm}^2)(\text{sec})$. Lower-intensity sample irradiation facilities also are provided.

The AARR facility features a 100 MW(t), pressurized light-water-cooled, beryllium-reflected reactor employing a fully enriched UO_2 -stainless steel cermet flat-plate core.* Although the coolant operating temperature is relatively low (reactor vessel inlet and outlet temperatures are 135 and 164°F, respectively, at 100 MW), the system is designed for a vessel inlet pressure of 750 psi. The objective here is to provide adequate subcooling for prevention of coolant boiling at the extreme core power density existing during normal operation.

Engineering design and construction of AARR was authorized by Congress as part of the fiscal 1965 authorizing legislation. Burns and Roe, Inc. (New York), the selected architect-engineer for the project, began the Title-I design effort in September, 1966, based upon the Argonne concept described in ANL-7190, p. 78. Except for preparation of the Title-I report, this design effort was completed during fiscal 1966, and is reflected in the facility description which follows this summary. Principal differences between the Argonne concept and the Title-I design are:

(1) The fuel-handling canal has been moved from the service floor of the Reactor Containment Building to the experiment floor, at the same elevation as the reactor pool. This results in a major simplification of fuel-handling procedures.

(2) The Storage and Mock-up Building has been replaced by an Active Material Handling Building, which contains an extension of the reactor and fuel-handling pools in the Reactor Containment Building. This pool extension provides sample-handling space for experimenters and affords a simpler means for ultimate removal (in casks) of spent fuel from the Containment Building. The pools in the two buildings communicate by means of an underwater containment-seal hatch.

(3) The Equipment Building has been relocated, reduced in size, and now houses only electrical equipment. Primary system equipment formerly located on the lower, below-grade level of the Equipment Building (which was part of the reactor containment volume) has been relocated to the Reactor Containment Building service floor.

(4) The Laboratory and Office Building has been reduced in size.

(5) The number of horizontal blind beam tubes has been reduced to six. However, the inside diameters of the blind tubes and the two through-tubes have been standardized at 5 in., as compared with the range of $2\frac{3}{4}$ to $6\frac{1}{4}$ in. in the earlier concept. Moreover, in the current design, the beam has a diameter of about 12 in. at the outer face of the reactor biological shield;

*In October, 1966, a decision was made to revise the facility design to accommodate the U_3O_8 -aluminum cermet, involute-plate core which had been developed and successfully operated in the High Flux Isotope Reactor (HFIR) at Oak Ridge National Laboratory. This revision is not reflected in the facility description or supporting research and development activities presented herein.

this permits splitting of the beam and performing two different experiments simultaneously at a single beam tube facility.

(6) The number of vertical sample irradiation facilities has been increased. Four hydraulic and two pneumatic rabbits have been added in the internal thermal column, and two hydraulic and two pneumatic rabbits have been added in the outer beryllium reflector. The low-flux irradiation thimbles in the water outside the beryllium reflector have been eliminated.

(7) The reactivity measurement facility and high-level cave have been eliminated.

(8) The primary coolant system heat exchangers have been reduced to three, with the primary coolant on the shell side, and secondary coolant on the tube side. This enables maintenance of a high velocity in the secondary coolant, which necessarily contains a relatively high level of impurities, and permits use of a significantly lower fouling factor in the design, with consequent savings in heat exchanger size and cost.

(9) The primary coolant pumps have been reduced to two, both of which are normally in operation.

(10) The separate emergency cooling circuits have been eliminated. In the revised design, emergency cooling is accomplished by energizing the main primary and secondary pumps with pony motors mounted on the pump shafts, and by using the main primary heat exchangers and cooling tower to dissipate the heat. The pony motors are supplied with Class I (uninterrupted) power.

(11) The facility is designed for a maximum power level of 100 MW, rather than the 240 MW previously contemplated.

The Preliminary Safety Analysis Report (PSAR) on AARR was completed and submitted to AEC. Review by the AEC Division of Reactor Development and Technology (DRDT), Division of Reactor Licensing (DRL) and Chicago Operations Office (CH) was begun.

Analytical and experimental heat transfer investigations were continued. Results of an earlier analog study of the effects of step reactivity insertions were confirmed, in part, by computations of ramp insertions using a digital computer code: a \$1.00 ramp insertion over a duration of 33 msec appears to be the threshold for fuel melting.

A major improvement was achieved in the detection of imminent burnout in steady-state heat transfer test sections, enabling at least a seven-fold increase in the burnout data obtainable from each test section.

For the transient heat transfer experiments, a pulsing d-c power supply was developed, and tests confirmed the capability of the device to simulate, in a test section, reactor transients of the magnitude and duration predicted by analysis to cause fuel damage in AARR.

The shutdown-emergency cooling test loop was assembled, checked out, and the test program initiated. Preliminary data indicate that at 750-psig system pressure, flow reversal from forced downflow to natural convection upflow could be accomplished at up to $\sim 180,000$ Btu/(hr)(ft²) average heat flux in the hot channel (~ 9 MW reactor power); at 15-psig system pressure, the limiting values are lower by a factor of ~ 2.5 . The data also show that, following reactor shutdown, maximum heat fluxes and reactor power level (i.e., the decay time) at which forced circulation core cooling can be stopped and core removal operations initiated probably will be limited by instability of natural circulation following flow reversal, rather than by thermal transients during the reversal. Although investigation to determine actual quantitative limits is continuing, the data obtained thus far indicate that limiting values are significantly higher than earlier expectations, and that provision of a forced circulation flow reversal system in AARR probably will be unnecessary.

A detailed fuel plate thermal stress analysis was performed, and preparations were made to confirm the results experimentally. Models were developed to express dynamic response of control blades to mechanical and hydrodynamic loadings.

A general-purpose hydraulics test loop capable of simulating AARR flow, pressure, and temperature conditions was made operational. The experimental program includes tests of flow- and temperature-induced deflections of fuel plates and subassemblies, control blades, and other reactor components. Development of special instrumentation to measure such deflections during flow testing was initiated.

Post-irradiation examination of reference 37 wt-% UO₂-stainless steel cermet fuel plate specimens showed that use of 85%-dense UO₂ produces less plate swelling at a given burnup than observed in previous experiments with fully-dense UO₂. Measured swelling rates were correlated satisfactorily with theoretical predictions. Subsequent blister tests indicated qualitatively that the reference fuel material should operate at powers well above 100 MW without serious irradiation damage.

A miniature, brazed subassembly of three fuel plates was irradiated to a burnup of 30 at-% U-235. Examination revealed no significant dimensional changes despite the thermal stresses generated in the assembly. Dummy stainless steel brazed-joint specimens were also irradiated, with no adverse effects on the brazing compound.

Reference composition fuel plates fabricated by commercial vendors in strict compliance with laboratory-developed procedures were, in some cases, found to be substandard. However, when contractors were allowed to revise the procedures consistent with their equipment availability and personnel capability, the end products were equal to, or better than, plates produced in the laboratory.

Methods of incorporating fixed burnable poison (boron) into the reference cermet fuel were investigated. It was found that the selected starting material (ZrB_2) broke down, and a substantial fraction of the boron was lost, if cermet temperatures significantly exceeded 1150°C during fabrication; at 1300°C , 98% of the boron was lost. However, if fabrication temperatures were maintained below 1150°C , less than 5% of the boron was lost. Coating the ZrB_2 with niobium prior to incorporation into the cermet afforded protection against boron loss up to 1175°C . Satisfactory boron-containing reference cermet fuel plates were produced by using the niobium-coated ZrB_2 and restricting fabrication temperature to 1160°C maximum.

Boron was also successfully incorporated into the reference cermet fuel material by an alternate method employing B_2O_3 - SiO_2 glass beads. Metallographic examination of the cermets indicated negligible bead damage during fabrication.

Several methods of preparing UO_2 -stainless steel cermets for the graded loading of AARR fuel were evaluated. The capability to obtain adequate dispersion homogeneities with 6 to 18 wt-% UO_2 was verified.

A characterization study was performed wherein eleven types of UO_2 particles, differing in basic fabrication processes, densities, additives, etc., were compared by fabricating cermet plates and measuring the degree of damage incurred by the various types of particles during the rolling process. The results were incorporated into the AARR fuel specifications.

Three different brazing alloys were investigated for their ability to produce sound brazed joints at the minimal brazing temperatures required to avoid loss of boron from the fuel cermet. The best minimum-temperature braze was obtained using GE-J8100 alloy in a hydrogen braze cycle of two hours at 2100°F . Several satisfactory full-size stainless steel dummy fuel subassemblies were brazed by this method.

Through-transmission, using a monoenergetic cobalt-57 isotope source, was adjudged most promising for inspection and control of UO_2 dispersion homogeneity in AARR fuel plate manufacture. The resolution with this source is sufficient to differentiate a variation of 0.8 wt-% UO_2 in an 0.08 in. square area of fuel plate.

Hydraulic and pneumatic test procedures were developed for evaluating the quality of brazed joints in production fuel subassemblies. Limited success was obtained with through-transmission techniques, the results being more qualitative than quantitative.

Stabilized europium oxide, containing a two-mol addition of TiO_2 per mol of Eu_2O_3 was selected as the reference absorber material in the AARR central control blades. Specimen cermet blades, containing 32 wt-% of the stabilized absorber in stainless steel, were fabricated in accord with the PM-3 reactor control blade specifications. The dispersion uniformity obtained was determined to be satisfactory by X-ray and neutron radiography.

The fabrication of a prototype control blade drive mechanism was begun.

An experimental photo-stress study was made of a full-scale aluminum core support grid prototype, employing load application by hydraulic jacks. The tests showed a constriction in the control blade slots through the support plate of less than 0.005 in. at a load equivalent to a 125-psi pressure drop through the core.

Detailed stress analyses were performed on the reactor pressure vessel for three proposed materials of construction. The results were used to determine optimum nozzle placements, and to assess radiation damage effects. Estimates were also made of the vessel potential for containing sudden internal energy releases which might be incurred by accidental reactivity insertions.

Steady-state thermal and hydraulic analyses were performed on the beam tube facilities to determine heat generation, coolant requirements and beam tube thimble metal and surface temperatures, and to design flow bypass orifices for the beam tube cooling jackets to provide adequate flow distribution without high water velocities. Analysis of thermal, pressure, and bending stresses, on the beam tubes indicated that the estimated values are well within allowable limits.

In connection with the development of the design for the hydraulic rabbit facilities to be included in AARR, an analog study was made to determine the effects of flow reversal on loop pressure fluctuations and on sample temperature rise during sample removal. A preliminary heat transfer analysis was performed using a digital computer method. An experimental test loop was constructed and used to corroborate the analytical data.

A series of dynamic loop corrosion tests, to determine the corrosion compatibility of stainless steel, beryllium and aluminum, was carried out at Oak Ridge National Laboratory under subcontract. Engineering data

were obtained on the corrosion rates of beryllium and beryllium-aluminum couples, with variation of the ratio of exposed surface area to water volume. Corrosion rates were acceptable, and no deleterious coupling effects were noted. Other tests simulating the use of primary water obtained directly from the reactor vessel to cool the aluminum beam tubes resulted in excessive metal temperatures and deposition of corrosion products. Follow-on tests with lower temperature coolant, which could be provided from an external system, produced satisfactory results.

Efforts to improve the analog model of AARR and develop an expanded computer program for analysis of proposed reactor control methods were continued. Extensive calculations were made to determine the reactor transient behavior under conditions of rapid reactivity addition; the findings were incorporated into the Preliminary Safety Analysis Report. Numerous analytical refinements were made in the transient mathematical model.

A program was initiated to determine the technical and economic merits of using on-line digital computer control in AARR.

1.2.2 Title-I Design

This section describes the Title-I design of AARR, which will serve as the basis for the detailed construction design (Title-II) work to be initiated in fiscal 1967. The Title-I design represents the combined effort of the Laboratory and Burns and Roe, Inc., the architect-engineer for the project.

The Title-I design effort began early in fiscal 1966, based upon the concept described in ANL-7190, p. 78. The differences between the two designs were effected for the most part (1) to improve utility to experimenters; (2) to provide greater ease and reliability of operation; (3) to increase the safety of the facility; and (4) to achieve greater simplicity and economy of construction.

A summary of the principal Title-I design parameters and features of the facility is presented in Table 1-2.

Table 1-2. Principal Design Parameters and Features
of Argonne Advanced Research Reactor (AARR)

Reactor Power Levels, MW	
Steady-state operation	100
Minimum steady-state burnout	250
Core Life at Full Power, days	90

Table 1-2 (Contd.)

Thermal Neutron Fluxes at 100 MW, 10^{15} n/(cm ²)(sec)	
Maximum unperturbed in ITC	3.7
In typical ITC sample ^a	
Maximum	2.7
Average	1.7
Maximum unperturbed in Be reflector throughout fuel cycle	≥ 1.0
Reactor Materials	
Fuel	
Fuel plate composition	UO ₂ -Type 347 SS cermet clad with Type 347 SS
UO ₂ in cermet, wt-%	37 ^b
U-235 in U, wt-%	93.2
Total U-235 per core, kg	~60.0
Burnable poison	Stabilized ZrB ₂
Primary Coolant and ITC Moderator	H ₂ O
Radial Reflector	Be + ~3% H ₂ O
Control Plates	
Absorber composition	Eu ₂ O ₃ · 2TiO ₂ -Type 347 SS cermet clad with Type 347 SS
Eu ₂ O ₃ · 2TiO ₂ in cermet, wt-%	~32
Follower material	
In-core control plate	Type 347 SS
Peripheral safety plate	Zircaloy-2
General Heat Transfer and Coolant Data	
System design pressure, psi	875
Normal operating pressure (vessel inlet), psi	750
Coolant design flowrates, gpm	
Total primary pumping capacity	27,200
Fuel channels	18,500
ITC containing reference rabbit facility insert ^c	330
Control plate region	2,200
Beryllium reflector ^c	3,070
Beam tubes, structures	560
Miscellaneous external flows (net)	2,540

^aRabbit samples in a fully-loaded ITC (assumed to contain 75% water and 25% aluminum), with additional neutron absorption corresponding to expected samples.

^bGraded to lower concentrations adjacent to ITC and at core periphery.

^cIncludes irradiation facilities in these regions.

Table 1-2 (Contd.)

System pressure drop, psi	175
Coolant temperatures (at 100 MW), °F	
Vessel inlet	135
Vessel outlet	164
Core Heat Transfer and Coolant Data	
Fuel plate and coolant channel dimensions, in.	
Total height	20
Active height	18
Thickness	
UO ₂ -Type 347 SS cermet	0.030
Cladding (each surface)	0.005
Total	0.040
Coolant channel thickness	
Normal	0.040
Hot	0.050
Total number of fuel plates	1,167
Total heat transfer area, ft ²	692
Volume of active core, liters	79.6
Power density, MW/liter	
Average	1.3
Maximum	5.0
Heat flux, 10 ⁶ Btu/(hr)(ft ²)	
Average	0.51
Hot spot	1.94
Burnout (end of fuel cycle, at operating pressure)	4.85
Temperatures, °F	
Bulk coolant	
Average (core outlet)	186
Maximum (fuel outlet)	250
Fuel plate surface	
Average	205
Maximum	378
Fuel plate interior	
Average	270
Maximum (under spacer)	707
Saturation temperature at hot spot	495
Coolant velocity, fps	45
Pressure drop across fuel subassembly, psi	110

Table 1-2 (Contd.)

Experimental Facilities	No.	Dia., in. ^d
Horizontal		
Blind beam tubes	6	5.0
Through-tubes	2 ^e	5.0
Vertical: Internal Thermal Column		
Hydraulic-operated rabbits	5	0.5
Gas-operated rabbit	1	0.1
Fast, gas-operated rabbit	1	0.5
Static (basket type)	4	0.5
Vertical: Outer Radial Reflector ^f		
Hydraulic-operated rabbits	2	1.0
	2	0.5
Gas-operated rabbits	2	0.5
Static (basket type)	2	2.0
Spare holes for future use ^g	3	1.5
	1	2.0
	6	2.5
Reactor Vessel		
Overall height, ft	29.5	
Inside diameter, ft	8	
Wall thickness, in.	4	
Upper main closure free diameter, ft	8	
Lower closure diameter, ft	4	
Base material	SA 302-B steel	
Cladding		
Inside	Type 304 SS	
Outside	Type 304 SS or Inconel-600	
Primary Heat Exchangers		
Number of units	3	
Thermal capacity per unit, MW	33.3	
Type	Vertical shell and U-tube	
Shell side fluid	Primary coolant	
Tube side fluid	Secondary coolant	
Materials		
Shell	Carbon steel	
Cladding (inside)	Type 304 SS	
Tubes	Incoloy-800	

^dSample diameter for rabbit facilities; inside diameter for other facilities.

^eIf desired, each through-tube may be used as two blind tubes.

^fHydraulic rabbits are installed in 1.5-in.-dia. holes, gas rabbits in 2-in. holes, and static baskets in 3-in. holes.

^gTwenty-four additional irradiation facilities may be made available by installing special, removable, inner reflector segments.

Table 1-2 (Contd.)

Primary Coolant Pumps		
Units required for 100-MW operation	2	
Head at design flow, ft of H ₂ O	500	
Coolant flow per unit, gpm		
Normal drive motor	13,600	
Pony drive motor (d-c)	3,000	
Horsepower per unit		
Normal drive motor	2,000	
Pony drive motor (d-c)	10	
Material (casing)	Type 304 SS	
Containment Building		
Geometry	Cylindrical, with ellipsoidal dome.	
Material	Reinforced concrete, steel liner.	
Dimensions, ft		
Inside diameter	120	
Inside height	122	
Thickness		
Side walls	2	
Dome	1	
Overpressure, psig	7.5	
Leakage, %/day	0.1	

1.2.2.1 Site, Buildings, and Auxiliary Structures

Site

The AARR complex (Fig. 1-10) is to be constructed on a 10-acre site which is near the geographic center of the Laboratory. With respect to existing experimental facilities, the site is about 500 ft northwest of CP-5 and within 1800 ft of the EBWR, JUGGERNAUT, and ZPR reactors.

Reactor Containment Building

Centrally located on the AARR site, this multilevel, steel and concrete structure (Fig. 1-11) measures 120 ft inside diameter, and 122 ft high from the service floor to the vapor-containment liner of the ellipsoidal dome. This steel liner (0.375 in. thick) is backed by reinforced concrete (24 in. thick).

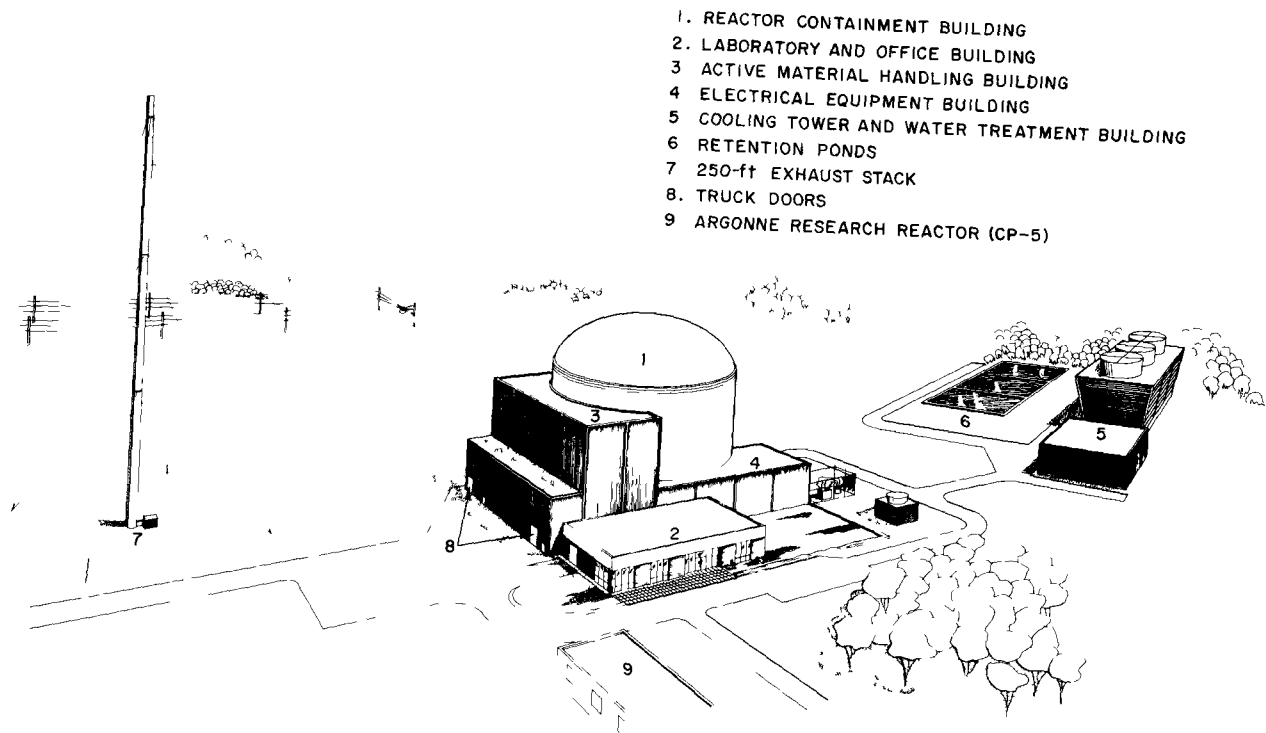


Fig. 1-10. Artist's concept of Argonne Advanced Research Reactor (Title-I design)

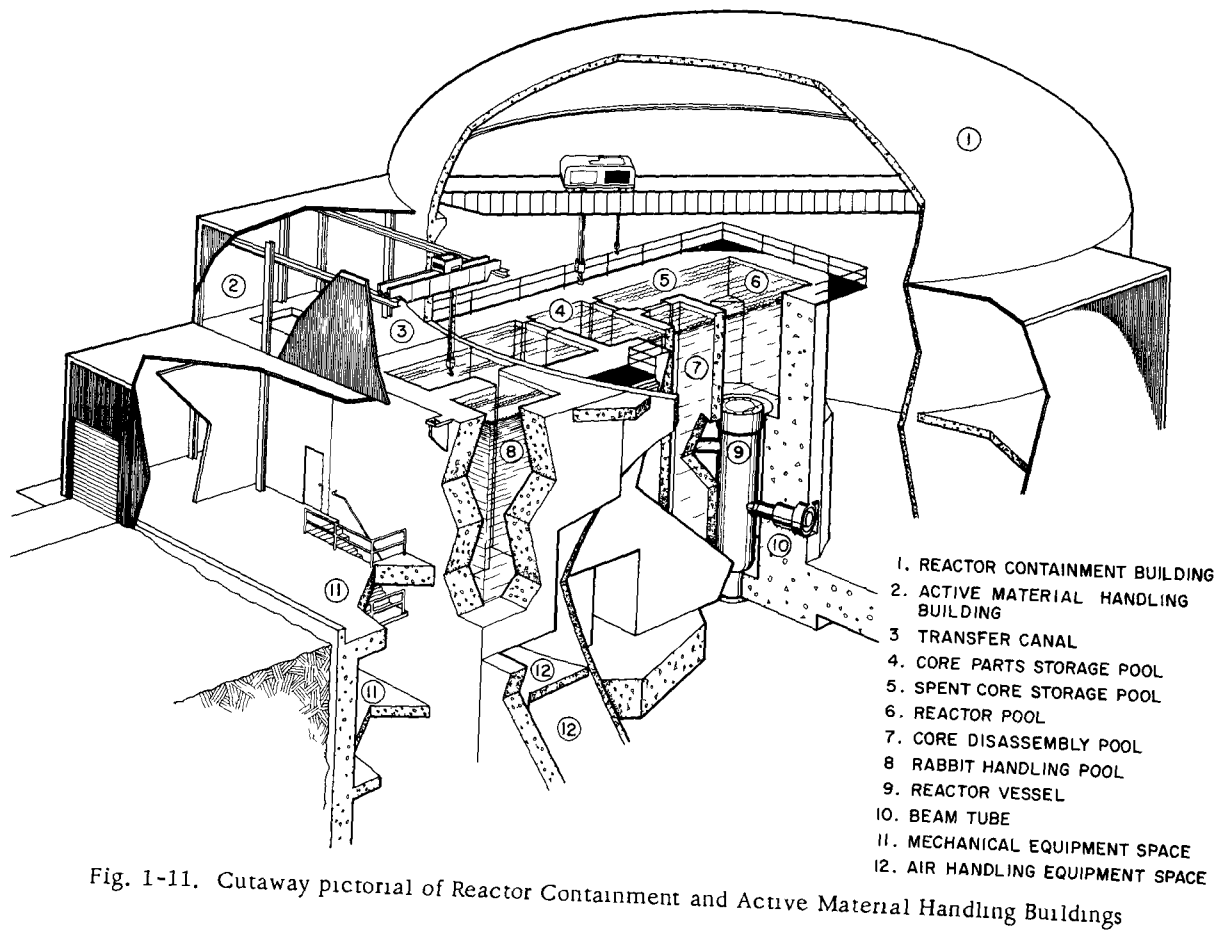


Fig. 1-11. Cutaway pictorial of Reactor Containment and Active Material Handling Buildings

On the service floor are located the primary cooling system, off-gas system, gas rabbit system, shield plug cooling system, high-pressure portion of the hydraulic rabbit system, irradiation facilities cooling systems, control rod drives, pool and canal cooling system, and the poison injection system. A shielded stairway leads up to the main floor.

Except for small areas near the building access air locks, the entire main floor area around the reactor and adjoining concrete-shielded pools is available for experimenters' equipment. The reactor vessel is completely submerged, with the core centerline $6\frac{1}{2}$ ft above the main floor level. In addition, the vessel is offset with respect to the building centerline to facilitate experiments with neutron beam lengths ranging up to 50 ft.

Large-size penetrations in the Reactor Containment Building include: (1) a personnel air-lock leading from the main floor to the service floor of the Laboratory and Office Building; (2) an emergency personnel air-lock leading from the main floor to the outdoors; (3) vehicle and equipment hatches leading from the main and service floors to an outdoor areaway; and (4) a personnel air-lock leading from the transfer canal level to the operating floor of the Active Material Handling Building. Small-size penetrations are provided for system piping, instrument and control circuitry, utilities, and ventilation ducts. All openings are designed to maintain leak-tight integrity of the containment structure.

The entire main floor is serviced by a polar crane having a 15-ton-capacity main hook and a 5-ton-capacity auxiliary hook. This crane is used in conjunction with a power-operated, personnel bridge, which is positioned over the reactor pool and transfer canal during refueling and/or unloading of irradiated experimental equipment. Spent fuel and other irradiated materials are transported through an underwater hatch in the transfer canal directly into the adjacent Active Material Handling Building.

Active Material Handling Building

Constructed of conventional structural steel framing, and enclosed with insulated metal wall panels, this building extends two stories above grade and three stories below grade. The above-grade level houses an extension of the transfer canal, an associated work area, and a pool which is used in conjunction with accelerated irradiations (rabbit facilities). On the grade level (first floor) and adjacent to the pools are located the air supply systems for the Reactor Containment and the Active Material Handling Buildings, the process chilled water system, and the power distribution panels for in-building equipment. On the below-grade levels are located the exhaust systems for both buildings and the pumps for the low-pressure rabbit transfer system.

This building is serviced by an overhead, 35-ton-capacity crane, with a 3-ton-capacity auxiliary hook.

Laboratory and Office Building

Located adjacent and west of the Reactor Containment Building, this masonry structure houses the facilities for personnel engaged in the operation, maintenance, and conduct of experiments in the AARR.

These facilities are disposed on two levels. On the main floor level are located a reception area, fourteen offices, a conference room, an instrument shop, a lunchroom, a records vault, a mens' locker room, and the normal ancillary areas. The service floor level, which communicates directly with the reactor experiment floor, contains a health physics laboratory and office, the control room, instrument cable and relay rack rooms, two chemistry laboratories, four counting rooms, a radiochemistry service room, and emergency scrub and change rooms. Also on this level are the building heating, ventilating, and air-conditioning systems. Both levels are serviced by a combined passenger-freight elevator with a 7500-pound capacity.

Electrical Equipment Building

This two-level structure adjoins the northeast side of the Reactor Containment Building. The basement contains four battery rooms, switchgear, two diesel-driven generators, and motor control centers. This equipment is part of the emergency power system used to sustain operation of vital reactor components upon loss of normal power. The normal power supply system is located on the grade level floor. System equipment includes 480-volt substations, motor control centers, and the 4160-volt switchgear. As shown in Fig. 1-10, the 13.2-kV switchgears and transformers are installed in a fenced-in area north of the Electrical Equipment Building.

Auxiliary Structures

These structures include: (1) cooling towers, a building which houses the secondary coolant system pumps, and water treatment equipment, all located about 250 ft north of the Laboratory and Office Building; (2) retention ponds for storing and testing secondary system blow-down water prior to its release to the environs; (3) a contaminated waste storage facility; and (4) a 250-ft exhaust stack. All contaminated solid and liquid wastes from the Reactor Containment and Active Material Handling Buildings are routed to the waste storage facility which is southwest of the Reactor Containment Building. All gaseous effluent from both buildings is monitored prior to discharge through the exhaust stack.

1.2.2.2 Reactor Components

Core Insert Assembly

Consistent with the decision to operate AARR at a power level of 100 MW(t), the Mark-I core is being developed to provide, for experimental purposes, unperturbed thermal neutron fluxes approaching $4 \times 10^{15} \text{ n}/(\text{cm}^2)(\text{sec})$ in the Internal Thermal Column (ITC), and $1 \times 10^{15} \text{ n}/(\text{cm}^2)(\text{sec})$ at the innermost tips of the horizontal beam tubes.

Designed for unit replacement, the core insert assembly (Fig. 1-12) comprises the 45-subassembly core, 12 control and safety blades, and supporting structures. These structures include the grid plate, core shroud, core holddown, ITC shroud, and lower shroud. All fuel subassemblies are supported and positioned by the grid plate. Tight lateral tolerances between subassemblies are maintained by accurately fabricating the upper holddown and grid plates. Each of the control and safety blades is guided primarily by the upper end fittings of adjacent subassemblies and shroud above the core. Within the core, the blades are guided by raised ribs on the subassemblies or the shroud channels. During loading or unloading operations, the blades are locked and supported in the lower shroud guides. Prior to these operations, the ITC shroud is removed and replaced with a suitable neutron absorbing material. This absorber material serves as an additional shutdown device during transport of a new or spent core.

As shown in Fig. 1-16, the core insert assembly, inner and outer radial reflectors, reflector shroud, and coolant flow shroud are mounted on the core and reflector support grid. This grid is bolted to the core and reflector support pedestal. The latter, in turn, is bolted to a support ring which is an integral part of the pressure vessel. Thus except for the control and safety blades, all static and dynamic loads of the core insert assembly are transferred to the vessel support ring.

The advantages of the packaged core concept are twofold. First, reactor downtime for refueling is foreshortened significantly. Second, a high degree of flexibility is provided for unit inspection outside the vessel, partial disassembly within the vessel, or design modifications for operation at higher power level.

Fuel Subassemblies. Each of the 45 fuel subassemblies (Fig. 1-13) is rhomboidal in cross section and consists of flat plates brazed to rectangular wire spacers at the sides and midsection. These spacers eliminate the need for side plates. Rhomboidal end fittings, fabricated from Type 347 stainless steel, are welded at the top and bottom; they are orificed to ensure adequate diversion of coolant flow throughout the multiplate assembly. The upper end fitting of each subassembly is identical, and all units are accommodated by the same handling and transfer devices. The lower end fitting, which tapers to a cylindrical cross section, seats in the grid plate.

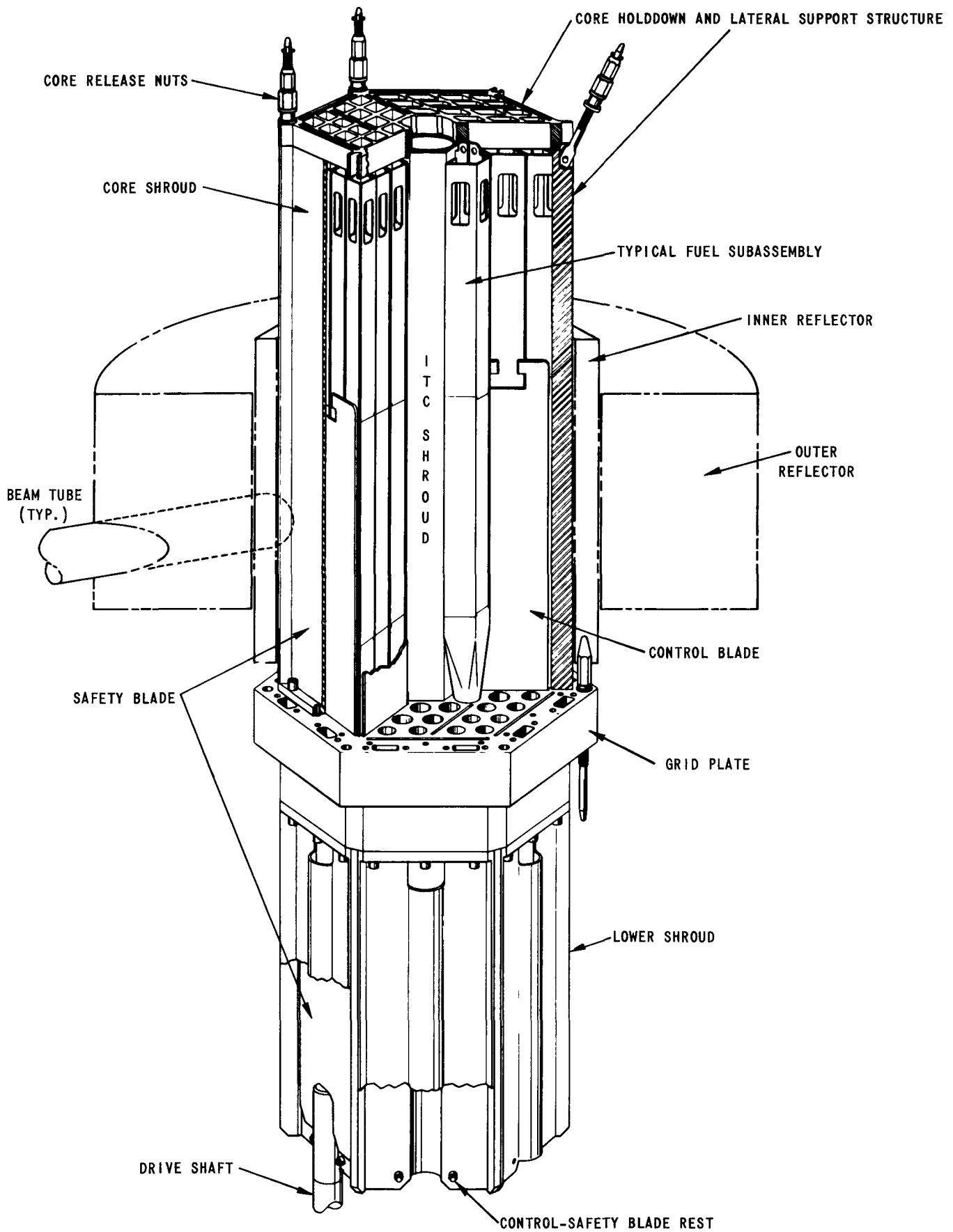
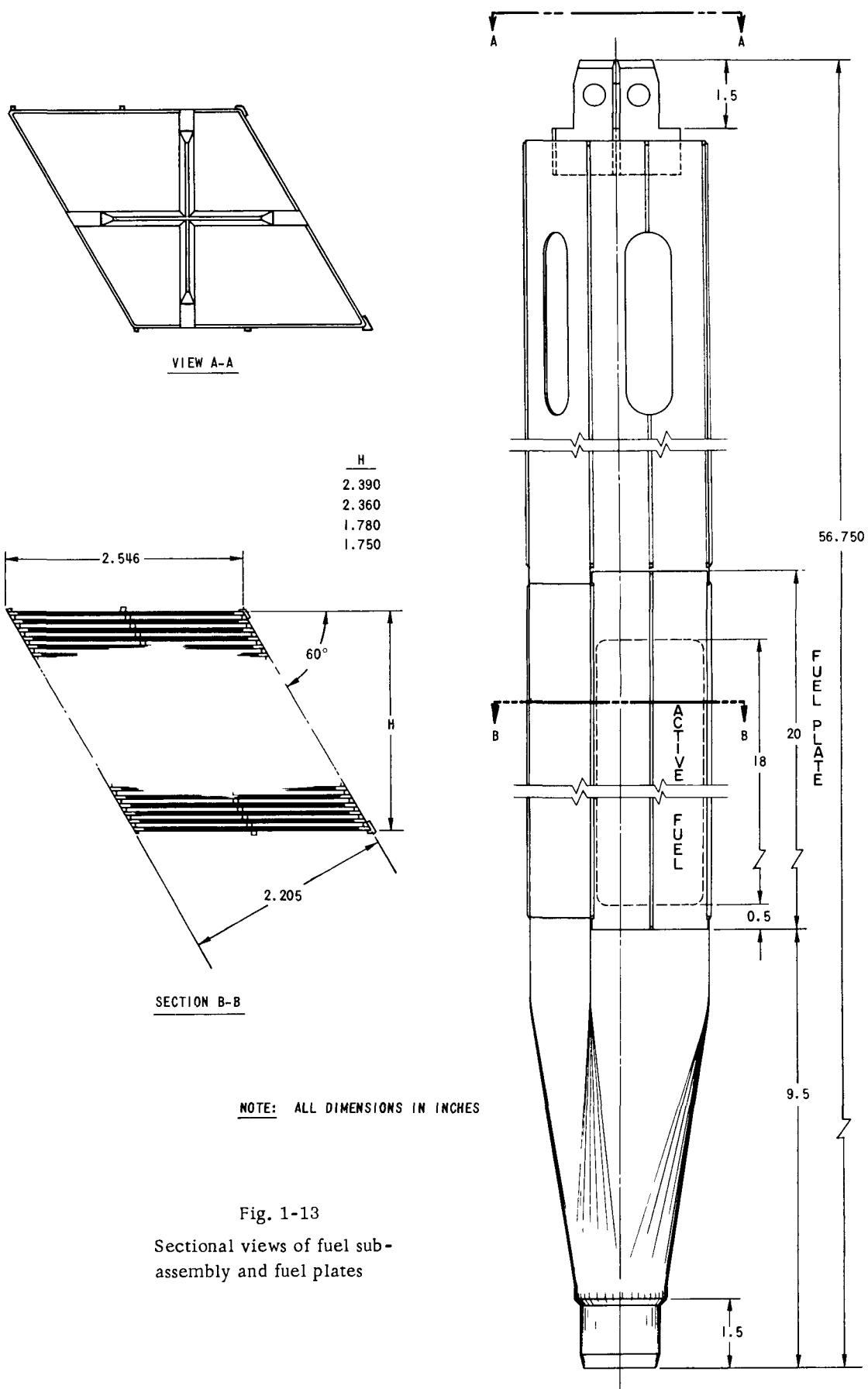


Fig. 1-12. Core insert assembly



Five types of subassemblies will be employed, differing only in number of fuel plates, fuel content, and spacing.

Fuel Plates. The total core loading comprises 1167 Type 347 stainless steel-clad fuel plates fabricated by the picture-frame technique. Each plate measures 20 in. long, 2.546 in. wide, 0.040 in. thick, and features an active fuel region 18 in. long, 2.370 in. wide, 0.030 in. thick.

The standard fuel plate contains highly enriched (93% U-235) spherical uranium dioxide (37 wt-% max.) uniformly dispersed in a Type 347 stainless steel matrix. A sufficient amount of stable boron compound (ZrB_2) will be added to the fuel to provide additional reactivity holddown during initial operations. To minimize power peaking at the inner and outer edges of the core, the subassemblies in these regions will contain plates of varying fuel content and coolant channel spaces. Figure 1-14 shows the fuel plate-spacing in subassemblies comprising one quadrant of the core loading.

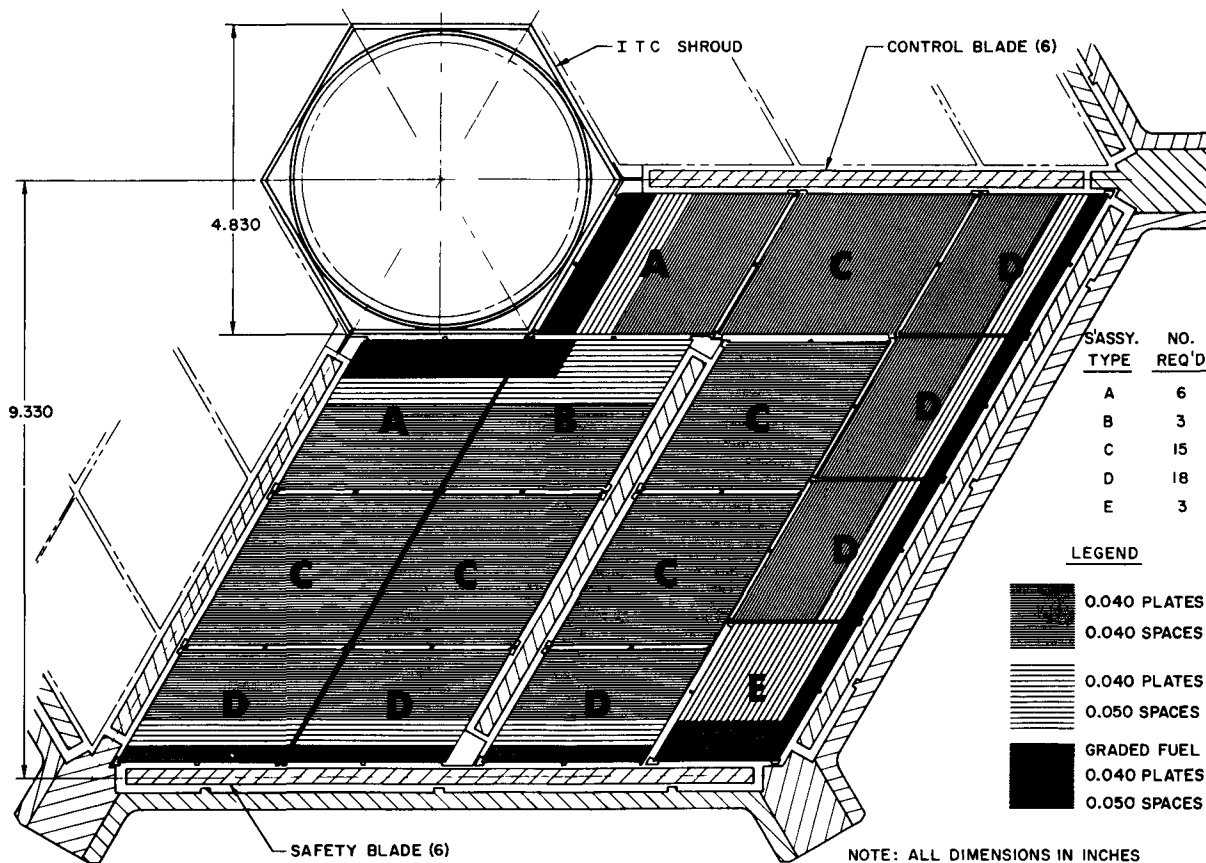


Fig. 1-14. Partial plan view of AARR core showing relative positions of standard and graded fuel subassemblies, and orientation of control and safety blades

Calculations indicate that a core loading of ~58 kg U-235 and 250 gm natural boron will provide a maximum of 9% available excess reactivity throughout the 90-day core lifetime.

Control Blades. In addition to the fixed burnable poison in the fuel plates, system reactivity is controlled by twelve flat blades which move vertically into or out of the core. As shown in the partial plan view of the core (Fig. 1-14), six blades are positioned in the fuel zone: three radially and three offset. These blades are used for long-term reactivity shim control; they also function as safety blades.

The other six blades bound the fuel zone at its outer radial perimeter. One will be used as a regulating blade, for automatic control of reactor power. The other five will be used only as safety blades (after equilibrium levels of xenon-135 are attained during reactor operation) to avoid flux-

depression effects in experimental facilities in the beryllium reflector. When used strictly as safety blades, the leading edge of the respective poison sections will be positioned ~1.5 in. within the active core region. This will be done to enhance the differential reactivity control worth of these blades in the first inch of blade motion.

As shown in Fig. 1-15, the blades differ only in width and in material employed for the respective follower sections. Each blade features a rectangular slot in the follower section, which is engaged by a rotary key in the drive shaft connector, and a T-slot in the absorber section for engagement and removal by a common grappling device. Extrapolations from reactor physics experiments in the AARR Criticality Facility indicate that, in the fresh reactor, the total reactivity control worth will be approximately 15%, distributed roughly equally among the twelve blades.

Inner and Outer Reflectors

Both reflectors form a 16-in.-thick region of beryllium around the core in the radial direction. Some reflection of neutrons is provided by the coolant above and below the core.

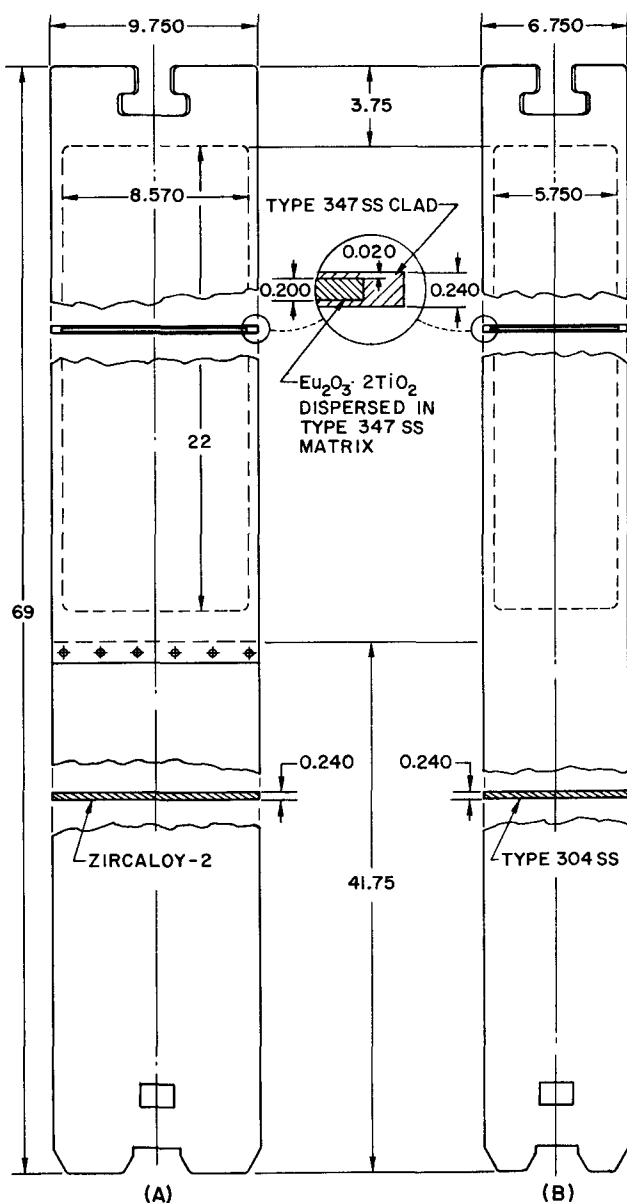


Fig. 1-15. Sectional views and composition of (A) safety blade and (B) control blade. All dimensions are in inches.

As shown in Fig. 1-16, the outer reflector is a segmented cylinder of beryllium (52 in. O.D.), with a central, hexagonal opening (~25 in. across flats) to accommodate the core and inner reflector. It extends 10 in. above and below the centerline of the active fuel zone, and is supported, axially, by the core-reflector support grid and reflector holddown, and, laterally, by the reflector outer shroud. The large, rectangular segments are pierced with coolant passages, vertical holes for rabbit facilities, and horizontal holes for blind beam tubes and through-tubes. Calculations indicate that the outer reflector should endure for a number of years before it need be replaced for reasons of corrosion, radiation damage, and/or buildup of tritium from (n, α) reactions.

The inner reflector measures 3 in. thick, and extends 15 in. above and below the core centerline. Since it is in a region of high neutron flux and high heat generation, the inner reflector is comprised of smaller rectangular pieces (30 in. long, ~9 sq in.). These pieces are removed (and can be replaced, if necessary) consistent with the proposed sequence of core unloading operations.

The combined reflector region is cooled by the primary coolant, which is bypassed around the fuel zone and flows downward through the passages, penetrations, and gaps maintained between the beryllium segments.

Reactor Vessel

The main design parameters and features of the reactor vessel are summarized in Table 1-3 and illustrated in Fig. 1-16.

Table 1-3. Summary of Reactor Vessel Design Parameters

Pressure, psig	
Operating	750
Design	875
Temperature, °F	
Operating	~135 and 164
Design	350
Shell Dimensions, ft-in.	
Main cylindrical section	
Inside diameter	8-0
Length	15-4
Hemispherical transition length	
	3-9.75
Lower cylindrical section	
Inside diameter	3-11
Length	6-3
Wall thickness (incl. clad)	
	0-4
Clad (inside and outside)	
	0-0.25

Table 1-3 (Contd.)

Closures and Penetrations

Top head		
Inside diameter, ft	8	
Thickness, in.	29	
Penetrations	<u>Total No.</u>	<u>Dia., in.</u>
Vertical facilities	7	1.75
Vertical facilities	6	2.75
Instrument	3	5.0
Quick-opening closure	1	31.5
ITC access	1	~5.5
Instrument	6	1.0
Bottom head		
Outside diameter, ft-in.	5-4	
Thickness, in.	~10.25	
Penetrations	<u>Total No.</u>	<u>Dia., in.</u>
Control blade drive shafts	12	2.125
Rabbit facilities	2	3.25
ITC access	1	~5.5
Shell penetrations	<u>Total No.</u>	<u>Dia., in.</u>
Coolant nozzles	2	24
Beam tubes	10	8.5
Emergency coolant nozzles	2	2.5
Material		
Base metal (shell and heads)	SA-302B or SA-212B	
Clad	Type 304 SS or Inconel-600	

As shown in Fig. 1-16, the vessel is submerged in a pool of demineralized water (pH = 7.0) which serves as a biological shield during reactor operation and, also, during fuel transfer. The bolted top head, which is approximately 18.5 ft below the pool surface, can be removed to expose the entire plan section of the vessel. In addition to numerous penetrations for experimental facilities and instrumentation, the top head features a central, 31.5-in.-dia., quick-opening closure to expedite removal and replacement of the core insert assembly. During these operations, the high purity (pH = 5.0-7.0) primary coolant in the vessel will merge with the pool water.

The upper vessel wall is penetrated by a 22-in.-I.D. coolant inlet nozzle located 5 ft-4 in. above the core centerline. A coolant outlet nozzle of identical diameter is installed 6 ft-6 in. below the core centerline.

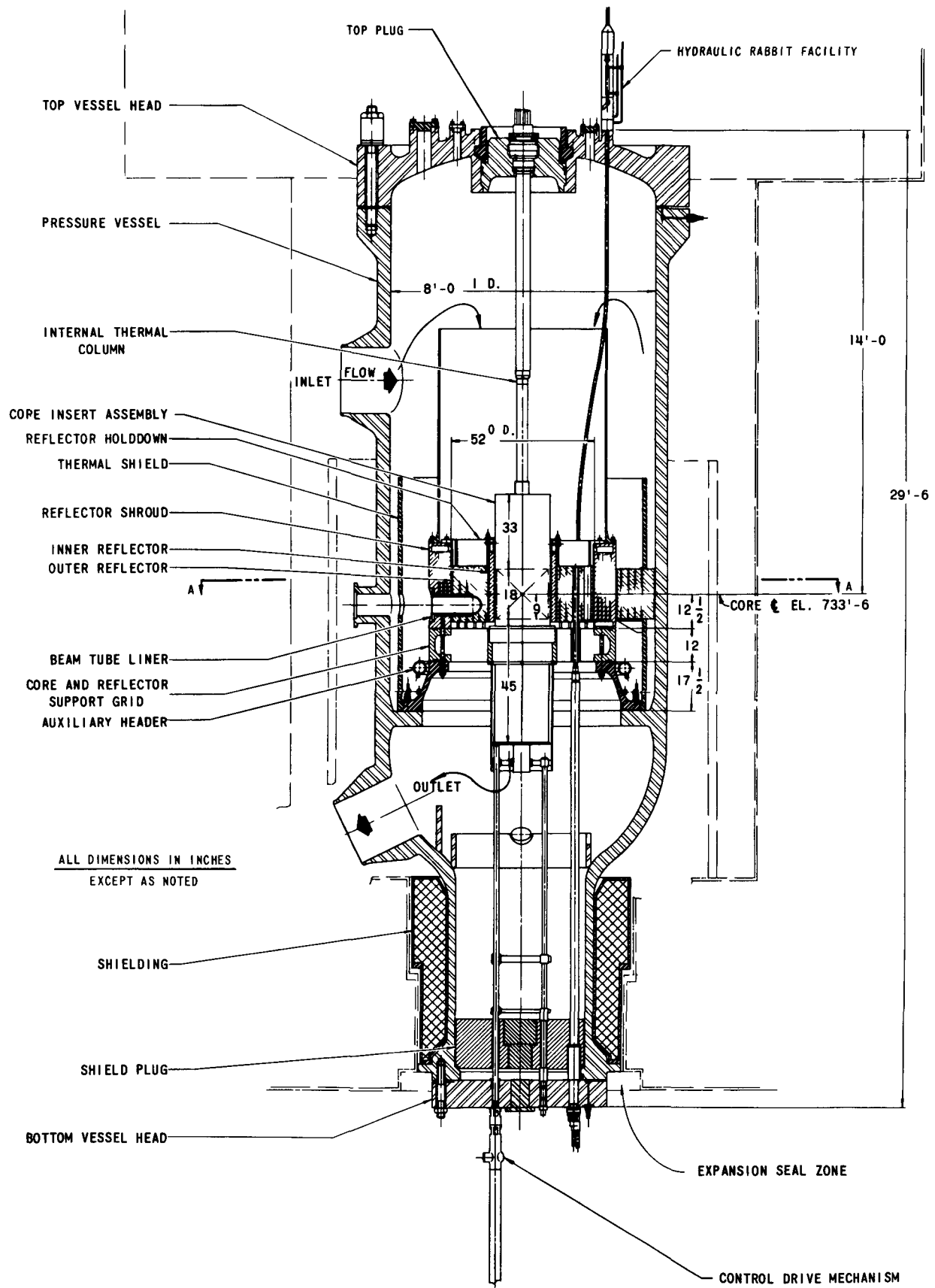


Fig. 1-16. Vertical section of reactor vessel installation in Reactor Pool. Also see Fig. 1-17 for plan view of Section A-A.

At a level corresponding to the core midplane, the vessel is penetrated by ten nozzles which accommodate the horizontal beam tubes. These nozzles (Fig. 1-17) are aligned with openings in the stainless steel liner of the Reactor Pool and concrete biological shield.

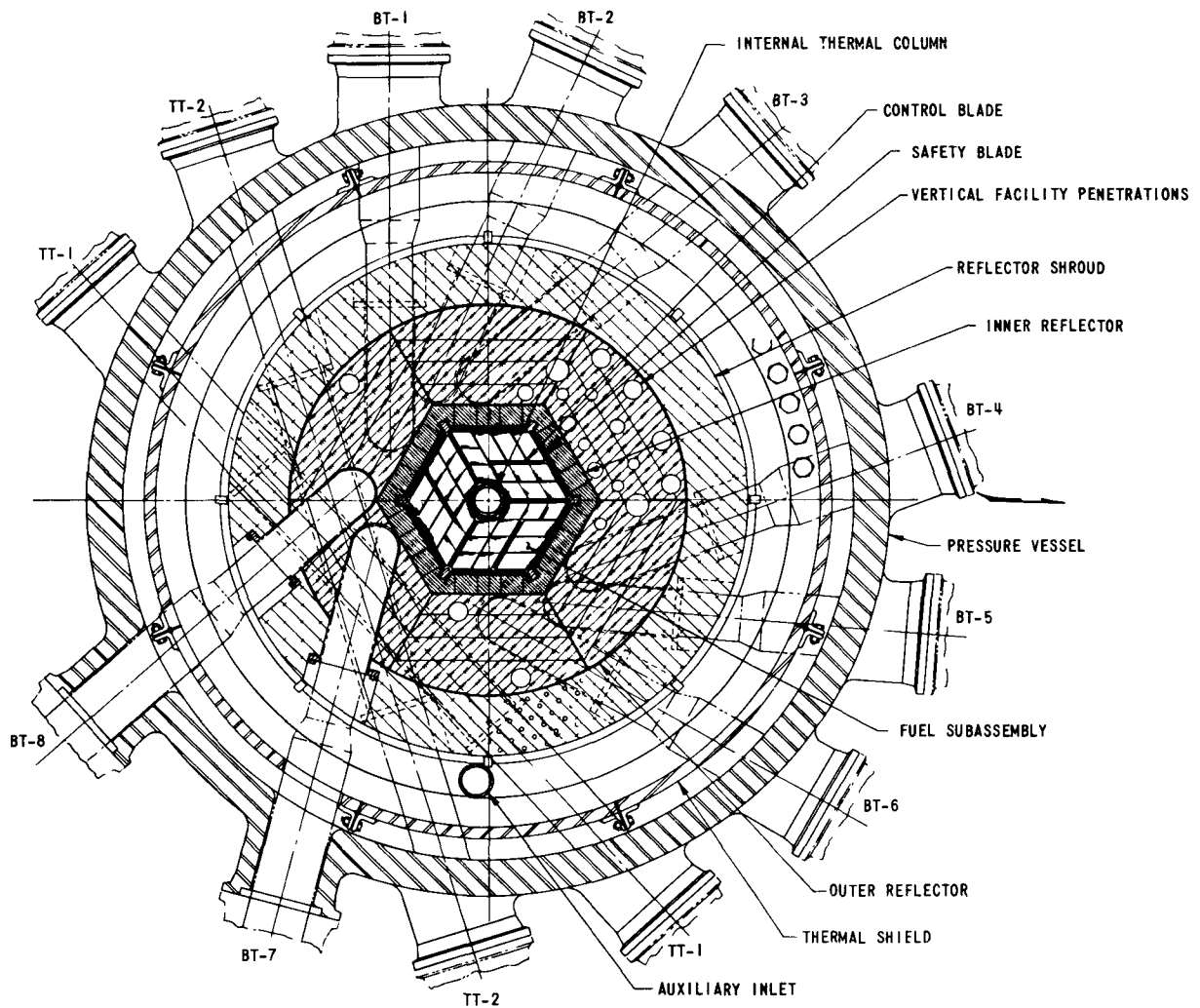


Fig. 1-17. Plan view of reactor vessel at core midplane. Beam tubes BT-7 and BT-8 are additive alternates.

To minimize vertical expansion of the vessel at operating temperature, the vessel supporting lugs and columns are placed close to the core midplane. In addition, bellows connections are installed between the biological shield penetrations and the beam tubes (see Fig. 1-20) to compensate for any misalignment or differential movement between the vessel and the tubes.

Primary coolant flows downward from the top inlet nozzle, through the core-reflector region, and exits through the bottom nozzle. Calculations indicate that during operation at 100 MW, the inner surface of the vessel above the pedestal support ring, including the top head, will be exposed to water at 135°F, while the surface below the core, but above the

smaller cylindrical extension, will be exposed to 164°F water. Moreover, the control rod nozzles and bottom section of the lower extension will be cooled and flushed with water which will flow upward and mix with coolant from the core. Hence, the transition zone between the 8-ft-dia. main vessel and the lower extension may be exposed alternately to 164 and 135°F water. The nature and extent of the surface stresses imposed by these temperature differentials will be investigated. If warranted, a thermal sleeve will be installed in this region.

The annulus between the beryllium reflector and vessel wall is filled with bulk coolant to shield the vessel against gamma and neutron radiation. One or more neutron windows may be installed in this region. In this event, the bulk of the nuclear detectors could be located outside the reactor vessel. Extending radially outside the vessel, the shielding consists of the pool water and a zone of magnetite concrete.

Control Blade Drive Mechanisms

Each of the twelve control blades is independently raised or lowered over a total travel of 20 in. by a vertical drive shaft which operates through a pressure breakdown seal in the vessel bottom head. Each shaft is actuated by a rack-and-pinion drive mechanism which is attached to the bottom head. Eleven of these mechanisms are identical; the twelfth is modified to operate as a regulating drive in conjunction with an automatic power controller. Except for the addition of an acceleration spring, the design is similar to the rack-and-pinion drives employed in the EBWR.

As shown in the reference design (Fig. 1-18), each mechanism consists of: (1) a gear rack with extension shaft and connector lock, which is rotated to engage or disengage the lower end of the control blade; rotation is effected by a special tool which penetrates the seal at the lower end of the drive housing; (2) a pinion and pinion shaft, which imparts linear motion to the rack; (3) a rotary, high-pressure, low-friction seal on the pinion shaft; (4) an electromagnetic clutch, which couples the pinion shaft to the output shaft of the drive motor during normal operation and is de-energized to permit rapid, downward insertion (scram) of the blade; (5) a compression spring, which in addition to gravity and hydraulic forces of the primary coolant flow, enhances blade acceleration during a scram; and (6) a hydraulic dashpot, which decelerates the blade at the end of the scram stroke.

In addition, each mechanism is equipped with: (1) a sensing device to ensure positive engagement (or disengagement) of the drive shaft and control blade; (2) cam-operated limit switches and a synchro transmitter geared to the drive motor output shaft to provide continuous blade position indication; and (3) a water back-flushing system to maintain the drive shaft piston and dashpot free of deposits or particulate matter. Finally, with possible exception of the regulating blade, the drive mechanisms will be energized by single-speed, reversible, a-c motors.

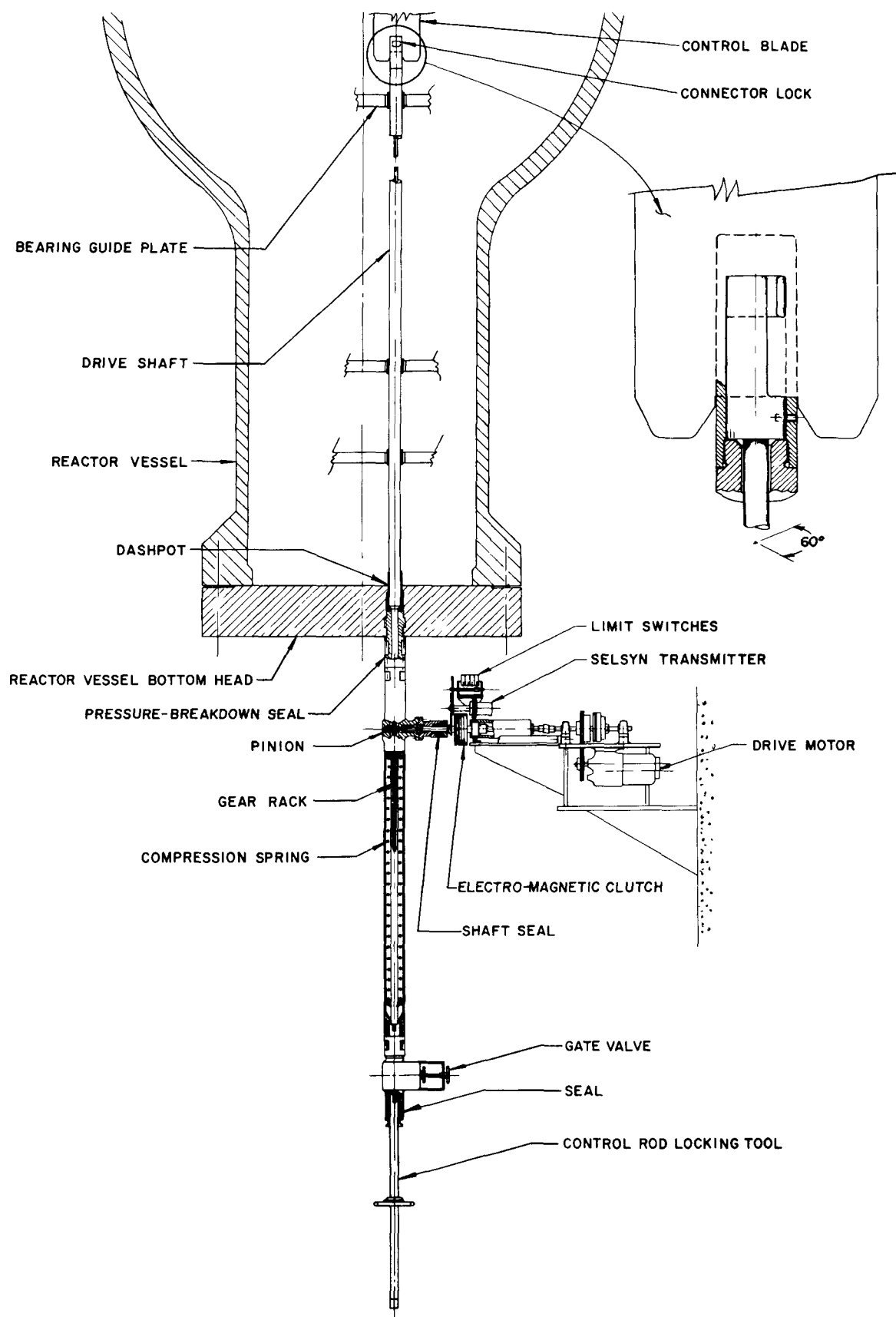


Fig. 1-18. Typical installation of reference design control blade drive mechanism

1.2.2.3 Fuel Handling

The fuel-handling system and sequence is designed to load and unload integral core insert assemblies and, if necessary, individual fuel sub-assemblies. In any event, until confined in appropriately shielded containers, all active cores or disassembled components thereof are transported to and from the reactor vessel while completely submerged in the light water-filled pools as shown in Fig. 1-19. Moreover, all operations involved in effecting these exchanges are observed directly from the personnel bridge crane which traverses the pools. Finally, suitable source and radiation detectors are employed to monitor certain operations which may reflect an increase in reactivity.

Spent Core

After reactor shutdown, the spent core is cooled by forced circulation of the primary coolant until the decay heat can be removed by natural circulation. At that time, the primary cooling system is reduced to atmospheric pressure.

The subsequent sequence of operations is described literally and pictorially in Fig. 1-19. In Step A, the ITC insert is released from the quick-opening closure plug by rotating a breech lock. In Step B, the water level is lowered by connecting a drain line to a pipe which extends downward into the pool.

Calculations indicate that removal of the inner beryllium reflector and substitution of water results in a reactivity loss of ~3%. Therefore, in Step C, a transport absorber is locked in the ITC shroud to provide additional shutdown margin. Also, twelve control blade locks are installed to prevent the blades from falling out of the core in the event the core is dropped by the handling fixture.

In Step D, the core insert assembly is transported through an underwater gate, lowered, and secured to a pedestal in the adjoining Spent Core Storage Pool. After a prescribed decay period, the assembly is removed through another gate and positioned on a pedestal in the adjacent Core Disassembly Pool (Step E). Here, the core components are disassembled and then transported to the Core Parts Storage Pool (Step F), where they are further disassembled and confined in shielded shipping casks. These casks are hoisted onto a dolly and transferred through the underwater hatch in the transfer canal leading to the Active Material Handling Building (Step G). Finally, with the aid of the building crane, the casks are removed from the canal, decontaminated, and then deposited onto a truck for transport to a processing site (Step H).

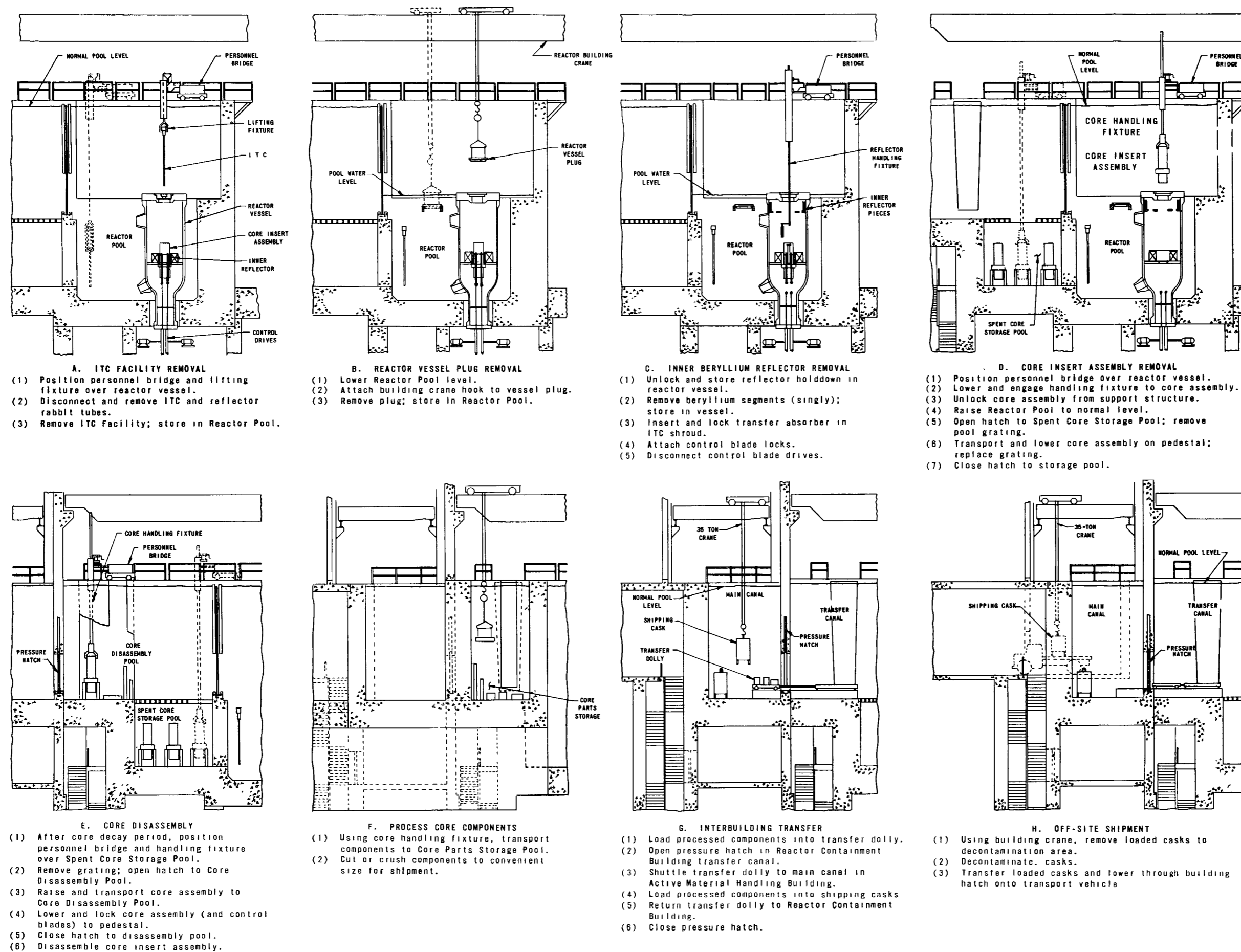


Fig. 1-19

Sequence employed in removing spent core from reactor vessel to shipping platform in Active Material Handling Building

New Core

Each new core insert assembly will either be shipped to Argonne by the fuel vendor, or it will be assembled on the Laboratory grounds other than at the AARR site. In either event, each core assembly will be inspected and subjected to physics measurements in an ANL critical facility to ensure compliance with specifications. If not needed immediately at AARR, the core will be dried, placed in a shielded container and stored elsewhere.

Upon arrival at AARR, the transport vehicle will position the shielded container beneath a hatch in the ceiling of the Active Material Handling Building (see Step H, Fig. 1-19). With the aid of the building crane, the core is removed from the container to an area near the main canal. At this point, radiation monitors and a source detector are attached to the core.

Again, using the building crane, the core is lowered into a dry tank in the main canal. This tank is filled with pool water at a controlled rate and the reactivity changes are monitored. Upon completion of the wetting operation, the core is hoisted from the tank, lowered onto the dolly in the main canal (see Step G, Fig. 1-19), and transported through the underwater hatches into the Reactor Pool.

With the aid of the core handling fixture, the core is transported from the dolly, lowered into the reactor vessel, and bolted to the support grid. This operation is also monitored for reactivity changes.

The balance of the loading sequence is essentially the reverse of the unloading sequence. Briefly, the control blades and drives are interconnected, the blade locks are removed, and each blade is tested for free movement. The shutdown margin with the transport absorber in the ITC shroud is determined. It is then withdrawn, at a predetermined rate, and ultimately removed from the Reactor Containment Building. At this time, the portable monitors and the source detector are removed from the core assembly and normal nuclear surveillance is restored. This surveillance is maintained while each of the inner reflector segments is installed; in addition, one of the control blades is poised for rapid insertion.

Following installation of the inner reflector and holddown, the quick-opening closure plug is removed from storage and installed in the reactor vessel top head, the ITC is inserted and sealed to the central opening in the plug, and the vessel is pressure tested to ensure leaktight integrity prior to start-up.

Damaged Core

In the event of a fuel plate rupture and consequent release of fission products, forced circulation of the coolant will be employed in conjunction

with the primary coolant purification system to remove the decay heat and the entrained fission products. When the activity has been reduced to tolerable levels, the core assembly will be removed from the vessel, as described previously, but transported directly to the Core Disassembly Pool for an additional decay period. This procedure is designed to minimize contamination of the respective pools.

Subsequently, the core will be disassembled and each fuel subassembly subjected to a leak detection test. Subassemblies with ruptured fuel plates will be loaded in separate sealed containers and transferred to the main canal. Here, they will be removed into shielded casks, equipped with adequate cooling systems, for off-site shipment.

1.2.2.4 Experimental Facilities

To a large degree, the basic features, number, location, and contemplated use of experimental facilities in AARR have been defined, and much of the design calculations have been performed. As described briefly in the following subsections, there will be available: (1) eight horizontal beam tubes (6 blind and 2 through-tubes) for physics studies with high-intensity, thermal neutron beams outside the reactor vessel; and (2) thirty vertical facilities for both long-term (static baskets) and accelerated (pneumatic and hydraulic rabbits) irradiation of samples in the internal thermal column (ITC) and outer beryllium reflector.

In addition, provisions have been made for: (1) future installation of two more horizontal blind tubes to transmit neutron beams of slightly lower than maximum flux intensity; and (2) replacement of static baskets in the ITC and reflector with pneumatic and hydraulic rabbits.

There are no irradiation facilities located in the inner beryllium reflector. However, by installing special, cored and removable beryllium segments, 24 additional static baskets could be made available for irradiation of samples over a period equal to the core lifetime at full power (90 days).

Horizontal Beam Tubes

Design Criteria and Philosophy. Conditions within the reactor vessel require that the beam tubes be designed to withstand: (1) a collapsing pressure of 875 psig; (2) thermal stresses created by the high-temperature coolant and by gamma and neutron heating; and (3) material damage by sustained exposure to gamma and neutron radiation. Finally, the tube material must have a low total absorption cross section to ensure transmission of beams at maximum neutron flux density.

Aluminum 6061-T6 was selected as the most suitable tube material. In addition to its structural strength and acceptable total neutron absorption cross section: (1) the material has a high thermal conductivity, which results in low thermal gradients, hence low thermal stresses, across the tube wall; and (2) it will not suffer severe changes in physical properties due to neutron radiation over a reasonable beam tube lifetime.

Standardization, interchangeability, and ease of assembly of beam tube components has been emphasized throughout the conceptual design phase. With one exception, i.e., length of the through-tube adapter, which is tailored consistent with the in-pile length of the tube, this philosophy also has reflected standardization of the reactor vessel nozzles, nozzle-tube interconnections and seals, tube penetrations and seals in the biological shielding, shield liners and mode of alignment, and assembly tools. As a result, fabrication costs can be reduced significantly, and initial installation, subsequent maintenance, and/or replacement of defective components can be carried out expeditiously.

Conceptual Design. Design concepts of the blind tube and the through-tube have been completed. A prototype blind tube (see ANL-7190, p.102) is being fabricated for tests designed to identify areas in need of further development and refinement.

As shown in Fig. 1-20, one end of both tubes is identical in all respects. Except for the hemispherical tip of the blind tube, both tubes have an inside diameter of 5 in., and a wall thickness of 0.45 in. In the case of blind tubes, the wall thickness tapers to 0.225 in. at the tip. At the opposite end, the through-tube terminates in a breech lock connection to the stainless steel tube adapter. This connector features a high-pressure bellows seal which compensates for axial thermal expansion of the tube during reactor operation. It is backed up by a split-ring seal to prevent catastrophic leakage in the event of a bellows seal failure.

The beam tube adapter extends from the biological shield face to the reactor vessel nozzle. Except for the Grayloc seal connection between the beam tube adapter and vessel nozzle, which will be serviced from atop the vessel, all assembly and disassembly operations will be performed through the beam port in the biological shield. As shown in Fig. 1-20, the design of all connections that are not readily accessible is based on the breech-lock principle to facilitate disassembly by remotely-operated tools. Installation of the beam tube represents the final phase of the assembly sequence.

The stepped design of the beam tube assembly furnishes a conically-shaped beam of high-intensity neutrons approximately 12 in. in diameter at the shield face. The width of the collimated beam is sufficient to permit performance of two experiments simultaneously by splitting the beam. The collimator adapter provides a connection for the installation of the experimenter's collimator.

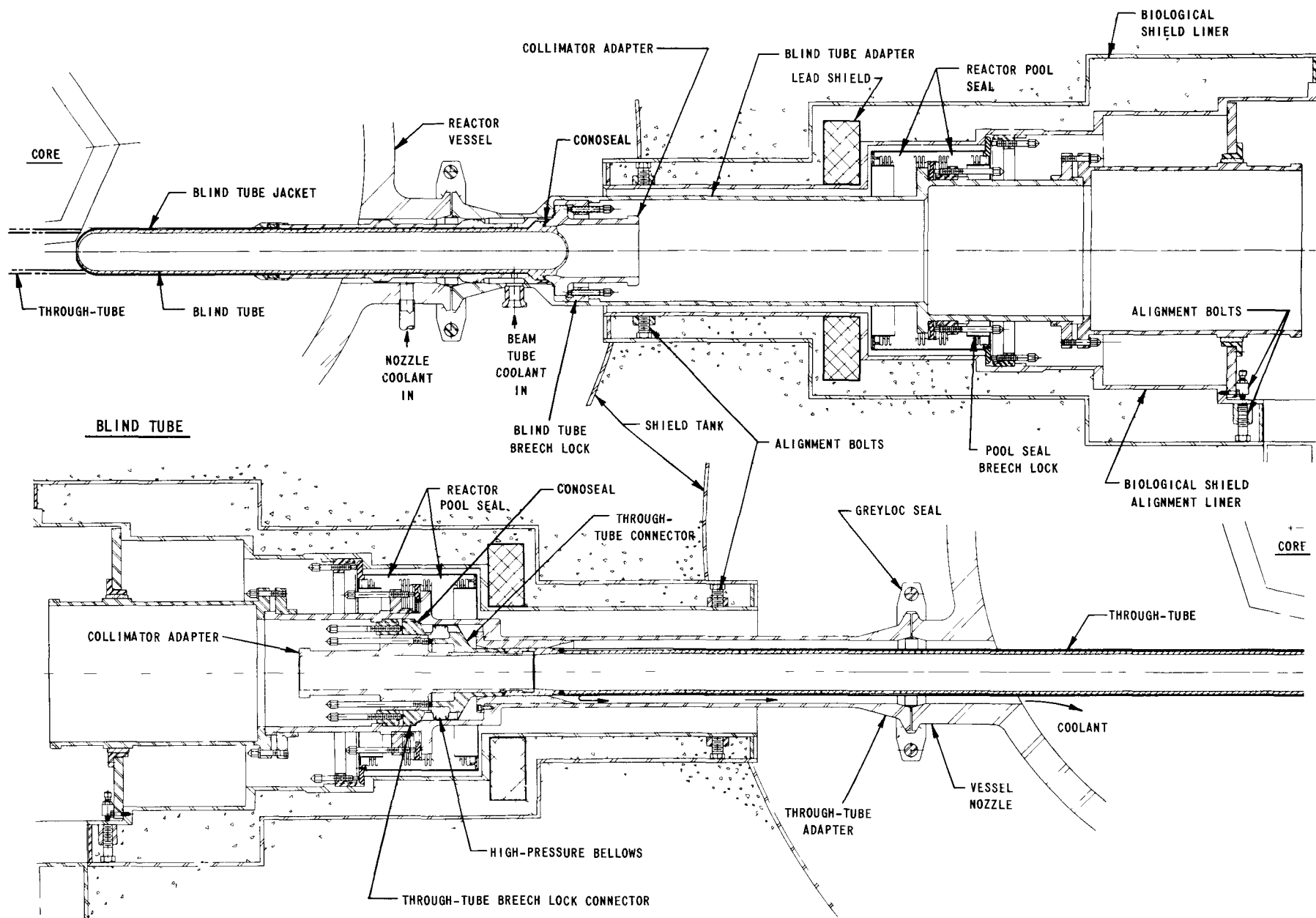


Fig. 1-20. Sectional plan view of typical through-tube and blind tube installation

Internal Thermal Column

Located centrally in the reactor core, the internal thermal column contains eleven facilities for short- and long-term irradiation of encapsulated samples in a region of high thermal neutron flux. These facilities (Table 1-4) are supported in a two-piece, interlocked assembly hereafter called the ITC Facility.

Table 1-4. Summary of ITC Irradiation Test Facilities

Type of Facility	Total No.	Sample Size, in.		Transfer Internal ^a	Exposure Time
		Dia.	Accrued Length		
Hydraulic Rabbits	5	0.5	24.0 (max.)	30 sec	
Fast Gas Rabbit	1	0.5	0.75 ^b	50 msec-1 sec	~1 msec (min.)
Gas-Cooled Rabbit	1	0.1	0.75 ^b	2.0 (min.)	1 sec (min.)
Static Baskets	4	0.5	18.0 (max.)	-	Core lifetime

^aFrom reactor to load-unload station.

^bOne sample per irradiation.

As shown in Fig. 1-21, the lower, tubular, reactor core assembly, which contains all the irradiation facilities, extends 19 ft from the top of the vessel and terminates about 5 ft below the core centerline. It is supported laterally by guides below the core. The upper end is interlocked with the top assembly which, in turn, is fastened to the closure plug by a breech lock which seals against rubber O-rings in the plug. Fittings for interconnecting the hydraulic and pneumatic tubes within the facility to the respective load-unload stations are installed in the top assembly.

Primary coolant flow is maintained through the hydraulic rabbit and static basket facilities by the pressure differential ($\Delta P = \sim 110$ psi) across the ITC Facility. Coolant enters the flow tube at the top of each hydraulic rabbit, flows downward through the annulus between the sample and tube, and discharges into the coolant below the core. Velocity of the bulk water within the facility support housing is intentionally kept low to prevent rapid introduction of voids. Accordingly, the outer surface is cooled by water which enters through ports in the bottom of the housing, flows up through the housing, then downward through the annulus formed by the housing and ITC shroud, and discharges through holes in the rabbit lateral support grid plate.

Helium is used to cool and to propel samples in the pneumatic rabbit facilities, as described in a later subsection.

Outer Beryllium Reflector

In addition to the eight horizontal openings for beam tubes and through-tubes, there are 19 vertical penetrations in the outer beryllium

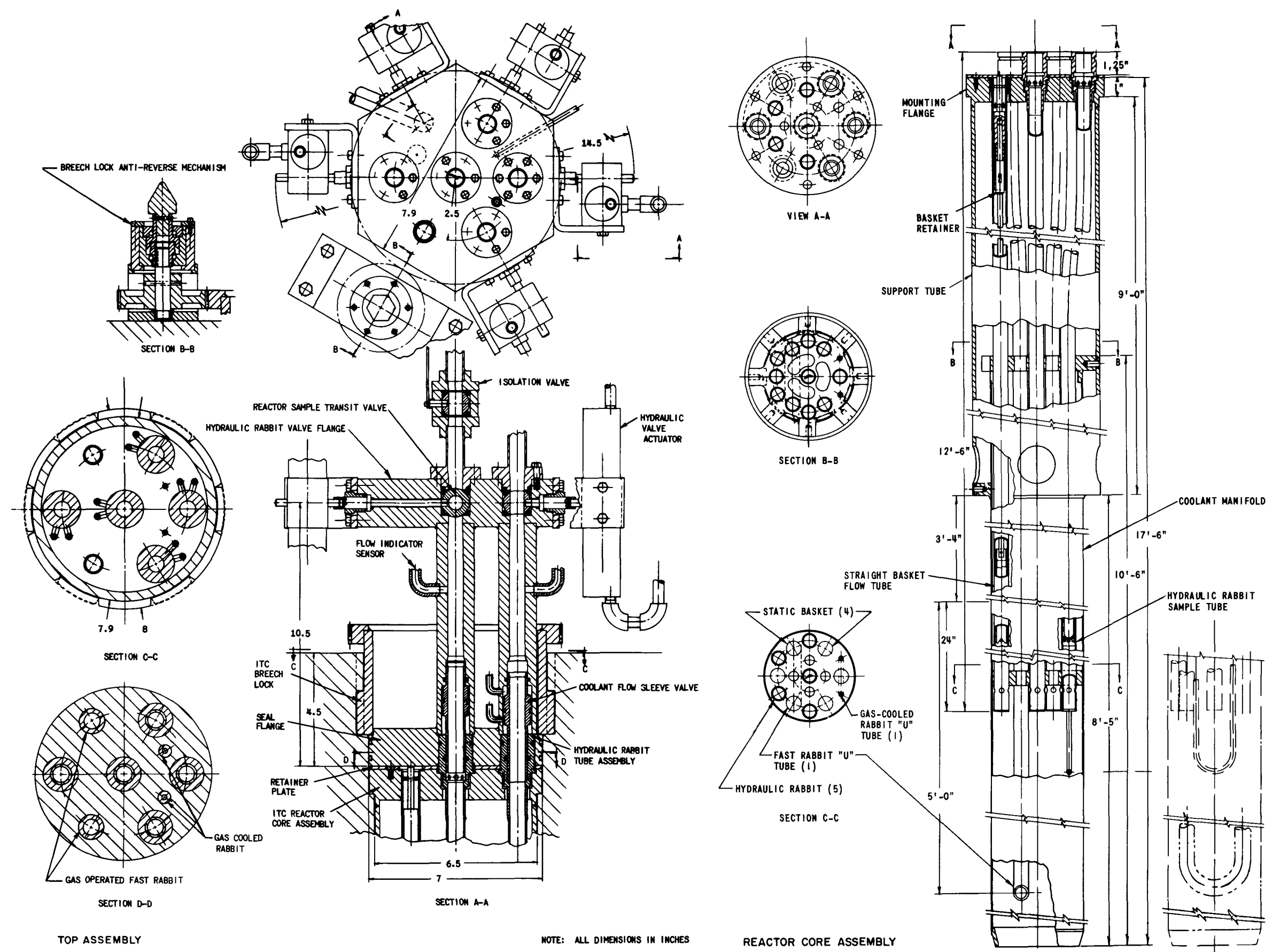


Fig. 1-21
Sectional views of ITC
Irradiation Facility

reflector. Each penetration is cylindrical and extends the full height of the reflector. Table 1-5 lists the respective diameters, radial orientation, and contemplated uses of these penetrations. Those listed as spares will be sealed temporarily with a beryllium filler rod of corresponding diameter.

Table 1-5. Summary of Irradiation Facilities Available in Outer Beryllium Reflector

Facility No.	Diameter, in.	Distance from Core Center, in.	Angular Orientation, ^a degrees	Contemplated Use	Sample Size, in.		Transfer Interval, ^b sec
					Diameter	Accrued Length (max.)	
V2-1	1.5	15.0	108	Hydraulic Rabbit	0.5	3.0	30
V2-3	1.5	15.0	150	Hydraulic Rabbit	0.5	3.0	30
V2-5	1.5	15.0	192	Spare			
V3-1	1.5	17.75	127	Spare			
V3-2	1.5	17.75	173	Spare			
V4-2	1.5	19.5	133	Hydraulic Rabbit	1.0	18.0	30
V4-4	1.5	19.5	167	Hydraulic Rabbit	1.0	18.0	30
V2-2	2.0	15.25	138	Possible Source	-	-	-
V2-4	2.0	15.25	162	Spare			
V2-6	2.0	15.5	285	Gas Rabbit	0.5 ^c	3.0 ^c	2.0 ^d
V4-3	2.0	19.5	150	Gas Rabbit	0.5 ^c	3.0 ^c	2.0 ^d
V5-1	2.5	24.0	40	Spare			
V5-2	2.5	24.0	125	Spare			
V5-3	2.5	24.0	138	Spare			
V5-4	2.5	24.0	162	Spare			
V5-5	2.5	24.0	175	Spare			
V5-6	2.5	24.0	260	Spare			
V4-1	3.0	19.5	118	Static Basket	2.0	18.0	
V4-5	3.0	19.5	182	Static Basket	2.0	18.0	

^aFrom Reactor & Building N-S centerline.

^bFrom reactor to load-unload station.

^cSingle sample.

^dExposure time = 1 sec (min.).

Figure 1-22 shows a typical static basket installation. Briefly, it consists of a tube, which extends downward into the reflector penetration, a locking mechanism for securing the contained sample, and a holddown device to fasten the assembly to the reflector top structure. When not used for irradiation tests, the basket is replaced with a beryllium filler. A holddown device and locking mechanism are also provided for the filler insert.

Again, using the pressure drop across the core, primary coolant enters each basket tube through orifices at the top, flows downward through the annulus between the tube and sample, and discharges into the bulk coolant through orifices in the tube bottom.

The hydraulic- and pneumatic-rabbit facilities are cooled internally and operated by the primary coolant and by helium, respectively.

Hydraulic Rabbits

Each hydraulic rabbit system is equipped to propel samples from load-unload stations in the Active Material Handling Building Rabbit Pool to transfer stations in the Reactor Pool. From these stations, the samples are routed to either the ITC or outer beryllium reflector, cooled throughout the exposure period, and then returned to the load-unload stations.

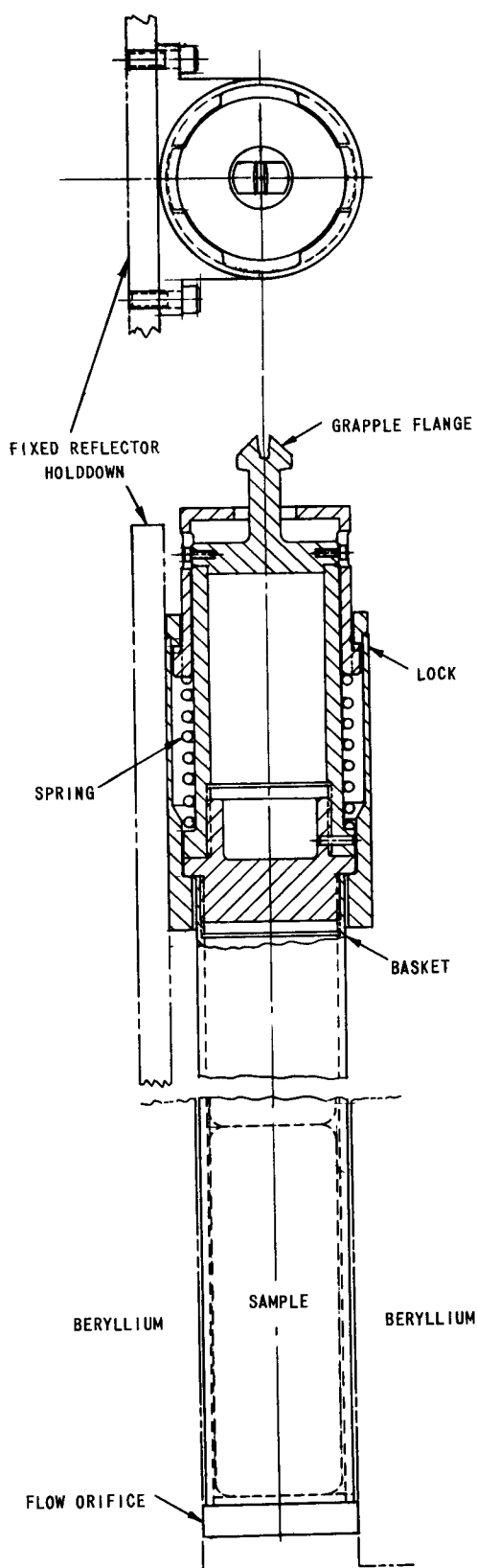


Fig. 1-22. Typical static basket irradiation facility in outer beryllium reflector

The portion of the system between the load-unload and transfer stations is a low-pressure circuit independent of the reactor, whereas the portion between the transfer station and the reactor is part of the high-pressure primary coolant system. All hydraulic tubes enter the reactor through the vessel top head.

In operation, samples are charged into the load-unload station and, by proper setting of the low-pressure system valves, are transported to the transfer station. At this point, the low-pressure system valves are closed, and the appropriate valves in the high-pressure primary system are opened. Primary coolant circulated by the irradiation facility cooling system booster pumps (at 785 psia) propels the samples into the ITC or reflector. Here, the samples are positioned by a mechanical stop in the tube bottom, and the propelling coolant discharges into the core outlet plenum (at about 640 psia).

Immediately after the samples are positioned within the reactor, the high-pressure transit valve is closed. Simultaneously, a sleeve valve assembly in the vessel top head is positioned to direct primary coolant from the core inlet plenum downward through the hydraulic tube and around the contained samples, as described previously. This mode of cooling continues throughout the irradiation period.

Preparatory to unloading, the high-pressure transit valve is opened. Also, the sleeve valve assembly is positioned to isolate the core inlet plenum and, simultaneously, to direct coolant flow from the core outlet plenum up through the hydraulic tube back to the transfer station. This station is vented to the primary degasifier tank. In addition, a portion of the pressure differential between the core outlet plenum (~640 psia) and the degasifier tank (~5 psia) is used to assist in effecting the flow reversal. After arrival of the sample in the

transfer station, the high-pressure transit valve is closed, the sleeve valve assembly is repositioned for the next loading, and the low-pressure system is used to return the sample to the load-unload station.

Pneumatic Rabbits

Except for the valving arrangement, sample transit time (see Tables 1-4 and 1-5), and reversal point within the reactor, the pneumatic rabbit systems are essentially similar in operation. Each system employs high-pressure helium to propel and to cool single, encapsulated samples in tubes leading from load-unload stations in the Laboratory and Office Building to the reactor vessel top head (ITC rabbits) or the bottom head (reflector rabbits). In all systems, the valves in the transfer tubes within the Reactor Containment Building are open only when a sample is in transit to or from the reactor. Also, since the operating gas pressure does not exceed 400 psia at any point in the systems, a tube rupture will not result in entry of gas voids into the reactor.

The gas-cooled rabbits in the ITC operate independent of those in the reflector. Each system employs two gas pumps, one operating and one standby. On the other hand, both rabbits in the reflector are serviced by a single gas system; hence, only one rabbit tube can be serviced at a time.

Figure 1-23 is a flow diagram which is representative of the gas-cooled systems in the ITC and outer beryllium reflector. In operation, the sample is inserted in the load-unload station, the valves in mode (3) are opened, and the sample is propelled into the ITC or reflector to a mechanical stop at the core midplane. The containment valves are closed (mode (4)), and the sample is cooled by the high-pressure gas throughout the exposure period. Subsequently, the containment valves are opened and the gas flow is reversed (mode (5)). Note: Damaged capsules, or capsules which are monitored above prescribed activity levels, are stopped within the shielded zone (Valve G). Upon arrival of the sample at the load-unload station, the containment valves are closed.

In the fast gas rabbit systems, the sample is propelled rapidly into the ITC, down through the reactor to a mechanical stop below the core. At this stage in the sequence, the containment valves are closed, the high-pressure gas is circulated to cool the sample, and a hold-up tank is pressurized to effect return of the sample. After the sample has decayed sufficiently, a release valve and the containment valves are opened, the gas flow is reversed, and the sample is returned to the load-unload station. Finally, the containment valves are closed to complete the cycle.

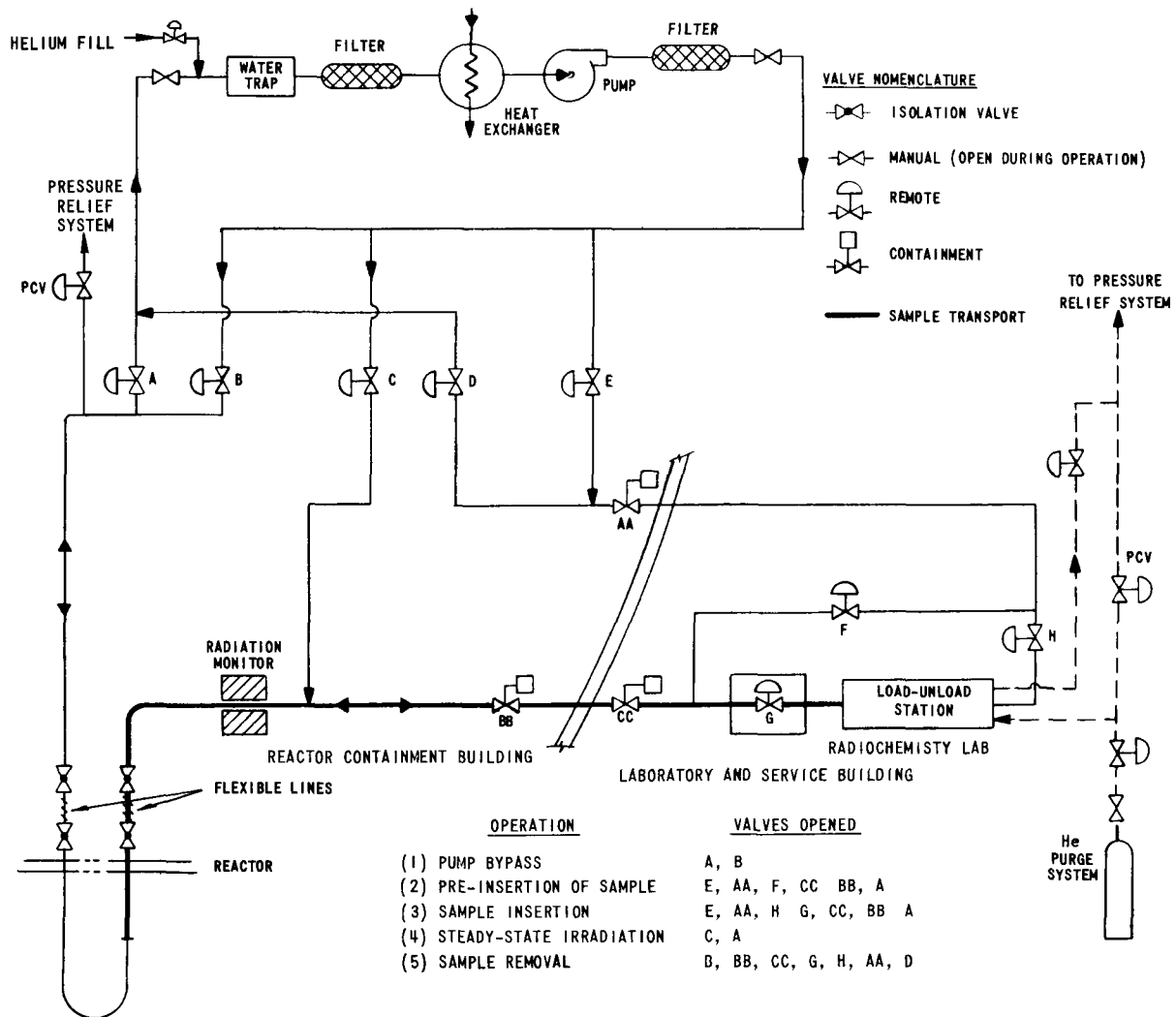


Fig. 1-23. Flow diagram for gas-cooled rabbits in ITC and outer beryllium reflector

1 2 2 5 Heat Removal and Auxiliary Systems

Primary Coolant System

The primary coolant system removes heat generated in the reactor and transfers it to the secondary coolant system for subsequent dissipation to the environment. In addition to the main coolant loop, the primary system includes six subsystems whose functions are described below.

Figure 1-24 is a simplified diagram, showing the flow distributions through the primary coolant loop and the related subsystems. The values are approximate and have not been corrected for coolant temperature differentials prevailing in various portions of the system.

Primary Coolant Loop This loop is comprised of the reactor vessel, three parallel-connected heat exchangers, a full-flow filter immediately

upstream of the vessel, two half-capacity pumps, 24-in. interconnecting piping, associated valves, and a pressure relief tank into which the safety valves discharge.

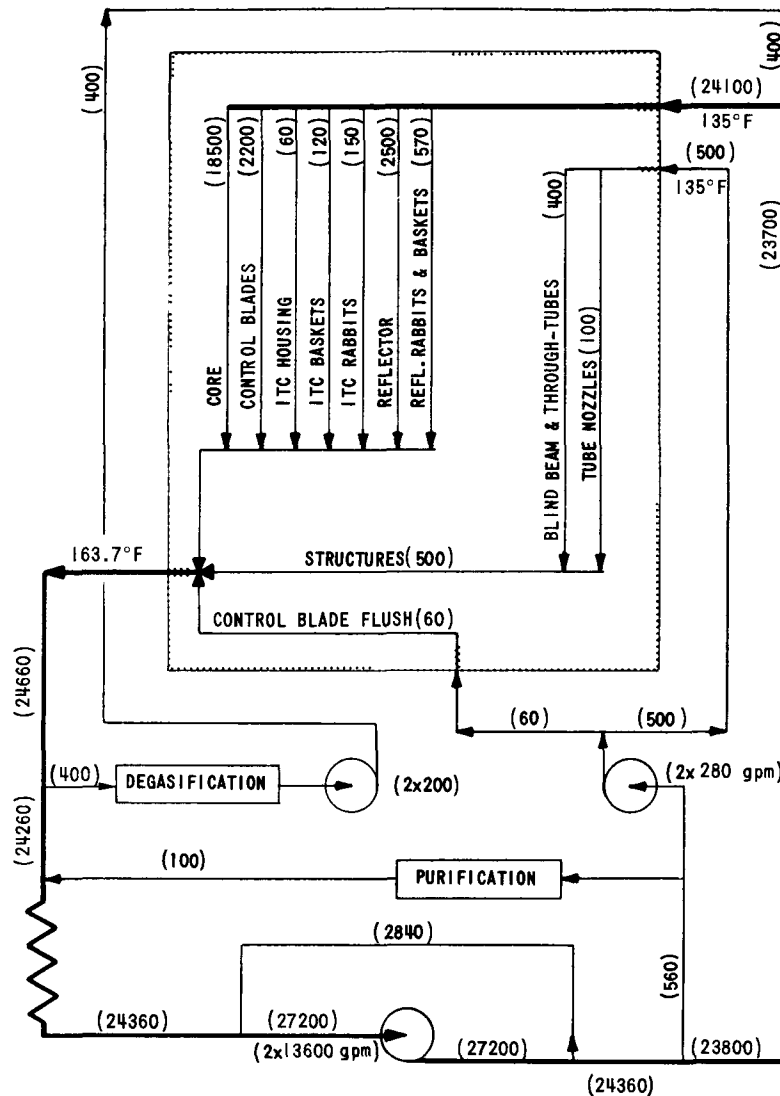


Fig. 1-24. Distribution of primary coolant flow (gpm) through reactor vessel components (shaded zone) and auxiliary systems

Each heat exchanger is of the vertical, shell-and-tube type, and is constructed in accordance with Section III, Class A, of the ASME Code and Class R of the TEMA Standards. Sized for 33.3 MW thermal capacity, each unit features Incoloy 800 tubes and a Type 304 stainless steel-clad, carbon steel shell with bolted bonnets. Primary coolant circulates on the shell side and secondary coolant on the tube side.

Each pump is a vertical, stainless steel, single suction, centrifugal unit, with a rating of 13,000 gpm at 135°F, 640-psia inlet, and 500-ft head. Each unit is coupled, through a controlled-leakage shaft seal, to a water-cooled a-c motor; estimated horsepower is 2000.

Type 304 stainless steel piping is used throughout this system, and conforms with the ASA Code for Pressure Piping (Power Section: B31.1) and applicable nuclear code cases. All joints are welded and, except for certain sections, the piping is designed for system operation at 250°F and 875 psig. Piping rated at higher pressures will be used in sections where valve closure can impose pump shut-off head in addition to system pressure.

Emergency and Shutdown Cooling. In operation, this system utilizes the primary loop components, with one exception: each pump is energized by a d-c pony motor which is mounted on the pump shaft in tandem with the a-c motor. Upon failure of main power or after reactor shutdown, each pony motor is supplied with Class I (uninterrupted) power to operate the pump at reduced speed. Under these conditions, either pump will circulate coolant at 3000 gpm, which is sufficient to remove the core decay heat.

Purification. In this system, coolant at 135°F and 100 gpm is circulated from the primary pump discharge line through a decay vessel to reduce the N^{16} activity. It then flows through a small heat exchanger, where the water is cooled to 120°F, and a series of filters and mixed-bed demineralizers. Finally, the purified water is returned to the main loop upstream of the heat exchangers.

Pressurization. Normal coolant operating pressure (750 psi) at the vessel inlet is maintained by two pressurizing pumps, with a combined capacity of 400 gpm. These pumps discharge into the main loop upstream of the reactor vessel; discharge is regulated by a control valve which is responsive to reactor inlet pressure.

A surge tank, blanketed internally with helium, is also connected to the piping upstream of the vessel. This tank absorbs any rapid surges in pressure or variations in the loop water inventory.

Degasification. The nature of dissolved and coolant-entrained gases removed by this system include: (1) atmospheric air in the cold coolant prior to start-up; (2) helium introduced from the surge tank; and fission product gases, if any. Some oxygen and hydrogen, produced by radiolytic decomposition of the coolant, is also removed; however, the quantities reach an equilibrium concentration which is essentially unaffected by the degasification system.

In operation, coolant at ~400 gpm is circulated through piping leading from the vessel to a pressure-reducing valve and into the degassifier tank. Here, the gases are removed, and cycled to the off-gas and tank vent system. Degassed water is pumped to a demineralized make-up water storage tank. From the tank, the water is returned to the loop by the pressurization system.

Irradiation Facilities Cooling. This system features two half-capacity pressure booster pumps which circulate coolant at 135°F and 500 gpm from the main pump discharge line, through the beam tube thimble jackets and vessel nozzles, and back into the reactor vessel. The total flow includes 60 gpm for continuous flushing of the control blade drive shaft nozzles and shock absorber, and intermittent propulsion-cooling of hydraulic rabbits.

Soluble Poison Injection System. Should the control blades become inoperable, and upon manual signal from the control room, this system will inject sufficient sodium pentaborate solution to reduce core reactivity by $\sim 2\% \Delta k/k$. This reduction is effected within 7.5 min. after the initiating signal.

The injection system is designed to function with the primary coolant system at normal operating pressures and at either normal or emergency coolant flowrates.

Secondary Cooling Loop

Heat absorbed by secondary coolant on the tube side of the main heat exchangers is removed through 24-in. carbon steel piping which leads to a cooling tower. Here, the heat is rejected to the atmosphere. Make-up water for the tower is obtained from the nearby Chicago Sanitary and Ship Canal via the Laboratory Water Treatment Plant.

Subcooled water is circulated back through the heat exchanger tubes by two half-capacity, a-c powered pumps. Water temperature is controlled by regulating the flowrate. Both pumps are also equipped with tandem-mounted, d-c pony motors to sustain coolant flow during an emergency and after reactor shutdown.

The cooling tower also serves as a heat sink for the irradiation facilities cooling system, the primary purification system cooler, and the Reactor Pool and Transfer Canal cooling system.

Pool and Canal Cooling System

Each pool (reactor, core storage, core disassembly) and the inter-connecting canals is serviced by a separate cooling circuit sized to remove ~ 0.34 MW of reactor or decay heat. A spare circuit is available for cooling either the reactor or core storage pools upon failure of their respective circuits. Use of the core disassembly pool circuit is restricted to prevent gross contamination of the entire pool and canal system. Heat removed from the pools is transferred to a chilled water system and, ultimately, to the cooling tower.

Chilled water is used in the pools and canals to avoid excessive evaporation within the Reactor Containment Building. Components of the chilled water system include a refrigeration unit, two pumps, and a surge tank. Condensing water for the refrigeration unit is supplied from the secondary coolant system. In operation, approximately 640 gpm of chilled water (45°F) is circulated, providing ~267 tons of cooling capacity. This cooling load is equivalent to the combined convective heat loss (0.94 MW heat) from the reactor vessel at full power and the decay heat from stored spent cores.

Provisions have been made for future installation of an air conditioning system as an emergency backup for the chilled water refrigeration system.

Purification of all pool and canal water is accomplished continuously through a common overflow system and mixed-bed demineralizer. Make-up water is introduced to a level-controlled tank in the overflow loop. When being used, the Core Disassembly Pool is isolated from the overflow system. The reactor pool, in addition to being connected to the overflow system, is serviced by a separate purification loop.

Two additional demineralizer units are provided. One is installed in the coolant loop of the Core Disassembly Pool, since operations within the pool may require large-scale removal of entrained contaminants. The other unit is available for service with any pool cooling circuit that may be accidentally contaminated during transfer of a spent core.

All pool and canal compartments are piped to a dump tank in an active waste storage facility. This tank is large enough to accommodate water from the largest pool. During refueling operations, it is used to drain and lower the Reactor Pool level. In all pools, drain pipes lead up to the surface level to prevent accidental loss of shielding water.

1.2.2.6 Instrumentation and Control

Instrumentation is provided for monitoring all parameters that are necessary to ensure safe operation of the reactor, experimental facilities, and process systems; and to protect plant personnel and the general public from exposure to harmful radiation.

All vital information is transmitted to the control room where essentially all routine operations, including reactor start-up and shutdown, are monitored and controlled.

Audible and visual alarms are actuated upon the occurrence of any potentially unsafe abnormality in plant condition. Corrective and protective action is initiated automatically, where required, by control and safety systems to prevent safe limits from being exceeded.

Nuclear Instrumentation. The nuclear instrumentation system is designed to monitor neutron flux from source level to approximately 300% of full power; to protect against excessively short period or high flux level; and to generate signals from the automatic neutron flux control system.

A total of eleven channels are employed. Of these, three redundant logarithmic count rate-period channels are used in the start-up range. A group of three redundant Log N-period channels is effective in the intermediate and power ranges, and overlaps the start-up channels approximately one decade. Protection against an excessively high neutron flux level is provided by three redundant linear channels, each with an effective range from approximately 5 to 150% of full power. A linear channel provides a signal for the automatic flux level controller and is effective in the range from about 1 to 100% of full power. Finally, a linear channel, equipped with a range switch, is used for sensitive indication of flux level in the intermediate and power ranges.

The start-up channel detectors are housed in thimbles which penetrate the reactor vessel. Detectors for all other channels are located outside the vessel. To enhance the neutron flux seen by these detectors, neutron windows are placed between the reflector and the vessel wall.

Additional neutron monitoring instrumentation will be temporarily installed to monitor reactivity changes during certain stages of core-handling operations and, also during installation of a new core until sufficient indication is provided by the permanent start-up channels.

Automatic Flux Control. This system will act through a servo-controlled regulating rod drive to maintain a preselected flux level within $\pm 1/2\%$; and, to change flux level at a constant period. Pending further analysis, this system also may be used to implement automatic setback of reactor power.

Process Instrumentation. The process instrumentation system is concerned with the measurement and control of all nonnuclear plant parameters. These include temperatures, flows, pressures, liquid levels, and chemistry of the primary coolant, secondary coolant and related process systems. Automatic control of reactor coolant inlet temperature and pressure is provided. Communication between all sensors, transducers, and their respective readouts, between control and controlled elements, is accomplished electrically.

Transmitters that are vulnerable to radiation will be installed as two-part units; the part susceptible to radiation will be mounted in an acceptably low radiation environment. In certain instances, spare sensors and transmitters will be installed in regions where access for repair or replacement of defective components is prohibited during reactor operation.

Although conventional analog instrumentation is employed, the design includes provisions for some degree of digital computer control in the future.

Radiation Monitoring System. This system is comprised of three subsystems equipped to continuously monitor working areas, process fluids, and plant effluents, respectively.

Area monitors will provide information relative to the ambient levels of gamma radiation, neutron radiation, and air particulate activity in all accessible areas within the facility that are subject to this radiation. The primary function of these monitors is the protection of working personnel.

Process liquid monitors will indicate activity levels in the primary and secondary coolant systems, in certain pools, and in the pool and canal cooling system. The primary coolant monitors will measure the level of N^{16} activity, which value will serve as a rough check on reactor power, and will also detect the presence of fission products in the coolant as an indication of fuel element rupture. Monitoring of the secondary side of various heat exchangers, whose primary fluids are or might be radioactive, will serve to indicate inadvertent leaks in these units.

Plant effluent monitors will measure the activity of gases exhausted to the stack. Individual monitoring will be provided for the Reactor Building exhaust, Active Materials Building exhaust, and the off-gas from the primary coolant. Automatic protective actions will be taken if the activity levels exceed preset limits. This will include directing the flow through filters and/or completely isolating a system from the stack. A combination particulate gas and iodine monitor in the stack will provide indication of the total activity of all effluents being released.

Reactor Safety System. The reactor safety system is provided to shut down the reactor automatically and rapidly to prevent safety limits from being exceeded. It comprises instruments and control devices that monitor plant parameters essential to reactor safety and provide inputs to the scram circuits through which power is supplied to the control rod magnetic clutches.

Where appropriate, redundancy is employed to prevent system nullification by failure of any one component or instrument channel, and to permit on-line testing. In general, three redundant channels, connected in two-out-of-three logic, will monitor the scram parameters. To the maximum extent feasible, each channel is designed to be physically and electrically independent of the other channels measuring the same variable.

Provisions for testing are arranged to permit verification of system integrity at any time without having to scram the reactor. Where technically and economically practicable, testing of instrumentation channels will include a complete channel from parameter change to final scram contact. Whenever a channel is made inoperative during a test, it will automatically generate a trip output signal, leaving the operable channels in a one-out-of-two configuration. Similarly, where feasible, trip output signals also will be generated automatically for any condition that interrupts normal channel operation. This includes removal of an essential module or subsystem from the protective circuits.

1.2.3 Supporting Research, Design, and Development

This section describes the nature and results of analytical and experimental work that has been and is being performed in support of the Title-I design outlined in the preceding section. This design reflected numerous revisions in the Preliminary Safety Analysis Report which was based on the plant concept described in the annual report for fiscal 1965. (See ANL-7190, p. 77.) Accordingly, the work in fiscal 1966 has been focussed primarily on reassessment of theoretical possibilities and consequences of a maximum credible accident consistent with the quality of design, materials, construction, operation, inherent stability, and engineered safeguards incorporated in the Title-I plant complex.

On April 6, 1966, a limited number of copies of the PSAR were forwarded for review by cognizant AEC-DRDT personnel. Their comments and questions were discussed at a joint meeting with ANL-AARR staff members on June 27-28, 1966. Final approval by the ACRS is expected in fiscal 1967.

1.2.3.1 Mark-I Core Development

Analytical and Experimental Heat Transfer

Both aspects of the heat transfer activities have a common objective: to operate the core at maximum power density consistent with plant safety and the production of maximum neutron flux for research purposes. During steady-state operation at 100 MW, the core conditions are expected to include a peak power density of ~ 5 MW/liter and a peak heat flux of $\sim 2 \times 10^6$ Btu/(hr)(ft²). Although steady-state analysis indicates the existence of large safety margins, these margins must be equally adequate during rapid power transients incurred by operational malfunctions and, particularly, by inadvertent reactivity additions.

Analytical. Thus far, two analytical methods have been employed to estimate the adequacy of the overall safety margins consequent to inadvertent reactivity additions. Earlier use of an analog model of the core

indicated that with the reactor initially operating at 100 MW, a \$0.90 step addition of positive reactivity represented the threshold for fuel melting at the hot spot. (See ANL-7190, p. 96.) This estimate was believed to be overly conservative; hence a method for achieving a more realistic assessment was sought. During the course of this search, the CHIC-KIN Code¹ was made available and, of the codes surveyed, it appeared the best suited for analyzing rapid power transients.

Subsequent calculations were made based on a \$1.00 ramp reactivity input (linearly inserted in 33 msec) at a steady power level of 100 MW, with no control rod action. Other input conditions and physical properties were selected to agree closely with values used in, and/or derived from, the analog model. The latter included the power vs. time behavior of the hot channel with skewed axial heat generation. (See ANL-7190, Fig. 1-33.)

These calculations constituted a parametric study involving three quantities:

Φ_{DNB} = Maximum surface heat flux which can be maintained with nucleate boiling; computed from the Zenkevich-Subbotin critical heat flux correlation.

f_r = Fraction of heat going into voids.

τ = Bubble collapse (or removal) time.

These quantities are essential to the physical description of transient boiling employed in the CHIC-KIN Code; their variation can have a profound effect on the course of hot channel behavior.

Briefly, the CHIC-KIN Code predicted that (1) pressure surges as high as 250 psi may occur upon initiation of subcooled local boiling during a transient, if the rate of vapor formation is rapid enough; and (2) very large local pressures (>2000 psi) also may occur during a time interval identified as the post power burst region, when a sizeable amount of vapor is present in the fuel channel. In the latter case, the fluid is at, or near, saturation conditions at the channel exit, and expulsion is predicted from both ends of the channel.

Whether such pressure surges will occur is subject to verification in the transient heat transfer tests which are to be conducted. To begin with, their magnitudes are questionable because the CHIC-KIN Code assumes a constant reference pressure and neglects sonic-velocity effects. Also, the pressure surges are affected by the number of axial sections used in the computations.

For the \$1.00, 33-msec ramp reactivity input at 100 MW, it is believed that values of f_r no less than 0.01-0.05 and values of τ no less than 10 msec constitute reasonably conservative estimates from a safety

viewpoint. However, values of f_r as high as 0.1 cannot be ruled out. Surface heat fluxes computed from the Zenkevich-Subbotin correlation should be conservative during the power burst, but might not be overly so when applied to the post power burst region.

In conclusion, the CHIC-KIN Code computations indicate that a \$1.00 ramp reactivity input of 33 msec duration at 100 MW, in the absence of control rod action, will lead either to fuel melting and/or pressure surges, with fluid expulsion at hot channel locations. This supports, in part, the threshold for fuel melting estimated from the previous analog studies, i.e., a step reactivity addition of \$0.90 at an initial power of 100 MW.

Steady-State Heat Transfer Tests. Both steady-state and transient heat transfer tests will be conducted sequentially in the same facility. As a consequence, the steady-state test series has been delayed pending improvements in burnout detection and tripping of power to the test section, and demonstrated feasibility of using the power supply for the transient tests. That the improvements in burnout detection and power tripping will be of immeasurable help to the steady-state test program is best illustrated by preliminary checkout tests. In these tests, a single test section was used to obtain 23 burnout points and about 95 specific data points. By comparison, three burnout points were obtained at the expense of three test sections, as reported in ANL-7190, p. 89.

Transient Heat Transfer Tests. The major activities related to these tests have been to demonstrate feasibility of using a 1500-kW, d-c power supply for resistance heating of simulated AARR fuel plate channel test sections, to design the test sections, and to develop an X-ray system for measuring void fractions during power transients.

Feasibility of the power supply has been demonstrated. Briefly, it consists of four rectifier units controlled by saturable, magnetic amplifiers. These amplifiers, in turn, are controlled by bias (excitation) currents which vary the amplifier impedance. In addition, the bias-control circuitry is wired such that the time of maximum pulsed power period can be varied from 30 to 100 msec, and the ratio of maximum to initial power for each period can be selected by varying the magnitude of the bias current.

For example, by pulsing a single rectifier unit from the lowest initial power, it is possible to obtain maximum-to-initial power ratios between 4 and 5 for a pulse duration of 38 msec. Since the power ratio decreases as the initial power is increased, it may be necessary to design different test sections to obtain data at each reactor power level of interest. However, as shown by the dashed curve in Fig. 1-25, the capability of operating in the ramp reactivity insertion range from \$0.75 to \$0.85 appears possible and may be sufficient to evaluate AARR response to these power transients.

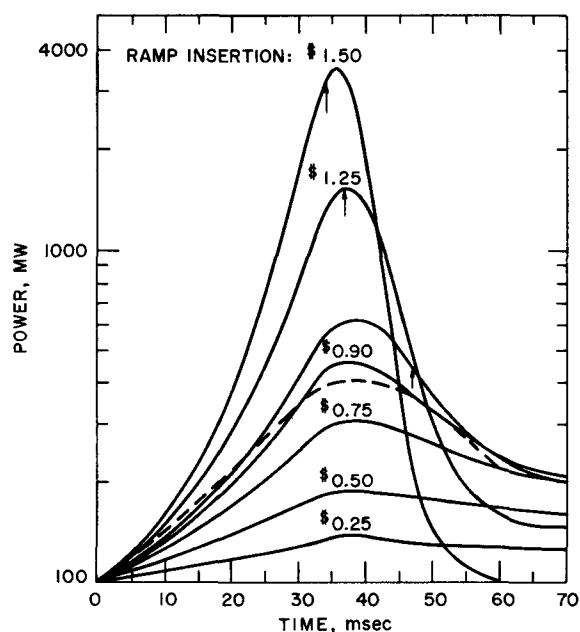


Fig. 1-25. Dashed curve indicates power-time relationship obtained with the 1500-kW, d-c power supply. Solid curves were plotted from earlier analog computations. Arrows on these curves indicate time critical heat flux occurred at the channel hot spot.

In addition to having sufficient strength and corrosion resistance, any test section installed in the heat transfer loop must be designed such that the heat flux at the wall-water interface corresponds to reactor design conditions and the overall electrical resistance matches the power supply requirements. In the case of the transient test section, an additional constraint is the wall heat storage during the power transient, i.e., the wall thickness and material must be balanced against each other.

Aided by an analog solution of the transient conduction problem, copper was selected as the material for the transient test section. As shown in Fig. 1-26, the present fabrication method consists of flattening an annealed copper tube and then machining the corners to prevent heat flux peaks.

Development of an X-ray system to measure void fractions caused by boiling during simulated power transients is proceeding satisfactorily. The criteria here is a system which will detect void fraction differentials in the range 0.05-1.0, with a 1-msec response. Specifications for the X-ray system have been drawn up, and procurement of the system and related equipment, i.e., rapid-response flowmeters and pressure transducers, has been initiated.

Shutdown-Emergency Cooling Tests. The objectives of these tests are twofold. First, to determine the allowable time intervals for specific operations, e.g., core unloading, following reactor shutdown. More specifically, burnout limits will be established for low coolant flowrates and power levels prevailing in the reactor during flow reversal from forced circulation downflow to upflow and subsequent natural circulation of primary coolant throughout the shutdown period. Second, to evaluate the merits and need of installing a forced circulation system to effect the desired flow reversal.

The loop constructed for these tests (Fig. 1-27) is a recirculating closed system, with forced circulation downflow or natural circulation

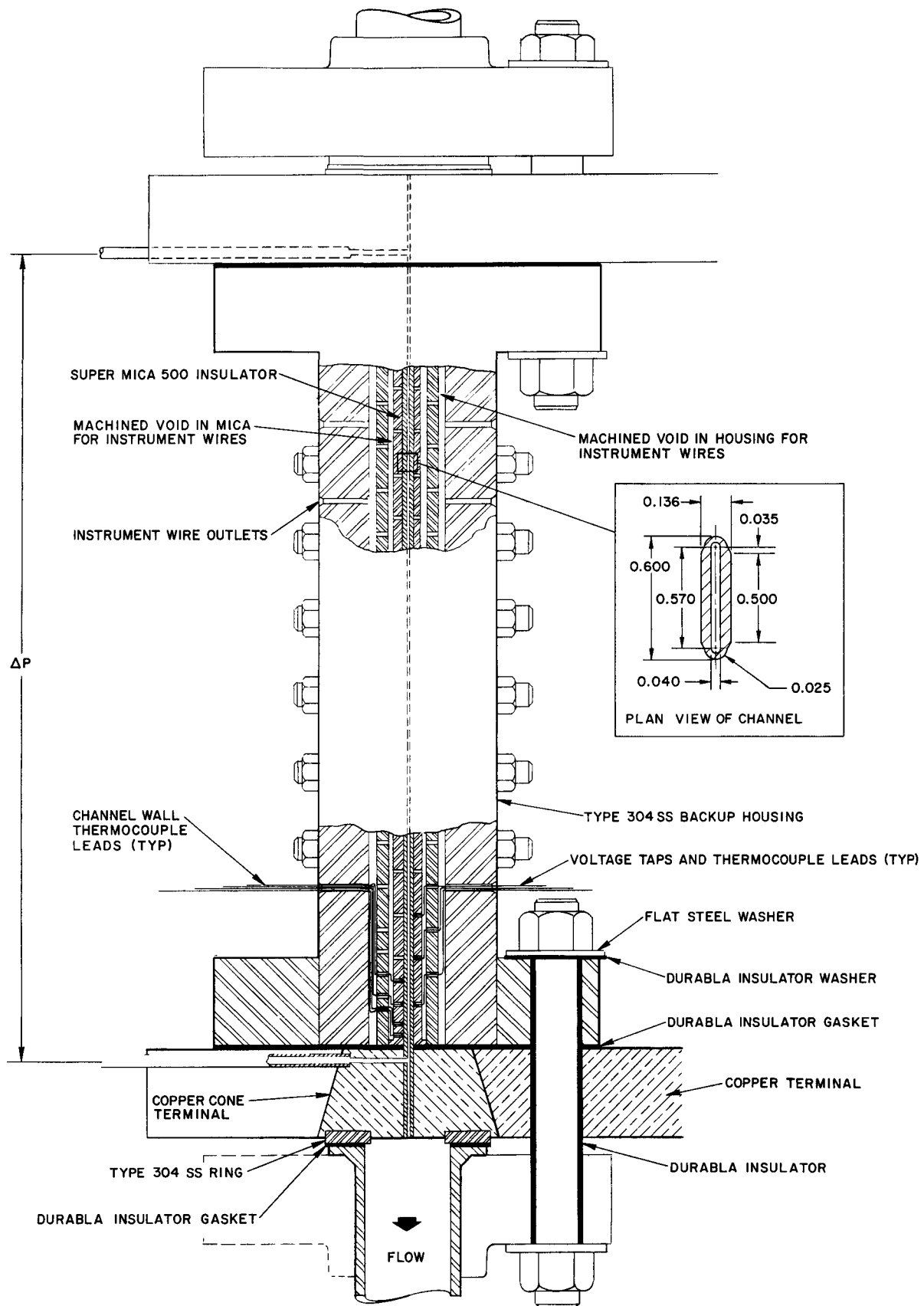


Fig. 1-26. Sectional views of simulated AARR fuel plate channel to be used in transient heat transfer tests

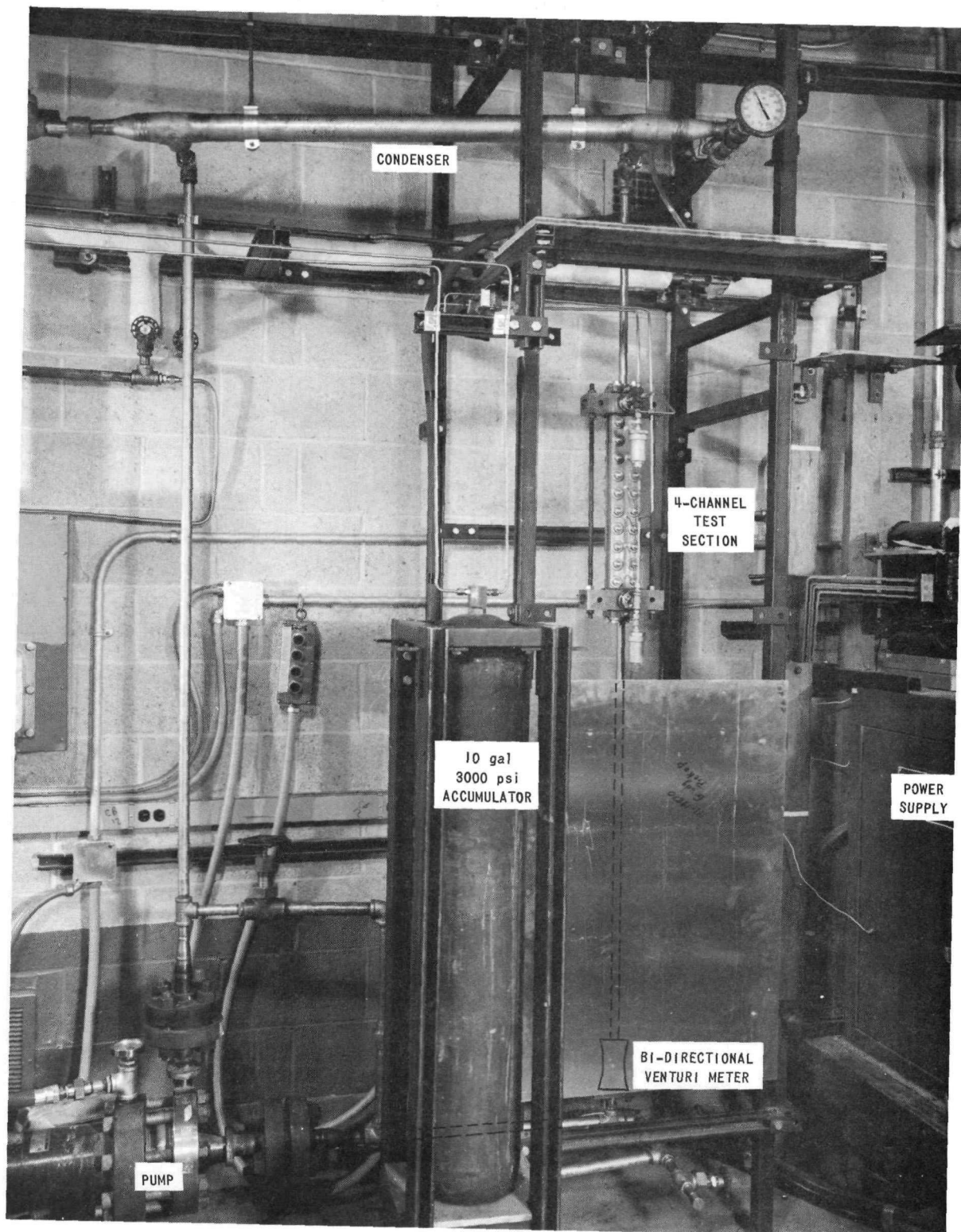


Fig. 1-27. Components of Shutdown-Emergency Cooling Test Loop

upflow through the 4-channel, heated test section shown in Fig. 1-28. Pertinent data on the loop and test sections are as follows:

System pressure	15-1000 psig
Pump capacity	30 gpm at 60-psi head
Power supply	40 kW, a-c
Hot channel/normal channel average heat flux ratio	~2.5
Maximum peripheral/average heat flux ratio in hot channel	2.2
Axial heat flux distribution	uniform

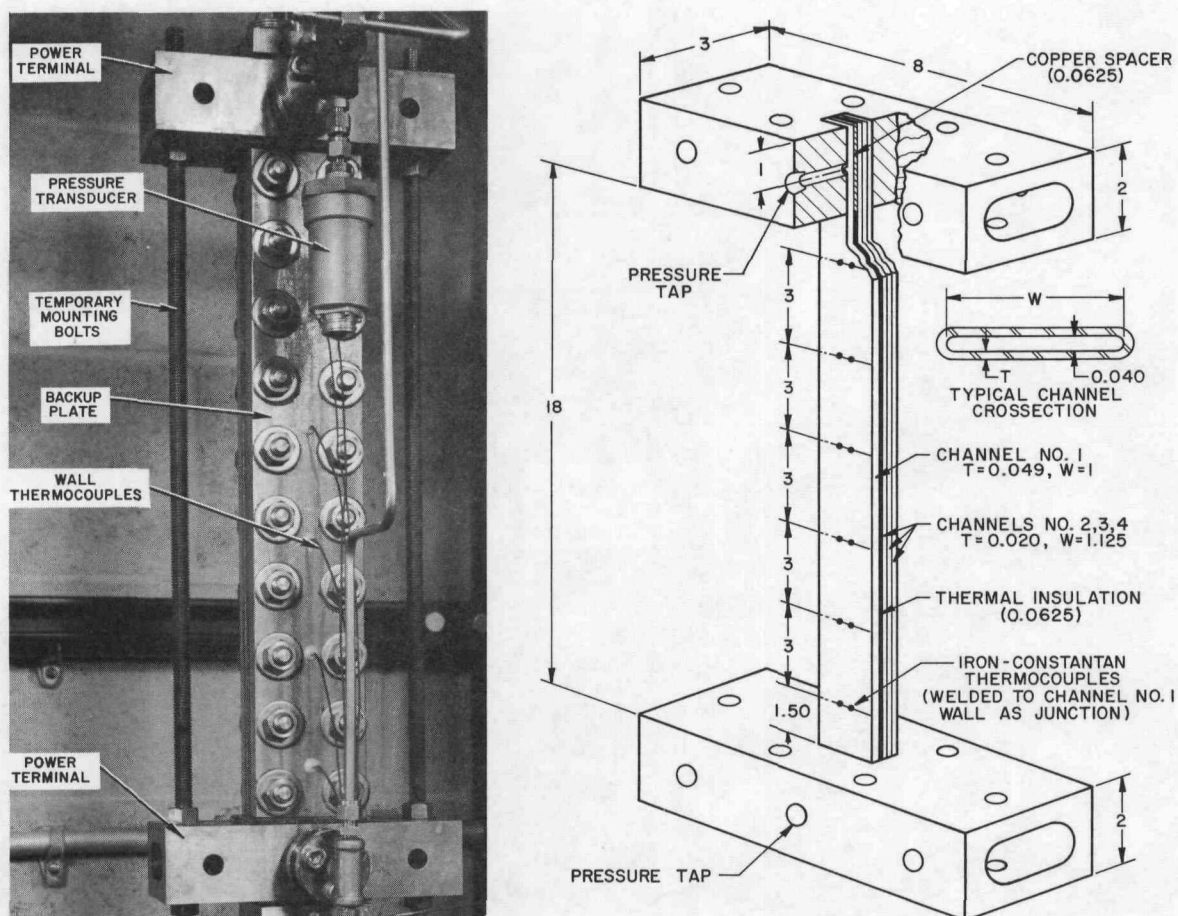


Fig. 1-28. Sectional views and instrumentation of 4-channel test section used for shutdown-emergency cooling studies

In operation, the pump is energized to establish forced circulation downflow of water at 7-8 ft/sec through the test section. Pumping is continued until the desired system pressure and test section power input are consistent with a fixed inlet temperature of 135°F. At this time, pump

power is interrupted and the flow reverses to natural circulation upflow. During the flow reversal period and up to the time natural circulation is essentially stabilized, inlet and outlet coolant temperatures and flowrates, power, and system pressure are recorded continuously. Hot channel outside wall temperatures are recorded at intervals of 5 sec/thermocouple, giving a complete profile every 30 sec. When defined burnout conditions are anticipated, i.e., wall temperature greater than the 855°F instrumentation limit, the uppermost wall thermocouple (which registers the highest temperature in natural convection) is switched to a fast-response (0.25 sec) continuous recorder. This recorder serves as a visual burnout alarm.

When a stable oscillatory pattern of natural circulation has been achieved, the pump is again energized to re-establish forced circulation downflow, and the test section power input is increased to the next desired level. This procedure is repeated until a defined burnout condition is achieved.

The 750-psi pressure range was investigated up to the defined burnout condition. At this condition, the hot channel average heat flux was 193,000 Btu/(hr)(ft²). No physical burnout was incurred. With a hot channel average heat flux of 187,000 Btu/(hr)(ft²), natural circulation flow was noticeably unstable, with minor indications of downward percolation from the heated channels. During flow reversal, the outside wall temperature of the hot channel peaked at 772°F. It then oscillated rapidly between the calculated nucleate boiling temperature of 750°F and a maximum value of 643°F throughout the period of natural circulation upflow. Preliminary analysis of the data indicates a safe flow reversal power level of ~180,000 Btu/(hr)(ft²) average in the hot channel. This corresponds to a reactor power level of ~9 MW.

A limited number of tests were made at near-atmospheric pressure (15 psig). For example, with an average flux of 70,000 Btu/(hr)(ft²), natural circulation upflow was highly unstable, but no measured wall temperature exceeded the calculated nucleate boiling temperature. Further investigation of this pressure region will be held in abeyance pending improvement of the fine power control scheme and related instrumentation.

The following conclusions are tentative and subject to confirmation by additional testing. Nonetheless, it appears that:

- (1) Reactor power level at which safe flow reversal can be accomplished is significantly higher at a system pressure of 750 psig than at near-atmospheric pressure.

- (2) Instability of natural circulation upflow poses a greater limitation (than the flow reversal thermal transients) on the reactor power level at which core-removal operations can be initiated after reactor shutdown.

(3) Limiting heat fluxes and reactor power levels at which flow reversal and natural circulation core cooling appear feasible are significantly higher than expected. Therefore, a forced circulation, flow reversal system in AARR is probably not required. However, the quantitative limits remain to be determined.

Thermal Stress and Hydraulics Analyses

Transient Thermal Stresses. Detailed analysis of transient stresses induced in fuel plates by both internal heat generation and sudden changes in coolant temperature was essentially completed. Computations indicate a significant temporal stress peaking in the plate, with the maximum stress being considerably less than would be estimated by assuming sudden changes in the plate surface temperature. The effect of internal heat generation is to increase the peak stress value and lengthen the time during which the stress is above some given level.

Figure 1-29 illustrates these effects and can be used in conjunction with the following equations to estimate stresses consequent to sudden changes in environmental temperature (ΔT). In these equations, $\bar{\sigma}$ and t' represent dimensionless stress and dimensionless time, respectively, with $\bar{\sigma}$ proportional to surface stress (σ_x) of the quenched plate.

$$\bar{\sigma} = -[\sigma_x(1 - \nu)/E\alpha(\Delta T)]$$

$$t' = \kappa t/L^2$$

$$\bar{\sigma} = \sigma_1 + C\sigma$$

$$C = QL^2/k(\Delta T)$$

$$m = hL/k$$

where

ν = Poisson's ratio

E = Young's modulus

α = coefficient of expansion

T = temperature

κ = diffusivity

k = conductivity

L = characteristic length ($1/2$ plate thickness)

σ_1 = dimensionless stress with no heat generation

$C\sigma$ = additional dimensionless stress caused by heat generation

Q = uniform internal heat generation rate

h = film conductance.

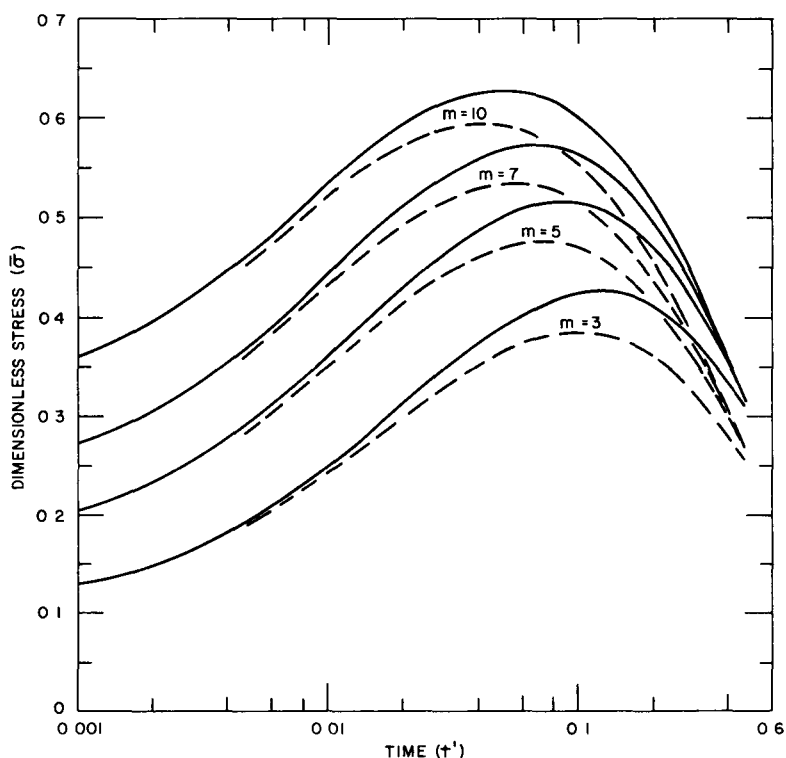


Fig. 1-29. Comparison of thermal stresses induced in fuel plate with (solid curves, $C = 0.5$) and without (dashed curves, $C = 0$) internal heat generation for corresponding Biot numbers

In the absence of a well-established theory on plate failure under these conditions, it is believed that failure would reflect not only the peak stress but, also, would be influenced by its duration. For example, consider a maximum heat generation rate of ~ 10 MW/liter and a Biot number (m) greater than 3. As shown in Fig. 1-29, quenching from an initial given temperature would, in addition to increasing the magnitude of the temporal peak stress, produce a 50% increase in the time during which the stress would exceed 80% of the peak stress of the quenched plate without internal heat generation ($C = 0$).

Follow-up Experiments Procurement and construction of a multi-purpose furnace and loading system is proceeding on schedule. When completed, it will be used for the related experimental program on thermally- and mechanically-loaded prototype fuel subassemblies.

Initial experiments will be performed on a model subassembly containing a single plate whose coefficient of expansion differs from the remainder of the assembly. The objective here will be to establish a correlation between theoretical and measured values of plate deflection as a function of temperature differential. Subsequent experiments will be made on simulated prototype subassemblies to determine gross deformation behavior.

Steady-state Pressure Drop. Estimates have been made of the pressure differentials as a function of axial positions in a reference coolant channel. Similar estimates were made for alternate positions of control and safety blades within their respective channels. Pressure drops across the ITC and reflector will be computed when dimensions of these components are firmly established.

In the meantime, a two-dimensional, ideal fluid flow model is being formulated for purposes of estimating the effect on pressure differential of flow orifices between adjacent channels. This model will be used in conjunction with the experiments designed to relate the shape and size of the orifices in the direction normal to the plane of the ideal flow analysis.

Flow-induced Dynamics. Flow-induced oscillation of fuel plates, control blades, shrouds, and shields can lead to coolant channel closure, fatigue failures, and ultimate buckling of load-carrying members. Exploratory analysis of control blade response to sudden, longitudinal, mechanical loadings is essentially completed. Work has started on the problem of hydrodynamic loadings.

However, due to the complexity of the problem, analog computer simulation is being considered. The initial model, which describes the flow-induced blade oscillation, assumes one-dimensional flow of incompressible fluid, with no cross flow between channels formed by the control blades. In the special case of steady-state flow, application of the principle of conservation of momentum yields a partial differential equation which can be solved by integration. Finally, with the assumption that pressure distribution in unsteady flow can be approximated by the steady-state pressure, the derived equation can be used to analyze the dynamic response of the blades.

General Purpose Hydraulics Test Loop

As the name implies, this loop (Fig. 1-30) was originally designed to provide a versatile facility for reactor-related hydraulics studies. Maximum operating conditions included pressure at 1235 psig, water at 500°F and 1200 gpm, and a ΔP of 450 psi through the test chamber. In order to achieve these conditions, the reference design specified installation of two 800-gpm pumps in series, and four, shell-and-tube-type heat exchangers.

However, because of the long lead time involved in obtaining this equipment, and the pressing need for hydraulics studies of AARR core components, the loop was made operational with one pump and two small heat exchangers. This equipment is sufficient to maintain the AARR test environment, which includes pressure at 600 psig, water at 110-400°F and 800 gpm, and a maximum ΔP of 240 psi through the test chamber. The second pump and two additional heat exchangers will be installed at a later date.

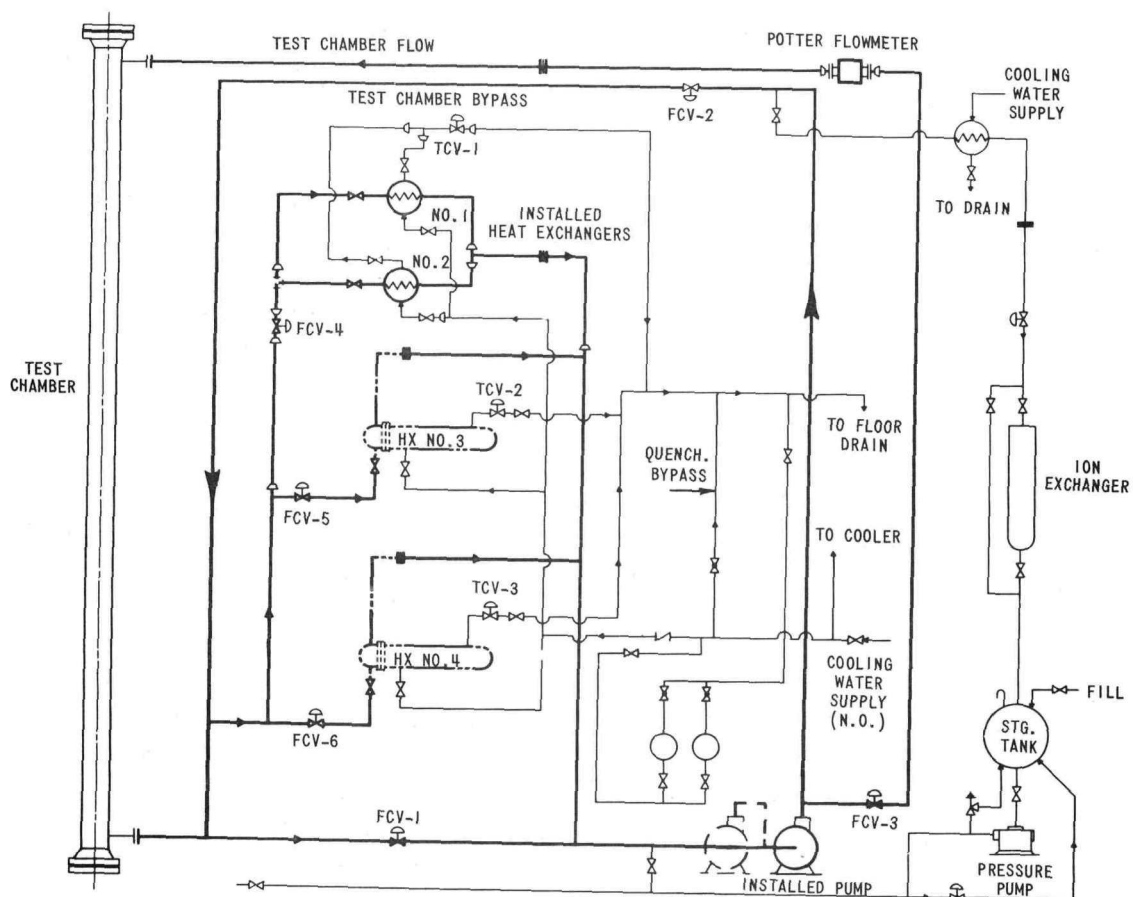
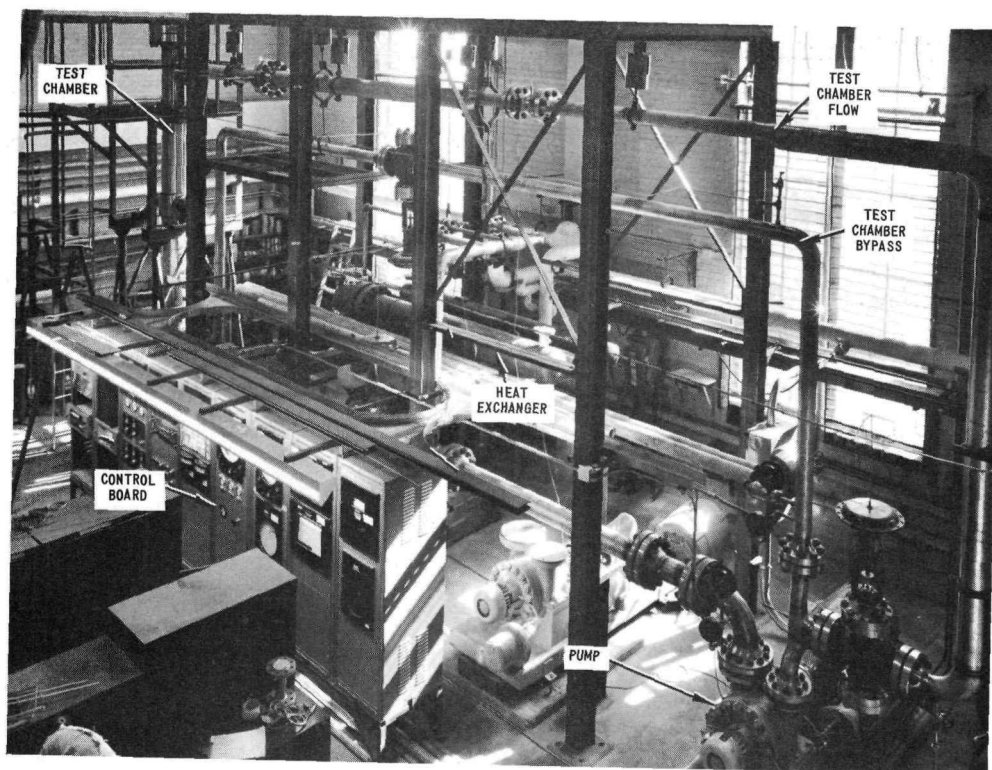


Fig. 1-30. General-purpose hydraulics test loop

Materials of Construction. For the most part, the primary loop is constructed of Type 304 stainless steel. The heat exchangers feature Inconel tubes, and the pump is fabricated from 11-13% chromium steel. Where applicable, the piping conforms with the ASA Code for Pressure Piping (Section B31.1), with the additional specification of 100% radiography during erection. Design of the heat exchangers and test chamber is consistent with the ASME Code for Unfired Pressure Vessels (Section VIII). Prior to initial operation, the primary side was hydrostatically tested at ambient temperature to 2175 psig to ensure a leaktight system.

Cooling water, supplied from the Laboratory canal system, is circulated at low pressure through the shell side of the heat exchangers. Accordingly, the loop piping and components are fabricated of black iron, cast iron, or bronze.

Operation, Control, Instrumentation. All heat input (~120 kW) into the facility is generated by pumping power (150 hp) and absorbed by the primary coolant. Because of the lack of insulation, initial loop operation at 400°F resulted in an excessive rise in room temperature. As a consequence, the loop will be partially or totally insulated, depending on whether this temperature level will be employed throughout the AARR test program.

With reference to the schematic flow diagram in Fig. 1-30, pump discharge may be directed through the test chamber, the test chamber bypass, or divided between the two. In addition, a portion of the flow returning to the pump may be directed to the tube side of the heat exchangers for cooling. The desired flow mode and temperature is effected by manual manipulation of four control valves: FCV-1 on the suction side of the pump, FCV-2 on the test chamber bypass line, FCV-3 on the test chamber flow line, and FCV-4 on the piping leading to heat exchangers No. 1 and No. 2. In this manner, the loop can be operated with flowrates ranging from 20 to 1600 gpm through the test chamber, depending on the ΔP through the test section in the chamber and the desired operating temperature.

Temperature control of the primary fluid is accomplished by valve TCV-1, which automatically regulates the flow of secondary cooling water through the shell sides of the operating heat exchangers. As shown by the dashed lines, two additional valves, TCV-2 and TCV-3, will similarly control cooling water to heat exchangers No. 3 and No. 4, respectively, when the reference design installation is completed.

Instrumentation installed thus far covers normal loop control functions and operational characteristics. Additional equipment is presently being installed consistent with the nature of the proposed initial tests. This equipment consists basically of hi-speed recorders to monitor changes in pressure, flow, and pump revolutions during pressure drop studies with a

control blade mock-up installed in the test chamber. This test series will be followed by an analog study of the "coast-down characteristic" of the loop.

Future studies will include flow- and temperature-induced stress and deflection of fuel plates, fuel subassemblies, control blades, etc.; pressure pulse characteristics of smaller flow loops that will be integrated into the parent loop; and measurement of pressure drops through prototype core and system components evolved during definitive design of the AARR. Development of instrumentation for these studies is presently focused on displacement transducers and Pitot tubes for use in conjunction with fuel plate deflection and flow measurements in fuel plate channels.

Instrumentation Development. Two cylindrical displacement transducers are being developed to measure fuel plate deflection: a capacity-type unit for high temperatures and pressures, and a variable impedance-type unit for low temperatures and pressures.

The capacity-type transducer is designed to operate at 500°F and 1250 psi, with a measurement range from zero to 0.040 in. It measures 1 in. in diameter, 0.50 in. long, with an attached 0.75-in.-long mounting stud, and is energized by an electronic bridge. The output signal, triggered by fuel plate displacement, will be transmitted to an electric recording oscillograph.

The variable impedance unit is designed to operate at 75-200°F and 200 psi, with a similar measurement range. It measures 0.625 in. in diameter, 0.625 in. long, with an attached 0.75-in.-long mounted stud and a 1.25-in. tubular extension. In operation, the transducer will be energized by an electronic oscillator-modulator unit; displacement signals will be transmitted to an electric recording oscillograph.

Prototypes of both units are being assembled for test purposes.

Special Pitot tubes will be used to measure flow through the fuel plate coolant channels. Each tube assembly measures 70 in. overall length, and consists of two concentric stainless steel tubes: an outer tube (0.040 in. dia., 0.004 in. wall), and an inner tube (0.020 in. dia., 0.004 in. wall). Both tubes are silver soldered at the sensing end, which is also flattened to 0.035 in. over a 4-in. length to facilitate insertion in the channels. Two holes are Eloxed 0.200 in. from the tip on the curved portion of the flattened section. At the terminal end, the tubes are connected through an O-ring pressure seal to a special rotatable valve and related readout circuitry.

Fuel Material Fabrication Development

Post-irradiation Evaluations of Cermet Fuels. These evaluations have centered on attempts to correlate the irradiation behavior of reference 37 wt-% UO₂-SS cermet fuel plate specimens to existing data on similar

cermets containing 24-30 wt-% UO_2 , or higher. The objective is to establish a basis for predicting life expectancy of the reference fuel in AARR. To this end, evaluations have been performed by Phillips Petroleum Co., ORNL, and BMI under subcontract with Argonne. Their findings are summarized as follows.

Thus far, measurements by Phillips on irradiated AARR-type fuel plate specimens show that use of nominal 85%-dense UO_2 results in appreciably less swelling at a given burnup than observed with fully-dense UO_2 . These measurements were made in the MTR-ETR hot cells on plate specimens ($1.25 \times 5.75 \times 0.040$ in.) which had been irradiated in the ETR to burnups ranging from 8 to 30 at-% U-235. During exposure, the fission product inventory across the face of the fuel plates in the ETR-G12 core position varied by a factor of two.

Detailed analysis showed that the net swelling rate in the cermet (Curves A, Fig. 1-31) agreed favorably with that predicted for the UO_2 when correction was made for proportionate volume relationship in the original, nominal 32 vol-% UO_2 -68 vol-% SS cermet. The spread in the cermet swelling rate is attributed to variation in burnup across the width and length of the fuel plates. Figure 1-32 shows the change in the UO_2 particle with increased burnup.

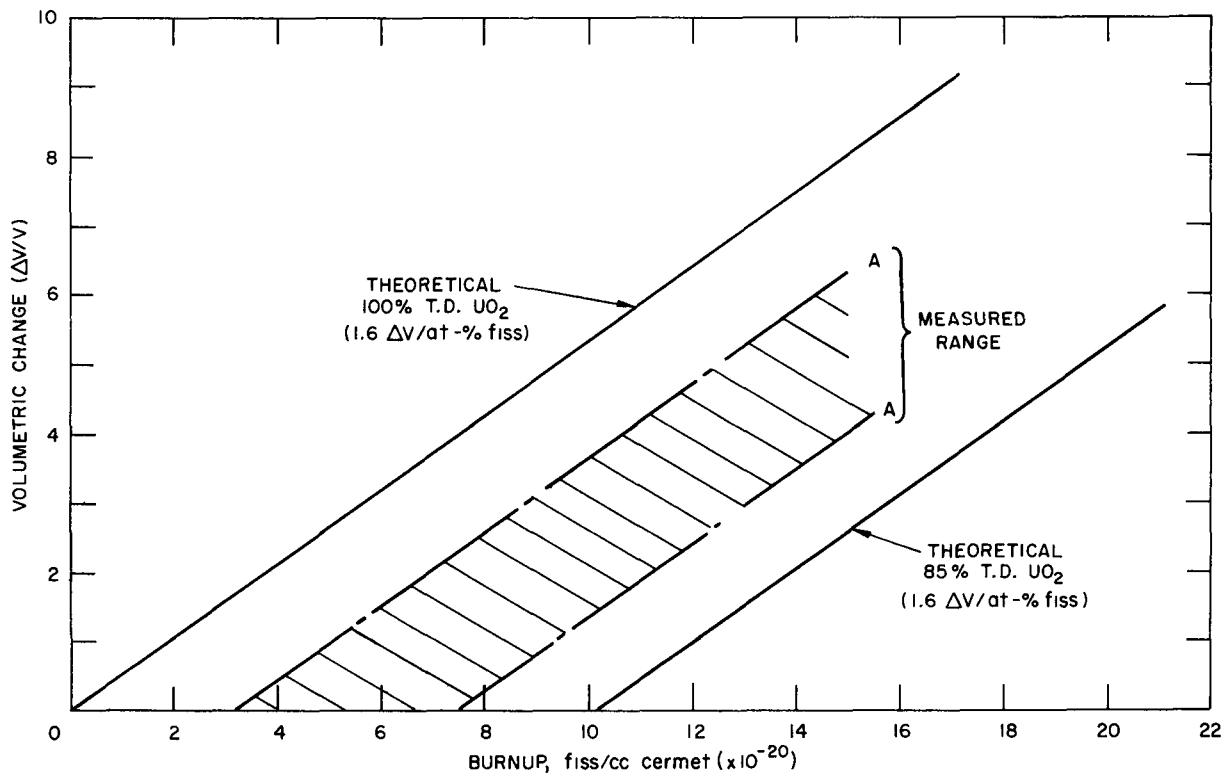
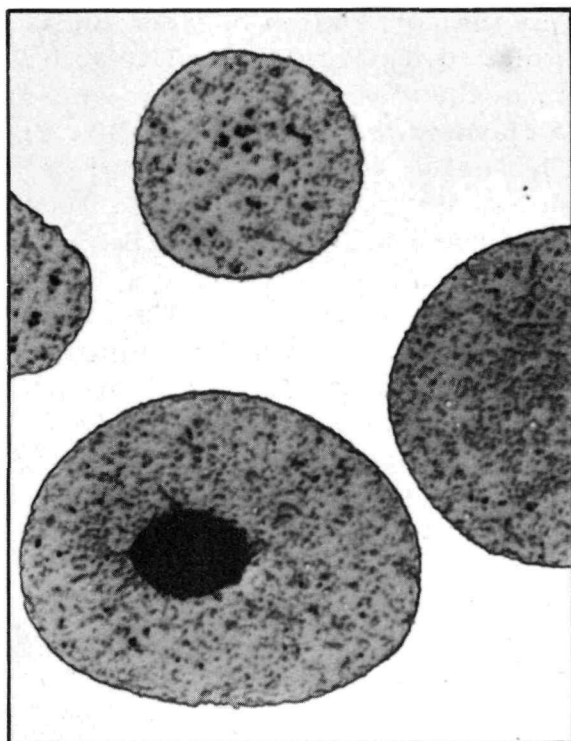
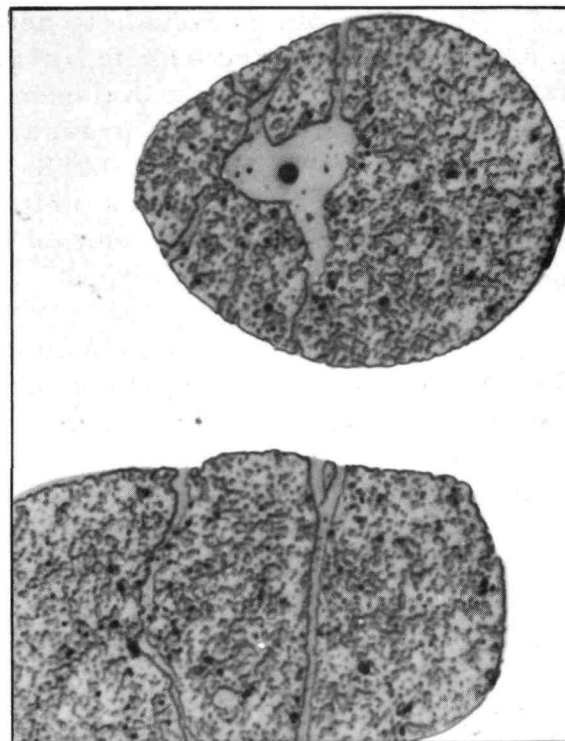


Fig. 1-31. Comparison between theoretical rates of fission-induced swelling in UO_2 and measured range of swelling rates in AARR 37 wt-% UO_2 -SS cermet fuel



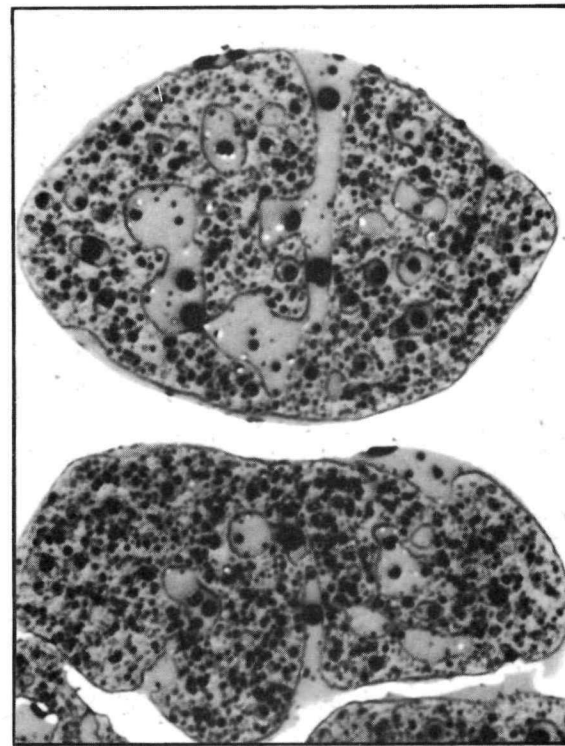
~8 at-% U-235



~10 at-% U-235



~18 at-% U-235



~24 at-% U-235

Fig. 1-32. Microstructures of cross section through AARR fuel plate samples after irradiation to various U-235 burnups. Average UO_2 particle diameter is 125 microns.

An attempt was made to determine the correlation between fuel plate temperature and burnup for gross instability of the fuel plate structure (i.e., matrix rupture due to inability of the matrix material to accommodate the fission product pressures at elevated temperatures). Blister tests were performed in the MTR-ETR hot cells, and the temperature at which the blister formed was plotted against the fuel burnup to establish a stability-instability relationship similar to that published on in-pile fuel failure.

Figure 1-33 is a composite plot of blister test data from Phillips and ORNL, and the stability curves derived by Keller² from available in-pile data on UO_2 -SS cermet fuels. The ORNL data were obtained from blister tests similar to those performed by Phillips. However, the samples included coupons and tubes containing cermets of higher UO_2 content (up to 50 wt-% UO_2 -SS). These samples were part of the Army Reactor Advanced Fuel Irradiation Test Program (terminated in May, 1964), and had been stored in the Oak Ridge Research Reactor pool since September, 1964. Most of the samples selected for blister tests contained the same type of UO_2 as did the plates irradiated in the ETR. Irradiation of the Army fuel was terminated at fairly low burnup (~ 7 at-% avg. - 15% peak); nonetheless, exposure was sufficient to establish a correlation between burnup and the onset of detrimental changes in physical properties.

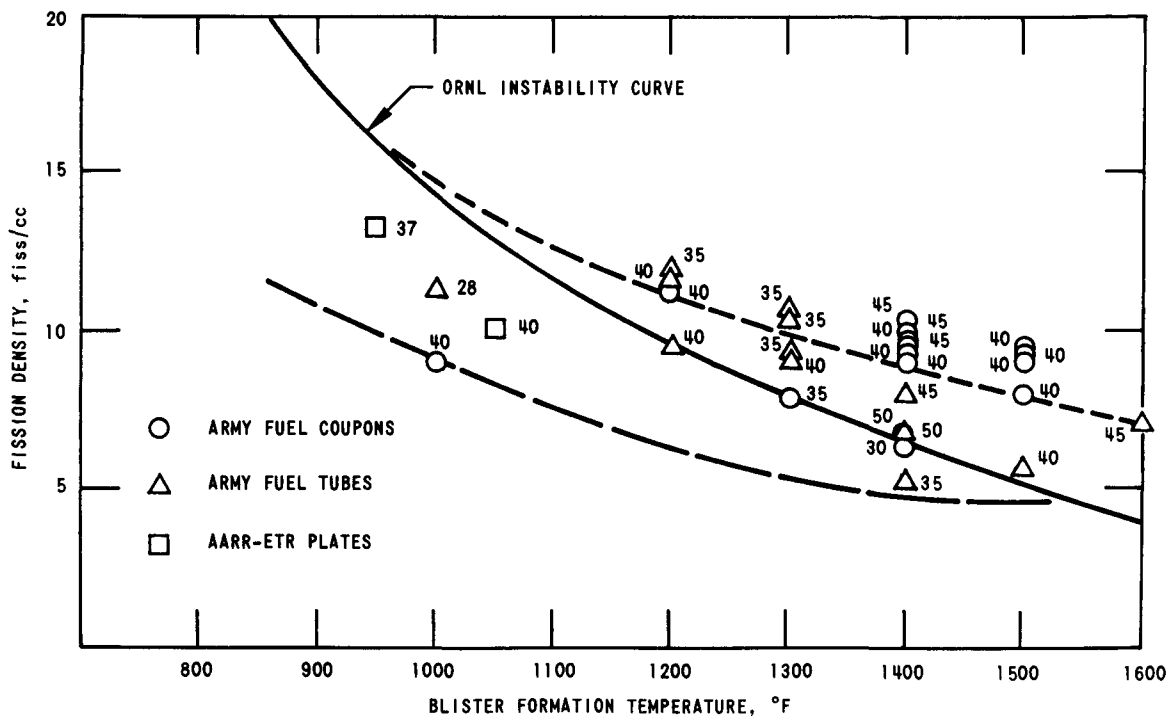


Fig. 1-33. Comparison of out-of-pile blister-test data on AARR reference fuel plates with similar data on Army Reactor fuel specimens. Dashed curves represent upper and lower stability limits established by Keller's correlation of in-pile data. Numbers adjacent to data points indicate wt-% UO_2 in Type 347 stainless steel matrix.

Direct correlation from out-of-pile tests to in-pile tests is questionable due to the gross difference in environments and materials behavior in the different environments. Only a qualitative evaluation of the results to date is possible. However, the relationship developed thus far for burnups up to twice the average end-of-core life burnup for the UO_2 -SS fuels indicates that the Mark-I core should be able to operate at powers well in excess of the present 100 MW design level without incurring serious irradiation damage.

These hot cell investigations will be extended to include other changes in physical and mechanical properties as a function of increased burnups.

In addition to the foregoing studies, a miniature, three-plate, brazed subassembly containing the reference cermet fuel, and several stainless steel dummy plates with brazed wire spacers were irradiated in the ETR. The objectives of these tests were twofold: First to evaluate the effects of thermal gradients (thermal stress) on dimensional stability of the three-plate subassembly and, second, to assess the change in properties of the brazing compound used to affix the wire spacers.

Preliminary inspection of the miniature subassembly after irradiation to peak burnup of ~30 at-% U-235 showed no significant dimensional changes. Additional tests on the subassembly and the dummy plates are scheduled for completion in early FY 1967.

Commercial Verification of Plate Fabrication. Two commercial fabricators were subcontracted to determine feasibility and reproducibility of Laboratory-developed procedures for fabricating the optimized 37 wt-% UO_2 -SS fuel plate structure. The end products were evaluated at Argonne.

These evaluations showed that attempts to follow explicitly the prescribed procedures resulted in substandard plates, in some cases. The greatest difficulty occurred in the blending and rolling processes, which require optimized combined input of material, equipment, and personnel capability. However, each fabricator was also allowed to adapt and revise the processes consistent with his personnel's capability, experience, equipment, and working conditions (including slight variations in the feed materials). Under these circumstances, the end product was adjudged equal to, if not better than, the fuel plates fabricated in the laboratory.

As a result of these findings, modifications have been made in the vendor qualifications, fuel plate and reference core specifications. In some areas, the specifications were upgraded consistent with the improved quality of the commercially fabricated plates.

Burnable Poison Addition to Reference Cermet Fuel

The reference cermet fuel will contain a fixed burnable poison of 0.4 to 0.6% natural boron equivalent. Accordingly, BMI and the Martin Co., were subcontracted to investigate means for eliminating the boron loss problem that had been experienced during fabrication of the Army Reactor cermet fuel.

Zirconium diboride (ZrB_2) was selected as a reference starting point because it was the most stable of better known compounds of boron. Subsequent analysis was made of the time-temperature relationships for formation of binary, ternary, and more complex eutectics of different combinations of Zr, B, Ni, Fe, and Cr. This analysis indicated that conventional methods of fabricating UO_2 -SS cermets resulted in gross reactions between these materials, with essentially total liberation of boron (in the form of boron hydride) to the atmosphere.

Martin Co. reported a severe H_2O - ZrB_2 reaction during heating of a UO_2 - ZrB_2 -SS compact in a hydrogen atmosphere above 1000°C . However, sequential vacuum heat treatments from 600 to 1000°C resulted in substantial stabilization of the ZrB_2 in the stainless steel matrix. Analysis showed that after sequential heat treatment, less than 5% of the ZrB_2 displayed evidence of appreciable reaction provided the temperature did not exceed 1150°C . At temperatures above 1200°C , both Martin Co. and BMI reported a gross reaction between the ZrB_2 and stainless steel, with substantial loss of boron. At 1300°C , in excess of 98% of the boron was lost.

Attempts to reduce the reaction included coating the ZrB_2 with Nb and with elemental stainless steel. Though effective against the H_2O reaction, the stainless steel provided very little protection above the 1500°C temperature range for the B, Fe, and B-Ni eutectics. On the other hand, the niobium coating (a 1-2 micron CrC_4 barrier between the Nb and ZrB_2) proved effective at temperatures up to 1175°C , and afforded some protection for short periods at 1200°C .

Figure 1-34 shows the effect of eutectic formations on the microstructure of fuel plates containing Nb-coated ZrB_2 in a 37 wt-% UO_2 -SS matrix. Plate (A) was heated well above 1200°C during fabrication, while plate (B) was exposed to temperature slightly below 1160°C .

As a result of these studies, sintering of the AARR cermet will be performed in a vacuum furnace, the fuel fabrication temperature will be limited to less than 1160°C , and the subassembly brazing temperature will be similarly restricted to less than 1160°C .

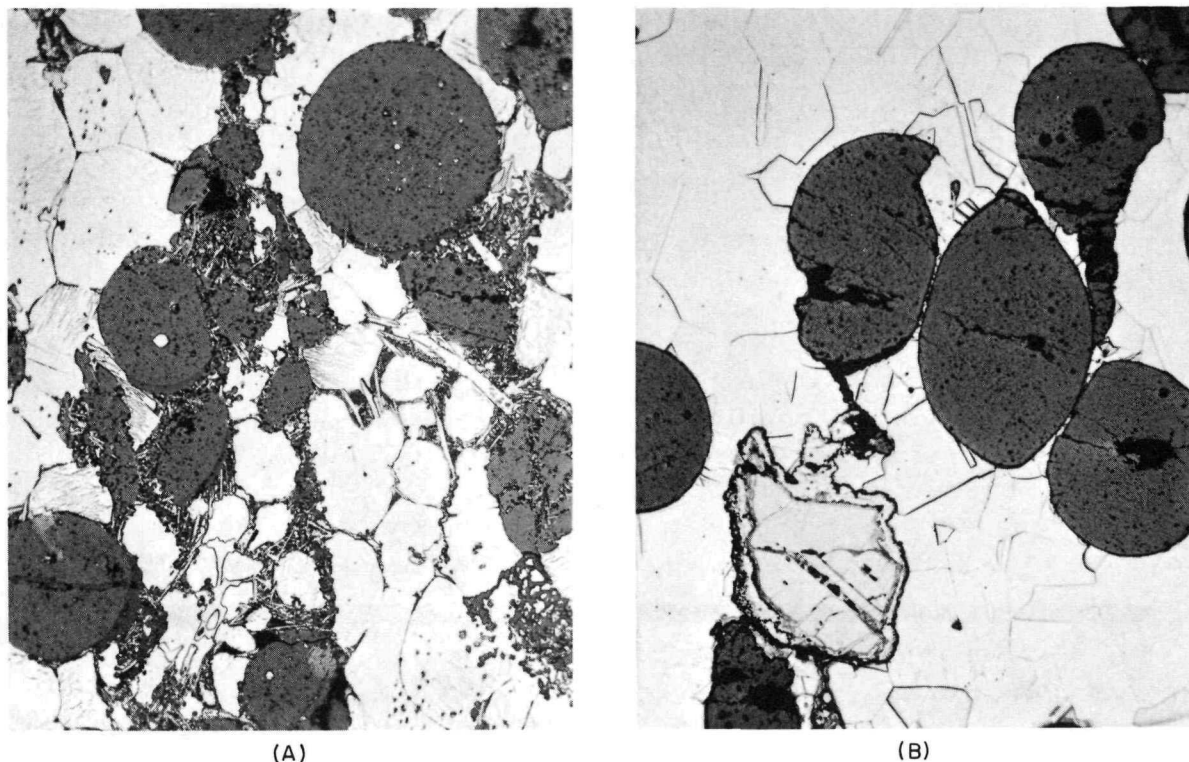


Fig. 1-34. Microstructures of 37 wt-% UO_2 -SS fuel plate containing Nb-coated ZrB_2 burnable poison. Plate (A), exposed to 1200°C during fabrication, shows evidence of gross reaction, while Plate (B), exposed to slightly below 1160°C , shows negligible reaction.

Studies were also started on an alternate burnable poison material: B_2O_3 - SiO_2 glass beads. These studies were implemented on the basis of unpublished data by ORNL which show promise. ETR-G12 irradiation specimen size samples were satisfactorily fabricated using the same techniques and process employed for the Nb-coated ZrB_2 -bearing fuel plates. Metallographic examination revealed negligible damage to the ~ 2 wt-% B_2O_3 - SiO_2 beads.

Graded Fuel Cermet Fabrication Development

As mentioned earlier, the Mark-I core will include subassemblies of graded fuel plates to prevent flux peaking at the core extremities. These plates will contain dispersions of 6 to 33 wt-% UO_2 in the stainless steel matrix. Since most of the work on dispersions has been conducted in the 18 to 32 wt-% range, studies were centered on achieving uniform dispersions of UO_2 in the 6-18 wt-% range.

Several approaches were taken. These included:

- (1) Fabricate a standard size compact with low UO_2 concentrations (6, 8, 10, 12, 14 wt-%) in a stainless steel matrix.

(2) Fabricate a compact of one-half standard thickness, double the UO_2 concentration (12, 16, 20, 24, 28 wt-%), and use a much thicker cladding.

(3) Fabricate a very thin compact of the reference 37 wt-% concentration fuel cermet and use a very thick cladding. For example, a 6 wt-% equivalent, 0.0045-in.-thick, 37 wt-% reference fuel cermet, with a very thick clad; or an 8 wt-% equivalent 0.0065-in.-thick, 37 wt-% reference fuel cermet, etc.

Of these, approach (1) produced the best overall dispersions in the 6 to 15 wt-% UO_2 range. They were accomplished with a special blending technique employing a specific ratio of different-sized stainless steel powders with the desired UO_2 concentrations. Above 15 wt-%, the standard blending process resulted in an adequately homogeneous dispersion. Figure 1-35 shows the degree of dispersion homogeneity obtained in each case with the 6 wt-% equivalent fuel loads.

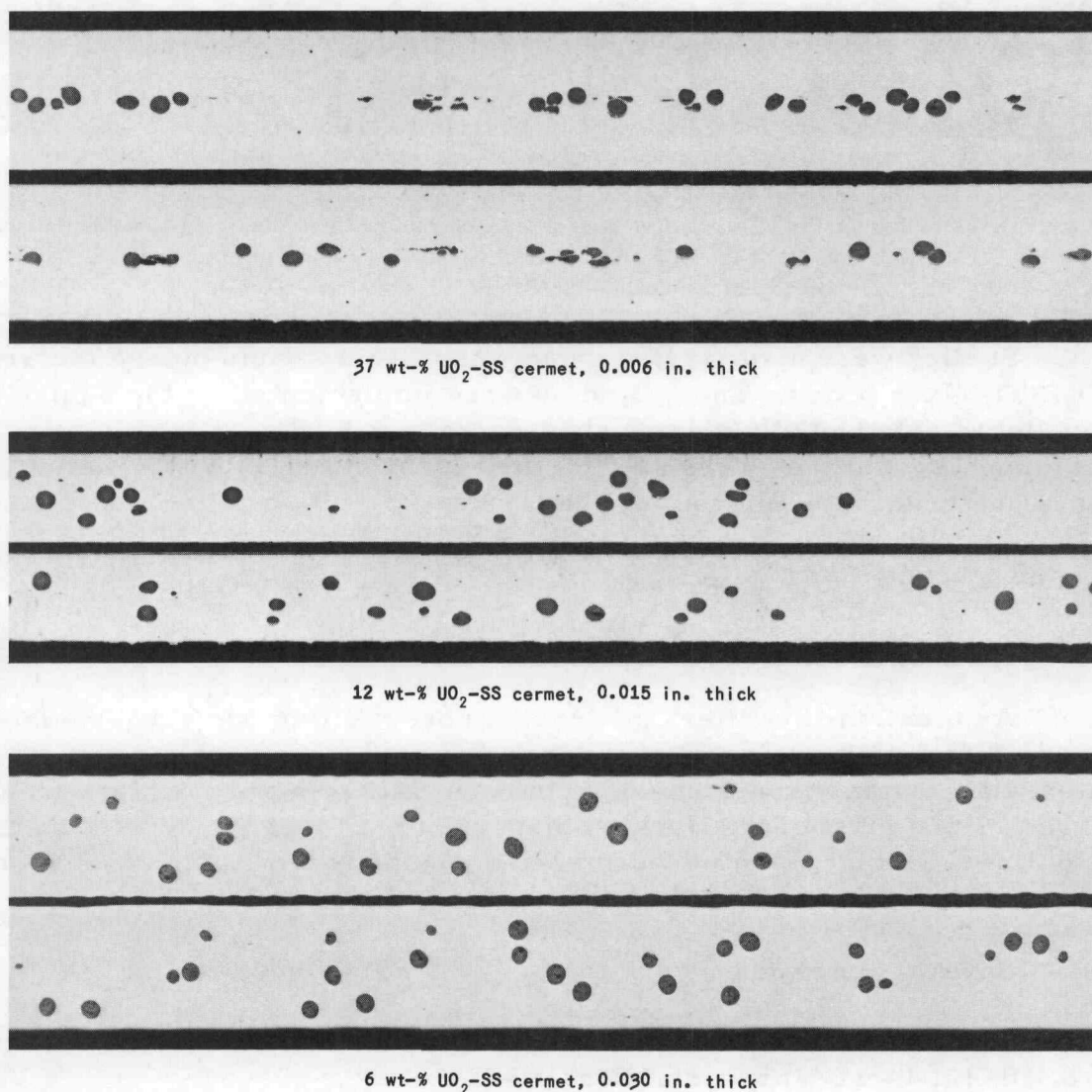


Fig. 1-35. Microstructures of cross sections from 6 wt-% equivalent UO_2 -SS cermet fuel plates showing typical dispersions of UO_2 concentrations

UO₂ Characterization and Evaluation

Studies were conducted at BMI to establish correlations between physical and chemical properties of various types of UO₂ spherical particles and their respective behavior during fabrication into fuel plates. In all, eleven types of UO₂ particles, which differed in basic fabrication process, density, and additives, were measured and characterized.

These particles were then used in the fabrication of 37 wt-% UO₂-SS cermet samples for subsequent destructive tests. Evaluation was based on the relative ability of the UO₂ spheres to withstand rolling pressures without significant densification, deformation, or crushing and stringering. Provided there was no marked displacement or distortion of the matrix, shear cracks were not considered detrimental. Such cracks have been found to heal during irradiation at an initial burnup of 5-10 at-% U-235, and have no apparent detrimental effect on the amount of fission products released from the UO₂.

The results of these studies are summarized in Table 1-6. In the case of samples B through J, where deformation and stringering was not excessive (<25%), the UO₂ particles experienced very little change in shape until the rolling schedule exceeded 4:1. Figure 1-36 shows typical microstructures of the specimens listed in Table 1-6.

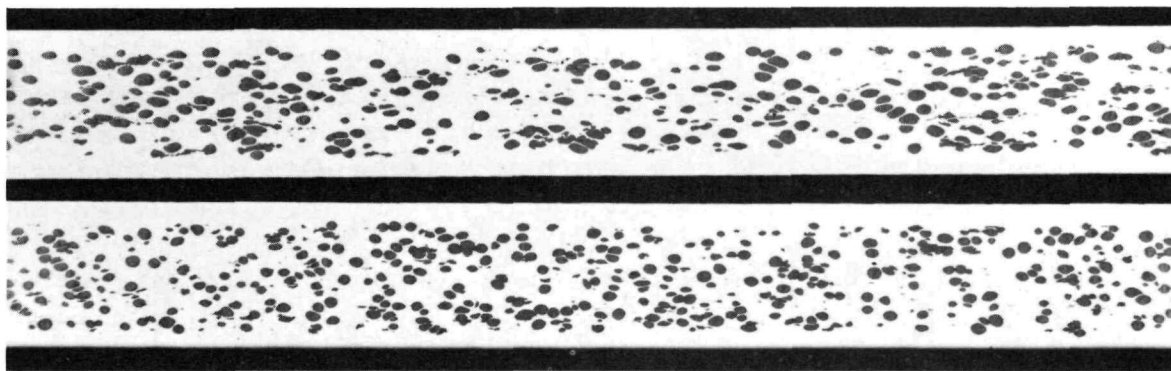
Table 1-6 Summary of UO₂ Particle Characterization and Evaluation Studies

Sample	Prerolled Particle Characteristics					Postrolled Observations		
	Mesh Size	Process ¹	Density ² % T D	Crush Strength gm/particle	Additive wt-%	Density % (approx.)	Particle ³ Deformation	Percent Stringered
A	-100 +140	H F S	60	50	None	Badly crushed and stringered		~90
B	-100 +200	H F S	72	127	None	>90	F B	~10
C	-100 +140	H F S	68	159	None	>90	F B	~5
D	-100 +140	H F S	70	168	2 C ₂ O	<80	S	~25
E	-70 +100	H F S	69	490	None	>90	F B	~15
F	-80 +100	H F S	-	188	None	>90	F B	-
G	-100 +270	H F S	79	231	3 ZrO ₂	<85	S	~30
H	-100 +140	H F S	78	211	2 C ₂ O	<85	S	~30
I ⁴	-100 +140	H F S	74	187	None	>90	F B	~3
J	-100 +140	H F F	75	240	1.3 Ti, 2 Ca	<85	S	~20
K	-100 +140	S B	80	218	None	>90	Irreg	~85
S	-100 +140	S G	97	800	None	~97	S ⁵	~5

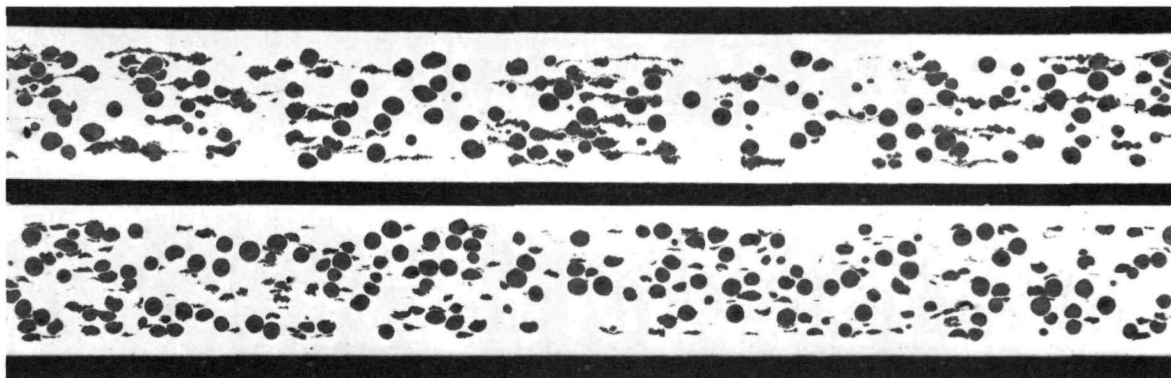
¹H F S High-fired spherical
H F F Hydrogen flame fired
S B Settled bed
S G Sol Gel
S Spherical
²Determined by Hg pycnometer

³F B Footballled with major/minor axis >1.5:1
S Spherical
Irreg Irregular particles
⁴Same as sample C
⁵Spherical but 20% cracked

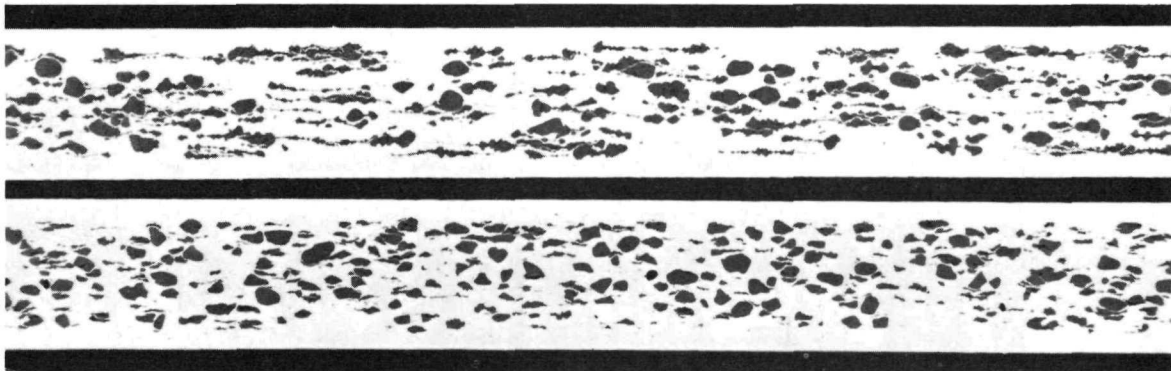
These data have been used in conjunction with known irradiation properties of UO₂ to establish preliminary Mark-I core specifications. Subject to verification by laboratory and commercial fabricators, they will be incorporated in the core procurement specifications.



Densification, plastic deformation, nominal crushing or stringing;
typical of non-additive high-fired samples B, C, and I



Random crushing, stringing, no plastic deformation; typical of high-fired
spherical and hydrogen flame-fired samples D, G, H, and J



Typical structure of low density-low crushing strength UO_2 samples A and K

Fig. 1-36. Typical microstructures of UO_2 particles after fabrication into
specimen 37 wt-% UO_2 -SS fuel plates. (Also see Table 1-6.)

Fuel Subassembly Development

Brazing Materials and Techniques. Each rhomboidal fuel subassembly will comprise a prescribed number of fuel plates brazed to spacer wires. Since the composition of each plate will include a burnable poison (ZrB_2), the time at temperature during the brazing cycle is of paramount

importance because of its effect on boron retention in the plate. Accordingly, three different brazing alloys, two braze cycles, and a variety of temperatures were investigated to determine the optimum braze cycle at the lowest possible temperature consistent with adequate strength.

The brazing alloys used were GE-J8100, Coast Metals NP, and Microbraz 50. Cycle times were either 2 hr at brazing temperature or 10 min. at brazing temperature followed by a 3-hr soak at a lower temperature. The temperature ranges for each brazing alloy are tabulated below.

Braze Alloy	Braze Temp., °F	Soak Temp., °F
GE-J8100	2100, 2120, 2130, 2150	2000
Coast Metals NP	2030, 2050, 2075, 2100	1800
Microbraz 50	1825, 1850, 1875, 1900	1700

Six-plate specimen subassemblies (Fig. 1-37) were brazed at each condition. Subsequent shear tests revealed that the 10-min. brazing temperature cycle produced unsound brazed joints. Of the specimens brazed for 2 hr at temperature, the best minimum-temperature braze (Fig. 1-38) was obtained using the GE-J8100 alloy at 2100°F. More sound brazes were produced at higher temperatures.

Full-size, stainless steel dummy subassemblies were also brazed, using GE-J8100 alloy and a "reference" hydrogen braze cycle of 2 hr at 2135-2145°F. These units will be machined and used in core mock-up tests.

Inspection and Quality Control

This activity is concerned with the development of nondestructive quality control and inspection procedures to ensure compliance with

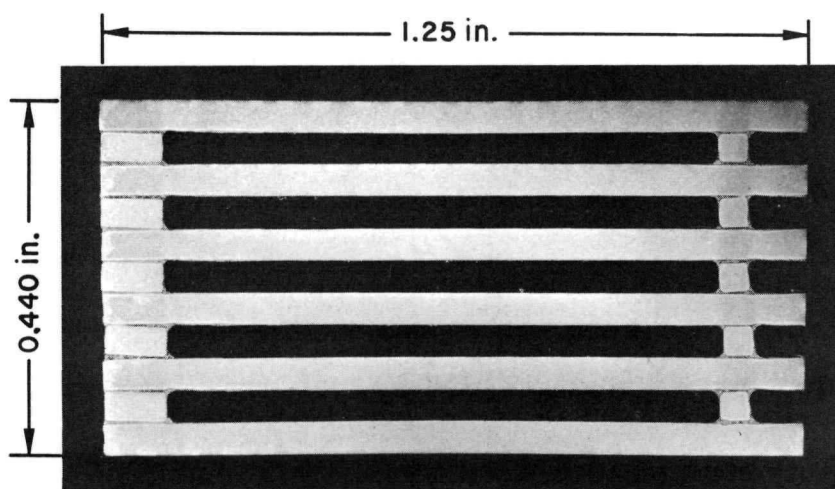


Fig. 1-37. Specimen 6-plate subassembly used in shear test evaluation of brazing alloys and temperatures

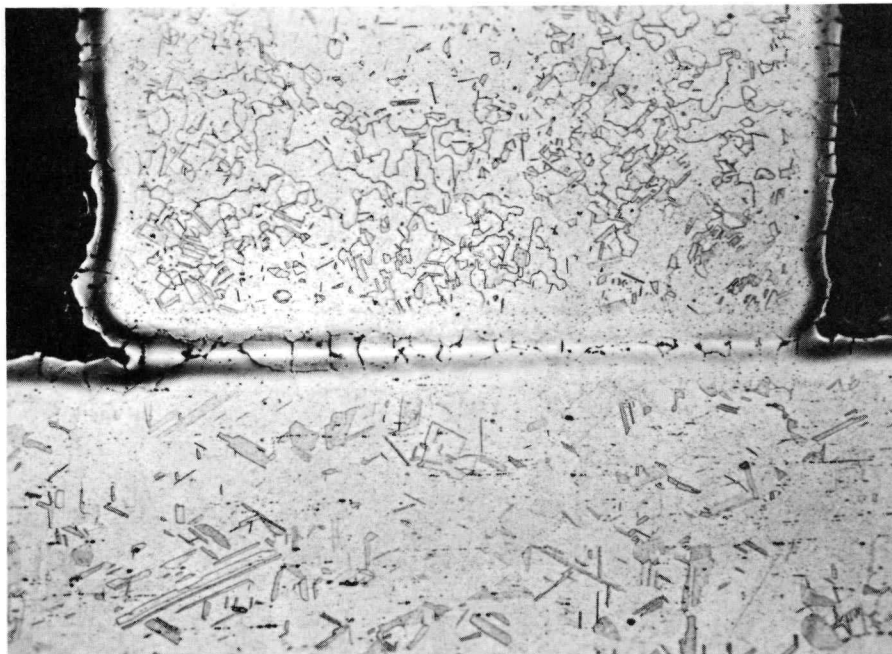


Fig. 1-38. Microstructure of plate-spacer braze obtained with GE-J8100 brazing alloy. Brazing cycle: 2 hr at 2100°F.

Mark-I core procurement specifications. Particular emphasis is on techniques for assessing the homogeneity of UO_2 dispersion in the stainless steel cermet matrix, and integrity of the braze between fuel plates and spacer wires. These techniques are being developed by the Illinois Institute of Technology Research Institute under subcontract with Argonne.

UO_2 Dispersion Homogeneity. Of all the through-transmission methods investigated thus far, the most promising results were obtained with a system employing a monoenergetic cobalt-57 isotope (120 keV). The 120-keV energy level was selected because it is slightly above the uranium "K" ring absorption edge at 116 keV. Thus when exposed to the 120-keV gamma rays, the mass absorption coefficient of UO_2 is nearly a relative maximum. On the other hand, the absorption coefficient of stainless steel at this energy level is sufficiently lower to produce a marked difference in net 120-keV gamma-ray attenuation. Consequently, a high degree of contrast is obtained in the readout equipment. (See Fig. 1-39.) Higher resolution of UO_2 particles in the stainless steel matrix may be possible with the aid of a differentiating amplifier that has been developed by UKAERE (Harwell). This amplifier and its associated readout also will be tested. If successful, the equipment will be incorporated into a complete fuel plate inspection package.

In the meantime, an evaluation has been made of the basic cobalt-57 photomultiplier gamma attenuation equipment, with conventional amplifiers and strip chart readout. As shown in Fig. 1-40, use of a 1-microcurie source

is sufficient to differentiate fuel loading variations of $<2\%$ (i.e., 0.8 wt-% UO_2 in the core) in an 0.08 in. square area of fuel plate. Difference in clad thickness of 0.001 in. produced a corresponding difference of 0.6% in transmittance.

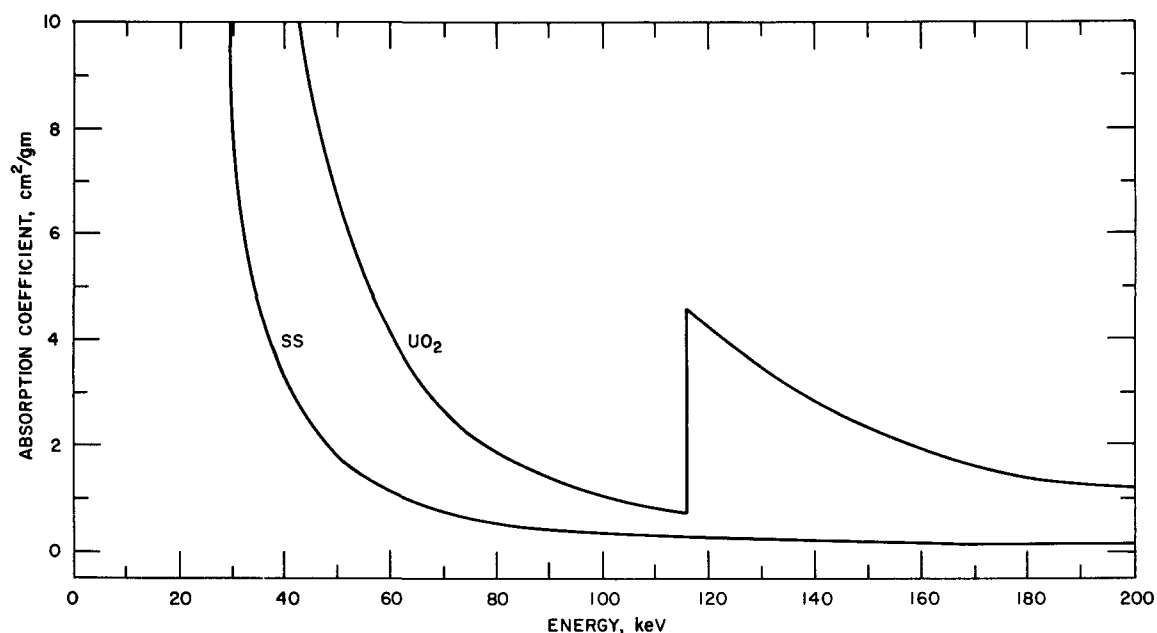


Fig. 1-39. Mass absorption coefficients of UO_2 and stainless steel

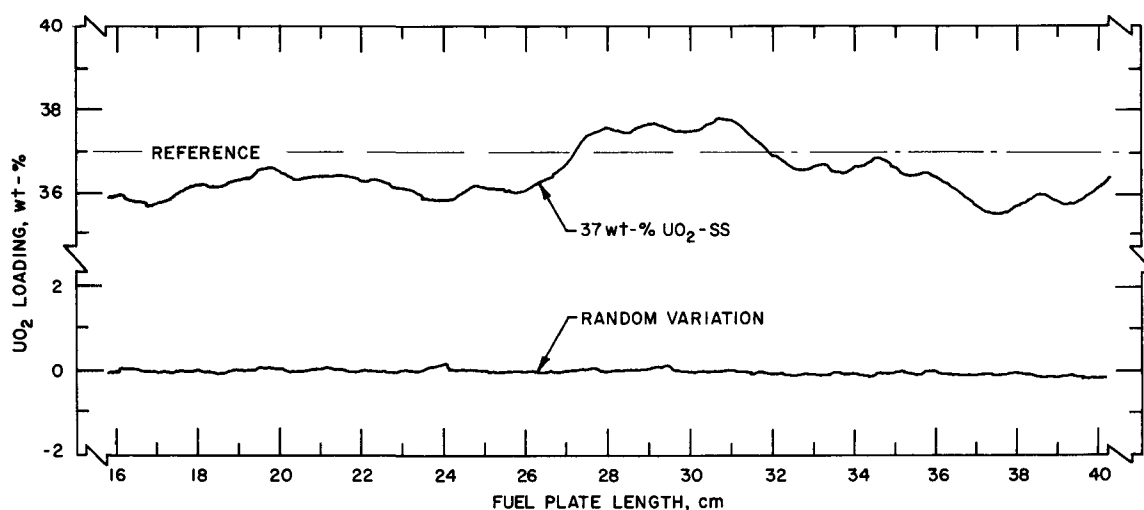


Fig. 1-40. Typical print-out of homogeneity in 37 wt-% UO_2 -SS fuel plate, using cobalt-57 source gamma-ray attenuation technique

In subsequent tests, the source strength will be increased by a factor of 10. This should permit the use of a smaller scanning aperture, thereby increasing the scanning speed and reducing the background "noise". This also results in increased speed and accuracy of the homogeneity measurement and evaluation process.

Brazed Joint Integrity. Hydraulic and pneumatic test procedures were developed for determining gross bond defects, along with more detailed techniques for detecting pinhole-type defects. However, efforts to develop through-transmission methods have met with limited success. The most recent test assembly uses a reflected Lamb wave with an ultrasonic transducer to identify unbonded areas. Thus far, the results have been more qualitative than quantitative.

1.2.3.2 Control Blades and Drive Mechanisms

Control Blade Materials. A rare earth, europium, is to be used as the absorber material in the central control blades because of its higher worth relative to that of hafnium. Control rods containing ~32 wt-% Eu_2O_3 in both the unstabilized and stabilized (2 mol addition of TiO_2 per mol of Eu_2O_3) have been used successfully in the Army Reactor Program. However, because unstabilized Eu_2O_3 reacts when exposed to water, the stabilized material has been selected for use in AARR.

Specimen control blades, fabricated to PM-3 Reactor specifications, were obtained to determine the dispersion characteristics of the stabilized material and to measure the Young's modulus of elasticity of the clad and unclad matrix. These specimens have a face clad ~0.021 in. thick. Subsequent X-ray and neutron radiographs revealed a relatively uniform dispersion of the europium-titanate in the matrix. (See Fig. 1-41.) Measurements by vibration and tensile methods gave a Young's modulus of 21×10^6 psi for the composite plate, and 18×10^6 psi for the unclad matrix.

Consideration is also being given to the use of hafnium in the peripheral control blades. No insoluble problems are anticipated in this event.

Accordingly, two full-size control blades are to be fabricated for hydraulic test purposes. One will contain the stabilized europium-titanate in a stainless steel matrix clad with stainless steel; it will also have a stainless steel follower. The second blade will have a hafnium poison section, with a Zircaloy-2 follower. Both blades will be equipped with a stainless steel upper end fitting.

Control Blade Drives. A full-scale prototype drive mechanism (see Fig. 1-18) is being fabricated for performance tests in an existing control rod flow test loop. The pressure vessel of this loop contains a simulated AARR control blade channel and dummy blade, with provisions for a bottom-mounted drive. Onset of the test program is also pending completion of modifications in the loop piping and valving.

Dashpot Evaluation. Independent bench-type tests with a dummy control blade have revealed the need for redesign of the dashpot. Two test drops, one at zero pressure and the other at 8 psi resulted in audible impact between the blade-mounted piston and the dashpot bottom.

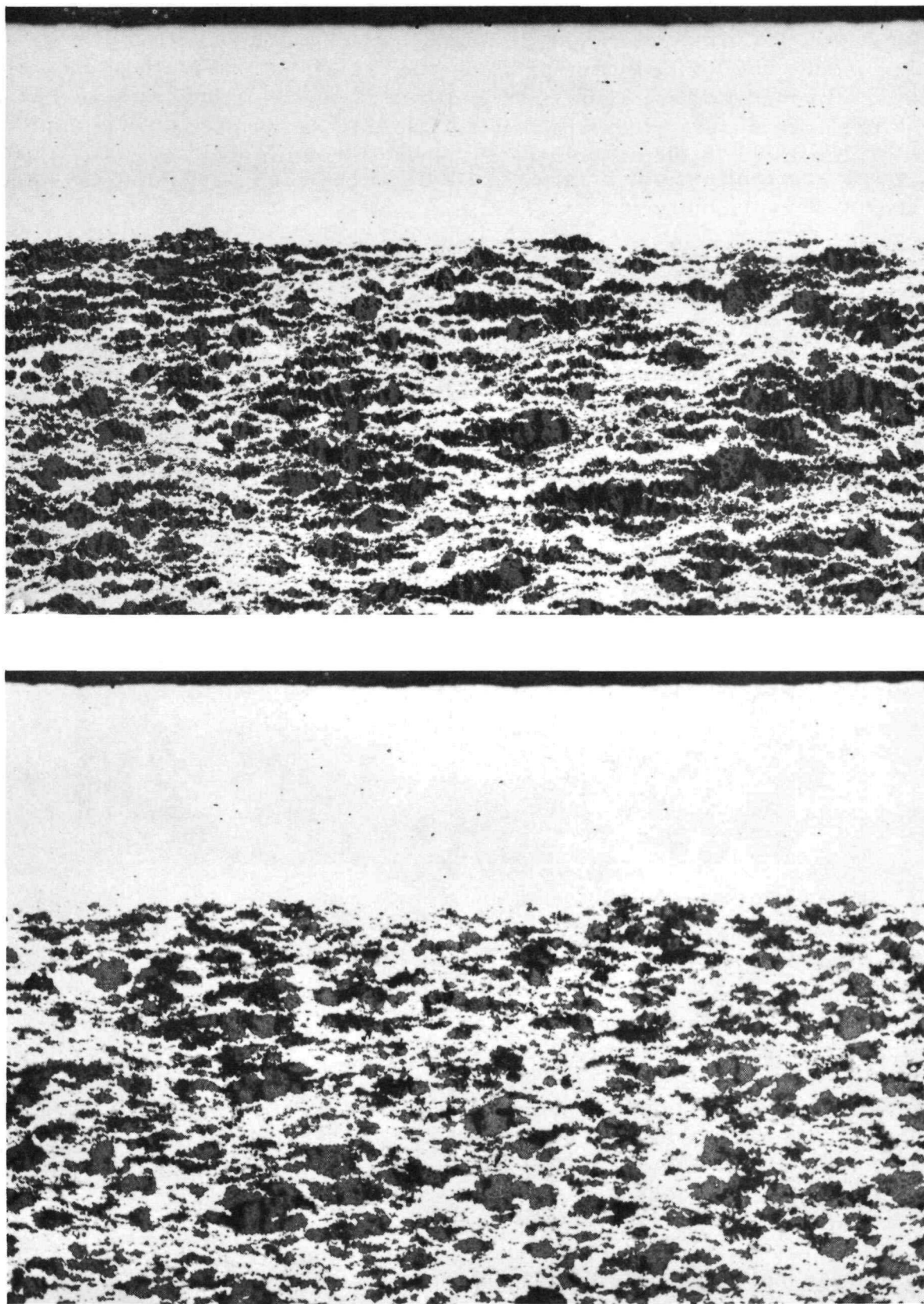


Fig. 1-41. (Top) Longitudinal and (Bottom) transverse microstructures of PM-3 control blades showing relatively uniform dispersion of stabilized $\text{Eu}_2\text{O}_3 \cdot 2\text{TiO}_2$ in stainless steel matrix

1.2.3.3 Stress Analyses of Core Support Grid

An exploratory photo-stress study was performed on the full-scale, aluminum core support grid shown in Fig. 1-42. The objective here was to provide visible indication of maximum stressed areas which would guide placement of additional strain gages for more comprehensive tests. Loading was accomplished by a set of hydraulic jacks each of which acted on a separate dummy fuel end fitting.

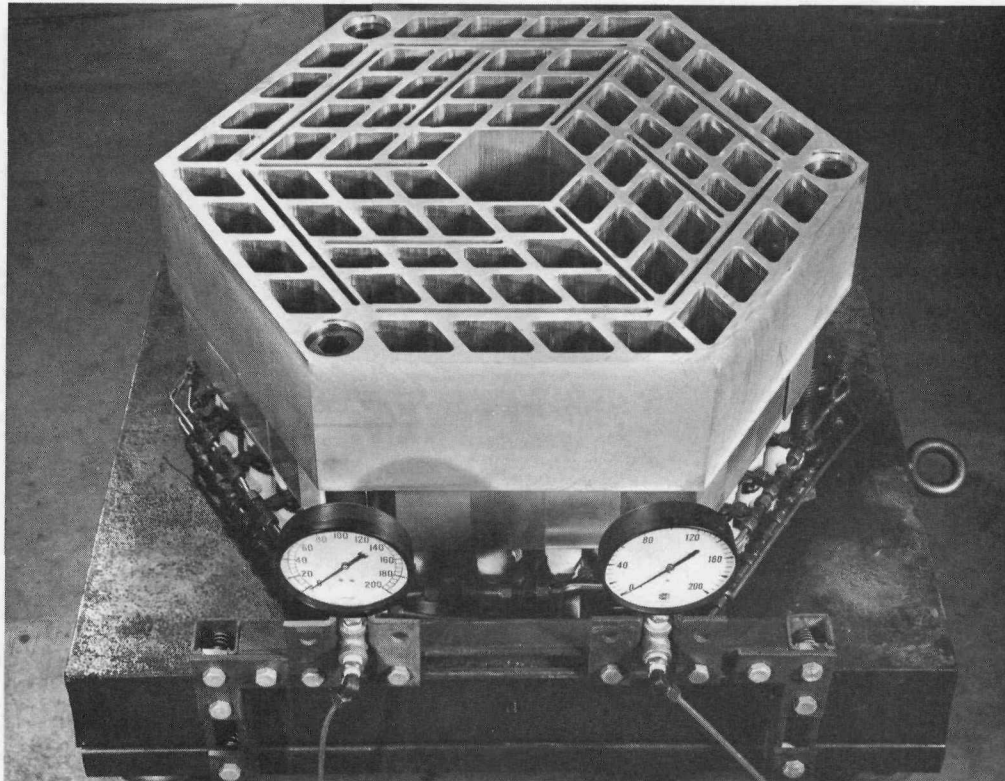


Fig. 1-42. Stress-analysis facility, with full-scale aluminum core support grid in test position

As a result of this study, the grid was reinstrumented, with a majority of strain gages being located near the junctions of the control blade slots. Stress data obtained from subsequent tests are currently being evaluated.

Supplementary stress studies were made to determine the changes in width of the blade slot as a function of load. Measurements were made with a specially designed strain gage probe capable of detecting dimensional changes of 0.0001 in.

These measurements indicated width changes of approximately the same magnitude at the top and bottom of the slots, but in opposite directions. This implies deformation of the support grid about a neutral plane midway between the upper and lower extremities. With an applied load of

25 psi, maximum closure of the four typical slots measured was less than 0.001 in. On the assumption that elastic behavior of the grid will prevail at increased loads, a pressure drop of 125 psi across the core will cause a slot constriction of less than 0.005 in.

1.2.3.4 Stress Analysis of Reactor Vessel

Stress analyses were performed for three vessel materials (SA212B, Type 304 stainless steel, and Inconel-600 alloy) to determine the relative stresses in (1) the shell belt-line containing nonradial beam tube nozzle clusters; (2) the top head with its quick-opening closure and numerous penetrations, and (3) the lower bolted-on head with its complement of openings. In each case, designs meeting the mandatory requirements of ASME Code, Section III could be effected; however, the design with SA212B was unique in that all stresses could be maintained in the elastic range.

The beam tube nozzles are located in a region of maximum neutron flux in addition to the highest level of gamma heating. Therefore, extensive stress analyses, incorporating stress concentration factor distributions around the nozzle-shell intersection, were performed to determine optimum placements of the nozzles. Special computations were included because functional design of the vessel is in variance with Par. N-446 of Section III: "...nozzles should not be placed in regions of high neutron flux." Irradiation damage, particularly at the low operating temperature, must be considered in three vessel areas: (1) the beam tube nozzles; (2) the heat-affected zone at each nozzle; and (3) the vessel wall adjacent to nuclear instrumentation.

A number of schemes were devised to reduce the radiation damage effects. These included: (1) increased vessel diameter to permit inclusion of water shielding to reduce beam tube nozzle damage; (2) relocation of shell-to-nozzle welds in order to utilize the shielding value of the vessel shell; (3) introduction of an internal local shield (8 in. of iron plus 4% water) in the aluminum window region. Computations indicated that the supplementary iron-water shield reduced the 40-year vessel irradiation exposure, in the window region, to 1×10^{18} nvt ($E > 0.1$ MeV) at the 100 MW power level.

Vessel Shell. Stress analysis of the vessel shell was performed with the aid of a computer program, SEAL-SHELL-2.³ This program is based on the finite-element method of calculation in which the shell is approximated by a series of straight or curved segments. Each segment may have different elastic properties and pressures, and may vary linearly in thickness. Each segment also may have a temperature distribution which varies arbitrarily throughout the thickness, but linearly along the segment. The segments are assumed to be interconnected at the nodal points; therefore, the essential elastic characteristics of a segment are represented by

the relationship between forces applied to the nodal points and the deflections resulting therefrom. In the SEAL-SHELL-2 program, the force-deflection relationship is obtained in the following manner:

(1) For each segment a displacement field is assumed and the strain energy is determined.

(2) By application of the principle of virtual work to the strain energy of each segment, the forces on each segment are determined in terms of deflections. Once the force-deflection relationship is known for each segment, the forces at the nodal points can be computed.

It should be noted that the approximation in the finite-element method is of a physical nature, i.e., a shell is substituted by a series of straight or curved segments. There need be no approximation in the mathematical analysis of these substitute segments. Also, the finite-element solution will converge to the true solution if the segment size is successively reduced.

Figure 1-43 shows the mechanical and thermal stresses computed for the Inconel-600 alloy shell. In these computations, the shell was approximated by 200 segments, with an average length of 2 in. The stiffness matrix was calculated from the strain energy through the principle of virtual work. Based on the theory of thick shells, mechanical and thermal stresses were calculated at the inner, middle, and outer surfaces of the vessel wall. Because of the numerous nonradial nozzle connections and possible neutron irradiation damage, lower limits of stress intensity than permitted by the ASME Code, Section III were adopted:

(1) The primary general and the primary local membrane stresses produced by mechanical loads were limited to S_m .

(2) The combined primary membrane, primary bending, and secondary bending produced by mechanical loads, discontinuities, or thermal expansion was limited to 90% of the material yield strength.

(3) The peak stress intensity was limited to S_a .

Multiplicity of nonradial beam tube nozzles in the cylindrical shell introduces stress concentration around the penetrations. Because of the close proximity of adjacent nozzles around the vessel circumference, the time-honored area replacement method of the ASME vessel codes was not expected to yield a reliable evaluation of the stress state. Accordingly, junction stresses were computed by Eringen's method which assumes that the beam tube nozzles are membrane closures. Table 1-7 lists the computed factors (S_c) around a typical nozzle penetration. These values are in good agreement with photoelastic test data.⁵

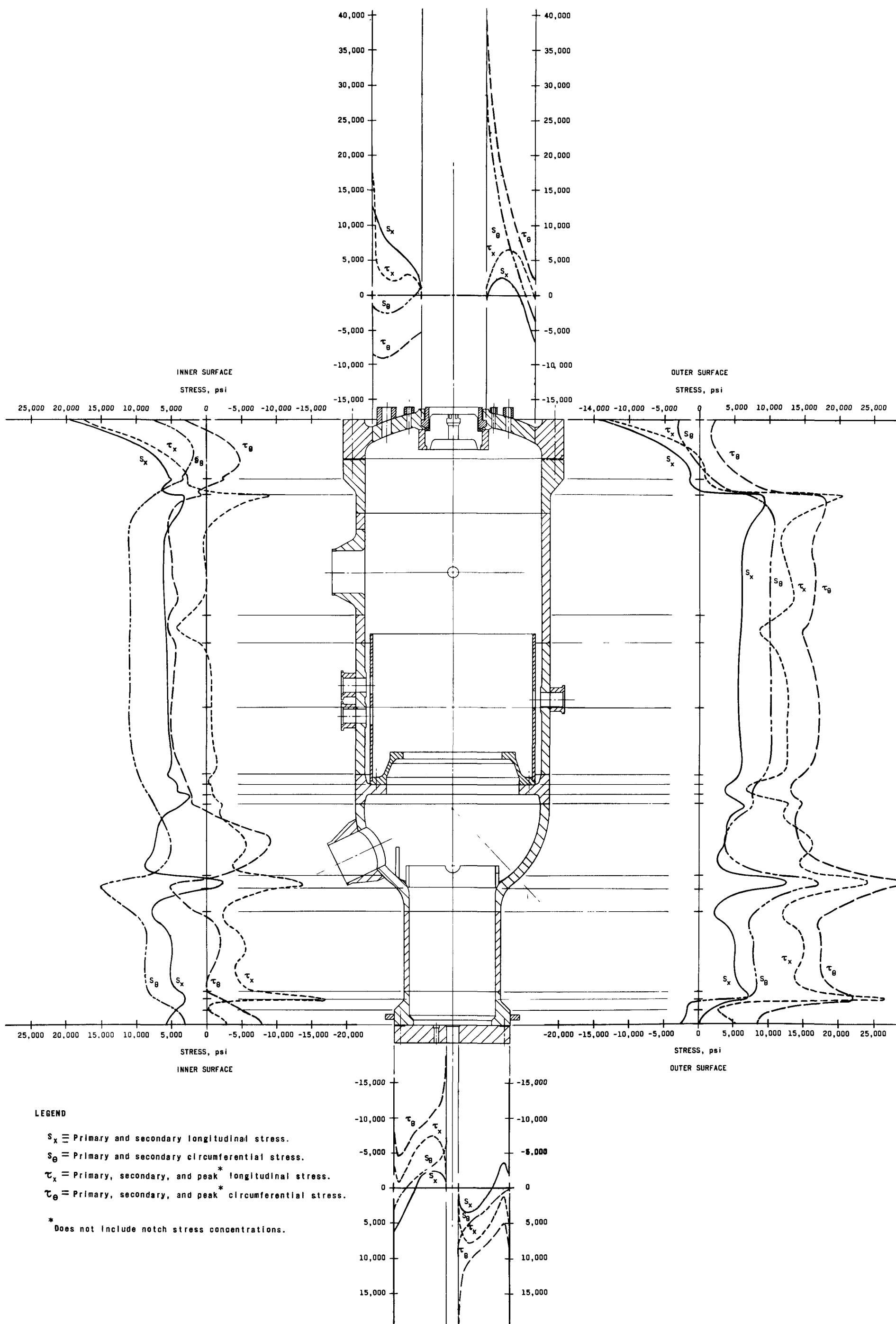


Fig. 1-43. Computed primary, secondary, and peak stresses in an Inconel-600 alloy vessel

Table 1-7. Calculated Stress Concentration Factors

Angle between Radial Line and Longitudinal Axis of Shell	S_c (Upper Surface)	S_c (Middle Surface)	S_c (Lower Surface)
0	3.308	3.286	3.263
22.5	3.068	2.892	2.716
45	2.469	1.904	1.340
67.5	1.842	0.863	-0.117
90	1.574	0.415	-0.745

Top Head. Numerous head configurations, ranging from the original flat plate to the current domed shape, and several penetration arrangements were analyzed to yield the optimum arrangement for experimental needs within the limitations imposed by stresses.

In the analyses, the top head was treated as a perforated plate and effective elastic constants were used in the computation of the equivalent stresses and deflections. Peak stress intensity due to any loading was limited to S_a to ensure against fatigue failures. To prevent gross plastic deformation, the average stress intensity across the minimum ligament section through the plate thickness was limited to S_m , while that across the minimum ligament width transverse to the plate thickness was limited to $1.5 S_m$, for the mechanical loads. For the combined mechanical and thermal loads, the stress intensity across the minimum ligament was limited to $3 S_m$.

Bottom Head. As in the case of the top head, numerous configurations were also analyzed to arrive at an optimum design at acceptable stress levels and deflections.

Nozzle Loads. The Bijlaard theory was used to determine local stresses in the vessel wall at the two 24-in.-dia. inlet and outlet nozzle-to-shell junctions. External forces and moments were first resolved in the three principal directions and then the vessel wall membrane bending, and shear stresses were calculated at the nozzle intersection. Because of the limited applicability of Bijlaard's theory to large nozzles, the calculated stresses were compared with available experimental data. Wherever a discrepancy existed, the larger value was used as the local stress due to external loading. For a particular loading of 31,000 ft-lb, on the inlet nozzle, a maximum additional shell stress was found. The pipe load stresses are very moderate and are easily accommodated by an extension of a uniform wall from the critical belt-line region to the top and bottom sections of the vessel.

Vessel Containment Potential. Exploratory calculations indicate that the vessel wall can absorb a 200 MW-sec core energy release. This energy release, which is twice that postulated for the maximum credible accident, is based on gross plastic deformation which would render the vessel inoperable but structurally intact. For slow-release nuclear excursions, the absorption potential of the wall increases by a factor of 3.

Neither the shock wave nor the quasi-static internal blast pressure consequent to a 200 MW-sec excursion is of sufficient intensity to render missiles of the top and bottom heads. The most probable missile is the central quick-opening plug in the top head, but only if it is in the unlocked position at the time of the excursion. In this event, it may be accelerated to a velocity sufficient to breach the containment building.

1.2.3.5 Factors Involved in Selection of Vessel Material

Selection of a material for the AARR reactor vessel is governed more by environmental and procurement factors than by strength. For the three materials employed in the stress analysis, the required shell thickness is about the same: ~4 in. The stress states, however, differ markedly because of large differences in the coefficients of thermal conductivity and expansion. These two properties define the magnitude of the computed thermal stresses and the combined stresses. For example:

- (1) Peak stresses in carbon steel (SA212B/SA105B) are below the yield strength of the material, i.e., the shell is elastically stressed.
- (2) Local peak stresses in the Inconel-600 material (see Fig. 1-43) approximate the yield strength in regions removed from the belt-line section.
- (3) Peak stresses in stainless steel Type 304 are at, or above, the yield strength of the alloy, i.e., the shell is stressed plastically and must be work-hardened to resist failure by fatigue.

The carbon steels require internal cladding to maintain primary coolant purity. Externally, the vessel shell is subject to corrosion by oxygenated (natural and radiolytic) pool water. Corrosion may be limited either by exterior cladding, or by chemically maintaining a (radiologically active) pool environment inoffensive to unclad steel walls. Stress calculations indicate a preference for loose cladding which (1) reduces the thermal gradient (and stresses) across the wall, and (2) raises the shell temperature. Moderate increase of the shell temperature, particularly in the belt-line section, also reduces the severity of the NDT problem associated with the low temperature (130°F) of the reactor.

Austenitic stainless steel Type 304, currently believed to be more radiation-damage resistant than the carbon steels, is ruled out as a shell material for at least two reasons:

(1) Cracking of the parent vessel material by either stress or chloride (or both) mechanisms. In either event, crack propagation is apparently uninhibited in structures stressed by tensile forces. In addition, clad cracking has been observed in arc-deposited cladding in the Elk River Reactor and in wrought spot-resistance welded cladding in the EBWR.

(2) Technology of welding thick plates. Consultations with qualified vessel fabricators failed to reveal established data on welds in austenitic stainless steel plates in excess of 2 in. thick. This lack of data closely parallels the recently developed mechanical properties for stainless steel plates 4 in. and thicker.⁶

Austenitic high nickel Inconel-600 alloy was selected as an alternate material because of its resistance to stress and chloride cracking, and probable resistance to radiation damage. Also, its thermal properties are intermediate between the carbon steels (SA212B/SA105B) and stainless steel Type 304, which results in tolerable thermal stresses. The magnitude of the thermal stresses across a solid Inconel-600 wall can be computed from Fig. 1-43.

Radiation damage over the vessel lifetime (40 year) poses a problem in two highly localized regions: (1) the "aluminum windows" which pass epithermal neutrons from the core region, and (2) through the vessel wall to the adjacent instrument cluster. A way was found to effectively reduce the vessel wall neutron-radiation damage effects by interposing an internal scattering shield of iron and water into the water zone between the beryllium reflector and the "aluminum-window." Studies were started to assess radiation-damage effects to the water-cooled beam nozzles by obliquely incident neutron beams.

1.2.3.6 Studies Related to Development of Beam Tube Facilities

Steady-State Thermal Analysis

The objective of this analysis was to determine the total heat generation, coolant requirements, maximum metal and surface temperatures for the beam tubes consistent with the present stainless steel core design.

Table 1-8 lists the calculated total heat generation in that portion of the beam tubes and jackets within the reflector. These results are based on heating values for a homogeneous reflector wherein large gradients in heat generation rates across the tubes are predicted.

Table 1-8. Total Heat Generated (kW) in Beam Tubes and Jackets at Reactor Power Levels of 100 and 240 MW

	100 MW		240 MW	
	Beam Tube	Jacket	Beam Tube	Jacket
Through-Tubes	11.2	1.8	26.9	4.4
Blind Tubes: BT-1, -3, -4, -6	9.7	1.6	23.3	3.8
Blind Tubes: BT-2, -5	7.2	1.1	17.2	2.8

Calculated maximum (hot spot) temperatures are given in Table 1-9. The hot spot is located on the core side of the tubes, and for the blind tubes is very near the junction of the hemispherical tip and the cylindrical section. At this location, the heating rate (at 240 MW) is 11 W/gm. The heat flux values are from one-dimensional calculations and have been adjusted for an estimated thermal growth of the blind tubes inward toward the core. For all tubes, the coolant flowrate is 50 gpm, which results in film coefficients on the order of 2000-2500 Btu/(hr)(ft²)(°F), depending upon the water temperature. Temperature drop across surface oxides is based on film thickness determinations from ANL-sponsored corrosion tests on Type 6061-T6 aluminum.

Table 1-9. Calculated Hot Spot Temperatures

Reactor Power, MW	Water Inlet Temp., °F	Peak Heat Flux, Btu/(hr)(ft ²)	Maximum Temperatures, °F		
			Local Water	Oxide-H ₂ O Interface	Tube Metal (Inside Surface)
<u>Blind Tubes</u>					
240	135	125,000	148	209	253
100	135	52,000	141	167	181
100	190	52,000	196	217	236
<u>Through-Tubes</u>					
240	135	60,500	140	170	184
100	135	25,200	137	150	156
100	190	25,200	192	203	212

Hydraulics

A series of flow bypass orifices for the beam tube jackets was designed to relieve unnecessarily high water velocities in the converging portion of the channel around the tip of the blind tubes and to obtain the

proper distribution of flow in this area. This is desirable to minimize pressure losses and may also reduce erosive effects. Design criteria for the orifice layout were to maintain adequate cooling over the tip and to prevent velocities over the tip and through the orifices from exceeding 150% of those in the straight annular channel. A design method based on simple momentum theory was developed which gave reasonable agreement with published data from somewhat similar geometries involving separating and joining flows with abrupt area changes and sudden flow reversals. This method was also employed in the design of the flow-distributing orifices at the coolant inlet.

A rough estimate of pressure losses for the reactor portion of the beam tube coolant circuit was made. Calculated losses on the order of 9 and 11 psi at 50 gpm were obtained for the blind and through-tubes, respectively. These values are subject to further analytical refinements and an experimental check on the prototype tube.

Beam Tube Emergency and Shutdown Cooling

Some limiting-type calculations were made to estimate beam tube temperatures after loss of flow with and without reactor scram. Although these situations presently cannot be rigorously examined, the following results were obtained through the use of simple analytical models which assume no transfer of heat from the local region under consideration:

Conditions after Loss of Flow with Reactor Scram from 240 MW

Time for blind tube metal to reach 350°F	>10 min.
Time for blind tube metal to reach 500°F	>45 min.
Time for coolant to reach saturation temp. (511°F)	>79 min.
Time to completely evaporate coolant locally	>167 min.

Conditions after Loss of Flow, Reactor at 240 MW without Scram

Time for blind tube metal to reach 500°F	>10 sec
Time to completely evaporate coolant locally	>81 sec
Rate of temperature rise of vapor "insulated" tube	~24°F/sec

Beam Tube Stress Analysis

Generalized charts for determining thermal and pressure stresses in the through-tubes and in the cylindrical portion of the blind tube have been prepared. Maximum stresses occur at the inside surfaces of the tube and are compressive. The stress due to external (design) pressure of 875 psia is 6300 psi. Theoretical tube buckling pressure has been calculated

to be within the range of 5600-6700 psi, assuming an ideal tube at uniform temperature. Thermal stresses calculated on the basis of uniform heating at the maximum rate were found to be 1360 psi.

Estimates of bending moments and stresses in the beam tube adapter have been made for various possible loading conditions. These stresses can arise from the weight of internal shielding in the adapter and/or restraint of the adapter during thermal growth of the reactor vessel relative to the biological shield. Although shielding loads and vessel temperatures have not been finalized, the estimated stresses are well within allowable limits for all presently foreseeable conditions.

1.2.3.7 Analytical and Experimental Studies of the Flow-Reversal Problem in Hydraulic Rabbit Facilities

Nature of Problem

One of the major problems associated with most re-entry-type hydraulic rabbit irradiation facilities is posed by coolant flow reversal, which prefaces sample removal operations. The time elapsed during flow reversal will reflect a temperature rise in the sample and coolant, and a fluctuation in the coolant pressure. With reference to AARR, an increase in coolant temperature combined with a decrease in coolant pressure could lead to boiling at the sample surface, an increase in reactivity due to void formation in the internal thermal column, and rapid shutdown of the reactor. In such event, continued increase in sample temperature could lead to partial or total meltdown of the sample. Under these conditions, a large surge of pressure resulting from flow reversal could terminate in failure of the facility tubing. Other problems related to the design of re-entry-type rabbit facilities include capacity to cool a sample during steady-state irradiation, heat transfer capabilities and limitations.

Most of these problems have been investigated analytically and experimentally, and the findings incorporated in the design of Hydraulic Rabbit Facility Development Test Loop for AARR. These findings are summarized in the following subsections.

Analytical Studies

Pressure Fluctuations. The flow system of a prototype Hydraulic Rabbit Facility Development Test Loop (Fig. 1-44) was simulated on an analog computer to determine the effects of coolant flowrate, duration of flow reversal, and position and capacity of surge tanks on pressure fluctuations promoted by flow reversal.

The results of these studies emphasized an important consideration in the design of a hydraulic rabbit facility. When a valve is closed, an

initially positive pressure fluctuation is generated on the inlet side of the valve, and an initially negative pressure fluctuation is generated on the discharge side of the valve. The respective fluctuations are a maximum adjacent to the valve and decrease in magnitude with distance from the valve. Hence, at some position in the flow system, a node exists where no pressure fluctuations are generated by flow reversal.

Figure 1-45 shows typical pressure fluctuations generated at Points 1, 2, and 3 in Fig. 1-44, when the "normally opened" valves are closed. This behavior dictates that sample position during steady-state irradiation should be at the nodal point of the flow system.

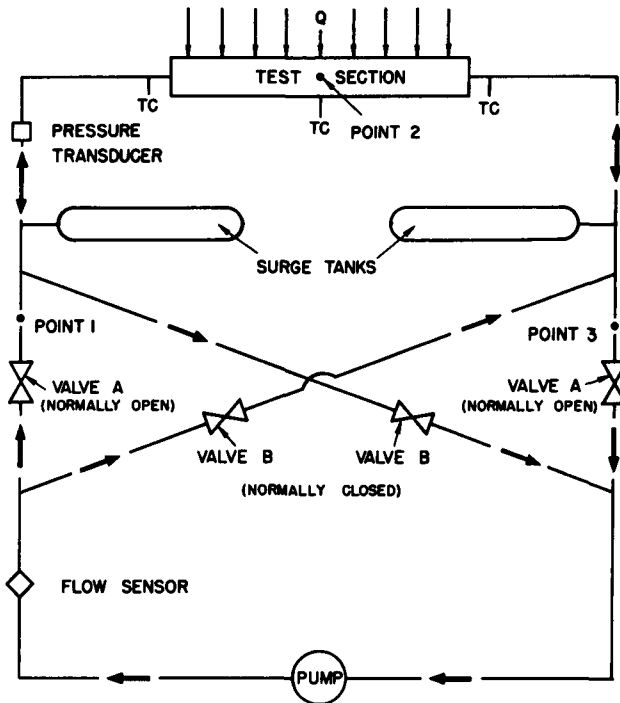


Fig. 1-44. Schematic of analog model of Hydraulic Rabbit Facility Development Test Loop

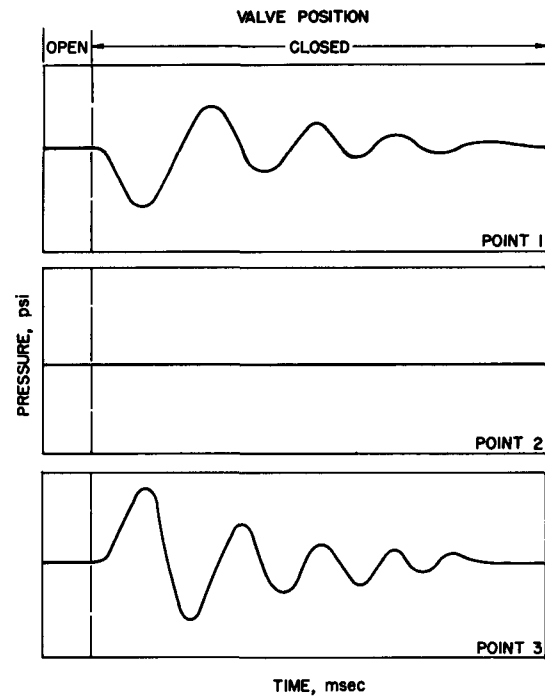


Fig. 1-45. Typical pressure fluctuations generated at specific points in analog model when "normally opened" valves A in Fig. 1-44 are closed, and valves B are opened to effect flow reversal

Other observations of interest to the test loop design were as follows:

(1) The magnitude of pressure fluctuations during flow reversal can be controlled and limited by appropriate sizing and positioning of the surge tanks. Flow reversal time increases as the size of the surge tank(s) is increased.

(2) The magnitude of the pressure fluctuations increases (a) as the flow reversal time decreases, or (b) as the coolant flowrate increases.

Temperature Rise. For a typical aluminum sample, calculations indicate a temperature rise of 10°F during a flow reversal time of 35 msec, and a maximum temperature of 210°F during removal operations.

Steady-State Heat Transfer. A digital computer program has been written which provides a heat transfer analysis during continuous sample irradiation. This program calculates the axial temperature distributions in the reactor vessel, and temperatures of the facility coolant, rabbit tube, sample (surface and internal), and primary coolant adjacent to the facility.

The analysis rendered by the program must be considered preliminary, since it is based on a facility composed of one rabbit tube and "straight through" coolant flow. By comparison, the present AARR design specifies two concentric tubes, with coolant return through the intervening annulus (re-entry type). Possible use of a third concentric tube, to increase coolant velocity (and heat transfer) is also under consideration.

Nonetheless, application of the program output to the present AARR facility is not as limited as would appear. For example, the heat balance must be altered only by the additional heat generation ($\sim 10\%$) of the second concentric tube. Temperature distribution also must be altered, but the primary objective of the preliminary analysis - sample temperature distributions - is essentially unaffected.

Thus far, the analysis indicates that the proposed rabbit facility is capable of removing heat generated by the fuel sample. However, the present cylindrical sample container does have heat transfer limitations. Moreover, in the case of a fuel sample, the internal temperatures of the cylinder might exceed the fuel melting point. To offset this limitation, the container design will be modified to ensure adequate heat transfer.

Experimental Studies

The scope of these studies included flow reversal times, pressure fluctuations, and sample temperature rise. These data were obtained during operation of the Hydraulic Rabbit Development Test Loop.

Test Loop. Except for the use of one surge tank (volume = 0.018 ft^3 air), the loop equipment and hydraulic system were designed and arranged consistent with information developed from the analog model (Fig. 1-44).

Briefly, the re-entry rabbit facility was simulated by a test section consisting of two, independently supported, concentric stainless steel tubes, 5 in. long. The inner tube measured 1.978 in. O.D., with a wall thickness of 0.062 in. The outer tube (2.360 in. O.D., 0.248 in. wall) was electrically heated (13 kW) to provide the desired heat flux. Sections of Plexiglas tubing

were installed in the 1-in. stainless steel piping upstream and downstream of the test section to observe any boiling that might occur during flow reversal. A Plexiglas section, containing a movable cylinder, was installed in a bypass line to provide indication of flow direction. Water was pumped through the system at 12 gpm.

As shown in Fig. 1-44, instrumentation consisted of a hydropoise flow sensor calibrated in both directions of flow, a pressure transducer, thermocouples, fast-response recorder, and oscilloscope. Special electrical switches were installed on the valve assemblies to trigger the oscilloscope during flow reversal. Traces were photographed with a Polaroid camera mounted on the oscilloscope.

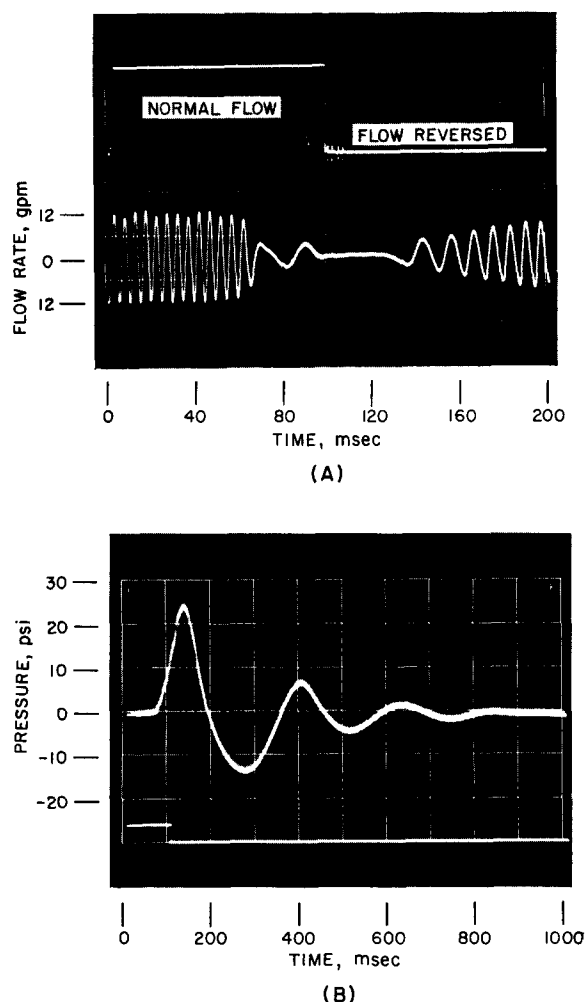


Fig. 1-46

Oscilloscope traces of (A) flow sensor output and valve position signals, and (B) pressure fluctuations resulting from flow reversal

Flow-Reversal Times. The procedure used to obtain these data consisted of opening the camera shutter, manually positioning the flow-reversing valve assemblies which triggered the oscilloscope, and then closing the camera shutter after a predetermined exposure time.

Figure 1-46(A) is a typical recording of the flow magnitude as a function of valve position. As the valves begin to close (or open, depending on direction of flow), the oscilloscope is triggered. When completely closed, the valves initiate a step change in the signal; total valve travel time is ~100 msec. Examination of Fig. 1-46(A) shows that the duration of no flow appears to be a maximum of 30 msec, that flow is 50% developed in the ensuing 40 msec, and fully developed in 100 msec after the period of no flow.

Pressure Fluctuations. As shown in Fig. 1-46(B) maximum pressure fluctuations of ~24 psi occurred adjacent to the valves during closure, and dissipated ~0.8 sec after the valves were completely closed.

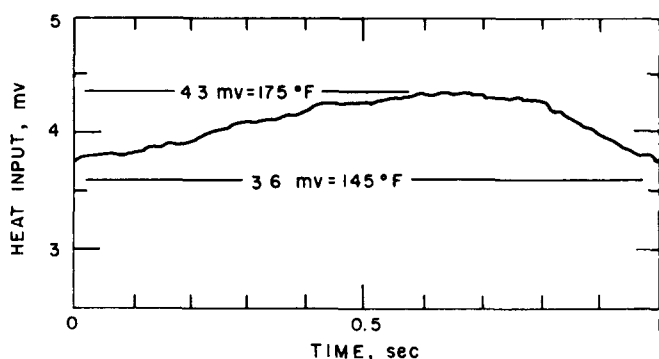


Fig. 1-47. Strip-chart recording of test section surface temperature rise during flow reversal

Temperature Rise.

Figure 1-47 shows a typical strip-chart recording of the surface temperature of the test section, as registered by chromel-alumel thermocouples. The indicated maximum temperature rise of 30°F exceeds the value of 22°F calculated for a sample generating 13 kW of heat. However, unlike the sample, the test section is not removed from the heating zone when the flow is reversed.

Therefore, corrections were made in the experimental data to account for the heat transfer to a mass of water heated just prior to flow reversal.

Analytical vs. Experimental. As shown in Table 1-10, where this correction is applied to the measured temperature rise, the foregoing experimental values all fall within the range of the analytical data.

Table 1-10. Comparison of Analytical and Experimental Data

Parameters	Analytical	Experimental
Temperature Rise	22°F	30°F
Reversal Time	20-45 msec*	35 msec
Pressure Fluctuations	60-17 psi*	24 psi

*Extrapolated limits.

Future Work. A full-scale hydraulic rabbit facility will be constructed for comprehensive performance-evaluation tests of prototype components.

1.2.3.8 Corrosion and Compatibility of Reactor Materials

The AARR reactor vessel will contain three principal materials in contact with the light-water coolant: (1) stainless steel in the fuel, control blades, and structural components; (2) beryllium in the reflector; and (3) aluminum in the beam tubes and other experimental facilities. Although these materials are conventional for water-cooled reactors, they will be exposed under more severe conditions in the AARR. For example, corrosion of anodic areas may be accentuated by the extremely low Be-Al to stainless steel surface ratio, and the similarly low Be-Al surface to H₂O volume ratio. Of major concern is the deposition of corrosion products on fuel clad surfaces and on the beam tube tips.

In the absence of corrosion data directly applicable to AARR conditions, and in view of their experience with similar studies for the HFIR, ATR, and ORR systems, ORNL was subcontracted to conduct the required test program. The results and observations, as of June 30, 1966, are summarized in the following subsections. All experiments were conducted in deionized water with a specific resistivity of 10^6 ohm-cm or greater.

Beryllium. Two series of loop tests were performed to determine the effect of Be surface-to- H_2O volume ratio on the corrosion rate of beryllium. Both tests revealed that the corrosion rate is linear with time and definitely dependent upon the ratio of exposed surface area to water volume. Moreover, as shown in Fig. 1-48, increasing the ratio by a factor of 10 reduces the corrosion rate by a factor of ~ 2 .

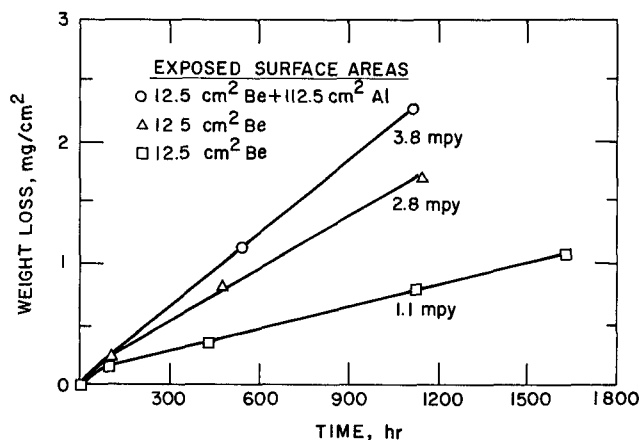


Fig. 1-48. Corrosion of beryllium in deionized water at 200°F and 44 fps

A review of long-term (~ 2 year) corrosion test data accumulated by ORNL during the aforementioned reactor programs also showed that beryllium corrodes at a constant rate. Therefore, since the Be surface-to- H_2O volume ratio in AARR will lie within the scope of the current tests, the corrosion rate of beryllium is expected to range from 1.1 to 2.8 mpy. This rate is acceptable.

Beryllium-Aluminum. In these tests, samples of beryllium and 6061-T6 aluminum were exposed simultaneously under similar loop conditions. At first glance, the results in Fig. 1-48 would indicate that the presence of aluminum accelerates the corrosion of Be; however, it is probable that the difference between 2.8 and 3.8 mpy represents the limits of reproducibility.

Aluminum Beam Tube Coolant Channel. Two series of corrosion tests were conducted on an electrically heated (60 cycle, a-c), 6.5-in.-long, specimen coolant channel (0.5 x 0.050 in.) fabricated from 6061-T6 aluminum. Ten thermocouples were spot-welded along the outer surface. The specimen was then covered with close-fitting insulation so that all heat generated in the specimen was removed by water circulated through the central channel.

Table 1-11 lists the first test series results based on circulating coolant from within the reactor vessel. This test was interrupted after 1818 hr by a power failure. Lower temperatures were registered upon

resumption of loop operation, indicating some spallation of corrosion products from the specimen. Upon removal after 2000 hr exposure, the specimen was found coated with a nonuniform black oxide. Metallurgical examination revealed a relative uniform attack, with metal losses increasing from 2 mils at the specimen inlet to 4 mils at the outlet.

Table 1-11. Effect of Using In-Vessel Coolant on Corrosion Buildup and Resulting Temperatures of Specimen Aluminum Beam Tube

Test Time, hr	Temperature, °F			Corresponding Oxide Thick., mil
	Interface at Axial Midpoint	Increase on Outside Wall	Total	
793	258	78	336	1.48
1507	258	130	388	2.47
2000	258	150	408	2.90

In view of the high aluminum metal temperatures recorded in the first test series, the second series was based on circulating coolant at lower temperatures from a system external to the vessel. The corresponding temperatures and oxide thicknesses are listed in Table 1-12.

Table 1-12. Effect of Using Independent Cooling System on Corrosion Buildup and Resulting Temperatures of Specimen Aluminum Beam Tube

Test Time, hr	Temperature, °F			Corresponding Oxide Thick., mil
	Interface at Axial Midpoint	Increase on Outside Wall	Total	
140	190-202	0	190-202	0
807	193.0	12.6	205.6	0.5
2000	194.5	17.0	211.5	0.66

After 2000 hr exposure, the specimen surface was smooth and light gray, with no evidence of film spallation or localized attack. Metallurgical examination revealed an actual metal loss ranging from 1.0 to 1.6 mils.

Aluminum-Beryllium-Stainless Steel. These loop tests were made to determine the effect of high heat fluxes, and the presence of aluminum and beryllium, on the corrosion and buildup of corrosion products on fuel cladding surfaces. The cladding was simulated by an electrically heated, Type 304 stainless steel tube (0.118 in. I.D., 0.015 in. wall). Again,

thermocouples were attached to the outer surface and insulation applied to ensure heat removal by the circulating water. The relative exposed surfaces of all materials and the surface-to-water volume ratios were consistent with values expected in the AARR.

Table 1-13 lists the temperatures and corresponding fluid film coefficients prevailing at the start of Phase I test. These values remained essentially constant during the 1004-hr test period.

Table 1-13 Typical Temperatures and Fluid Film Coefficients for Simulated Stainless Steel Cladding during Al-Be-SS Compatibility Test - Phase I Heat Flux = 40×10^6 Btu/(hr)(ft²), Coolant Velocity = 47 fps

TC* Spacing, in	Temperature, °F			Fluid Film Coefficient, Btu/(hr)(ft ²)(°F)
	Outer Surface	Water Interface	Bulk Water	
1 00	568	350	132	18,100
1 25	584	366	136	16,700
2 25	592	374	148	17,500
3 25	613	395	161	16,700
3 25	574	356	161	20,500
4 25	619	401	176	17,500
5 25	630	412	187	17,500
5 50	629	411	190	17,000
6 25	657	419	200	18,000

*Distance from tube inlet

Long-term Phase II tests are in progress. The objective here is to evaluate the corrosion behavior of the tube at simulated AARR core conditions and core lifetime.

Table 1-14 lists the temperatures and film coefficients at the outset of the Phase II test. Thus far, 1465 hr of testing have been accumulated, with no significant change in temperature. This test is scheduled for completion in July, 1966.

Table 1-14 Typical Temperatures and Fluid Film Coefficients for Simulated Stainless Steel Cladding during Al-Be-SS Compatibility Test - Phase II Heat Flux = 2.1×10^6 Btu/(hr)(ft²), Coolant Velocity = 47 fps

TC* Spacing, in	Temperature, °F			Fluid Film Coefficient, Btu/(hr)(ft ²)(°F)
	Outer Surface	Water Interface	Bulk Water	
1 25	454 0	345 5	236 0	19,000
2 25	465 0	356 5	245 0	18,700
3 25	464 0	355 5	252 0	18,400
4 25	471 0	362 5	258 0	18,200
5 25	475 0	366 5	265 0	18,700
5 50	484 0	373 5	267 0	18,100
6 25	482 0	375 5	272 0	18,400

*Distance from tube inlet

Couple Corrosion. Crevice and galvanically coupled samples of beryllium, aluminum, and stainless steel are also under long-term corrosion test in an isothermal loop containing deionized water at 200°F and velocities of 44 fps and 2 fpm. Visual examination of all samples after 1000 hr of exposure revealed no evidence of corrosive attack. This test is scheduled for termination in early FY-1967.

1.2.3.9 System Dynamics and Transient Analysis

Control Systems Analysis

This activity is an extension of the fiscal 1965 effort directed toward improvement in the analog model of AARR and an expanded computer program to be used for supporting analysis of proposed methods of reactor control. (See ANL-7190, p. 96.) When completed, the model will describe the dynamic behavior of the reactor core, major process systems, and their control mechanisms consequent to nominal disturbances of the reactor steady-state and programmed power maneuvers. Control stability, and speed and accuracy of responses are the primary goals of the analytical effort.

Thus far, two subprograms have been developed. One consists of equations which describe core neutronics, heat transfer, and coolant conditions. The other is a hybrid code, which is used in conjunction with the PDP-7 digital computer to calculate the transport delays in process variables. Current effort is centered on development of equations for subprograms that describe the behavior of primary heat exchangers and all controllers in major control loops.

Ultimately, all of these subprograms will be integrated to provide an overall simulation of the controlled reactor. No major obstacles are anticipated in the production of a comprehensive, operating analog program.

Transient Analysis and Safety Studies

Revised Estimates. Earlier estimates of reactor transient behavior (see ANL-7190, p. 97) were recalculated because of subsequent changes in design parameters, particularly those relating to neutronic, thermal, and safety-system characteristics. As in the earlier studies, the calculations were performed using a modified version of the core model used to predict transient responses of the HFBR. Adjustments were made in both the mathematical model and analog computer program to reflect the aforementioned design changes.

The detailed results were incorporated in the approval copy of the Preliminary Safety Analysis Report for AARR. Briefly, the calculations consisted of: (1) parametric studies to determine the general characteristics

of reactor responses to rapid reactivity additions; and (2) determinations of reactor behavior and effect of safety system action for specific hypothetical accidents during operation at 100 MW. The significant findings are as follows:

(1) For rapid reactivity insertions less than $\beta_{0.85}$, the reactor inherently limits the initial power burst through temperature-dependent reactivity compensation. Rapid safety system action is not required to suppress the ensuing power rise.

(2) For rapid reactivity insertions much greater than $\beta_{0.85}$, presently conceived safety systems are ineffective in limiting the initial power burst. Peak power occurs within tens of milliseconds following initiation of the transient and some fuel melting will be incurred.

(3) For certain specific accidents (e.g., inadvertent control rod withdrawal, cold water injection in the core, and massive voiding of the bulk coolant within the Internal Thermal Column), safety system action will prevent fuel melting. Calculations indicate that even with all blades positioned for low differential worth, an initial scram acceleration of $<2g$ should be adequate to limit transients incurred by postulated accidents. Moreover, with appropriate restraints imposed upon maximum withdrawal of the blades from the active core, an initial scram acceleration of $1g$ is sufficient to prevent fuel melting.

Analytical Refinements. Extensive planning studies have resulted in implementation of a long-term program involving further refinements of the current mathematical model. These refinements are essential to the successful conduct of a comprehensive analysis of AARR transient behavior under hypothesized accident conditions. Specific items identified for detailed analysis included:

- (1) Space-time dependent neutron kinetics.
- (2) Transient heat transfer and hydraulics, including void formation.
- (3) Mode of thermal expansion of the reactor core.
- (4) Effects of transient thermal stresses upon fuel plates and other potentially vulnerable structures.
- (5) Effects of pressure pulses, originating from coolant boiling and thermal or chemical interactions of molten fuel and coolant (steam or water), upon reactor core and primary system containment.

Initial programmatic efforts have centered on subroutines for heat transfer and hydraulics analyses, and digital code revisions for neutron

kinetics studies. Equations for first approximation to transient heat transfer and hydraulic conditions in core coolant channels have been developed and are being programmed for computer solutions. Ultimately, the results will be compared with data obtained from the proposed transient heat transfer tests.

Consistent with the above-mentioned program, an analysis was made to evaluate the margin of error incurred in calculated transient temperatures by neglecting the temperature dependence of fuel plate thermal properties. Basic data for this evaluation were obtained from a detailed thermal model as provided by the G.E. digital code THTB (ANL designation: RE-322). Time dependence of heat generation was selected from analog calculations of coupled neutronic and thermal responses to various reactivity perturbations. Comparison calculations of plate and coolant temperatures for a given heat generation function were then made assuming (1) constant and (2) temperature-dependent conductivities and specific heats of the plate metal.

The worst case studied corresponded to a step-function reactivity addition of \$1.50. In this case, the maximum error incurred by the use of constant thermal properties was less than 6% in metal temperatures, and less than 3% in coolant temperatures. Also, the estimated maximum error reflected in the calculated reactivity feedback is less than 10%. Accordingly, it is concluded that the use of constant thermal properties for fuel plate materials provides sufficient accuracy for transient temperature calculations.

Digital Computer Control

A two-phase program is underway to determine the technical and economical merits of using an on-line digital computer in the AARR control scheme. Thus far in Phase I, basic design criteria have been formulated and four major levels of computer participation in plant operation have been outlined for further investigation. Ultimately, the results of this investigation will lead to selection of the most promising computer control complex for comprehensive evaluation (Phase II).

Phase I studies are being performed by the AARR architect-engineer (Burns and Roe) in collaboration with cognizant ANL personnel. Briefly, these studies include: (1) a review of the Title I plant design and functional requirements for various operating modes; (2) preparation of logic and functional equipment block diagrams; (3) establishment of computer requirements; (4) a survey of the computer equipment market; and (5) preparation of preliminary equipment specifications and comparison cost estimates.

A review of the preliminary plant design and operating objectives has resulted in formulation of the following basic design criteria for computer application in AARR:

(1) The digital control system shall not inhibit operation of, nor shall it replace any portion or function of, the normal safety system.

(2) The plant shall be operable without the computer.

(3) In the event of a computer failure, the computer outputs to the process controllers shall hold the value in effect just prior to the failure.

Computer functions associated with four major levels of participation in plant operation that were selected for further investigation are listed below. (Note: Functions at each level include those listed for all lower levels.)

Level 1: High- and low-speed data logger
Alarm scanner
Historical data storage
Selected calculations

Level 2: Additional calculations and routines
Operator guide

Level 3: Steady-state closed-loop control with minor perturbations

Level 4: Closed-loop control with major perturbations

The following calculations and routines have been selected for study from among those required to implement the above functions. Appropriate additions and/or deletions will be made as indicated by a continuing evaluation.

- (1) Rabbit tube facility data readout
- (2) Reactor thermal power
- (3) Reactor total thermal energy production
- (4) Approach to criticality
- (5) Relation between thermal power and neutron flux measurements
- (6) Comparison of redundant plant parameter measurements
- (7) Historical data storage and retrieval
- (8) Trending
- (9) Computer and instrument system diagnostic tests
- (10) Control rod position and acceleration
- (11) Effects of Xe and Sm
 - a. Time remaining before xenon and samarium poisoning after shutdown
 - b. Outage time after xenon and samarium poisoning
 - c. Optimum reactivity control during power cutback

- (12) Reactivity measurement (Rho-meter)
- (13) Protective system response time
- (14) Protective system operating sequence
- (15) Valve sequence and timing
- (16) Beam port safety

REFERENCES

1. J. A. Redfield, *CHIC-KIN - A Fortran Program for Intermediate and Fast Transients in a Water-Moderated Reactor*, WAPD-TM-479 (January, 1965).
2. D. L. Keller, *Predicting Burnup of Stainless-UO₂ Cermet Fuels*, *Nucleonics*, 19, No. 6, 45-48 (June, 1961).
3. C. M. Fredrich, *SEAL-SHELL-2: A Computer Program for the Stress Analysis of a Thick Shell of Revolution with Axisymmetric Pressure, Temperature, and Distributed Loads*, WAPD-TM-398 (December, 1963).
4. A. C. Eringen, A. K. Naghdi, and C. C. Thiel, *State of Stress in a Circular Cylindrical Shell with a Circular Hole*, W. R. C. Bulletin No. 102 (January, 1965).
5. C. E. Taylor and N. C. Lind, *Photoelastic Study of the Stresses Near Openings in Pressure Vessels*, University of Illinois T. & A. M. Report No. 270 (March, 1965).
6. C. R. Mayne, *Interpretive Report on the Properties of Austenitic Stainless Steel Plate Four Inches and Thicker*, Welding Research Supplement 29, 335-385 (January, 1964).

✓ 1.3 EXPERIMENTAL BOILING WATER REACTOR (EBWR)

Plutonium Recycle Experiment

1.3.1 Summary

Inspection, repair, and modification of primary and secondary system components (e.g., piping, valves, filter units), in preparation for the Plutonium Recycle Experiment, was essentially completed by late October, 1965. The findings and corrective measures employed are described in the following subsections.

Earlier evaluation of the reactor pressure vessel (i.e., cracking of internal cladding) and implementation of a continuing vessel surveillance program were described briefly in ANL-7190, p. 107, and comprehensively in ANL-7117.¹ Consistent with the latter program, the upper half of the shock shield in the vessel was modified to include removable windows for

observations of corrosion, corrosion rates, and possible propagation of incipient cladding cracks in the steam, water-line, and below-water-line zones. As yet, there are no data on corrosion effects at operating temperature (488°F).

After a series of loading experiments, cold criticality was achieved on September 22, 1965, with a loading of 22 plutonium-fueled subassemblies.² These experiments were followed by zero power transfer function measurements preparatory to approach to power.

1.3.2 Plant Inspection, Repairs, and Modification

1.3.2.1 System Piping, Welds, and Valving

In addition to the welds and valves of the newly-installed ion-exchange system, combinations of radiographic, ultrasonic, and dye-penetrant examinations were performed to establish the soundness of (1) primary steam piping inside (to turbine) and outside (to Reboiler Building) the containment shell; (2) primary safety valve piping; (3) start-up heater piping; (4) feedwater piping between the reactor face and shutoff valves; (5) primary purification system piping; (6) pressure-resisting valve bodies connected to the primary coolant piping; and (7) condensate piping below the turbine.

Stress analysis (by Spielvogel's Method³) of the high-pressure steam piping system indicated that the nominal stress was slightly below 8,000 psi during operations at 600 psi. Radiography revealed that about 50% of all the primary piping welds contained unfused weld roots and some cracks, which nullified the original conservative design for 800-psi system pressure. All substandard welds were removed, rewelded, and radiographed to ensure sound welds.

Of the 34 cast valves ($1\frac{1}{2}$ in. and larger) attached to the primary system piping, 31 were adjudged Class-II castings (as defined by ASTM Radiographic Standard E71-52) and suitable for further service. One of the remaining three valves - a 3-in. feedwater flow control valve - was no better than Class V; it was repaired, by welding, to meet Class II standards. The other two - both $1\frac{1}{2}$ in. water column shutoff angle valves - contained large blow holes; these were repair-welded to Class-I soundness. None of the cast valves showed evidence of leakage in prior service.

Approximately 50% of the (Velan) forged, austenitic stainless steel angle and globe valves in the ion-exchange system contained surface cracks. All dye-penetrant-indicated cracks were explored by grinding; however, none of the cracks was deep enough to warrant replacement of the valves. In all instances, plaster-cast measurements revealed that the remaining

wall thickness equalled or exceeded that specified by ASA Valve Standard B16.5. Local grinding explorations were then faired out to reduce stress concentration factors.

1.3.2.2 Lower Allowable Maximum Operating Steam Pressure

The springs of both 800-psig safety valves installed during EBWR conversion for 100-MW operation were replaced with new springs which limit maximum system steam pressure to 650 psig. This lower safety valve "popping" pressure was established because: (1) the plant neither has been operated nor is intended to be operated with a steam pressure above 600 psig; and (2) the piping design is a conservative interpretation of the 1955 ASA Pressure Piping Code (B31.1, para. 122) for welded, austenitic stainless pipe and includes an 0.065-in. "C" factor for plain end pipe. Finally, even at 650 psig, the steam-discharge capacity of the modified valves is well above the steam-generating capability of the plutonium-fueled core.

As a precautionary measure, the original two, 800-psig, safety valves are still connected to the primary system; they are set to relieve at 700 and 725 psi, respectively.

1.3.2.3 Feedwater Full-Flow Filters

As reported in ANL-7190, p. 113, one of the two, stainless steel-clad, carbon steel filter units (No. 2) was removed from service, while its counterpart (No. 1) and two all-stainless steel units (Nos. 3 and 4) were adjudged amenable to repairs or reinforcement in order to meet code requirements. The nature of this work was as follows.

In Unit 1, a small crack in the carbon steel portion of the lower head-to-shell weld was ground out and rewelded. Additional weld metal was applied onto the cover-to-flange weld to reduce stresses in the flange. Porosity and small cracks in the inlet and outlet nozzle welds also were ground out and the joints rewelded. An overstressed, slip-on-type, inlet connection flange was replaced with a welding-neck-type fitting salvaged from Unit No. 2.

Small cracks were detected in the longitudinal seam, the lower-head-to-shell seam, and the upper, circumferential welds of Unit No. 3. These were ground out and the joints rewelded. A moderately overstressed filter body flange was corrected by welding a peripheral, reinforcing ring (4 in. high, 1/2 in. thick) to the top and bottom edges.

An identical closure flange deficiency was observed in Unit No. 4, and corrected in a like manner. Finally, a lamination irregularity in the

shell plate was explored by grinding and found to be a shallow (<0.010 in.) surface defect. This defect is insignificant, since the shell thickness is based on a 90% weld joint efficiency factor.

1.3.3 Reactor Kinetics

Major effort was focussed on maintenance, modification, and check-out testing of the control rod oscillator drive mechanism, control circuitry, and digital data-recording equipment preparatory to zero power transfer function measurements on the plutonium-fueled core. This equipment had been stored since completion of the 100-MW experiments in December, 1962. In addition, revisions of the codes which reduce the digital data to transfer function information were completed consistent with the change-over from the IBM-704 to the CDC-3600 computer. These codes include the operations of autocorrelation, cross correlation, and noise rejection. Finally, two fission detectors (with separate counting channels) were purchased. Designed for operation at evaluated temperatures, both detectors were installed in the core to evaluate their capability for monitoring near-source-level activity during the cold-critical experiments.

1.3.3.1 Cold-Critical Experiments

The detailed nature and results of these experiments are reported elsewhere.² Briefly, they included measurements of control rod worths, boric acid worths, temperature coefficients of reactivity, shutdown margins, and verification of eight-rod and nine-rod shutdown criteria for the full loading.

This loading comprised 36 central subassemblies, each containing fuel pins fabricated from a homogeneous mixture of 1.5 wt-% PuO_2 (8 at-% Pu-240) and depleted UO_2 . Extending radially outward, the balance of the loading consisted of 60 shim subassemblies (2 rows) containing fuel pins of UO_2 enriched to 6% in U-235, 49 outer subassemblies containing natural UO_2 fuel pins, and an antimony-beryllium source. Each subassembly has an active height of 4 ft and contains 36 fuel pins (0.372 in. O.D.) clad in Zircaloy tubing (0.025 in. thick).

Throughout these experiments, both detectors performed satisfactorily. They will be further evaluated during the hot-critical experiments at approximately 340°F.

1.3.3.2 Zero Power Transfer Function

Upon completion of the cold-critical experiments, the oscillator drive was coupled to the central control rod and the zero power transfer function was measured. This was done by sinusoidally oscillating the rod $\pm 1/8$ in. from 0.1 to 1.0 rad/sec and $\pm 1/4$ in. from 1.0 to 55 rad/sec

around a mean withdrawn position of 18.5 in., while the outer eight rods were held at 18.9 in. with a boric acid concentration of 6.78 gm/gal of reactor water.

Transfer function data were taken simultaneously with analog and digital recording equipment. These data are now being compared with an analytical transfer function, which is representative of the composite plutonium-uranium core.

Similar transfer function measurements will be made at selected intervals during the approach to power. These data will be extrapolated to determine the upper power limit for stable operation of the plutonium-fueled core.

REFERENCES

1. N. Balai et al, *Inspection, Evaluation, and Operation of the EBWR Reactor Vessel*, ANL-7117 (November, 1965).
2. R. Avery, *Reactor Physics Division Annual Report: July 1, 1965 to June 30, 1966*, ANL-7210 (to be published).
3. S. W. Spielvogel, *Piping Stress Calculations Simplified*, (New York: McGraw-Hill Book Co., 1951).

✓ 1.4 ARGONNE NUCLEAR ROCKET PROGRAM

1.4.1 Summary

The Argonne Nuclear Rocket Program was implemented in January, 1963, to determine the technical feasibility and performance potential of refractory metal-fueled, fast reactors for advanced space propulsion systems. The program was terminated in July, 1966.

During the course of the program, two reference system designs were evolved to provide a focus for the development effort: a 100,000-lb-thrust system (see ANL-7190, p. 124) and a 10,000-lb-thrust system. Divisional effort in support of these systems included: (1) studies of various engine operating characteristics, control schemes, operational procedures, nuclear transients, and their effects on overall system stability; (2) parametric studies of engine-weight-thrust characteristics of promising concepts; (3) development of correlations, computer programs, and experimental apparatus for analyzing, verifying, and testing structural integrity of single components and integrated systems; and (4) construction and operation of unique out-of-pile test loops and facilities to evaluate the behavior of refractory-metal fuels and other structural materials under simulated operating conditions.

For security reasons, the findings reported herein are confined to unclassified aspects of the 10,000-lb-thrust system and supporting analytical-experimental studies performed up to date of program termination.

1.4.2 10,000-lb-thrust System

1.4.2.1 Description

In this system (Fig. 1-49), the reactor consists essentially of a cylindrical core of W-UO₂ cermet fuel elements contained within an Inconel pressure vessel. This vessel is surrounded by a radial beryllium reflector and an outer vessel made of aluminum. Reactor control is accomplished by lateral movement of segments of the reflector.

The system operates on a bleed cycle. Hydrogen propellant is pumped into the entrance manifold of the regeneratively-cooled nozzle and then up through the nozzle tubes. The flow continues through a nozzle extension which surrounds the core, and discharges into a forward plenum above the reflector. At this point, the flow continues down through the reflector and returns in the forward plenum upstream of the reactor where it enters the core. From the core, the hydrogen is exhausted through the nozzle. Some of the hot hydrogen is bled from the nozzle, mixed with hydrogen from the nozzle coolant tubes, and passed through the turbine to provide hydrogen pumping power. This hydrogen is then exhausted overboard.

1.4.2.2 Engine Weight vs. Thrust Characteristics

Comparisons were made of the engine weight-thrust characteristics for U-235 and U-233 fueled systems in the thrust range of 5,000-30,000 lb.

The analysis consisted of a reactor criticality study in which the critical volume was determined as a function of core L/D ratio, porosity, and reflector thickness. These data served as input in a parametric computer code which ultimately defined a reactor that satisfied all criticality and heat transfer requirements. Engine weights (turbopump, nozzle, etc.) used in the analysis were based on extrapolations of component weights in the NERVA system and other detailed design studies.

The results (Fig. 1-50) show that topping-cycle engines are from 300 to 700 lb heavier than the hot-bleed engines in the specified thrust range. However, the topping cycle provides an additional 25 sec of specific impulse. Thus ultimate choice of cycle will depend on the spacecraft mission and relative importance of the question: Is one second of specific impulse worth 12 to 18 lb of engine weight?

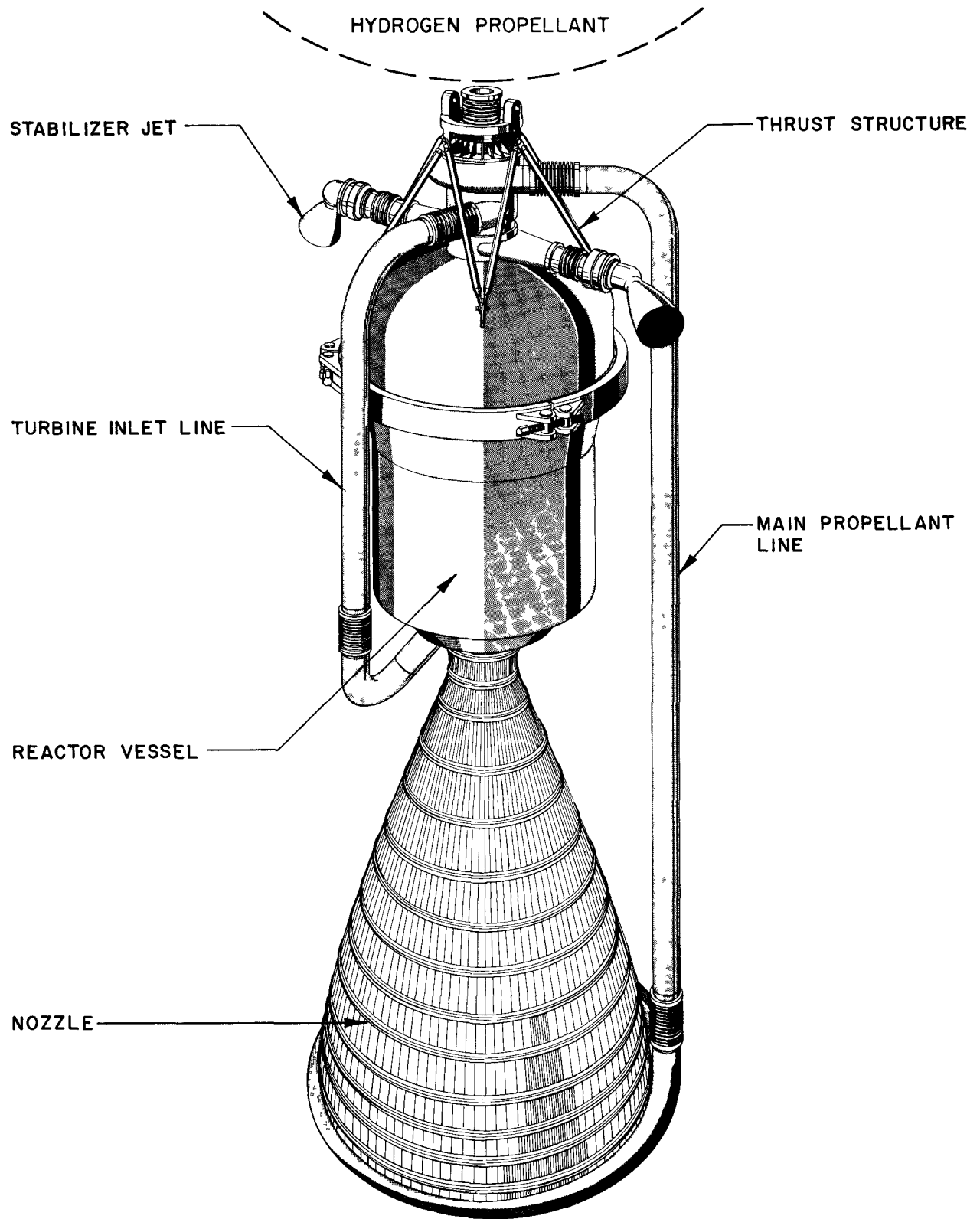


Fig. 1-49. Concept of 10,000-lb-thrust [200 MW(t)] fast reactor rocket engine

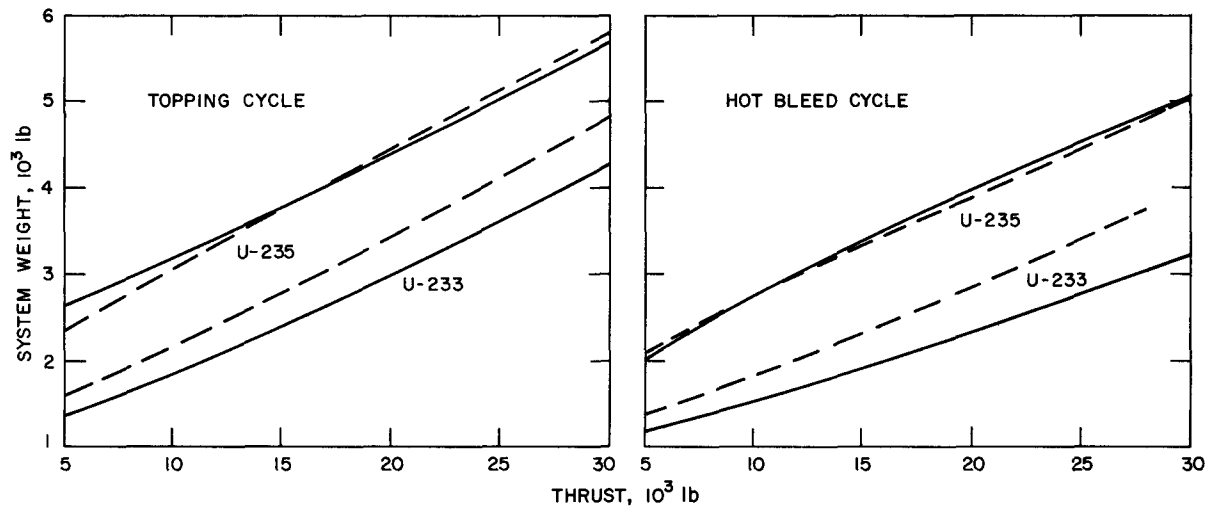


Fig. 1-50. Weight-thrust characteristics of topping-cycle and hot-bleed cycle nuclear rocket engines fueled with U-235 and U-233. Solid and dashed curves pertain to use of 4-in.-thick and 8-in.-thick beryllium reflectors, respectively.

In general, the study revealed that a number of lightweight configurations are feasible for small, fast reactors using tungsten as a structural material.

1.4.3 Argonne Hydrogen Flow Facility

This facility comprises a large and a small hydrogen test loop for the purpose of evaluating candidate fuel specimens in high-velocity, high-temperature hydrogen. The large loop was described in ANL-7190, p. 133; it is designed to operate with power inputs up to 1000 kW. The small loop is scaled down to operate with power inputs up to 50 kW. In both loops, hydrogen is cycled from high-pressure storage trailers, through a system of pressure-regulating valves, to an electrical-resistance heater mounted in the lower end of a water-jacketed pressure vessel. Here, the gas is heated to temperatures up to 2450°C, and then passed over fuel specimens in the upper end of the vessel. From the vessel, the gas flows through a water-cooled heat exchanger, a flow control valve, and discharges to the atmosphere.

Hydrogen flow is measured in a critical flow nozzle that had been calibrated against a precision venturi using both nitrogen and hydrogen. Fuel specimen and heater temperatures are sensed with Ircon radiation pyrometers. Heater current input is measured to within 0.4% by means of a Dyn/Amp system. Automatic shutdown is initiated by system malfunctions such as low hydrogen flow, low system pressure, overheating of the heater, and loss of power to the cooling water pump.

At the time of program termination, both loops were being operated for simultaneous evaluation of fuel specimens and development of prototype heaters. These heaters are shown in Fig. 1-51.

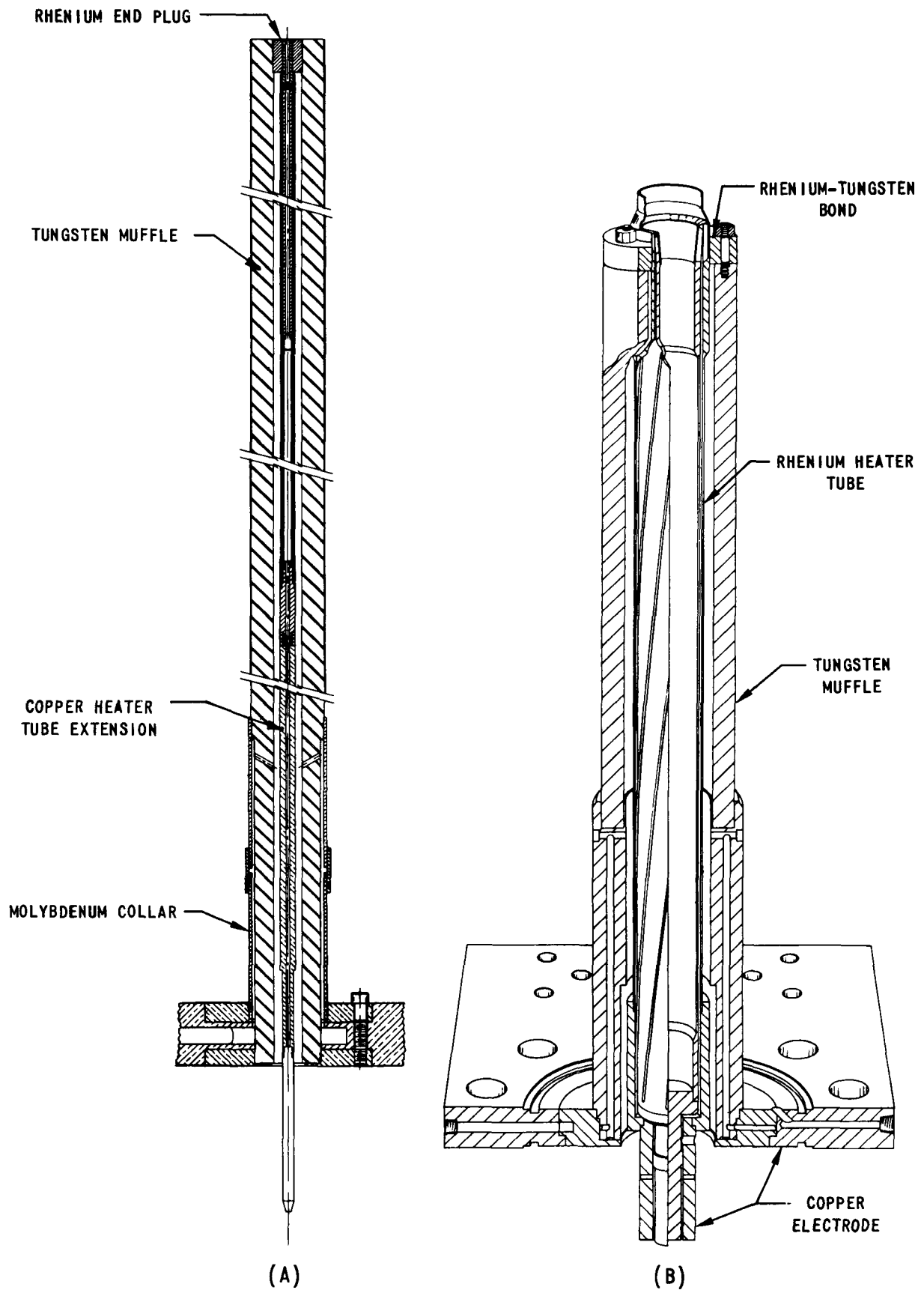


Fig. 1-51. Sectional views of single-flow-passage, resistance heaters under development for use in (A) small and (B) large hydrogen flow test loops

1.4.3.1 Loop-Heater Performance

50-kW Loop. This loop has been operated intermittently since December, 1965. During this period, two heaters of the type shown in Fig. 1-12(A) were fabricated and tested. On each occasion, failure occurred after 12 hr of loop operation. The conditions prevailing at time of failure were as follows:

Hydrogen flowrate	19.6 SCFM
Maximum specimen temperature	2450°C
Maximum heater voltage	24.2 V
Maximum heater current	1,665 A
Maximum heater power	40.3 kW
Estimated maximum heater temperature	2750°C
Approximate number of thermal cycles from room temperature to 2750°C	16

In both cases, failure was attributed to the larger expansion coefficient of the rhenium material. This resulted in gradual disruption of the bond between the rhenium end plug and the adjacent tungsten muffle. There was no evidence of failure due to creep in the region of maximum temperature.

Except for the heater failures, operation of this unique system was essentially self-controlled. Once established, hydrogen flow and pressure were maintained with minimal adjustments. Power input to the heater was controlled automatically; use of the Data-trak system permitted any thermal cycle desired, with good reproducibility of cyclic conditions. Heater operating characteristics were in accord with those predicted by a one-dimensional computer code using the Taylor-Kirchgessner hydrogen correlation.

1000-kW Loop. The final test run with the heater shown in Fig. 1-12(B) was of shorter duration. After 6 min. at 613 kW (28,800 A at 21.3 V), the power was gradually decreased because of overheating of the liquid metal contacts at each end of the heater. Maximum temperatures achieved during the 6-min. period were 2440°C for the heater, and 2270°C for the fuel specimen. Again, heater malfunction was attributed to failure of the bond between the rhenium collar and tungsten ring at the upper end.

This loop has been disassembled and placed in storage.

1.4.4 Structural Mechanics

The objectives of the structural mechanics program were centered on concurrent development of analytical models and experimental facilities for assessing structural integrity of the reference system designs. With

one exception - the High-Temperature Model Testing Facility - this section summarizes the terminal efforts in support of investigations initiated in FY-1965.

1.4.4.1 Deformation Analysis of a Grid Plate Support Structure

Experimental analysis has confirmed the adequacy of using closed form solutions of the deflection equation and its derivatives to provide realistic estimates of stress and deformation of hydraulically-loaded grid support structures.

The structure analyzed consisted of two, parallel, circular plates interconnected by many equally-spaced members. Theoretical investigation of the overall deformation proposed superposition of two components representing plate bending: one about a common, intermediate neutral axis, and the other about their individual internal neutral axes. In addition, the theory depends on the validity of the distributed bending moment concept to develop the second component. This approach was also applied to the analysis of coupled beams.

The tests were made on acrylic plastic models of coupled beams and circular plate structures. (See Fig. 1-52.) Twenty-seven beam and eight plate configurations were employed to identify the influence on deformation behavior of parameters such as type of load (uniform pressure or concentrated application), length and spacing of grid members, and span length of the beams. All models were instrumented to determine central deflection, strain in the parallel plates, and bending strain in one of the grid members.

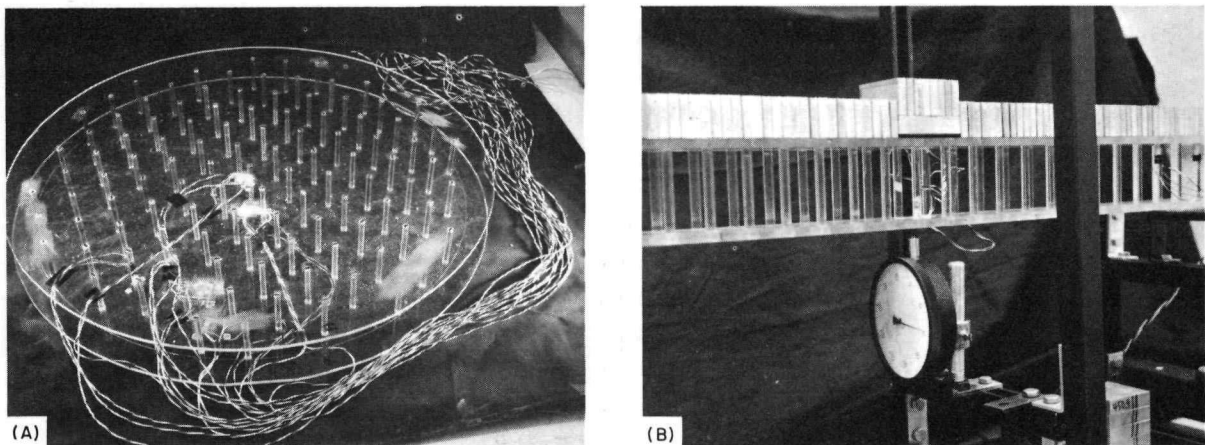


Fig. 1-52. Typical acrylic plastic models of (A) circular grid plates and (B) grid beams used in support of deformation analysis

Comparison of the experimental and theoretical beam data indicated agreement within 10% for the midspan deflection, and within 20% for the strain measurements. In the case of the circular plate models, the deflections were from 7 to 28% greater than predicted by theory.

A detailed description of this study is contained in ANL-7145.¹

1.4.4.2 Experimental Study of Shell Deformation and Stability

Figure 1-53(A) shows the instrumentation scheme developed to experimentally evaluate stress and deformation of an internal cylindrical shell when subjected to an external collapsing load. Basically the scheme consists of using a constant scanning device over the full shell circumference, but confined to a uniform band of photoelastic material. In addition to affording improved overall shell surveillance, the photoelastic measurements, when coupled with strain gage output, provide a means for separating membrane and bending strains. This strain separation is a necessary feature of subsequent stress analysis.

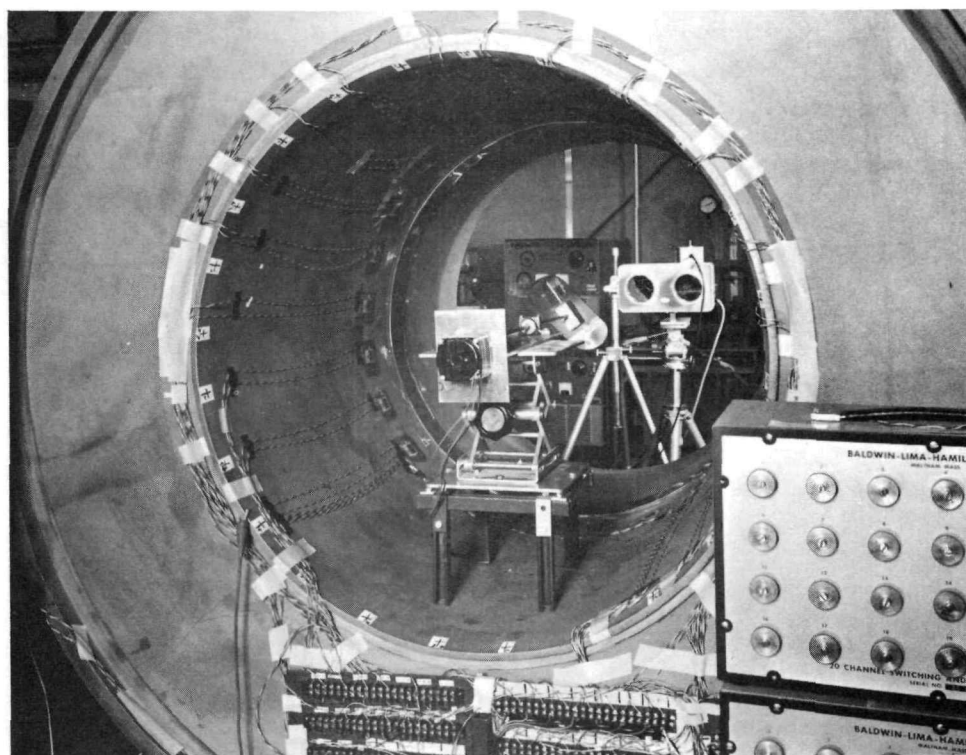
Figure 1-53(B) shows the test setup used to monitor the inner shell of the prototype, double-walled, steel vessel. The structure was stiffened by twelve, equally-spaced, axial ribs which connected the inner and outer shells. The inner shell was subjected to external pressure by hydraulically loading the annular region.

1.4.4.3 Vibration Exciter Facility

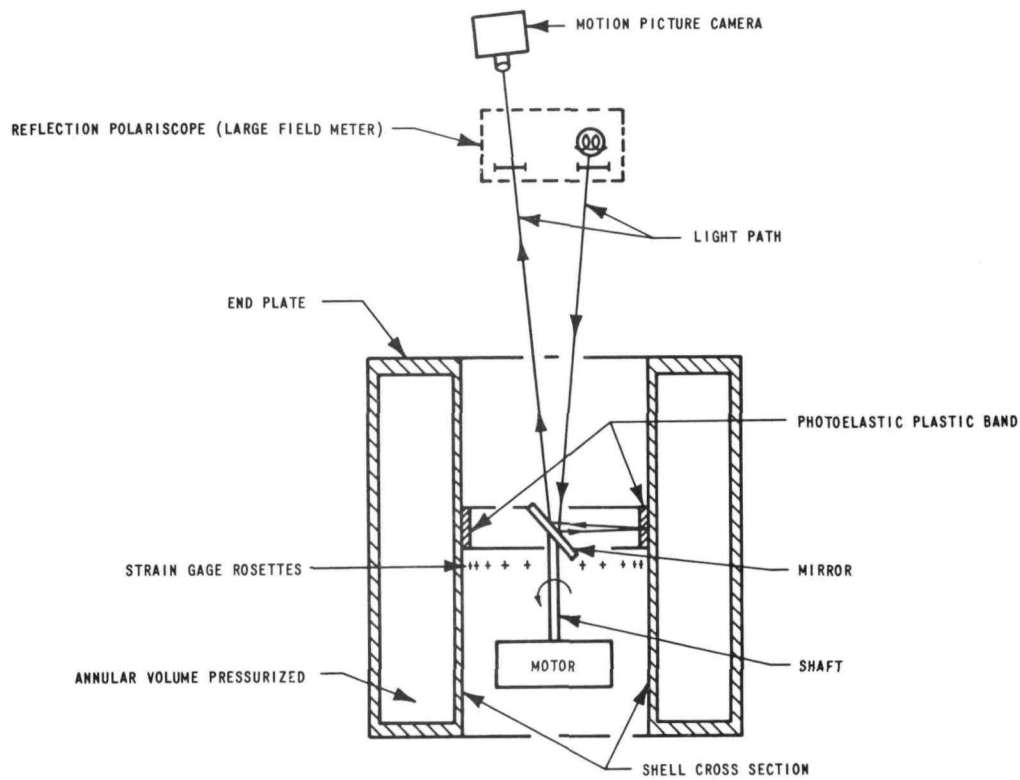
This facility was constructed and made operational for the purpose of developing models in support of dynamic stress and deformation analysis of fuel rod assemblies, reflector components, and other supporting structures. It provides for simultaneous visual, photographic, and tape recording of data from test specimens vibrated at frequencies from 5 to 3,000 cps, with an amplitude accuracy of ± 1 db.

Fuel Element Clusters. A vibration test fixture was designed to accommodate clusters of simulated fuel elements ranging from one to a maximum of 163 elements. The elements were simulated by hexagonal steel rods (0.5 in. across flats, 24 in. long). The objective was to determine the number of elements required to give results that could be extrapolated to a prototype cluster of fuel elements.

The shaker was servocontrolled to impart a constant displacement amplitude, sinusoidal motion to the fixture. Magnetic tape recordings were made of the following measured variables: (1) input displacement and acceleration; (2) strain at the root of the center rod; and (3) strain at the root and acceleration at the free end of a rod in the outer row. These data were processed on a spectrum analyzer to obtain frequency response plots.



(B)



(A)

Fig. 1-53. Instrumentation used to monitor membrane and bending strains in hydraulically-loaded inner shell of double-walled steel vessel

The results of these tests, as represented by the first and second mode natural frequencies and corresponding magnification factors,* are given in Figs. 1-54 and 1-55. As shown in Fig. 1-54, the natural vibration frequencies of a rod in a cluster do not vary significantly from that of a single rod. Slow-motion movies as well as strain gage information also revealed that mode shapes are unaffected by, or independent of, cluster size. Figure 1-55 shows that the first and second mode magnification factors decrease as the cluster size is increased. This is attributed to the corresponding increase in energy dissipation.

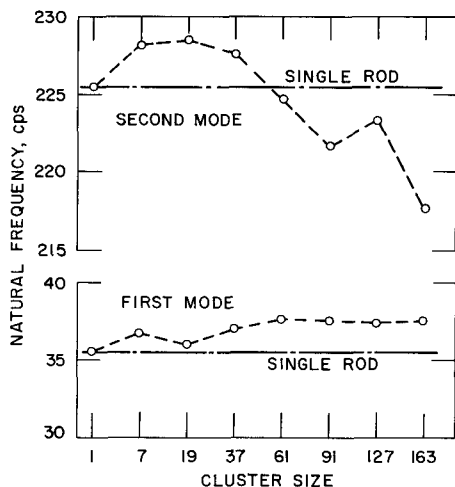


Fig. 1-54

Averaged values of first- and second-mode natural frequencies of simulated (steel) fuel rods

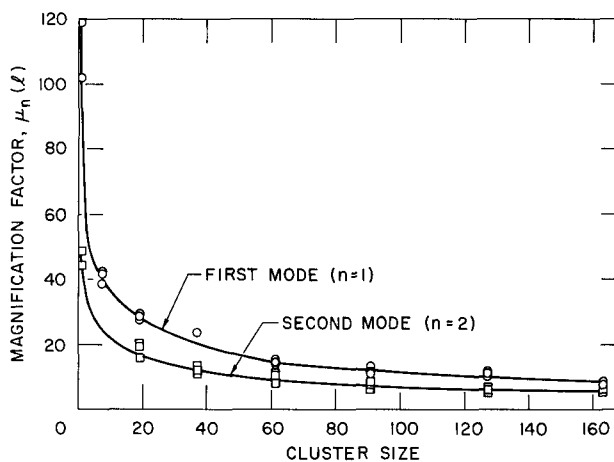


Fig. 1-55

First- and second-mode magnification factors for simulated (steel) fuel rods

An attempt was made to identify a parameter that could be used to relate the results from the various clusters tested. The only invariant observed was the ratio of first to second mode magnification factors. For tests with a 2-mil, peak-to-peak input, this ratio is approximately 1.72.

Identification-Evaluation of Damping Models. Due to the close spacing of fuel elements in the core, interaction among the elements can be expected when the reactor is subjected to a disturbance. In order to predict displacement amplitudes and to obtain estimates of impact velocities (information which might then be used in applying various damage criteria to the elements), a mathematical model describing the dynamic behavior of an in-core element is required. Dissipation of energy is an important consideration in such modeling. Accordingly, three damping mechanisms were considered as defined by the damping force intensity:

*Ratio of output to input displacement amplitudes.

$$f_D(x,t) = \begin{cases} c_V \frac{\partial y}{\partial t} & , \text{viscous damping} \\ c_S \frac{\partial^3 y}{\partial x^2 \partial t} & , \text{stress damping} \\ c_L \frac{\partial^5 y}{\partial x^4 \partial t} & , \text{load damping.} \end{cases} \quad (1)$$

A theoretical analysis was carried out with the assumptions that (1) Euler beam theory applies and (2) damping is sufficiently small that the mode shapes and natural frequencies are unaffected. Briefly, the analysis consisted of equating a theoretically-derived expression for beam deflection at resonance to the experimentally-observed response, and solving for an effective damping factor. This factor is a linear combination of the damping coefficients associated with the assumed damping mechanisms. For "pure forms" of the proposed damping, a ratio of first-to-second mode magnification factors can be formed. This ratio is constant at any section along the beam. If the mode shapes and natural frequencies are known, the values of the ratio depends only on the type of damping assumed.

For a cantilever beam, the following values are obtained:

$$R(\ell) = \begin{cases} 0.288, & \text{viscous damping} \\ 4.46 & , \text{stress damping} \\ 11.3 & , \text{load damping.} \end{cases} \quad (2)$$

The value of the ratio is rather sensitive to the particular type of damping. This suggests a method of identifying the dominant damping mechanisms, i.e., comparing experimentally-determined ratios of first-to-second-mode magnification factors with values corresponding to pure forms of the damping. For example, experimental results from cluster tests gave a value of approximately 1.72. Comparison of this number with those of Eq. (2) indicates viscous and stress damping may be the dominant mechanisms to be included in the model.

The associated damping coefficients can be evaluated by using experimental results at first and second mode resonance to write two simultaneous equations from the linear combination of damping coefficients. Both equations are easily solved for the two unknown damping coefficients.

1.4.4.4 Transient Thermal Stresses in Fuel Element Coolant Channels

Of the various operating transients to which core elements could be exposed, the most likely to produce serious thermal stresses would be the sudden introduction of cold hydrogen. To determine the effect of such an event on the thermal stress state of the fuel element coolant channel clad, the following problem was considered:

The channels were assumed to be infinitely long, unconstrained hollow cylinders at a uniform initial temperature. At some given instant, coolant of a differing temperature transfers heat from the inner surface of the channel while the cylinder begins generating heat at a uniform rate. The external surface of the cylinder is perfectly insulated and all material properties are assumed temperature independent.

The boundary value problem was resolved by applying recently-developed extensions of finite Hankel transforms² and then substituting the solution for the temperature field into the conventional expressions for stresses in long tubes subjected to radial variations in temperature. This results in series expressions for the various stresses which involve summations over the roots of the transcendental equation used in defining the Hankel transforms. For small values of the Biot number and thin cladding tubes, the necessary roots may be easily determined and it is found that consideration of only the first two terms in the stress expressions is sufficient to produce accurate results.

From the cladding dimensions, the ratio of inner-to-outer radius was taken as $y_0 = 1.20$ and an upper bound on the Biot number was conservatively assumed to be $\beta = 1.0$ (thermal stresses increase with increases in β in the present problem). Using the above values, a typical stress expression (dimensionless circumferential stress at the inner surface) is

$$\hat{\sigma}_{\theta} \cong 0.064 [\exp(-4.26\tau) - \exp(-257.2\tau)] \quad (3)$$

where τ is dimensionless time measured from the time of introduction of coolant, and the heat generation rate is assumed zero.

Equation (3) gives a maximum stress of $\hat{\sigma} \cong 0.06$. By comparison, a value of 1.0 would be computed by neglecting the effect of boundary conductance ($\beta = \infty$) and assuming an equivalent instantaneous change of surface temperature. This result is typical of all the stress components and reflects the importance of including the effect of small values of the Biot number.

1.4.4.5 Possible Influences of Anisotropy on Thermal Stress Solutions

A proposed method for incorporating various details of the internal structure of a fuel element into thermal stress computation was to consider the element as a homogeneous but nonisotropic solid. Element geometry and probable method of fabrication indicated that the appropriate anisotropic behavior to use would be transverse isotropy (i.e., a material with one preferred direction and such that all plans normal to this direction are isotropic). Such a material possesses five elastic constants, as compared to two constants of ordinary isotropy. Moreover, few thermal stress problems have ever been solved for anisotropic bodies.

Therefore, prior to attempting a complete analysis for the prototype element, simple example problems were studied to gain insight into the analytical and numerical difficulties peculiar to an anisotropic treatment. These problems included: (1) a transversely isotropic space having zero temperature with the exception of a half-infinite circular cylinder of unit temperature lying in the direction of the axis of symmetry; and (2) a transversely isotropic infinite right circular cylinder whose surface has a finite circumferential temperature band while the remaining surface is at zero temperature.

Analytical solutions of both problems were completed and sufficient numerical computations were performed to indicate that the use of such models does not introduce any serious mathematical difficulties.

1.4.4.6 Multipurpose High-Temperature Model Testing Furnace Facility

At the time of program termination, a facility was being constructed to evaluate the structural behavior of candidate materials and/or prototype component models in a high-temperature vacuum or gas atmosphere. As shown in Fig. 1-56, the integrated universal testing machine, furnace, and force applicators provide the capability for applying lateral, torsional, and/or axial force loadings to test specimens or models at ambient temperatures up to 5900°R. Control consoles for the universal testing machine, furnace power supplies, high-vacuum system, and readout instrumentation are located within the experimental area. The system is supplied with 600 kVA of 3-phase, 440 volt power.

High-Temperature Furnace. This component (Fig. 1-57) consists of a large (58 in. O.D.), double-walled, water-cooled chamber fitted with vacuum, hydrogen, water, instrumentation, viewing, and force applicator openings. The furnace is suspended from a moveable dolly and is locked into the centerline of the testing machine frame. Structural models or test samples are centrally positioned in the hot zone by test machine grippers which extend through the top and bottom of the furnace.

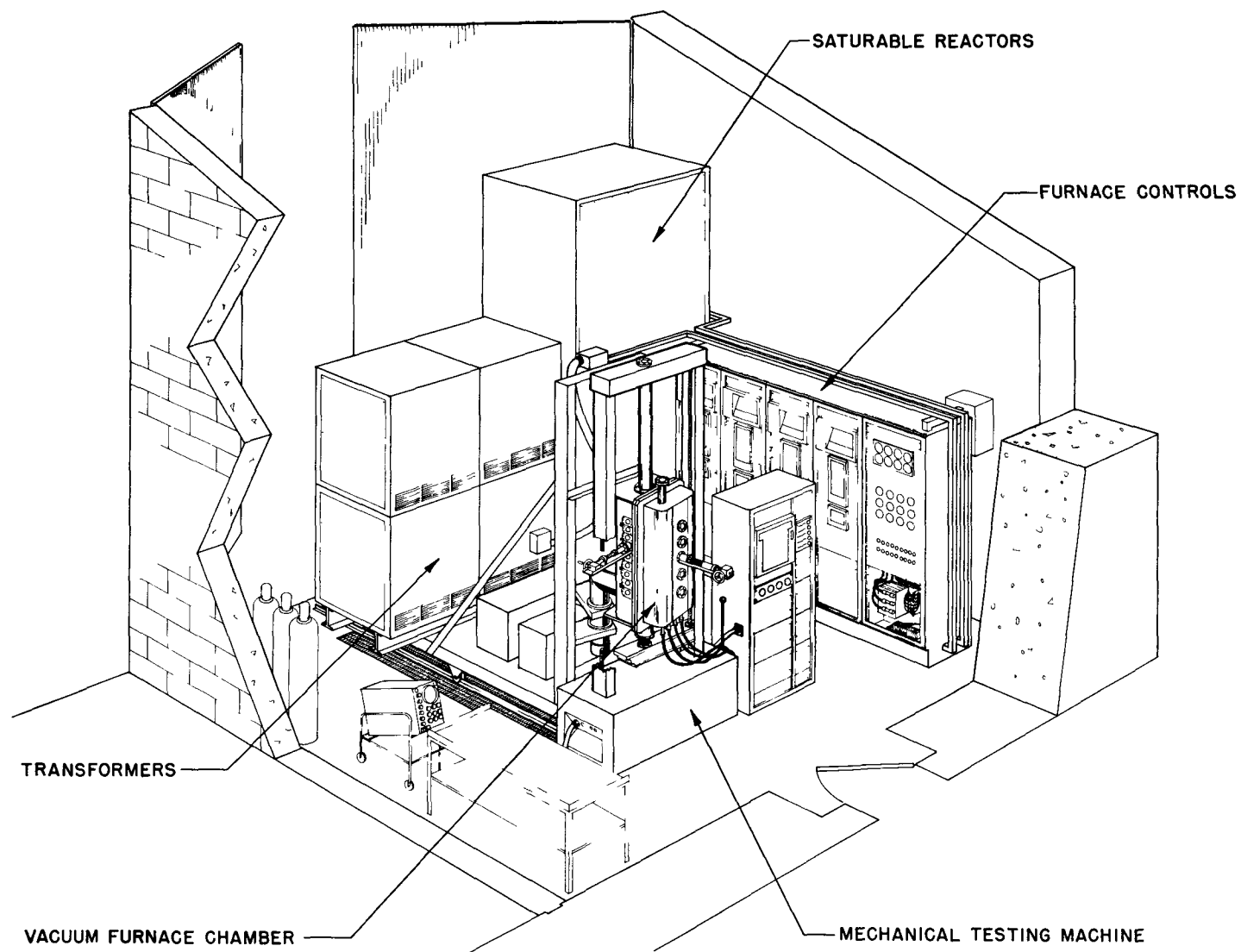


Fig. 1-56. Multipurpose high-temperature model testing facility

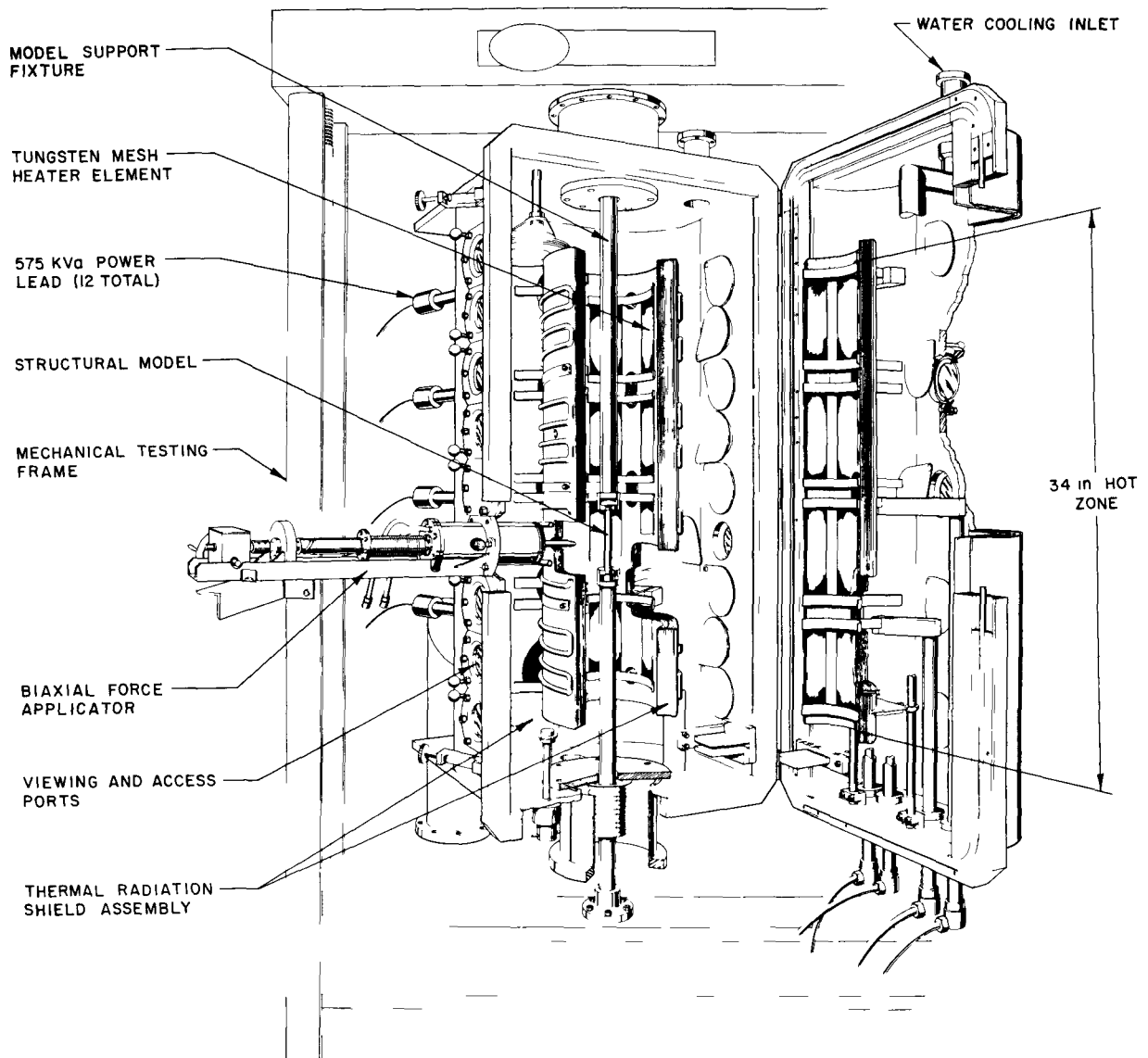


Fig 1-57 Components of high-temperature furnace chamber

The 34-in.-high furnace hot zone consists of four, tungsten-mesh heating elements (7 in. I.D., 8 in. long) which are supported from independent power bus bars. This power input arrangement permits significant variations in axial temperature gradient. A water-cooled thermal shield pack is installed around the heaters to reduce thermal radiation loss from the hot zone.

Force-Applicator System. This system (Fig. 1-58) is used to apply a precise force to the transverse plane of the test model. Model deflection vs. load is measured by a linear potentiometer and force transducer mounted in the rear of the force probe.

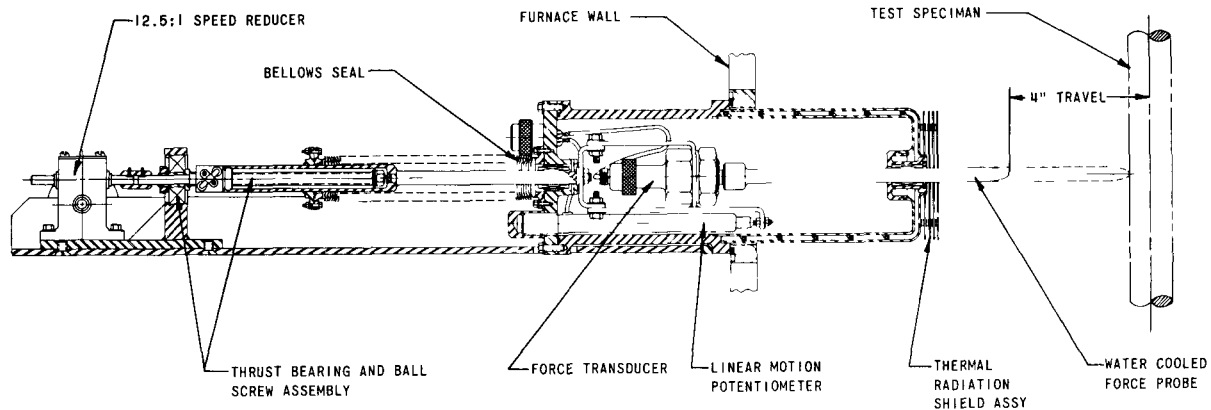


Fig 1-58. Sectional view of prototype biaxial force-applicator system

The force probe consists of a water-cooled tungsten rod, one end of which is coupled to a thrust bearing and ball screw assembly and mounted to the transducer within the force applicator package. The opposite end of the probe projects through the thermal shield in the furnace hot zone and impinges against the test model. Furnace atmosphere is protected by a bellows seal on the force train assembly.

The force applicator drive can be either a manually-operated gear reducer for simple experiments, or a servo drive operated with a differential-summing circuit control for force vs. deflection studies. In addition, a number of force applicator packages can be mounted to the furnace viewing ports at various elevations and lateral positions to impose a variable axial or radial force distribution on the test model. Finally, the test system will also accommodate other deflection monitors, e.g., Optron equipment for optically measuring stress-strain relationships at extremely high temperatures.

Status of Facility. Funds have been allocated for procurement and fabrication of the furnace. The universal testing machine and associated instrumentation have been approved and funded, but have not been released for procurement. Design of a prototype force-applicator system has been completed.

REFERENCES

1. H. Halle, *Deformation Analysis of a Circular Coupled-Plate Structure*, ANL-7145 (March, 1966).
2. G. Cinelli, *Extension of the Finite Hankel Transform and Application*, Int. J. Engng. Sci., 3, 539-559 (1965).

Section 2

FAST REACTOR RESEARCH AND DEVELOPMENT2.1 Advanced Systems and Concepts2.1.1 1000-MW(e) Metal-Fueled Fast Breeder Reactor Concept

The Division's participation in the intralaboratory design study of a 1000-MW(e) fast breeder reactor concept for central station power application was completed with the preparation of a formal integrated report in fiscal 1966.¹ Table 2-1 lists the main characteristics of the reference vanadium-titanium clad, metallic uranium-plutonium-fueled core that was evolved. A concise description of the modular core, power plant, supporting facilities, and related costs also was published in the fiscal 1965 Annual Report. (See ANL-7190, p. 143).

Table 2-1. Main Characteristics of 1000-MW(e) Sodium-Cooled
Metallic-Fueled Fast Reactor Plant

Thermal Power, MW(t)	2513
Net Plant Efficiency	0.398
Core	
Type	Modular
Height, cm	91
Diameter, cm	105
Regions	2
Total U + Pu Weight, MT	17.9
Fissile Concentration, wt-%	
Inner Region	13.5
Outer Region	17.5
Blanket Weight, MT	
Axial	16.5
Inner Radial	14.9
Outer Radial	47.4
Sodium Temperature, °F	
Inlet	720
Outlet (avg.)	1000
Power Density (avg.), kW/liter	450
Breeding Ratio	1.48
Refueling Fraction	1/3
Doubling Time for Reactor Inventory, yr	7.6
Reference Clad Material	V-20 Ti

Work performed during fiscal 1966 included further development of mechanical design aspects to ensure a tight, reproducible core configuration, and a comparative fuel cycle cost estimate based upon using stainless steel cladding. The results of these studies are summarized in the following paragraphs.

As described in ANL-7190, the reactor consists of a ring of six core modules which, from a nuclear standpoint, were very loosely coupled. A mechanically tight core assembly was obtained by using a series of lower grid plates of dissimilar materials and consequent thermal expansion differentials to exert a force against touching pads on the respective subassemblies.

Additional fuel cycle cost estimates were prompted by the prospects of using a less expensive cladding material. The reference burnup of 6 at-% was based on calculations which assumed a zero strength for the U-Pu fuel and a strong cladding to restrain the fission products, with only a small, total deformation. Because of its strength characteristics and compatibility with the fuel, vanadium-20% titanium clad was selected. However, materials studies have indicated that when alloyed with ~25 at-% zirconium, the uranium-plutonium fuel would be compatible with stainless steel. The attendant advantages are: (1) increased melting point of the fuel; and (2) decreased cladding costs.

In order to examine, in an approximate fashion, the influence of these advantages on fuel cycle costs, fuel compositions were adjusted and, due to the increased fuel strength, an allowable burnup of 7 at-% was assumed. The results of these calculations together with the main cost factors are given in Table 2-2. Compared to a hypothetical burnup of 7 at-% in V-20% Ti, the use of stainless steel cladding reduces the estimated fuel cycle cost by 0.1 mill/kW-hr. This is about the same magnitude of cost difference as would prevail in going from 6 to 7 at-% burnup in the V-Ti

Table 2-2. Equilibrium Fuel Cycle Costs for Metallic-Fueled Systems with Close-Coupled Reprocessing Facilities Serving Three 1000-MW(e) Plants

Annual Capacity Factor	80%		
Annual Charge on Working Capital	9%		
Fissile Plutonium	\$10/gm		
Chemical Reprocessing	\$60/kg		
	Case I	Case II	Case III
Avg. Core Burnup, at-%	6	7	7
Fuel Material	U-Pu-Ti	U-Pu-Ti	U-Pu-Zr
Clad Material	V-20 Ti	V-20 Ti	SS
Avg. Refabrication Cost, \$/kg	130	130	90
Unit Energy Cost, mills/kW-hr			
Refabrication	0.63	0.54	0.39
Chemical Reprocessing	0.29	0.25	0.27
P _{uf} Credit	-0.47	-0.45	-0.38
Working Capital	<u>0.57</u>	<u>0.58</u>	<u>0.52</u>
Total Fuel Cycle Cost	1.02	0.92	0.80

cladding. With the success of some recent experiments in approaching 10 at-% burnup in metal fuel samples,² there appears to be flexibility in design approach to obtain high burnups in metallic fuels.

2.1.2 Engineering Design and Cost Study of Sodium-Heated Steam-Generator and Turbine-Generator Islands for 500-MW(e) and 1000-MW(e) Central Stations

2.1.2.1 Objectives and Scope

This study represents a second joint effort by Division personnel and United Engineers and Constructors, Inc. (UEC) to establish design trends for large, sodium-cooled, fast-breeder-reactor-powered central stations. In addition to updating the results of the first study (see ANL-7190, p. 148), three more steam conditions were evaluated with respect to net thermal efficiency and capital costs of the turbine-generator island; and for two steam conditions, costs of the steam-generator island were estimated.

2.1.2.2 Study Procedure

The working arrangement with UEC was similar to that of the initial study phase except that Division personnel were more involved in the engineering aspects of the sodium and steam components for the steam-generator island. For each set of steam conditions, engineering flow sheets and equipment layouts were developed consistent with specifications which electrical utilities and safety commissions might establish for normal operation. Design of the steam generator was based on the Babcock and Wilcox concept which is being developed under AEC funds. Selection of equipment for the steam-electric-generating island was based on UEC experience.

Cost estimates were prepared in accordance with the Federal Power Commission Uniform Code of Accounts. They included all direct and indirect costs related to materials, labor, and equipment; excluded were land, interest during construction, and certain of the purchasers' indirect costs.

2.1.2.3 Turbine-Generator Island Costs

The turbine-generator island costs include all equipment from the inlet steam line at the T-G building wall to the high-voltage terminals of the main transformer.

Table 2-3 lists the comparative costs for all the nominal 1000-MW(e) cases with an optional single tandem compound turbine arrangement. The net station efficiencies have been adjusted slightly to provide uniformity among the cases considered in the first and second study.

Table 2-3. Influence of Steam Conditions on Thermal Efficiency and Capital Costs of the Turbine-Generator Island for 1000-MW(e) Nuclear-Powered Central Stations

Steam Condition: Pressure - Initial/Reheat Temp., psig - °F/°F	Net Thermal Efficiency, %	Capital Cost, \$/Net kW
(A) 3500 - 1000/1000	43.5	44.40
(B) 2400 - 1000/1000	42.6	43.15
(C) 1800 - 900/900	40.4	47.36
(D) 1000 - Dry and Saturated	33.9	56.99
(E) 1450 - 1000	38.5	48.37
(F) 2400 - 950/950	41.8	45.48
(G) 2400 - 950	39.5	50.31

The results for the 1000-MW(e) cases lead to the following comments and conclusions:

(1) Excluding Case D (1000 psig D&S), the estimated net thermal efficiencies are close (i.e., 38.5% low - 43.5% high). For reasonable conditions, steam cycles for fast sodium-cooled reactors may be generally characterized as providing a net station heat rate of 8300 Btu/kW-hr.

(2) Again excluding Case D, the capital costs per net kilowatt range from \$43.15 (Case B) to \$50.31 (Case G).

(3) Based on an average energy cost of $27\text{¢}/10^6$ Btu for the steam, an annual capacity factor of 80%, and annual capital charges of 13%, the four steam cycles with sodium reheat (Cases A, B, C, F) yield costs within ~0.2 mills/kW-hr, while Cases D and G with no sodium reheat are about 0.3 mills/kW-hr more expensive. Although the assumed average steam energy cost is a gross simplification, this approach does provide some perspective on design trends for T-G islands.

(4) It would appear that the T-G island for sodium-cooled fast reactors could exhibit a capital cost advantage of about \$10/kW(e) over islands for water-cooled thermal reactors.

The results for the nominal 500-MW(e) output are similar: net thermal efficiencies are slightly lower and the unit capital costs are 15 to 20% higher than those for a like cycle at 1000-MW(e) nominal output.

2.1.2.4 Combined Steam-Generator and Turbine-Generator Island Costs

Ideally, the total power plant, including the fuel cycle, should be investigated in order to specify the design trends. A step in this direction is to couple the steam-generator and turbine-generator islands.

For this purpose, two of the seven steam conditions investigated for the turbine-generator island were selected for estimating costs of the steam-generator island. The selections were based on previous studies which indicated that (1) temperature selection is more important than steam pressure because temperature levels influence cost on a larger number of plant components; (2) a 2400 psig - 950°F/950°F sodium reheat steam cycle might be close to optimum; and (3) use of a sodium reheater, in addition to increasing capital cost, would increase plant complexity and, probably, decrease reliability.

Accordingly, engineering estimates were made of the steam-generator island costs for 2400 psig - 950°F/950°F steam with sodium reheat, and 2400 psig - 950°F with nonsodium reheat. In both cases, the overall battery limits were the high-temperature sodium inlet line to the steam generator and the secondary sodium pump discharge line at one interface, and the high-voltage transformer output terminals at the other.

The results are listed in Table 2-4. Before making any comparisons, a few comments on the 2400 psig - 950°F cycle are appropriate. This cycle, as described in the UEC study, has a very high moisture content in the low-pressure cylinder of the turbine. Discussions with turbine manufacturers revealed there was no readily available information on this cycle nor on commercial means of alleviating the moisture content. Basically, neglecting new materials or turbines designed for high moisture, external moisture separation or live steam reheat are possibilities for lowering moisture content. However, each of these solutions has an effect on the heat rate and capital cost.

Table 2-4. Estimated Costs of Combined Steam-Generator and Turbine-Generator Islands with and without Sodium Reheat

Case	Steam Condition, psig - °F/°F	Net MW(e)	Cost, \$/kW(e)		
			S-G	T-G	Combined
(F)	2400 - 950/950	1029	36.66	45.48	82.14
(G)	2400 - 950	1001	29.69	50.31	80.00

The results of the combined study lead to the following comments and conclusions:

(1) Ignoring the influence of obtaining an allowable moisture level in Case G, and assuming an 80% annual plant capacity factor, 13% charges on capital, with an incremental energy cost of $15\text{¢}/10^6$ Btu, one finds a 0.03 mills/kW-hr differential which favors the sodium reheat cycle.

(2) Adjustments for obtaining an allowable moisture content would increase the differential, probably by a slight amount. Plant simplifications could increase the reliability of the nonsodium reheat cycle.

These statements should be tempered by the fact that only two steam conditions were considered along with a particular type of sodium-heated steam generator. A more comprehensive study of alternate engineering and equipment designs could modify the foregoing observations. Finally, it is interesting to note that linking the turbine-generator and steam-generator islands tends to foreshorten the extremes indicated by studies confined to the T-G island. An even greater impact on apparent design trends can be expected upon inclusion of reactor island and fuel cycle details.

2.1.3 1000-MW(e) Fast Breeder Reactor Follow-On Program

2.1.3.1 Retrospect

This program is a continuation of four, AEC-sponsored core design studies performed independently by Allis-Chalmers, Combustion Engineering, General Electric, and Westinghouse in 1963. The common objective of these studies (designated Phase I) was to evaluate the technical feasibility of sodium-cooled, ceramic-fueled, fast breeder reactor concepts for use in a central station plant of 1000-MW(e) net capacity, with a turbine inlet steam temperature of 1000°F . This plant would have as a goal the production of electric power at minimum cost consistent with a breeding ratio of ~ 1.20 and a reasonable fuel-doubling time. Each study was limited to the core geometry, physics, thermal characteristics, and materials; the reactor vessel; core instrumentation and mechanical devices for control and safety; and fuel-handling mechanisms.

In their terminal reports, each of the participating organizations concluded that (1) it was technically feasible to design a fast breeder reactor core with a thermal output large enough (~ 2500 MW) to produce 1000 MW(e); and (2) it was deemed advantageous that the studies be extended to include the "Total Plant Concept." These conclusions were supported by subsequent ANL-AEC evaluation of the four different core concepts that were presented.

2.1.3.2 Follow-On Program

On August 16, 1965, the Laboratory was authorized by the AEC to execute technical management and guidance of Phases IIA, IIB, and III, which comprise the follow-on program. Briefly, Phases IIA and IIB cover, respectively, design optimization and cost optimization of the reactor and primary system, while Phase III includes both design and cost optimization of the secondary-sodium and steam turbine-generator systems.

At the outset, each of the aforementioned contractors was requested to submit proposals for Phase IIA and IIB studies in preassigned counterpart portions of the overall plant complexes. Subject to Division approval, these "vertical" studies would be pursued to a depth sufficient to permit assessment and recommendation to the AEC of the most promising integrated "Total Plant Concept" for definitive research, design, and development.

On October 13, 1965, Atomics International was authorized to prepare a work schedule covering their proposed Phase III effort under separate contract to the AEC and management by the Division. Ultimately, the approved schedule was confined to six tasks. In essence, these tasks encompassed a parametric study to evaluate various combinations of sodium temperatures, steam pressures and temperatures in terms of relative capital costs and operating costs of secondary sodium/steam turbine systems for a 1000-MW(e) Fast Breeder Reactor Power Plant.

In addition to submitting their proposals for Phase IIA and IIB studies by the end of November 1965, each Phase I contractor included a commentary on problems inherent in the "vertical" approach. Particular emphasis was placed on the merits of a "horizontal" approach: each contractor indicated a strong preference for conducting comprehensive analyses and evaluations of his own "Total Plant Concepts." The latter approach prevailed at subsequent review meetings (December 6-10, 1965) attended by cognizant AEC, ANL, and contractor personnel.

Pending receipt of AEC authorization to proceed on this basis, Atomics International was advised to terminate its Phase III studies, since such studies would be incorporated in the revised bid package. At the time of notification, AI had completed Task II (Initial Scoping Effort) and prepared a preliminary design of the secondary-sodium and steam turbine-generator systems. A terminal report is in press. Where applicable, the findings will be used in the continuance of the Follow-On Program.

Upon receipt of AEC authorization on February 21, 1966, a tentative outline of the Scope of Work, reporting procedures, etc., was prepared by the Division and forwarded to each contractor for comments. These comments were reviewed at a subsequent meeting with the contractors on March 30, 1966. At that time the scope of work was finalized and incorporated in a Request for Proposals.

Briefly, the scope of work for each contractor encompasses the Nuclear Steam Supply System and Energy Conversion System of a limited number of concepts (or variations of a particular concept), of 1000-MW(e) liquid metal fast breeder reactors. For administrative convenience, the work is to be performed consistent with the following four tasks:

Task I: Develop one or more 1000-MW(e) LMFBR central station power plant concepts on the basis of established ground rules and an estimation of the technology attainable in 1980. In addition, consider the effects of fissile and fertile material costs, installed capacity and growth rate of the power industry, efficient utilization of natural resources, safety, and other pertinent factors.

Prepare design descriptions and perform preliminary evaluations, indicating the concept (and alternates) which merit selection as the Reference Concept.

Task II: Prepare detailed system and subsystem design descriptions for the Reference Concept selected in Task I and, in such detail as may be warranted, for any alternate concepts of promise.

Task III: Prepare detailed evaluations of the Reference System and Subsystem designs described in Task II, as well as any alternates that may be agreed upon. Include fully documented trade-off studies and applicable parametric studies. Upon completion of Task III, submit final report to the Laboratory.

Task IV: Concurrent with the final report, prepare a document outlining the research, development, and component testing recommended as essential to the successful design and construction of a safe, economically competitive 1000-MW(e) LMFBR. Where significant uncertainties exist in the technology, potential cost savings shall be weighed against the projected costs of a successful development program.

2.1.3.3 Current Status of Program

Proposals for the "follow-on" program have been received from Atomics International, Babcock & Wilcox, Combustion Engineering, General Electric, and Westinghouse. Allis-Chalmers asked to be excused because of their announced withdrawal from the reactor business. Babcock & Wilcox was requested to submit a proposal because of their interest and experience. An unsolicited proposal was received from Atomics International because of similar interest and pending termination of their Phase III work.

In summary, the five proposals are being evaluated. Initial design concepts described in the respective documents cover a variety of core geometries, fuels (carbide and oxide), refueling methods, and primary system and containment configurations. It is expected that the outcome of these

evaluations will assist the AEC in (1) defining the future course of the LMFBR research and development program; and (2) assessing the scope and capability of industrial participation in that program.

2.2 Materials and Components

Continued development of advanced fast breeder reactors for safe and economic power generation is dependent upon availability of materials and components capable of sustained exposure to, and operation in, intense fast neutron radiation and/or sodium at temperatures up to 1200°F. Their availability depends upon the results of comprehensive screening, development, and performance evaluation of existing or prototype materials and components in facilities designed to simulate and to maintain specific operating conditions and environments of interest. These facilities also must provide for simultaneous evaluation and calibration of in-line or auxiliary components or techniques for monitoring, controlling, or removing impurities (e.g., carbon, oxygen, fission products, etc.) that may be contained or entrained in the sodium coolant. Unless controlled or removed, these impurities could affect adversely the physical and mechanical properties of candidate materials and components, and thus reflect inaccurate assessment of their potential performance characteristics and service lifetime in prototype advanced fast reactor systems.

All of these factors are being considered in the design and conduct of the fast reactor materials and component development program at Argonne. The Divisional efforts, the related test facilities, and the progress during fiscal 1966 are described briefly in the following subsections.

2.2.1 1200°F Component and Materials Evaluation Loop

Sustained trouble-free operation of control rod drives, pumps, valves, instrumentation, piping, etc., at the target sodium temperature of 1200°F places a severe demand on materials used in the fabrication of these components. For example, at this temperature, stainless steels operate in a region of decreased tensile strength. Thus in addition to corrosion, they are subject to further deterioration as a consequence of stresses imposed by static or dynamic loading, or wear due to rubbing, sliding, or rolling contact between surfaces. Stresses placed upon the materials are also dependent upon component configuration.

These and other aspects of component and material performance and behavior will be investigated in the loop shown in Fig. 2-1. Scheduled for completion in 1967, the major features include:

- (1) A large number of positions for installation of instrumentation.
- (2) Modular construction for greater flexibility in removal or addition of test components.

(3) A high-capacity, electromagnetic pump to supply a wide variation in sodium flowrate.

(4) Flanged connections atop the surge tank for installation of materials wear testing machines.

(5) A data-acquisition system connected to an extensive array of loop instrumentation for collecting and processing test data.

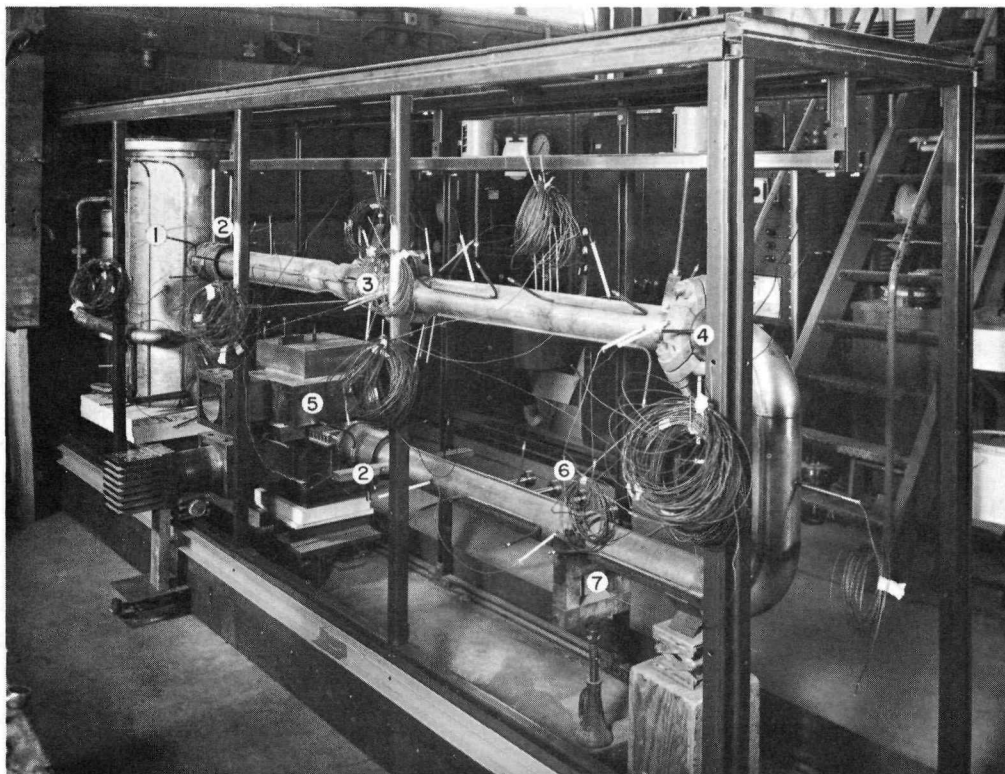


Fig. 2-1. 1200°F Components and Materials Evaluation Loop prior to application of insulation. Shown installed are: (1) surge tank; (2) pipe bellows; (3) throttling valve; (4) Conoseal flange; (5) electromagnetic pump; (6) pressure transducers; (7) flowmeter. Modified Falex wear tester will be installed on top the surge tank (1). Coils of wire will lead from thermocouples to data-acquisition system (not shown).

A number of components have been installed as part of the initial test series. They include 4-in. Conoseal flanges, pipe bellows, a throttling valve, and certain instrumentation, e.g., flowmeters and pressure transducers. Their location, along with other loop components can be seen in Fig. 2-1.

Also shown in the figure is the large number of thermocouples that have been installed throughout the loop and at strategic locations on individual components. While a number of these thermocouples comprise part of the sodium temperature-flow control and monitoring system, the majority supply sensing voltages to the data-acquisition system. This system

periodically scans these voltages and records the data on punched paper tape in biocatal flexowriter code for subsequent computer processing or graphical analysis. The latter is performed rapidly by a Hewlett-Packard X-Y plotter, which can be programmed to produce graphs of pertinent parameter relationships.

Physical erection of the loop is 90% complete. The data-acquisition system was selected, purchased, and installed in the laboratory. Coupling of this system to the loop monitors is nearing completion.

2.2.2 High-Temperature (1200°F) Sodium, Long-Term Environmental Test Loop

Since its construction in 1957, the test objectives of this 2-in., Type 304 stainless steel loop have been redirected from evaluation of d-c electromagnetic pumps in sodium at 25 gpm and 1550°F, to that of material compatibility in 1200°F sodium. More recently, interest has been focussed on the condition of the loop proper, since the structure has accumulated 12,000 hr of operation, including 8,000 hr at 1200°F.

Interest was triggered by a chemical analysis of the sodium, which was performed in late fiscal 1965. This analysis revealed only modest increases in Fe and Ni content, despite the fact that the loop features no provisions for cold trapping or hot trapping of the sodium.

Encouraged by these results, a section of the loop piping was forwarded to U.S. Steel Co. for chemical, physical, and microstructural analyses. For purposes of comparison, similar analyses were performed on a pipe section "as received" during construction of the loop. The following data have been extracted from their report.

Table 2-5 lists the results of chemical analyses of both exposed and "as received" pipe sections. Of particular interest is the percent increase in nitrogen (from 0.14 to 0.24) and sodium (from <0.01 to 0.0270) on the sodium side (I.D.) of the exposed section.

Table 2-5 Chemical Analyses of AISI Type 304 Stainless Steel
Loop Piping As Received and after Exposure for 8,000 hr
to Dynamic (24 gpm) Sodium at 1200°F

Sample	Analyses Location	Composition, %														
		C	Mn	P	S	Si	Cu	Ni	Cr	Mo	V	Ti	Al	Co	N	Na
As-received	Outside surface	0.063	1.87	0.020	0.012	0.45	0.15	10.4	18.5	0.10	0.05	0.01	0.004	0.05	0.06	<0.01
	Midthickness	0.027	*	*	*	*	*	*	*	*	*	*	*	*	0.06	*
	Inside surface	0.082	1.85	0.020	0.012	0.46	0.15	10.2	18.3	0.10	0.05	0.01	0.004	0.05	0.06	<0.01
Exposed	Outside surface	0.068	1.83	0.020	0.010	0.48	0.15	10.2	18.2	0.10	0.05	0.01	0.007	0.05	0.14	<0.01
	Midthickness	0.027	*	*	*	*	*	*	*	*	*	*	*	*	0.06	*
	Inside surface	0.084	1.86	0.020	0.010	0.44	0.15	10.3	18.3	0.10	0.05	0.01	0.007	0.05	0.24	0.02

*Not determined

AISI Composition Range for Type 304 Stainless Steel, %

C	Mn	P	S	Si	Ni	Cr
0.08	2.00	0.045	0.030	1.00	8.0	18.0
Max	Max	Max	Max	Max	12.0	20.0

Tensile, yield strength, and hardness tests of the exposed section yielded values which were above the minimum specified by ASTM. When flattened in the normal direction of pipe curvature, there was no evidence of cracking; however, when flattened in the opposite direction, cracks about 0.005 in. deep were observed in the area of maximum stress.

Microstructural analysis of the exposed section revealed the existence of a lamellar phase on the sodium side, but not on the air side. Electron-probe microanalysis of this phase indicated areas higher in chromium and slightly lower in iron and nickel than that found in areas not associated with the lamellar phase. These observations, coupled with the high nitrogen content of the pipe I.D., suggest that the lamellar phase is predominantly Cr_2N .

In summary, the foregoing investigations indicate that the Type 304 stainless steel piping has not suffered any marked deleterious changes in mechanical properties. However, the detected increase in nitrogen and sodium in the pipe I.D. emphasizes the need for a more scientific approach to resolving the physicochemical mechanisms which might affect the strength and ductility of existing and prototype materials upon sustained exposure to high-temperature sodium.

Such an approach has been initiated, and tentative avenues of endeavor have been identified. Among others, they include analytical and experimental studies to determine the nature of intercrystalline boundaries in polycrystalline materials; the relative orientation of linked crystals and their chemistry in high-temperature sodium; and the effect of increasing (horophilic) or decreasing (horophobic) concentrations of dissolved components of crystalline boundaries on structural integrity. Subsequent accomplishments of this research activity will be reported under the heading: Physicochemical Mechanics of Metals in Sodium.

2.2.3 Material Compatibility Test Facility

The facility shown in Fig. 2-2 is being used to determine the effects of geometry, surface finish, static loading, and sodium quality on the self-welding characteristics of like or unlike materials when immersed in static sodium at temperatures up to 1200°F.

In operation, five pairs of test specimens are positioned in an electrically-heated autoclave ($L=D=12$ in.) partially filled with sodium of a predetermined quality. Loadings are transmitted to the samples through bellows-sealed push-rods ($5/8$ in. dia.) which operate through the flanged closure.

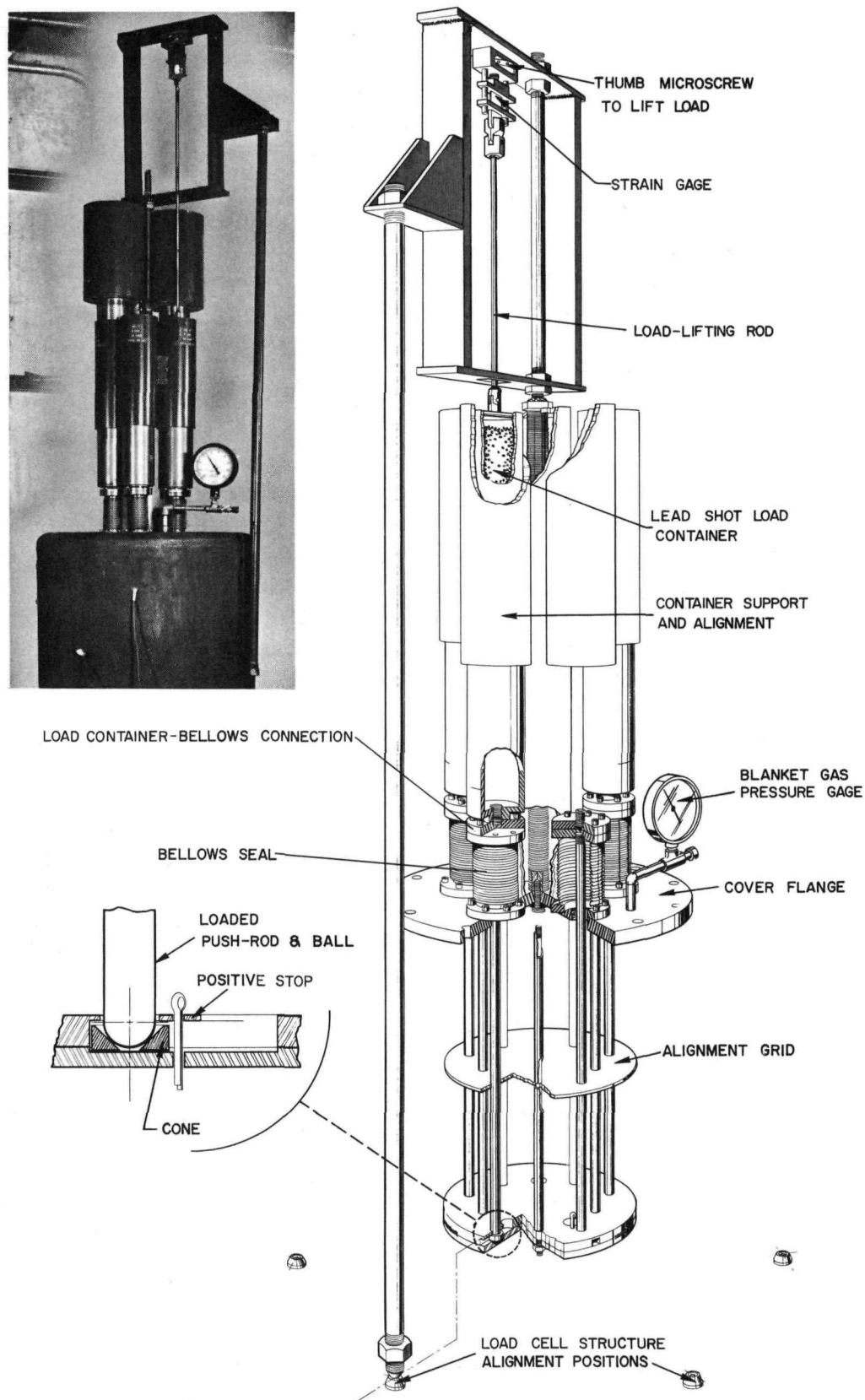


Fig. 2-2. Apparatus for evaluating self-welding characteristics of various material combinations and configurations under static load in sodium at temperatures up to 1200°F. Inset shows simulated EBR-II subassembly-core grid configuration used in current tests.

Five Type 304 stainless steel ball-and-cone configurations are under test. They represent the curved seating surfaces of subassemblies bearing against the flat, chamfered core support grid openings in the EBR-II. The objective is to determine whether or not sticking will occur at temperatures beyond those of EBR-II (700°F), up to and including 1200°F.

In these tests, the balls (1 in. dia.) at the end of the push-rods (representing the subassemblies) are forced into the inverted frustum of the cones (representing the grid openings) under different loads and at a given sodium temperature. As shown in the inset of Fig. 2-2, the cone is allowed to lift with the ball if there is any adhesion. In such event, the cone encounters the restraining plate and is separated from the ball. The measured force required to effect this separation indicates the strength of the self-welded bond or sticking that has occurred.

Approximately 865 hr of testing has been accumulated thus far. During this period, loads of 11.5, 21, 38, 80, and 119 lb were applied to the specimens in sodium at 1200°F. The minimum load corresponds to the seating force of a typical EBR-II core subassembly, while the maximum load is equal to the yield strength of the alloy at the test temperature. Some sticking was experienced with the 80- and 119-lb loads; however, in both cases, a force of less than 10 lb was required to effect separation.

Of particular significance is the post-test appearance of three push-rod-ball-cone assemblies shown in Fig. 2-3. Corrosion is noticeable in the region where the rods penetrate the free surface of the 1200°F sodium. Subsequent metallurgical tests and examinations of the five push-rods revealed: (1) changes in microstructure; (2) severe sensitization, indicated by a modified 1-hr Strauss test; (3) extensive carbide precipitation in the grain boundaries; and (4) reductions in tensile strength, impact resistance, and hardness.

A new complement of identical push-rod-ball-cone assemblies has been installed and will be tested for a period considerably in excess of 800 hr.

2.2.4 Modified Falex Machine for Wear Tests in High-Temperature Sodium

Operation of certain in-reactor and auxillary mechanisms such as control rod drives and fuel-handling machines is in the category of intermittent demand rather than high-speed continuous action. In particular, the majority of these mechanisms include components that operate under loads and/or involve loaded surfaces in sliding or rolling contact. Thus the capability of these mechanisms to operate reliably upon demand, over long periods of time, is dependent upon selection of materials that are mutually compatible in contact with each other and the high-temperature sodium

coolant anticipated in advanced fast reactor systems. To facilitate selection of materials that satisfy these criteria, a modified Falex machine (Fig. 2-4) has been developed and proof tested at Argonne.

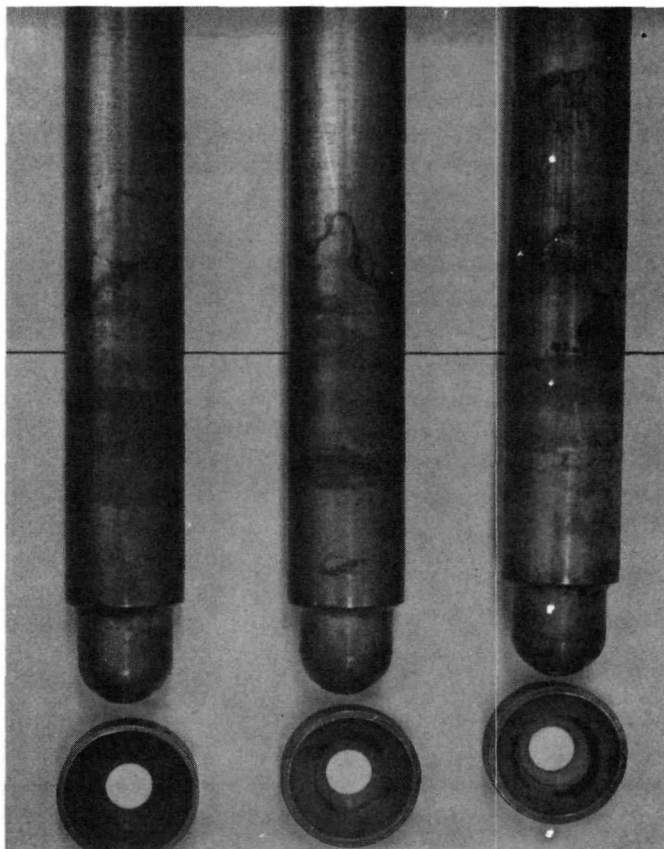


Fig. 2-3. Appearance of push-rods, balls, and cones of Type 304 stainless steel loaded to 119 lb in 1200°F sodium. Discolored areas evidence extent of corrosion attack on push-rods.

2.2.4.1 Operational Characteristics

Designed to evaluate the wear characteristics of various material combinations in sodium at 1200°F, the machine operates as follows: The tubular body, which is sealed to an opening in a loop or test vessel, supports two levers which squeeze two vee blocks against a central, rotating shaft extension while immersed in the sodium. Both vee blocks and the shaft extension represent the materials being evaluated; they can be removed and replaced with similar configurations of other like and unlike materials of interest. (See inset, Fig. 2-4.)

The squeezing action on the test specimens is applied at the upper end of the loading lever by means of the ball-screw, sector wheel, and bellows assembly mounted on the side of the tubular body. Rotation of the test shaft extension is imparted by the drive shaft of a constant-speed, d-c motor atop the body. Throughout the test, constant pressure is maintained on the loading lever by a weight suspended from the sector wheel.

Rate of wear is recorded electronically by motion of this lever which, in turn, moves the core in a linear, variable, differential transformer.

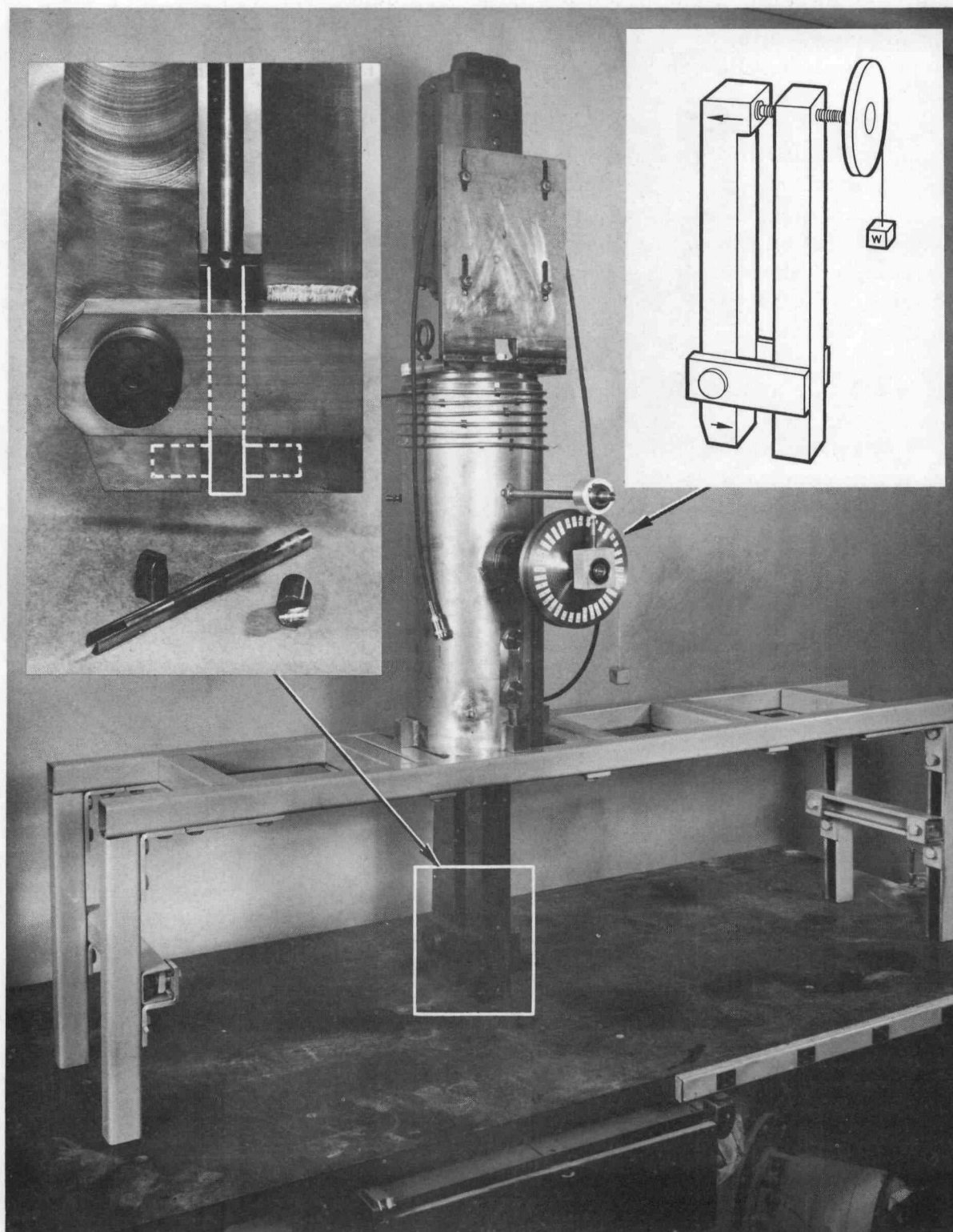


Fig. 2-4. Modified Falex wear tester for evaluating candidate materials in high-temperature sodium. Insets show (left) specimen vee blocks, shaft extension, and supporting structure which are immersed in the sodium, and (right) simplified sketch of ball screw-sector wheel-loading lever assembly.

During the course of testing, the outer water cooling coils around the vapor dome provide a reflux temperature region below the screw mechanism. A wire mesh in this region operates as a flooded member. This arrangement minimizes condensation and deposition of sodium in the mechanism region, since sodium has an appreciable vapor pressure at 1200°F.

In addition to recording rate of wear, the machine can be used to measure the rate of expansion due to frictional heating of the test specimens. Friction is determined from the changes in current required to drive the constant-speed, d-c motor. Also, the onset of galling is clearly evident by the torque behavior of the motor and the fluctuations in the wear readout. Finally, by replacing the d-c motor with an impulse drive, the machine can be used for start-stop, wear studies.

2.2.4.2 Mode and Objective of Evaluations

Initial screening tests of various material combinations will be conducted in inert gas at 1200°F. Promising combinations will then be subjected to more extensive tests in sodium at 1200°F.

The major parameters of significance to wear of materials are defined in their properties. For example, the coefficient of wear in inert gas can be expressed by the function:

$$C_w = \frac{K_2}{\pi D^3 N} \left(\frac{\epsilon}{D} \right)^a \left(\frac{BA}{F} \right)^g \left(\frac{EA}{F} \right)^h$$

where

ϵ = surface roughness

D = shaft diameter

N = number of shaft revolutions

F = applied force

B = hardness

E = modulus of elasticity

K_2, a, g, h = constants

For control purposes, a material of known hardness, surface finish, and modulus of elasticity will be subjected to a predetermined number of shaft revolutions and applied loads while wear is measured. From these data, the constants K_2 , a , g , and h will be determined. Other materials will be substituted and the corresponding constants denoted. Similar tests will

be conducted in sodium at 1200°F. The ultimate objective will be to relate the various relevant parameters in mathematical functions which describe the respective test models.

2.2.4.3 Proof Tests, Scheduled Construction and Availability

Proof tests of a prototype unit confirmed that the machine is capable of recording both wear and expansion. These tests were conducted with carbon and stainless steels in inert gas at room temperature and at 1200°F. Both materials exhibited very poor wear properties in the high-temperature gas; breakdown occurred in a matter of minutes with low (~20) rpm and light (275 psi) loading. Diametral variation due to frictional heating of the shaft was measured to an accuracy of 0.000018 in. A Stellite and Carboloy configuration evidenced wear of 0.0016 in. after 12 hr at 1200°F and under a load of 660 psi.

Nine modified Falex machines are scheduled for installation and operation in early fiscal 1967. Three will be installed in the 1200°F Component and Materials Evaluation Loop, and four in static sodium pots. The other two will be used to establish controls in inert gas at temperatures ranging from room to 1200°F.

2.2.5 1200°F Sodium Furnace-Tensile Testing Machine

The test objectives of this unique facility are to isolate and assess the relative effects of high-temperature sodium, fast neutron irradiation, tension, compression, and biaxial stresses on the mechanical properties of thin-walled tubes simulating, for example, fuel element clad.

As shown in Fig. 2-5, the lower end of a tubular test specimen, up to 8 in. long and 0.50 in. O.D., is engaged by a chuck in the bottom of a Type 304 stainless steel tank (8-in. pipe, 14 in. long) filled with sodium at temperatures up to 1200°F. This chuck and tank are an integral part of a rod extension which is engaged by the lower gripper of a universal tensile machine. At the upper end, the specimen is welded to a similar rod extension which penetrates a bellows seal and is engaged by the upper gripper of the tensile machine.

This arrangement permits elongation or compression of the tubular specimen while maintaining an argon atmosphere above the sodium in which the specimen is immersed. Biaxial stress can be applied by pressurizing (with argon) the specimen I.D. through a 1/16-in.-dia.-bore in the upper rod extension. The tensile machine may then be programmed to cycle the stressed tube through any predetermined stress range.

Initial testing of an unirradiated EBR-II blanket element tube was terminated after 20,000 cycles due to failure of the bellows seal. At the

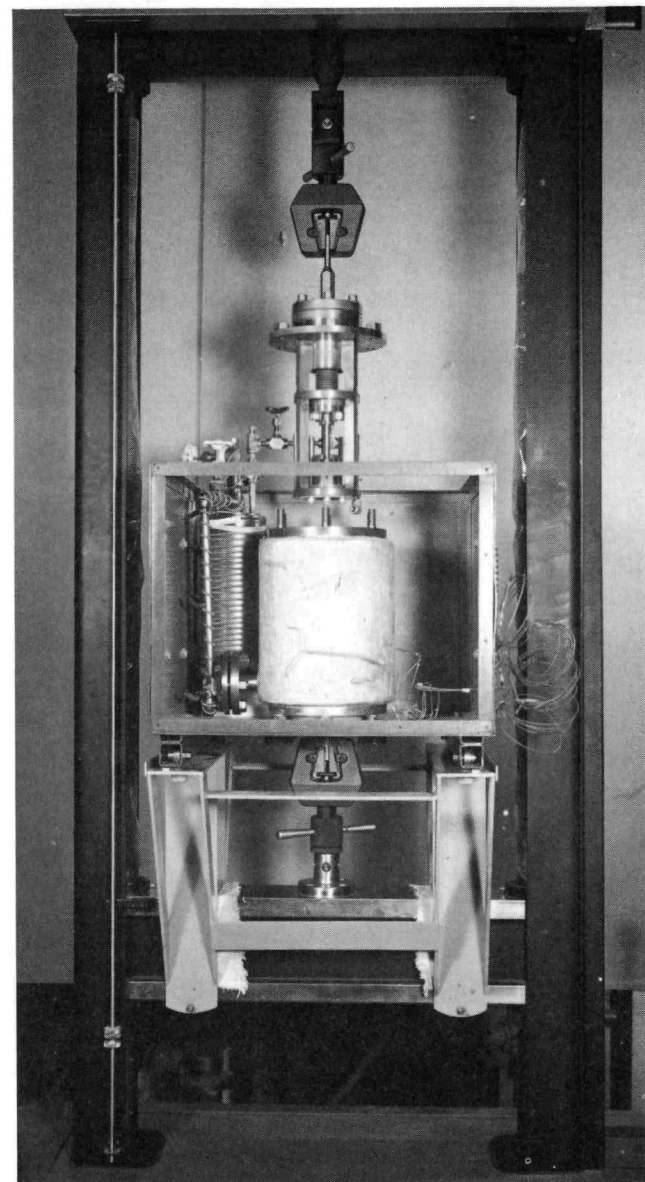
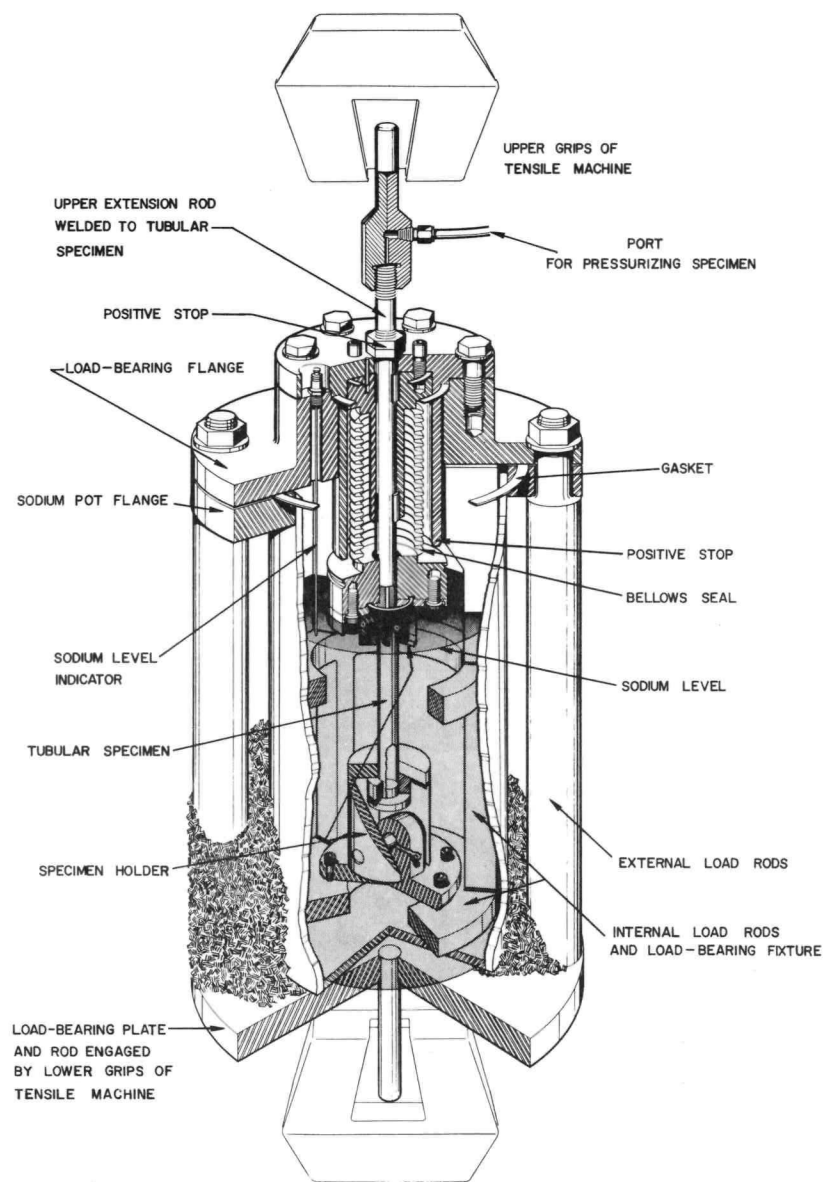


Fig. 2-5. 1200°F sodium furnace-tensile testing machine

time of termination, the tube had been cycled to 70% of its yield strength at 1200°F. Visual inspection of the tube revealed no macro surface defects. A more thorough metallurgical examination was deferred in order to investigate the cause of the bellows failure.

2.2.5.1 Nature of Bellows Seal Failure

Upon removal from the test facility, the bellows assembly was steam cleaned, washed with distilled water, and soaked in ethyl alcohol for 72 hr. It was then washed three more times with distilled water and allowed to dry in air.

When thoroughly dried, metallurgical and mechanical test specimens were removed from three sections: adjacent to the failure, and 1 in. and 2 in. above the failure. These sections had been exposed to temperatures ranging from 1200°F at the failure, to about 1000°F at the uppermost section. (Note: Sodium vapor is contained in the O.D. of the bellows and atmospheric air in the I.D.) After removal of the test specimens, the remainder of the bellows assembly was stored in an air atmosphere.

Microscopic examination of specimens from the 1000°F section revealed incipient intergranular corrosion on the sodium vapor side, but not on the air side. Corrosion of the intermediate section (~1100°F) was more pronounced on the sodium side and moderate on the air side. A modified (15-min) Strauss test, followed by electrical resistance measurement on this section revealed a 50% increase in resistivity (2.7×10^{-4} vs. 3.3×10^{-4} ohm-cm), indicating a sensitized condition.

Similar examination and testing of specimens adjacent to the failed area revealed gross intergranular corrosion on the sodium side, and a 200% increase in electrical resistivity (2.0×10^{-4} vs. 4.3×10^{-4} ohm-cm). Samples subjected to a standard (48-hr) Strauss test completely disintegrated after 1 hr.

The degree of sensitization in each instance was confirmed by bend tests. For example, five 180-degree bends were required to start fracture, and four additional bends to complete failure, of specimens from the 1200°F section. By comparison, 12 bends were required to start, and 11 additional bends to complete, fracture of specimens from 1 in. above the failed area. In all cases, the surface on both sides "powdered," more deeply on the sodium side, leaving a tough, inner core which required additional bends to fracture.

A simple alkalinity test with litmus paper lends support to the belief that sodium vapor is affecting the grain boundaries of the bellows microstructure. After two weeks' storage in air, the balance of the "thoroughly cleaned" bellows assembly was coated with a white powder. One drop of distilled water on each convolution indicated that the powder has basic or alkaline chemical properties.

Present work is focussed on 1600°F solution annealing the replacement bellows assembly, and to determine in subsequent tests whether such pretreatment can measurably increase bellows lifetime in a sodium vapor environment.

2.3 Sodium Quality Control

Development and evaluation of in-line and off-line instrumentation for sodium oxide and impurity control has been expanded to encompass a broad program to improve analytical equipment and techniques available in the Division. This program includes the accelerated design, development, and construction of a Bypass Tube Sodium Sampling and Distillation Facility to provide a presently-needed analytical service in existing sodium systems and facilities. It also includes construction of a multiloop sodium quality control facility wherein existing and newly-developed analytical devices and sampling techniques can be simultaneously evaluated, calibrated, and cross-compared under rigidly-controlled sodium temperatures and impurity content. Finally, the analytical capability of the Sodium Quality Control Laboratory has been enhanced by the acquisition of a 1024-channel counting system for activation analysis of impurity content in sodium, an atomic absorption spectrophotometer for trace analysis of nonactive impurities, and a mass-spectrometer-type gas analyzer to monitor the atmosphere during vacuum distillation sampling operations.

Certain aspects of this program were implemented during fiscal 1966, and the accomplishments are summarized in the following sections. These sections include the progress of investigations introduced in ANL-7190.

2.3.1 Sodium Vapor Trap Development

Three additional ANL-designed, sodium vapor traps were fabricated and installed for further proof tests in inert gas lines leading to major components of the former FARET Core Test Loop. These traps are capable of removing sodium vapor from argon vented at up to 40 ft³/hr from a system containing sodium at 1200°F.

Each trap consists of a series of concentric stainless steel baffles which slope downward inside a vertical, 8-in. length of 2-in., Schedule 40 stainless steel pipe. The trap outlet is maintained at a temperature slightly above the sodium melting point. In operation, the argon-entrained sodium droplets deposit on the baffles and return by gravity to the bulk sodium in the system. Earlier bench-type tests of a prototype unit gave measured efficiencies of 97 and 99% at flowrates of 5 and 20 ft³/hr, respectively.

Further proof tests of the newly-installed traps will be made in conjunction with an FFTF support program being developed to utilize available test facilities at Argonne.

2.3.2 Sodium Sampling Methods

Application of three prototype methods of sampling sodium from a loop at temperatures up to 500°F has met with limited success. These methods included dip-sampling through a small glove box, vacuum-cup sampling, and guillotine cut-off of a sodium sample extruded from a bypass sampling tube.

While no problems were encountered during dip-sampling operations, subsequent analyses of all samples yielded excessively high and erratic values of oxygen content. In all cases, the excessive oxygen was attributed to air and moisture which diffused through the rubber glove material into the glove box.

There was also considerable variation in the oxide measurements made with the vacuum-cup sampling technique. Observations through quartz windows in the distillation chamber revealed that inconsistencies in the height of the sodium meniscus in a 14 cm³ hemispherical cup could result in a sample volume difference of ~30%. Redesign of the samples, along with provisions for control of the filling operation, is expected to resolve this problem.

Use of the guillotine-type cutter to section sodium extrusions of uniform volume was ineffective due to sticking of the cut-off pellet to the blade.

2.3.3 Sodium Quality Measurement Loop

Originally constructed for EBR-II cold trap studies, this 2-in., Type 304 stainless steel loop was modified to accommodate and simultaneously evaluate various instrumentation and methods for analyzing the impurity content in sodium at various flowrates and temperatures.

Except for occasional shutdown for repairs, the loop was operated continuously at 600°F from July 1, 1965 to April 26, 1966. During this period, two United Nuclear electrochemical oxide meters, a Blake resistivity meter, a distillation analyzer, and a plugging meter were employed to monitor the impurity content in sodium circulated at 10 to 12 gpm. A considerable quantity of data was taken from these instruments. In addition, bypass line freeze samples were removed periodically for amalgamation chemical analysis.

However, subsequent comparisons of the data revealed considerable inconsistencies. For example, the oxygen content of the plugging meter varied $\pm 20\%$ during consecutive runs; smaller variations were noted in the voltage output of the electrochemical cells. The Blake meter was too sensitive to sodium temperature, flow, and other indeterminate causes. Finally, the distillation method was inaccurate because a uniform sample size could not be withdrawn into the distillation cup.

Some of the above difficulties were enhanced by the fact that the actual oxygen content was ever changing due to (1) storage of oxide in cold legs of dead-end pipes and large, bellows-sealed valves originally incorporated in the loop; and (2) inadequate temperature control of the long pipe runs. Therefore, the loop is being deactivated. Subsequent evaluations will be performed in the Sodium Analytical Loop, which is nearing completion.

2.3.4 Sodium Analytical Loop

When completed, this loop will be used to evaluate, calibrate, and cross-compare existing or newly developed in-line analytical instrumentation and sampling techniques for sodium quality control in engineering systems and loops. Cross-comparisons will emphasize accuracy, speed of response, and reliability of operation.

Constructed of Type 304 stainless steel and designed to ensure accurate control of sodium temperature and oxide impurity content, the basic 600°F, 15-gal-capacity test facility comprises three loops (with no valving) connected to a common supply of sodium. As shown schematically in Fig. 2-6,

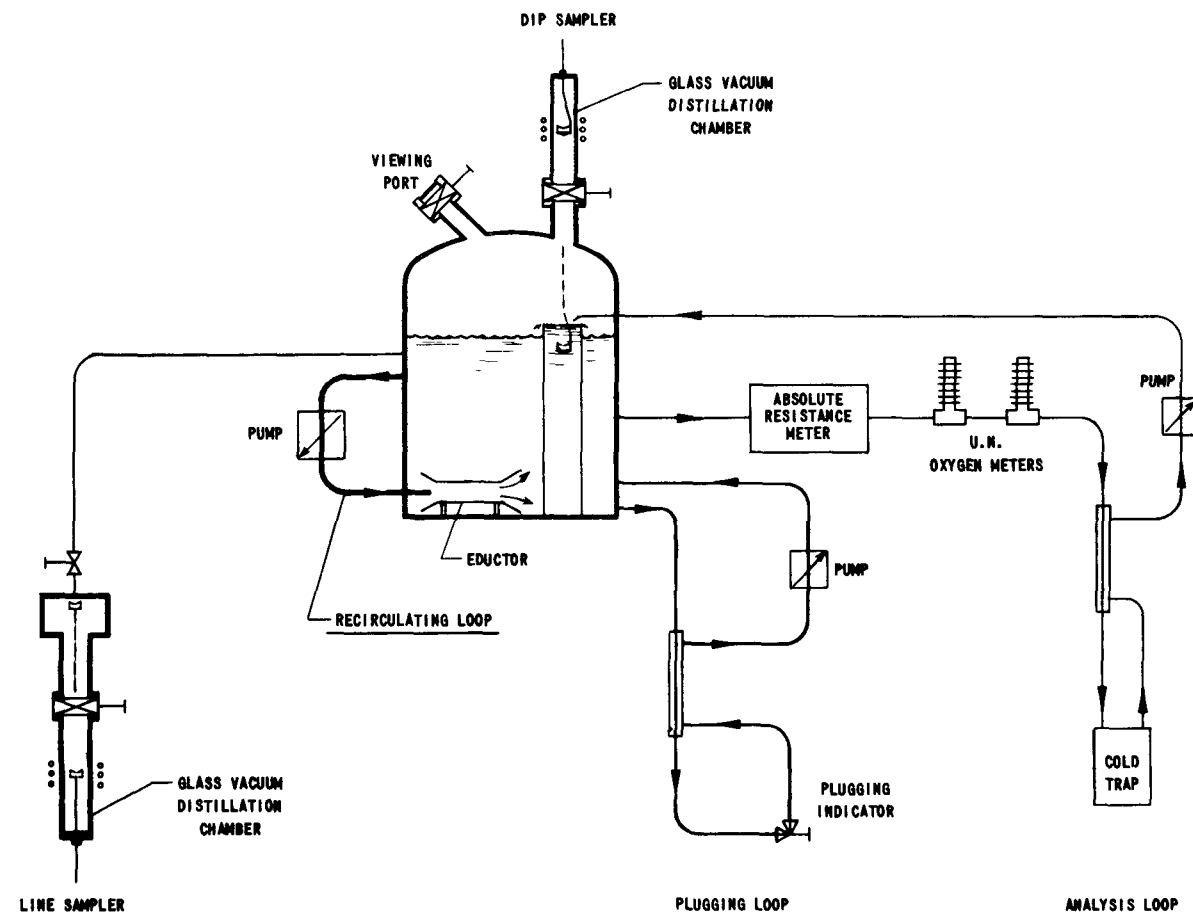


Fig. 2-6. Schematic of multiloop facility for evaluating and cross-comparing in-line and off-line instrumentation and sampling techniques for sodium quality control

two of the loops (1/2 in. O.D., 7/16 in. I.D., 1/32 in. wall) are equipped to accommodate candidate in-line analytical instrumentation and plugging indicators, respectively. The former include a d-c Absolute Resistance Meter and two United Nuclear oxygen meters. Local temperature and impurity gradients are eliminated by means of the third loop. This loop recirculates sodium from the upper region of the vessel back into the neck of an eductor located at the bottom of the vessel.

The facility includes provisions for evaluating line- and dip-sampling techniques. As illustrated in Fig. 2-6, the line sampler will be connected to a 1/4-in. tube leading from the vessel; the dip sampler will operate through a 2-in. valved access port atop the vessel.

Design and fabrication of all major components is essentially completed. Installation of the support structure is under way.

2.3.5 Sodium Quality Control Laboratory

The analytical capability of this laboratory has been improved markedly by the addition of a 1024-channel counting system, an atomic absorption spectrophotometer, a mass spectrometer-type gas analyzer, and provisions for controlling temperature and humidity in the work area.

The multichannel system will be particularly useful for qualitative and quantitative determination of activated impurities in reactor-grade sodium. These impurities range from the type normally present in "as received" sodium, to particles originated by corrosion, erosion, or solubility of structural or fuel cladding material. Regardless of the source, activation analysis is generally more sensitive (higher detection limits) than conventional analytical methods.

Complementing the multichannel system is the newly acquired spectrophotometer. It will be used for trace analysis of nonactive impurities in sodium. With this unit, 38 of the more commonly determined elements can be detected within the range 1.0 to 0.005 $\mu\text{g/ml}$. Interference effects, experienced by other instrumental or wet chemical analyses, are almost totally absent.

Finally, the mass spectrometer will be used to furnish qualitative indication of off-gases that might be generated during vacuum distillation sampling of system sodium. Sensitivity of this instrument, expressed as minimum detectable total pressure, is 1.5×10^{-13} Torr. With minor modifications, it can be adapted for analysis of blanket gas and glove box atmosphere during sampling operations.

2.4 In-Core Instrumentation

Originally implemented in support of the FARET concept,^{3,4} the work under this research activity is being reoriented consistent with Argonne's role as the AEC's center for fast reactor development. One objective is to provide instrumentation essential to the design, development, construction, and experimental use of the FFTF. The exact nature of the instrumentation required, and the test facilities and environments in which they are to be evaluated, is pending completion of negotiations between Argonne and FFTF personnel. Tentatively, it is expected that much of the work will represent an extension of the fiscal 1966 effort, which is summarized in the following subsections.

The scope of this effort has ranged from out-of-pile and in-pile testing of existing or modified commercially-available thermocouples, flowmeters, lead connectors, seals, and cables, to similar testing of new and unique counterparts for sensing and transmitting in-core parameters and variables in sodium-nuclear radiation environments ranging from 650°C to in excess of 2400°C.

In the case of fuel-pin thermocouples, for example, combinations of candidate refractory materials as well as prototype assemblies are initially screened with respect to their thermoelectric properties, electrical resistivity, and compatibility in inert gas furnaces at temperatures up to 2800°C. Promising units are further evaluated in terms of their ability to measure centerline temperatures of fuel pins in test capsules during sustained exposure to a high temperature, high thermal- and fast-neutron flux and gamma environment in the CP-5 reactor.

2.4.1 Thermocouples

2.4.1.1 Hot Zone Errors

When refractory oxide-insulated thermocouples are used to measure fuel pin temperatures above 1000°C, the shunting effect of the insulation material can reflect a significant error in the measured values. The magnitude of this hot zone error has been theoretically predicted by treating the thermocouple as a distributed parameter transmission line, and solving the resulting differential equations. It was found that the error depends upon the materials, dimensions, and temperature distribution along the length of the thermocouple. This was affirmed by subsequent furnace testing of 0.010-in.-dia. W-3% Re/W-25% Re wires, insulated with 99.8% thoria of the crushable type, and spaced on 0.020-in. centers in a tantalum sheath (0.062 in. O.D., 0.010 in. wall).

Figure 2-7 lists the calculated and measured hot zone errors for the corresponding temperature distributions and hypothetical thoria resistivities. Curve B approximates the resistivity of the thoria used in the thermocouple

tests. As evidenced by the accompanying table, there is good agreement between calculated and measured errors. However, comparison between Curve B and Curves C and D indicates that the computational procedure is sensitive to minor variations in resistivity, particularly for values greater than 10 ohm-cm. This table also shows that use of thoria represented by Curve A in the current tests would have reflected the least hot zone errors.

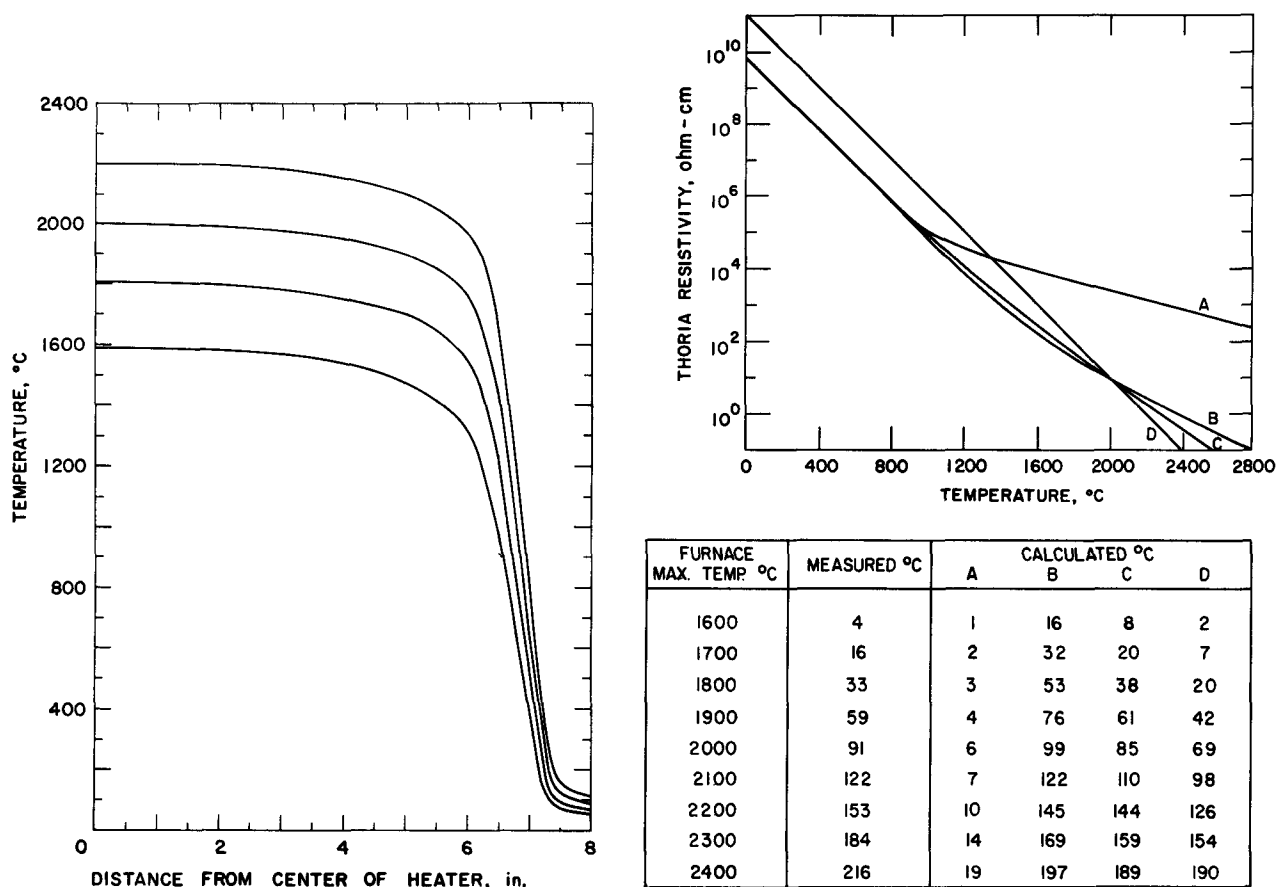


Fig. 2-7. Measured and calculated hot zone errors for thoria-insulated, tungsten-rhenium thermocouple wires sheathed in tantalum

2.4.1.2 Resistivity of Refractory Oxides

Knowledge of the resistivity of refractory oxides is essential to the development of thermocouples to monitor temperatures up to 2800°C. If these values can be well defined, important computations (hot zone errors) can be made to assist in selecting the material combination and size of thermocouple best suited for a given temperature environment.

Alumina. At present, thoria appears to be the only oxide suitable for use as electrical insulation in sheath-type thermocouples at temperatures above 2300°C. It has a high melting point (~3300°C) and is compatible with refractory metals and alloys being considered for sheathing and/or wire elements. However, since the electrical properties of thoria in this temperature

region are not well known,⁵⁻⁸ and pending procurement of an ample supply for test purposes, the proposed resistivity-measuring technique was checked out on a more well-defined insulating oxide, i.e., alumina, to establish a control.

Resistivity measurements were made on both crushable and vitrified types of alumina insulators. In each instance, the specimen (0.055 in. I.D., 0.161 in. O.D., 3 in. long) was positioned between two tantalum coaxial electrodes and heated to the desired temperature in a dry helium atmosphere. Resistivity data were taken with the aid of a transistor curve tracer. The values reported here represent the initial slope of the current-voltage traces.

It was found that the resistivity of both types of alumina was influenced by two separate effects, both related to the time-temperature history of the test specimen. One effect is the "freezing-in" of high-temperature lattice defects brought about by rapidly cooling the alumina. The other is an apparent stoichiometric change which occurs in the alumina when it is heated to in excess of 1800°C in the presence of the tantalum electrodes.

The effect of "freezing-in" of defects on the resistivity is best illustrated by measurements made on a vitrified alumina sample. This sample was heated and maintained at 1400°F until the resistivity stabilized at 1.82×10^6 ohm-cm. It was then heated to 1900°C for three minutes and then rapidly cooled (in ~2 min) to 1400°C, whereupon the resistivity measured 2.27×10^5 ohm-cm and was slowly drifting higher. The initial value of 1.82×10^6 ohm-cm was restored by heating the sample to 1900°C for three minutes followed by a slow cool-down (~20 min) to 1400°C. This process was repeated many times, with the same results.

The foregoing observations lend support to the theory that: (1) so long as the sample temperature is not held in excess of 1800°C for more than 30 min, no stoichiometric change occurs in the alumina; (2) rapid cooling of the sample does "freeze-in" lattice defects which are present at high temperatures and causes an abnormally low resistivity at the lower temperatures; and (3) if the sample is cooled slowly, the high-temperature defects "anneal" out, and the normal low-temperature resistivity is restored.

In subsequent tests, a sample of vitrified alumina was heated to and held at 1900°C for $5\frac{1}{2}$ hr. During this period, the resistivity increased from 3.64 to 10^2 ohm-cm to a maximum of 9.1×10^2 ohm-cm, and the color of the alumina changed from white to light gray. Spectrographic and microprobe analyses indicate that the darkened alumina is not contaminated with tantalum, but appears to be substoichiometric alumina. The lost oxygen, most probably, has been adsorbed by the tantalum.

After the long heat at 1900°C, the normal resistivities (i.e., with no "frozen-in" defects) increased slightly at temperatures above 1600°C and decreased slightly at temperatures below this value. These data are plotted

in Fig. 2-8. They are slightly higher than values published in the open literature,⁵ and approach the apparent "resistivity" for helium gas. Thus the discrepancy may be due to gas gaps that exist in the resistivity probes.

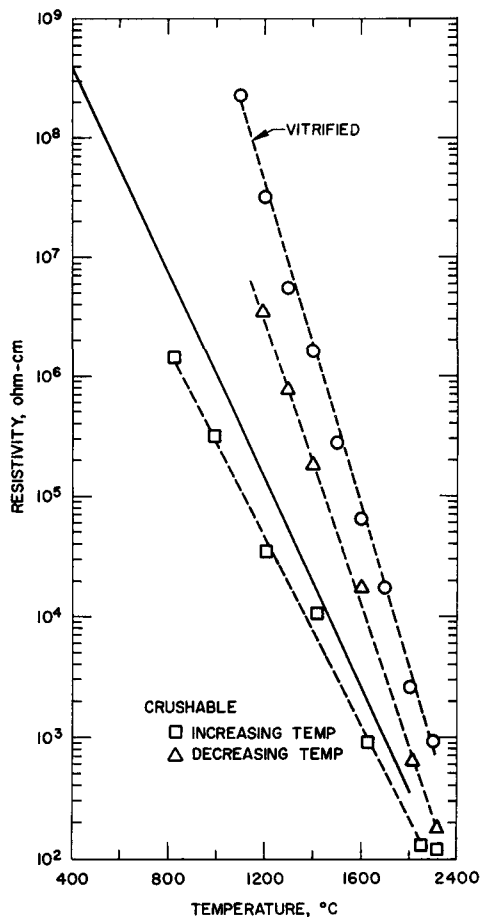


Fig. 2-8. Resistivity of vitrified and crushable types of alumina. Solid curve represents average values obtained from open literature.

attributed to a stoichiometric change. What effect this change has on the resistivity of thoria is not known at this time.

2.4.1.3 In-Pile Tests

The work reported here is an extension of exploratory irradiation tests of four capsules containing tungsten-rhenium thermocouples for measuring centerline temperatures in UO_2 and in UO_2PuO_2 fuel pellets. (See ANL-7190, p. 60.)

In addition to the successful performance of the couples, these tests demonstrated that the design of high-temperature capsule HT-1 was capable of achieving a test temperature of $>2300^\circ\text{C}$ in the CP-5 reactor at maximum power (4.5 MW). This capsule contained UO_2 fuel pellets which were

The difference between resistivities for vitrified and for crushable alumina is due principally to the ratio of wire-to-insulation contact area. Unlike the crushable alumina insulation, the vitrified alumina is slip fit over the wires; this results in point or line contacts and, consequently, higher resistivity. This is evident from the plotted data for crushable alumina in Fig. 2-8. As the sample temperature was increased to 1900°C , the measured resistivities were low, as expected. At the conclusion of these measurements, the sample was held at 1900°C for 1 hr, during which time the alumina presumably vitrified. As the temperature was decreased slowly, the measured resistivities approached those of the vitrified alumina.

Vitrified Thoria. Pieces of vitrified thoria (99.8% or better purity) also evidenced changes in color from white to very dark grey when heated to $>2400^\circ\text{C}$ in a helium atmosphere and in the presence of tantalum or W-25% Re.

Spectrographic analysis indicated no contamination of the samples; therefore the darkening of the thoria has been

monitored by a tantalum-sheathed, thoria-insulated, W-3% Re/W-25% Re couple. In addition, tantalum spacers were positioned between the fuel and capsule wall, and the capsule was backfilled with argon.

To determine whether the centerline fuel temperatures could be varied over a range of values by changing the fill gas, an identical counterpart of the HT-1 capsule was assembled, backfilled with helium, and installed in the reactor.

Figure 2-9 is a plot of the time-temperature history of the capsule as monitored by the single thermocouple during the 6-day test. During initial start-up, the capsule temperature behaved normally, reaching an equilibrium value of $\sim 1680^{\circ}\text{C}$ at the full reactor power level. This temperature remained essentially constant for about 40 hr, at which time the reactor was shut down routinely. Upon resumption of reactor operation two hours later, the capsule temperature again behaved normally during start-up. However, after about two hours at maximum power, the indicated temperature (1825°C) dropped abruptly to 1600°C and then soared to 2225°C . It then

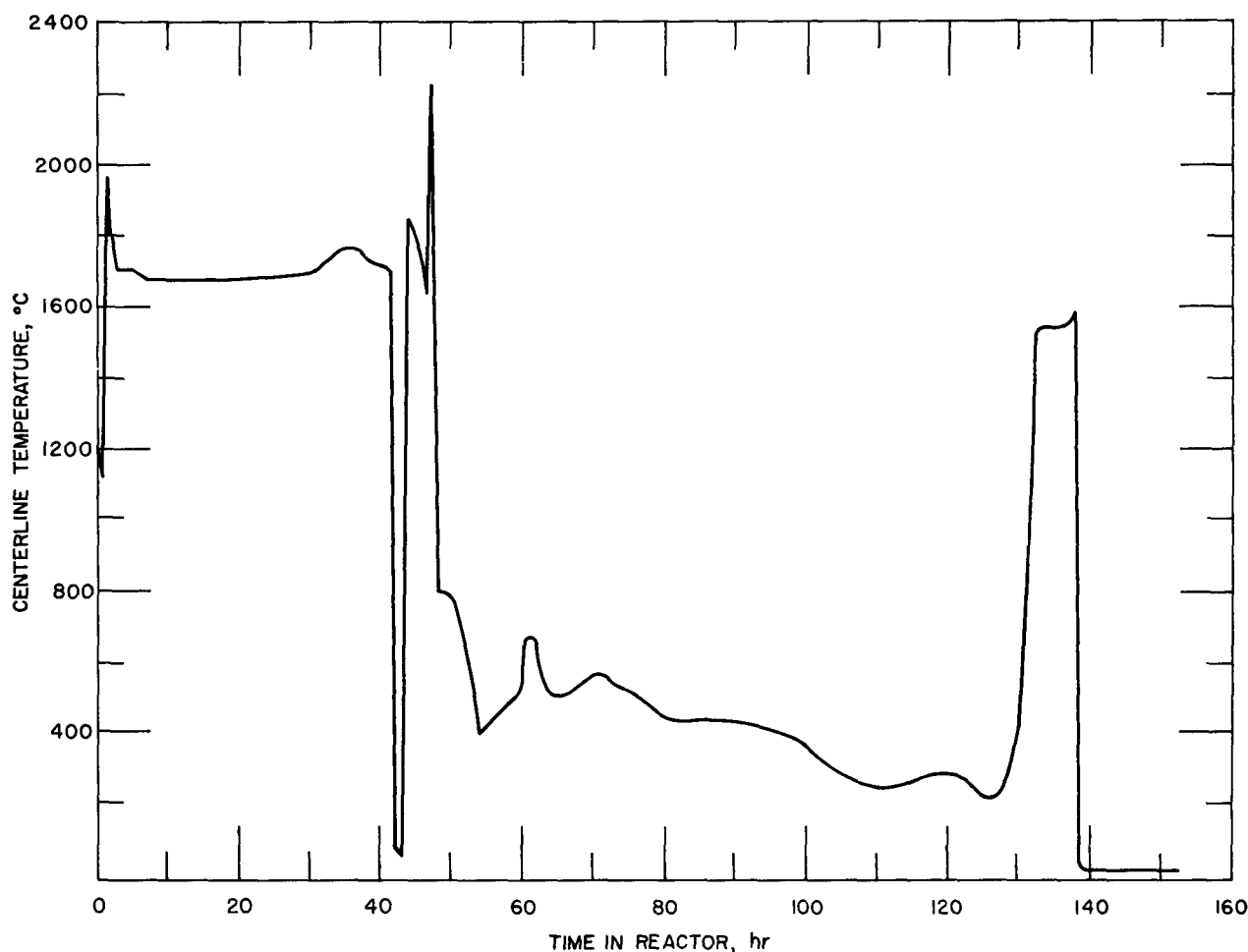


Fig. 2-9. Centerline temperatures of UO_2 fuel pellets as monitored by prototype thermocouple in CP-5 irradiation capsule HT-2

dropped rapidly to 800°C and from this value continued to decrease slowly and erratically to about 200°C. Throughout this period, the reactor power level had not been changed. Six hours prior to termination of the test, the capsule temperature increased suddenly to about 1540°C and remained essentially at this value until the reactor was shut down as scheduled.

Post-test examination of the capsule in a hot cell revealed that the fuel had cracked and disassembled. The tantalum spacer rods and thermocouple sheath had deteriorated badly, as if some reaction had occurred. The cause of the deterioration or the nature of the reaction, if any, will be investigated in out-of-pile tests. Accordingly, further in-pile tests will be held in abeyance, pending completion of this investigation.

In summary, the test objective was achieved: a lower centerline fuel temperature was obtained with the helium backfill. Also, useable signals were transmitted throughout the 6-day test. With reference to the terminal rise in temperature, it is theorized that at this point the thermocouple was actually monitoring the behavior of the cracked fuel.

2.4.2 In-Core Electromagnetic Flowmeter

This meter (Fig. 2-10) is one of three concepts originally developed for measuring sodium coolant flow through fuel subassemblies in the FARET core. Tests are underway to determine its impedance (without sodium) and signal noise levels in a helium atmosphere at temperatures up to 650°C. Concurrently, the flowmeter is being alternately thermal cycled and soaked to "cure" the magnets.

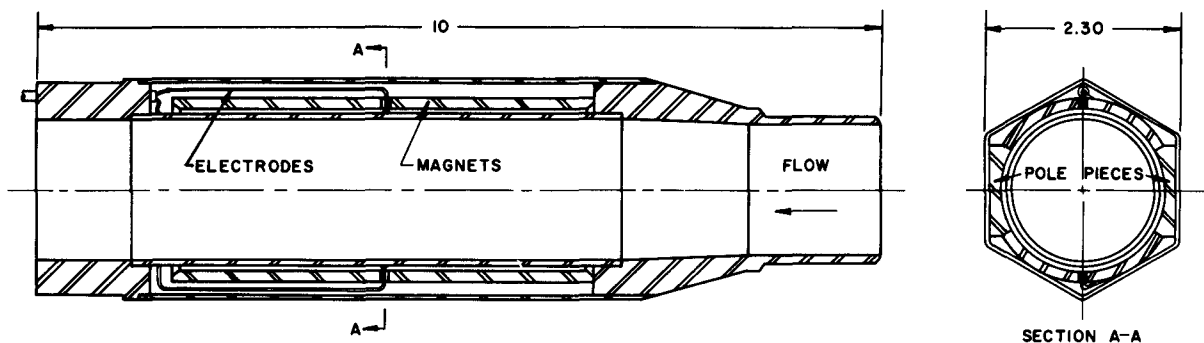


Fig. 2-10. Sectional views of electromagnetic flowmeter for measuring sodium coolant flow through a fuel subassembly. Materials of construction include Type 304 stainless steel body and electrodes, Alnico-VB magnets, and soft-iron poles

Figure 2-11 shows the time-temperature-magnetic flux history of the Alnico-VB magnets after four cycles up to 690°C and two 72-hr soaks at 650°C. Owing to thermocouple effects, no detectable emf is being generated, even with a 50°C-gradient across the meter at a mean temperature of 650°C. Most of the measured resistance is due to approximately 14 ft of

No. 24 AWG stainless steel wire leading to the readout instruments. The equivalent flowmeter resistance was calculated to be ~34 ohms at 23°C and ~40 ohms at 650°C.

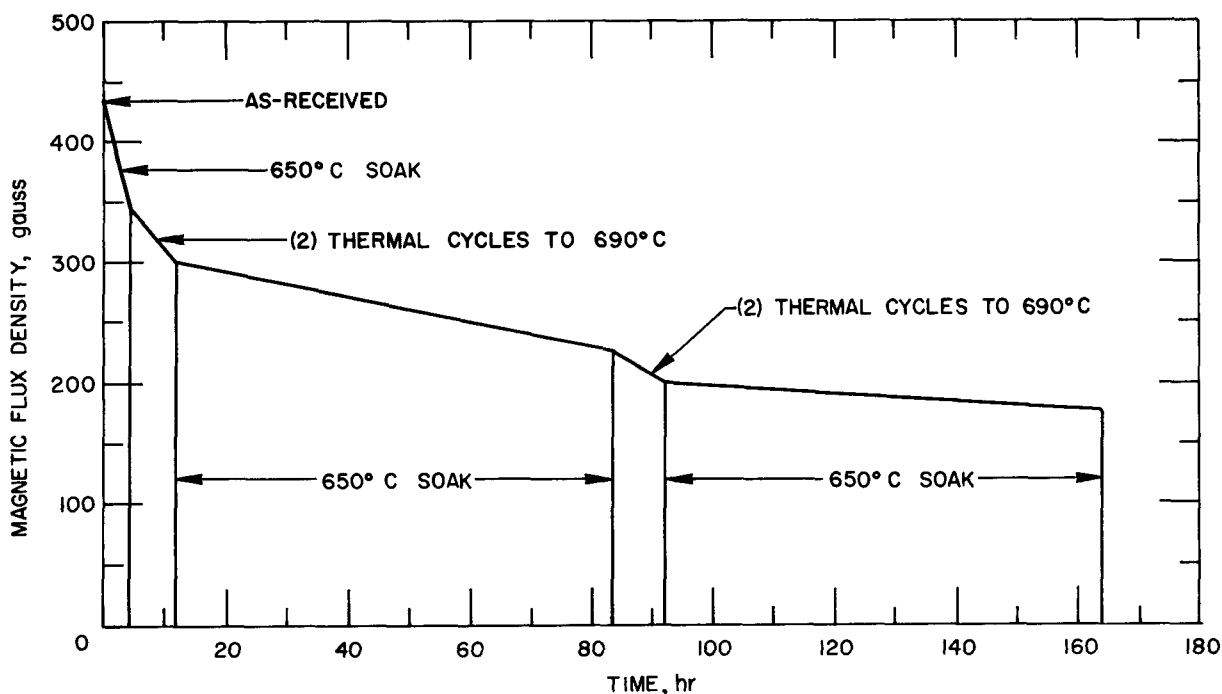


Fig. 2-11. Effect of thermal cycling and soaking in helium on magnetic flux density of Alnico-VB magnets in prototype electromagnetic flowmeter

REFERENCES

1. L. E. Link et al, *1000 MWe Metal-Fueled Fast Breeder Reactor Concept*, ANL-7001 (in press).
2. Reactor Development Program Progress Reports: ANL-7245 (July, 1966), p. 5, and ANL-7249 (August, 1966), p. 1.
3. L. J. Koch and M. R. Sims, *Reactor Engineering Division Annual Report, July 1, 1964 to June 30, 1965*, ANL-7190 (March, 1966), p. 59.
4. G. F. Popper and A. E. Knox, *FARET In-Core Instrument Development - Terminal Report*, ANL-7161 (June, 1966).
5. Pratt and Whitney Aircraft Co., *Investigation of Magnetohydrodynamic Power Generation*, Vol. IV: Materials, PWA-2125 (December, 1962).
6. L. N. Grossman, *Electrical Insulators and Spacers for Nuclear Thermionic Devices*, GEST-2022 (February 10, 1964).
7. S. M. Lang and R. F. Geller, *The Construction and Operation of Thoria Resistor-Type Furnaces*, J. Am. Ceram. Soc., 34, No. 7, 193-200 (July, 1951).
8. M. Foex and M. P. Lebeau, *Electrical Conductivity of Thoria at High Temperatures*, Compt. rend., 215, 534-536 (1942).

Section 3

✓ LIQUID METAL HEAT TRANSFER RESEARCH PROGRAM

3.1 Objectives

The overall objectives of this program are: (1) to acquire theoretical and experimental data on liquid metals during single- and two-phase flow, boiling, and condensation in forced convection systems; and (2) to use these data to derive new methods or to improve engineering computations traditionally employed in designing liquid metal heat transfer equipment or in predicting temperature gradients in reactor coolant channels.

3.2 Boiling Sodium Studies3.2.1 Objective

The specific objective of these studies is to obtain experimental information pertinent to the two-phase heat transfer and fluid flow behavior of alkali metals, particularly sodium at a temperature of 2100°F and a pressure of about 8 atm. Variables to be investigated include boiling heat flux and temperature difference up to the critical heat flux, boiling and adiabatic two-phase pressure losses, vapor volume fraction, and boiling stability parameters. Ultimately, the tests will be extended to include the transient behavior of flowing, two-phase sodium in response to various types of power excursions. Knowledge of the transient phenomena is vital to the safe operation of high-temperature-sodium-cooled fast breeder reactor systems.

The foregoing tests are to be conducted in the recently completed 2100°F Boiling Sodium Test Facility.

3.2.2 2100°F Boiling Sodium Test Facility

This facility was described in the FY 1965 Annual Report (ANL-7190, p. 159). Briefly, it comprises a loop fabricated from Nb-1% Zr tubing (0.500 in. O.D., 0.035 in. wall) and major components, all enclosed within a chamber that can be evacuated to a pressure of 10^{-7} to 10^{-8} Torr. The loop proper was constructed at CANEL to Argonne specifications. Major components installed at Argonne included a thermal radiation-treated boiler, an adiabatic riser section, a radiating coil condenser, and an electromagnetic, helical induction pump.

Upon its arrival from CANEL, the loop was wrapped with Nb-1% Zr ribbon for corrosion protection. Tantalum condenser shutters (to control heat loss) were positioned, and the assembly fastened to the loop support and balancing structure. This integrated assembly was then installed in

the vacuum chamber. Thermocouple and pressure transducer assemblies, and the pressurizing system were attached through ports in the chamber. Finally, after a period of chamber bakeout and operation at low vacuum, the loop was charged with sodium which had been circulated for several weeks in the 1300°F hot trap system.

The loop is undergoing shakedown and calibration at low sodium temperatures. Thus far, all major components and instrumentation have operated satisfactorily. Initial boiling tests will be conducted using the thermal-radiation-heated boiler. Developed at Argonne, the thermal radiation heater is capable of supplying heat fluxes up to 10^6 Btu/(hr)(ft²).

3.2.3 Advanced Heater Development

An electron bombardment heater (EBH) capable of generating heat fluxes well in excess of 10^6 Btu/(hr)(ft²) is being developed as an eventual replacement for the thermal radiation heater. To this end, several small-scale experiments have been conducted to gain experience with EBH operation and to identify the mechanical and geometric factors influential to successful design. The results of these tests were reported in ANL-7190.

The present design is being employed as a heat source in a sodium pool boiling experiment in conjunction with the Reactor Safety Program. With reference to the inset schematic in Fig. 3-1, the centrally located, 16-in.-long heater consists of a 0.030-in.-dia. wire cathode positioned inside a tubular anode. Both thoriated-tungsten and tungsten wires are being evaluated. The anode is fabricated from Type 316 stainless steel (1.05 in. O.D., 0.219 in. wall). Temperatures are monitored by chromel-alumel

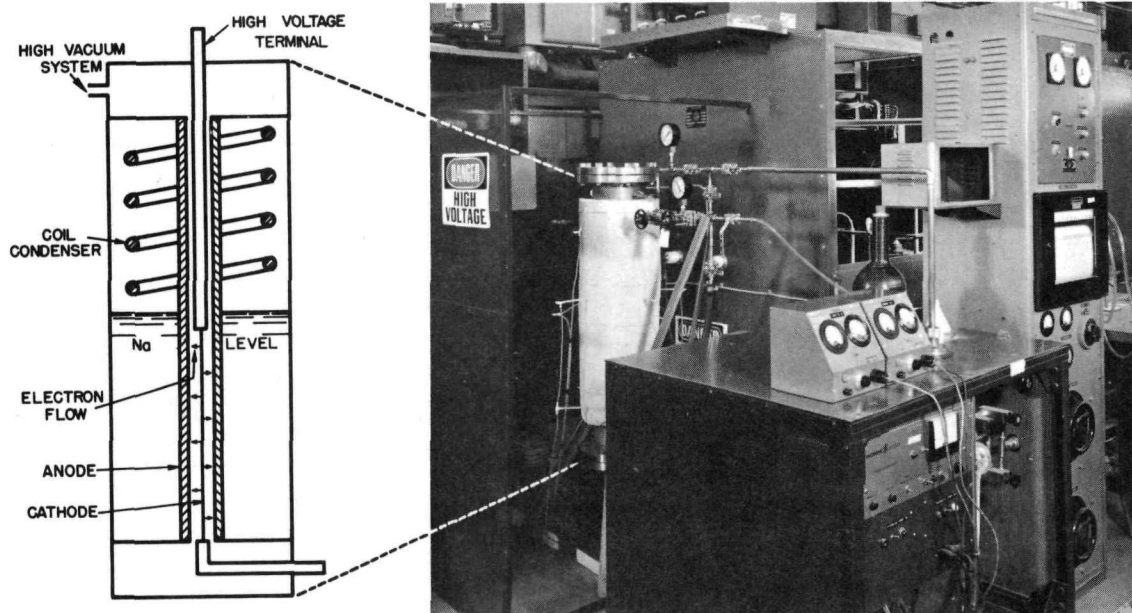


Fig. 3-1. Apparatus Used in Electron-bombardment-heated Sodium Pool Boiling Experiment. Also shown is a schematic of the EBH-boiler installation.

thermocouples attached to the tube wall. Heat is removed from the boiler by condensation of sodium vapor on cooling coils installed above the sodium level. The power supply is variable from 500 to 20,000 V, and is capable of delivering 200 kW at 10 A.

Over 500 hr of steady-state and transient testing have been accumulated. During this period, heat fluxes exceeding $300,000 \text{ Btu}/(\text{hr})(\text{ft}^2)$ have been supplied to the anode, with peak sodium temperatures up to 1350°F . This includes an emission current range to 3.55 A at a corresponding cathode-to-anode potential up to 7700 V.

Thus far, this series of tests has yielded information pertinent to cathode lifetime, as well as the effects of vacuum, anode voltage, and other factors upon cathode emission characteristics. Preliminary analysis indicates: (1) that either thoriated-tungsten or tungsten wires can be employed for experiments where heater lifetimes must exceed 1000 hr in vacuums ranging from 10^{-6} to 10^{-8} Torr; and (2) that pressure is the most important variable with respect to cathode lifetime. More stable emissions and longer cathode lifetimes (hundred of hours) have been experienced in the 10^{-4} to 10^{-6} Torr range than at pressures less than 10^{-4} Torr.

These tests will be continued in order to obtain information essential to completing the Argonne design or selecting one of two large (150 kW) EBH configurations recommended by a commercial vendor for use in the Nb-1% Zr loop. The latter designs - one a triode and the other a diode - were evolved from a study contract with EIMAC Corporation. Both designs were recommended consistent with the following criteria:

- (1) Maximum heat flux: $10^7 \text{ Btu}/(\text{hr})(\text{ft}^2)$.
- (2) Transient capability: heater shall be capable of increasing the heat flux two orders of magnitude within one second.
- (3) Geometry-Materials: heater shall supply electrons to a 5/16-in.-I.D., vertical, Nb-1% Zr tube.
- (4) Environment: heater shall operate in a vacuum range from 10^{-6} to 10^{-8} Torr at temperatures up to 2100°F .

An analysis of both heaters indicates the triode design would provide greater flexibility in controlling power transients; however, on the basis of dimensional stability and uniform heat flux, the diode design appears to be the leading candidate.

3.3 Evaluation of Traditional Liquid-Metal Heat Transfer Design Computations

3.3.1 Objectives and Methods of Approach

Traditional design computations involving turbulent forced convection heat transfer in ducts are based on two major assumptions. First, it is assumed that, for all practical purposes, heat transfer coefficients are independent of duct length, i.e., use of "fully developed" heat transfer coefficients is sufficient. Second, that these coefficients, when expressed as Nusselt or Stanton numbers, are functions of Prandtl and Reynolds numbers only. There is considerable experimental and theoretical justification for these assumptions when applied to turbulent flow of nonmetallic fluids. With liquid metals, however, these assumptions can result in design inaccuracies, depending on the application. For example, both assumptions are usually unjustified in the design of simple liquid metal-to-liquid metal heat exchangers.¹ One or both assumptions may be invalid for predicting temperatures in liquid metal-cooled reactor channels, depending, for example, on the heat flux distribution.¹

Evaluations of traditional design computations used for "sizing" and performance analysis of liquid-metal heat exchangers, and for predicting liquid-metal temperatures in reactor coolant channels are the main interests of the research summarized here. The research procedure consists of detailed mathematical analyses based on "first principles" rather than on use of heat transfer coefficients. Results of these analyses are then used to investigate the validity of the above-mentioned assumptions and their effect on the accuracy of predictions by traditional design relationships. When possible, experimental verification is sought. Attempts also are made to obtain "improved" prediction techniques when conventional ones are found too complex and/or inaccurate.

Of necessity, "first principles" are applied to relatively simple configurations; otherwise the required mathematical analyses become too complicated for definitive investigations. Thus far, only double-pipe heat exchangers and geometrically simple coolant channels are being investigated. Extensions to more complicated configurations, including shell-and-tube exchangers and actual reactor coolant channel geometries, are planned for the future.

3.3.2 Heat Transfer in Double-Pipe Heat Exchangers

A concise but relatively complete summary of accomplishments in this category of research, from inception through fiscal 1966, has been published.²

During fiscal 1966, the previous specialized mathematical analyses³ were generalized to include laminar or turbulent flows, various geometrical configurations, and both cocurrent and countercurrent operations. Practical aspects of these generalizations consisted mainly of unified definitions of the quantities η and ϕ which occur in suggested "improved" heat exchanger design expressions. The quantity ϕ , called the "effectiveness coefficient," multiplies the exponential terms in the familiar effectiveness vs. NTU-type of relations and, thereby, accounts for heat transfer coefficients not being independent of duct length. The quantity η is the ratio of the actual fully-developed overall heat transfer coefficient to the overall coefficient computed from fully developed heat transfer coefficients pertaining to the duct boundary condition of uniform heat flux; it accounts for the dependence of individual channel Nusselt numbers on the heat exchanger operating conditions, in addition to the usual Prandtl and Reynolds number dependence. Thus ϕ and η are in the nature of correction factors related to the two main assumptions upon which traditional heat exchanger design relations are based. When ϕ and η are both equal to unity, these relations apply in their simplest form.

Major effort was concentrated on the liquid metal-to-liquid metal, countercurrent, turbulent flow case, and included revisions of the mercury heat transfer loop for countercurrent flow experiments. The main objective of these experiments, which began in late fiscal 1966, is to determine values of ϕ and η for comparison with predictions of the mathematical analysis.

The most significant accomplishment of the analytical effort during FY 1966 was the discovery of an accurate computational procedure, based on first principles, for predicting overall heat transfer rates in countercurrent flow heat exchangers. Prior to this period, no satisfactory procedure was available because of the unusual mathematical aspects of countercurrent operation that are inherent in analyses based on other than fully-developed heat transfer coefficients.

In order to adjudge the value of the research to heat exchanger design, a series of exploratory computations were performed to predict the heat transfer areas required to achieve specified overall heat transfer rates. Comparisons were then made with areas predicted by traditional heat exchanger design relations based on fully-developed uniform flux heat transfer coefficients. There were significant differences between the respective predictions.

The extent of these differences is shown in Table 3-1. In this table, the specified overall transfer rates are expressed in terms of heat exchanger efficiency. This efficiency is defined as the ratio of the actual overall heat transfer rate of a specific exchanger to that of an exchanger

with infinite heat transfer area at the same operating conditions. These conditions, specified by the dimensionless parameters H , K , and K_w apply to a concentric tube heat exchanger with a narrow annulus.

TABLE 3-1. Percent Differences in Predicted Heat Transfer Areas

$H = 0.5; K = 0.05$			Specified Efficiency	$K = K_w = 0.05$		
$K_w = 0$	$K_w = 0.05$	$K_w = 0.1$		$H = 0.1$	$H = 0.5$	$H = 1$
170	64	58	0.5	-	64	32
105	56	43	0.6	635	56	24
78	49	34	0.7	243	49	16
65	42	28	0.8	169	42	9
52	35	26	0.9	146	35	2
47	32	18	0.95	137	32	0

The parameter H is the familiar heat capacity flow rate ratio and is defined by

$$H = C_2 W_2 / C_1 W_1 \quad (1)$$

where C is the fluid specific heat, W is the mass flow rate, and subscripts "1" and "2" refer to the tube and annulus side of the exchanger, respectively.

The parameter K is a relative thermal resistance for heat flow from within the fluid in the annulus and is defined by

$$K = (k_1 k_1^+ / k_2 k_2^+) (a_2 / a_1) \quad (2)$$

where a_2 is the width of the annulus, a_1 the inside radius of the tube, and k the fluid thermal conductivity. Heat transport by turbulent diffusion is accounted for by the dimensionless parameter k^+ . For the tube side

$$k_1^+ \approx 0.87 + 0.0031 \text{ Pe}_1^{0.8},$$

while for the narrow annulus

$$k_2^+ \approx 0.97 + 0.0033 \text{ Pe}_2^{0.8},$$

where Pe is the Peclet number.

The parameter K_w represents the relative thermal resistance of the tube wall and is defined by

$$K_w = (k_1 k_1^+ / k_w) (b / a_1), \quad (3)$$

where k_w is the thermal conductivity of the wall material and b the wall thickness.

Equations (2) and (3) require that $b \ll a_1$, a condition usually met in practice.

The values of H , K , K_w in Table 3-1 are representative of operating conditions for actual heat exchangers with narrow annuli. Under these conditions, the traditional heat exchanger design relations always predicted heat transfer areas that were larger than actually required to obtain the specified overall heat transfer rate. Consequently, except for cases with $H = 1$ and moderate to large heat exchanger efficiencies, use of these relations will result in costly, oversized heat exchangers.

For purposes of exchanger design, the newly discovered computational procedure is lengthy and requires the services of a large digital computer. On the other hand, the suggested "improved" traditional relations, which include the quantities ϕ and η , are much simpler to apply; however, they require that these quantities be known as a function of exchanger operating conditions. Accordingly, the analytical effort is also focussed on means of simplifying, as much as possible, their dependence on operating conditions. Table 3-2 lists typical values of ϕ and η as a function of H , K , and K_w . The effectiveness coefficient ϕ also depends on the heat exchanger efficiency (or, equivalently, the heat exchanger length),

TABLE 3-2. Quantities Related to the Turbulent Liquid-Metal Countercurrent Flow Double-Pipe Heat Exchanger

K	H	$K_w = 0$		$K_w = 0.05$		$K_w = 0.1$	
		$\phi(\infty)$	η	$\phi(\infty)$	η	$\phi(\infty)$	η
0.01	0.1	0.6	4.74	0.8	2.39	0.8	1.851
	0.5	0.78	1.468	0.85	1.229	0.88	1.160
	0.9	0.966	1.037	0.976	1.025	0.982	1.018
	1.1	0.971	0.971	0.979	0.979	0.985	0.985
	2.0	0.85	0.851	0.881	0.890	0.91	0.916
0.05	0.1	0.63	3.50	0.8	2.18	0.82	1.767
	0.5	0.792	1.318	0.856	1.206	0.892	1.147
	0.9	0.968	1.033	0.978	1.023	0.983	1.017
	1.1	0.973	0.974	0.981	0.981	0.986	0.986
	2.0	0.86	0.863	0.888	0.898	0.914	0.922
	10.0	0.7	0.770	0.79	0.823	0.83	0.861
0.10	0.1	0.67	2.76	0.8	1.990	0.827	1.678
	0.5	0.811	1.269	0.867	1.181	0.899	1.133
	0.9	0.971	1.029	0.979	1.021	0.984	1.016
	1.1	0.975	0.977	0.982	0.983	0.986	0.987
	2.0	0.86	0.878	0.894	0.908	0.918	0.929
	10.0	0.75	0.795	0.79	0.842	0.83	0.876

but for sufficiently large efficiencies the dependence is negligible. As a result, when the quantities ϕ and η in Table 3-2 are applied as correction factors, the traditional effectiveness vs. NTU-type of relationship can reproduce most of the values for $H < 1$ in Table 3-1.

3.3.3 Temperatures in Reactor Coolant Channels

Research in this category was relatively limited during fiscal 1966. During the latter part of this period, an analytical investigation of the importance of axial heat conduction in the coolant was begun. This mode of heat conduction is usually neglected in analytical and experimental studies of liquid metal, turbulent convection heat transfer as well as in design considerations. Justification for this assumption is based on studies which do not consider certain features of actual reactor coolant channels that may possibly exercise a greater influence on axial heat conduction. Two of these features - nonuniform heat flux distributions, and inlet and outlet flow configurations - are currently under investigation.

REFERENCES

1. R. P. Stein, *Liquid Metal Heat Transfer*, Advances in Heat Transfer (eds.) T. F. Irvine and J. P. Hartnett (New York: Academic Press, Inc., 1966), Vol. III, pp. 101-174.
2. R. P. Stein, *Mathematical and Practical Aspects of Heat Transfer in Double Pipe Heat Exchangers*, Proceedings of the Third International Heat Transfer Conference, Chicago, Ill., August 7-12, 1966, Vol. I, pp. 139-148.
3. L. J. Koch and M. R. Sims, *Reactor Engineering Division Annual Report, July 1, 1964 to June 30, 1965*, ANL-7190 (March 1966), p. 162.

Section 4

✓
MAGNETOHYDRODYNAMICS4.1 Liquid-Metal MHD Generators for Central Station and Space Power4.1.1 Objectives

The overall objective of these studies is to develop and evaluate the technical feasibility and performance potential of coupled reactor-liquid metal magnetohydrodynamic energy conversion cycles for commercial and space power applications.

There are several incentives for developing such "unconventional" binary power cycles. First, from a commercial viewpoint, effective further development of the steam cycle is rapidly nearing an end. Although relatively small gains in efficiency have been achieved by increasing steam pressure and temperature, they have not been very successful, economically. Second, conventional energy-conversion cycles cannot be used as auxiliary power sources for spacecraft because heat transfer and weight considerations dictate operation at a minimum sink temperature of $\sim 1400^{\circ}\text{F}$. Third, no conversion process exists today which can efficiently extract useful energy at temperatures above 1100°F . Finally, the need for developing unique cycles is particularly justified since continued advances in reactor, materials, and space technologies are likely to raise the temperature barriers on power systems.

One power system which holds promise features a liquid metal MHD generator coupled to a nuclear reactor heat source. The concept can be developed either as a compact power source for spacecraft or as a topping unit for a conventional steam plant which functions as the sink or bottoming cycle. In the latter case, extensive thermodynamic cycle analyses indicate that overall efficiencies of 50-55% can be achieved with a maximum operating temperature of 2000°F , as compared to $\sim 40\%$ at 1050°F for the best steam plant operating today (see ANL-7190, p. 167).

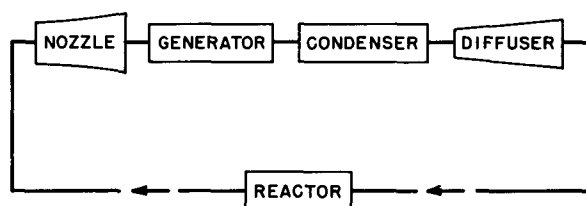
Experimentally, the initial objective is to establish the key component efficiencies, using scaled-down systems. An understanding of the loss mechanisms in model components is prerequisite to the design of large-scale counterparts.

Three investigations were completed during the reporting period. They relate to the performance of d-c conduction two-phase and film-flow generators, and to materials constraints on a-c induction generators. The results are summarized in the following sections.

4.1.2 D-C Conduction MHD Generator Operations with Two-Phase Liquid-Metal Flows

4.1.2.1 Generator Concepts

Figure 4-1 shows a highly simplified liquid-metal MHD power cycle which is based on the premise that MHD generators can operate with two-phase flows. In operation, the effluent from the heat source (reactor)



enters the nozzle where partial expansion occurs. The two-phase mixture then flows through the MHD generator where the expansion process is completed and power is extracted in a manner similar to the plasma cycle.

Fig. 4-1. Concept of two-phase liquid-metal MHD generator power cycle

Because the flow pattern of a two-phase mixture changes from a dispersion of gas in liquid to a dispersion of liquid in gas as the mixture quality is increased, the electrical conductivity of the fluid changes rapidly. In the low-quality regions, the two-phase mixture can be treated essentially as a homogeneous fluid. Data taken on an air-water system indicate that the electrical conductivity in the void fraction range $0 < \alpha < 0.9$ can be readily predicted by Maxwell's relationship:

$$\sigma/\sigma_{TP} = (2 + \alpha)/2(1 - \alpha) \quad (1)$$

Beyond this point, deviations occur and become increasingly larger until the ratio becomes infinite at a mixture quality of $x \sim 0.50$ ($\alpha = 0.9987$). The latter condition is indicative of total dispersion of the liquid phase in the gas phase. The data also indicate that beyond void fractions of 85-90%, where the liquid phase begins to disperse in the gas phase, electrical conduction is essentially through the liquid film on the wall. Therefore, a limited quality and void fraction range exists where it is feasible to pass the two-phase mixture directly through the generator without a radical drop in performance.

Accordingly, for the case of very high-void-fraction-liquid dispersed in a gas flow regime, a film-flow generator was conceived. In this concept (Fig. 4-2), the liquid-vapor effluent from a rectangular, high-aspect-ratio-nozzle impinges at a small angle ($\sim 15^\circ$) on the lower surface of the generator. Upon impingement, the liquid is separated from the vapor and a high-velocity film is formed. This film interacts with the magnetic field and builds up in thickness as electrical energy is extracted. Separation and power generation may occur simultaneously. By using a film flow generator, transitional kinetic head losses between separator

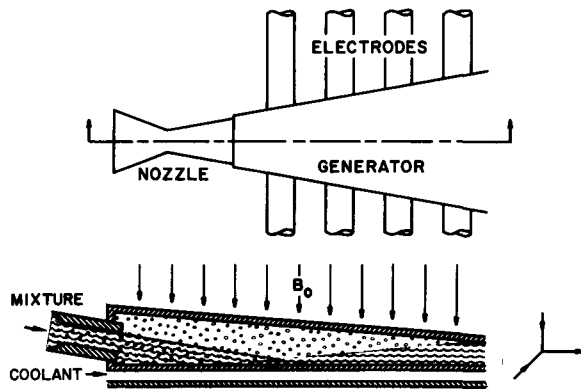


Fig. 4-2. Concept of film-flow MHD generator

and generator are eliminated. Also, end losses on the high-velocity side of the generator are removed since the fluid enters as a highly-dispersed mixture.

4.1.2.2 Test Models and Procedures

Lucite models of both generators were performance tested in a large NaK-N₂ loop shown schematically in Fig. 4-3. The magnet (16 in. dia.) is a low-impedance unit

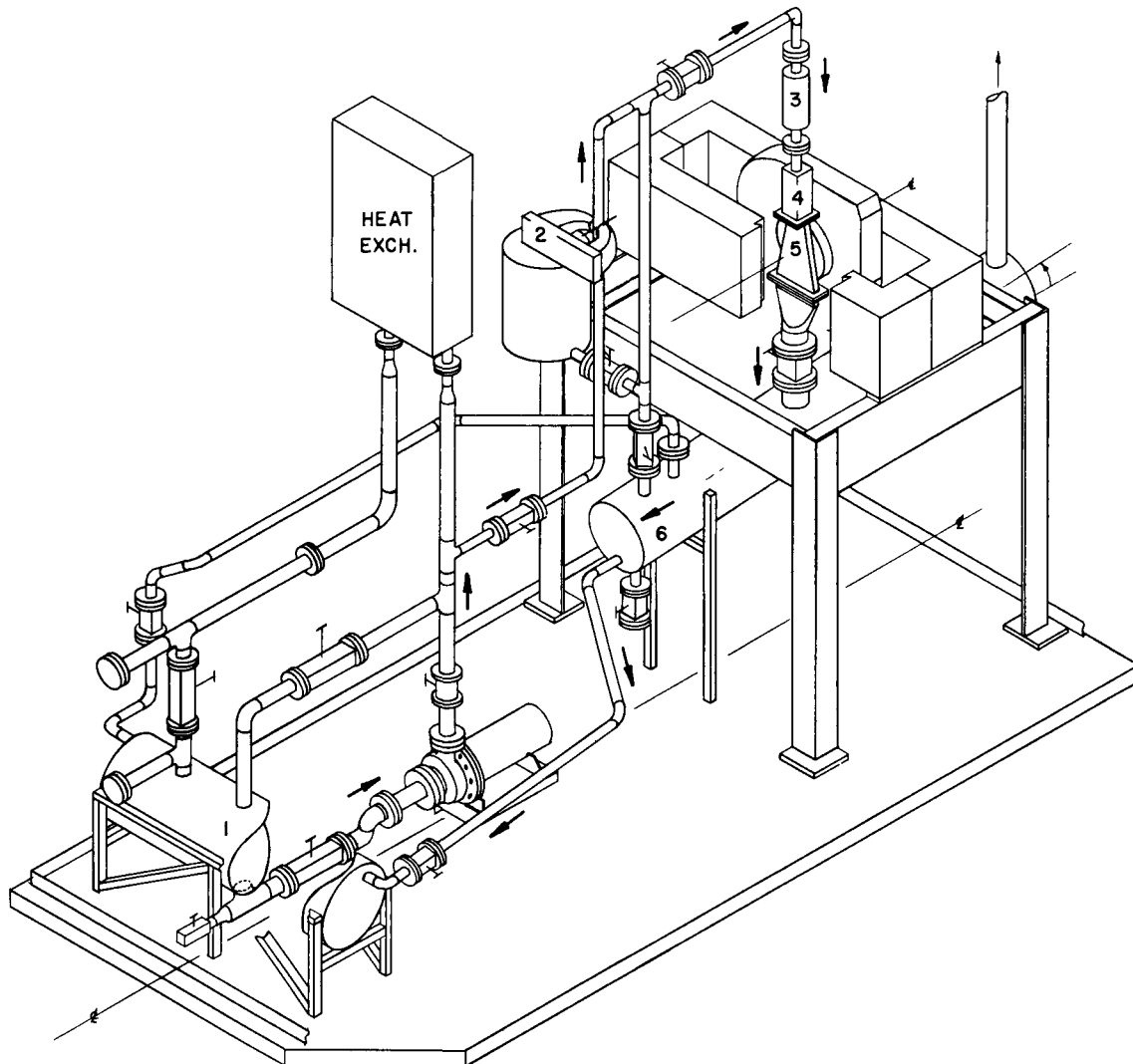


Fig. 4-3. NaK-N₂ loop used to evaluate performance of MHD generators. NaK is pumped from the supply tank (1) through the EM flowmeter (2) into the injector (3) where the NaK is mixed with dry N₂. The two-phase mixture flows through the nozzle (4) and generator (5) into the separation tank (6). At this point, the N₂ is exhausted to the atmosphere and the NaK flows back to the supply tank.

between magnet yokes and generator channel can be varied between 2 and 20 in. Intensity of the magnetic field is continuously adjustable from 500 to 17,000 gauss, with a nonhomogeneity of less than 0.5%.

The two-phase flow generator was of variable cross section design, with an aspect ratio (C = ratio of length to width) of 2.75, based on a log mean width of $a_m = 5.5$. Dimensionally, the inlet measured $3/8$ in. x 2 in. and the exit $3/8$ in. x $9\frac{1}{4}$ in.

With one exception (height = 1.625 in.), the dimensions of the film-flow generator were identical to those of the two-phase flow unit.

Performance data for both generators were taken over the following parameter ranges: mixture quality, $0 < x < 0.06$; liquid flowrate, $0 < W_l < 3.75$ lb/sec; and magnetic field intensity, $0 < B_0 < 12,000$ gauss. The maximum measured power achieved was 237 watts.

4.1.2.2 Results

Because of the limited parameter ranges covered, the data for both generators can be adjudged as preliminary. At most, the observations and trends in each instance are indicative of possible limitations in performance.

Figure 4-4 shows the efficiency of the two-phase flow generator as a function of magnetic field strength for various inlet mixture qualities.

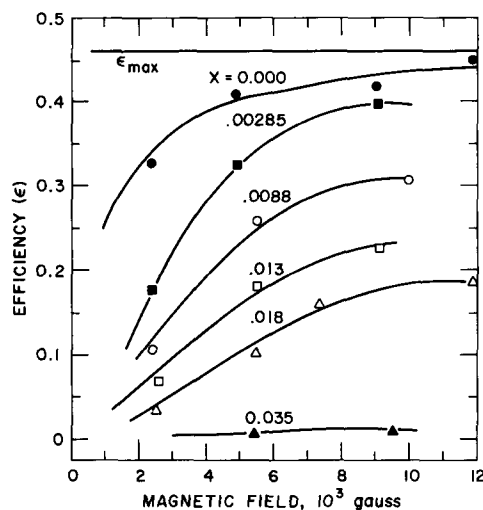


Fig. 4-4. Effect of mixture quality and magnetic field strength on efficiency of liquid-metal two-phase flow MHD generator. Uppermost curve is the theoretical maximum efficiency.

Also shown is the maximum theoretical efficiency, as given by the relationship

$$\epsilon_{\max} = \left\{ \left(1 + \frac{4 \ln 2}{C\pi} \right) + 2 \left[\left(\frac{2 \ln 2}{C\pi} \right) \left(1 + \frac{2 \ln 2}{C\pi} \right) \right]^{1/2} \right\}^{-1} \quad (2)$$

The theoretical upper limit is only a function of generator geometry. This is supported by the data for operation at zero quality, which approaches the theoretical limit as the field strength is increased. This trend reflects the reduced proportion of the total pressure drop that can be attributed to frictional losses. For a fixed flow-rate, as the field is increased, the ΔP across the generator increases whereas the frictional losses remain essentially constant.

However, as the mixture quality and void volume fraction are increased, the generator efficiency decreases gradually until a mixture quality of 0.02 is reached. Beyond this point, the power output and efficiency drop suddenly to zero. This sudden drop in performance can be viewed more realistically on a void fraction basis, since data taken on a

quality basis can be misleading in an extrapolation to other fluids and parameter ranges. Accordingly, the drop-off in efficiency occurred at void fractions greater than 0.85.

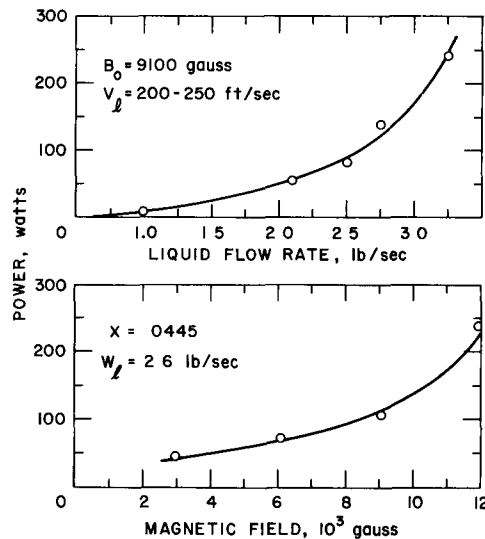


Fig. 4-5. Typical power trends of film-flow MHD generator as a function of liquid flowrate and magnetic field strength

With respect to the film-flow generator, Fig. 4-5 shows typical trends of power with liquid flowrate and magnetic field strength. These trends may be attributed to skin friction. For example, the data plotted in the upper curve were taken at a fixed magnetic field strength of 9100 gauss and in a liquid velocity range of 200-250 ft/sec. It can be shown analytically that the velocity loss is inversely proportional to the liquid flowrate for a specified drag force. Therefore, as the total liquid flow is reduced, the velocity and kinetic energy loss in the fluid film is increased. Similarly, for a fixed flow-

rate and quality, represented by the data in the lower curve, the relative effect of friction is reduced as the magnetic field strength is increased. The generator, in effect, becomes shorter. The data show promise of improved performance with a larger-scale generator.

4.1.3 Reduction of End Losses in MHD Channels

4.1.3.1 Nature of Problem

The presence of electric-conducting fluid upstream and downstream of the generator electrodes and applied magnetic field provides paths for flow of substantial leakage currents. In generator channels of low aspect ratio, these electrical end losses may reach alarming proportions and even preclude net power generation. The problem of accurate prediction and reduction of these losses is of particular significance when applied to liquid metal MHD generators.

A number of investigators have suggested insertion of insulating vanes at the extremities of the generator channel. They have shown analytically, for example, that installation of an infinitely long vane on the centerline of a parallel channel would double the effective aspect ratio.

Similarly three equally spaced, infinitely long vanes at each end of the channel would quadruple the effective aspect ratio. In each instance, the end losses would be reduced commensurable with the increased aspect ratio.

The effect of finite-length vanes is not so easy to assess; in particular, configurations involving vanes of varied lengths. Such configurations have potential applications in systems where fluid velocities are high enough to produce significant viscous losses.

4.1.3.2 Analog Approach

To gain some insight into the effectiveness of such vanes, an analog study was made with Teledeltos conducting paper. In principle, it consisted of measuring the resistance of the plane analog model of an MHD channel by applying a potential (~ 50 mV) across the electrodes and measuring the resulting current, which normally ranged about $100 \mu\text{A}$.

Two series of tests were made. The objective of the first series was to determine the finite length of centerline insulating vanes whose effect would be essentially identical to that of infinitely long vanes. The following conditions were chosen as a yardstick: (1) the shunt resistance (R_s) should differ no more than 5%; and (2) the potential between one electrode and any point in the field should differ no more than 2%.

After several tests with channels of various aspect ratios, it was concluded that both conditions were satisfied provided the vane length was equal to or greater than 3.5 times the channel width, this result being relatively independent of the aspect ratio.

The second series of tests were focussed on determining a vane configuration which would effectively reduce the electrical end losses without contributing to excessive viscous losses, even at relatively high fluid velocities.

Figure 4-6 shows a typical vane configuration installed in the downstream end of a constant-area generator. The lengths of the respective vanes are equal to $2.5h$ (centerline), $0.5h$ (intermediate), and $0.25h$ (short).

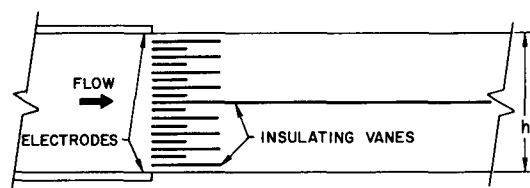


Fig. 4-6. Schematic of insulating-vane configuration in downstream end of constant-area MHD generator channel

A similar configuration would be installed in the upstream end.

4.1.3.3 Observations

When applied to a channel of aspect ratio $C = 2$, this configuration changes the ratio of internal resistance to shunt resistance (R_i/R_s) from 0.221

to 0.080, thereby increasing the effective aspect ratio to ~ 5.5 . Neglecting friction, the maximum theoretical efficiency is increased from 40.4 to about 56.8%. Applied to a channel of aspect ratio $C = 4$, this same configuration would reflect a decrease in R_i/R_s from 0.110 to 0.040, thus increasing the efficiency from 52.1 to 67%.

A similar installation of proportionally longer vanes in channels with aspect ratios of 2 and 4 increased the maximum theoretical efficiencies to 66 and 74%, respectively.

If it is assumed that the vanes are streamlined, so that no enlargement or contraction losses occur, and that pipe friction formulas apply, it may be shown that, in the presence of friction-losses, the efficiency of an MHD generator is

$$\epsilon_{\text{gen}} = \left[1 - \eta \left(1 + \frac{R_i}{R_s} \right) \right] / (1 - \eta) F \quad (3)$$

where η is the generator loading and the friction parameter $F = k\rho fU / \sigma W_0 B_0^2$. Here, ρ is the density, f the Moody friction coefficient, and k a numerical factor which accounts for area contraction, length of vanes, etc., and is usually of order 10. For a liquid metal generator with $U = 20$ m/sec and $B_0 = 30,000$ gauss, a typical value of F would be about 0.03. The variation of maximum theoretical efficiency with channel aspect ratio for several values of F is shown by the dotted lines in Fig. 4-7. It is clear that the effect of friction, while relatively unimportant for high B_0 -low U generators, becomes critical for generators with high fluid velocities. In the latter case, a gain due to introduction of insulating vanes may be easily offset by an increase in friction loss.

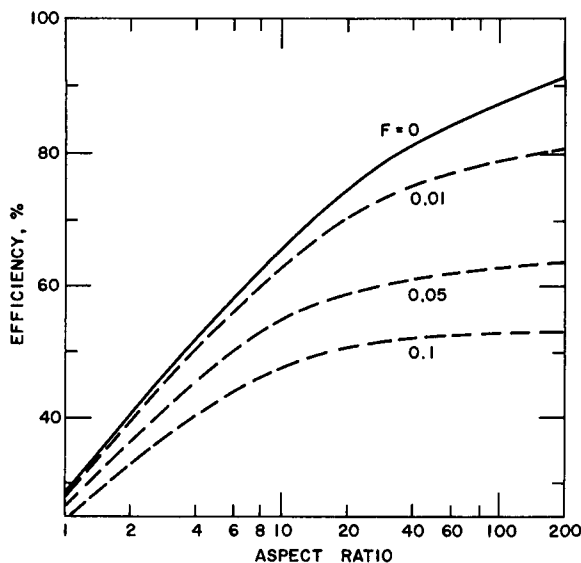


Fig. 4-7
Variation of maximum theoretical generator efficiency with aspect ratio and friction parameter (F)

4.1.4 Materials Constraints on A-C Induction MHD Generators

4.1.4.1 Background

An MHD induction machine consists of a channel containing a flowing, electric-conducting fluid and a set of exciter windings which produce a traveling magnetic field. Currents are induced in the fluid by relative motion between the field and fluid. In the case of liquid metals, the high electrical conductivity of the liquid phase yields a magnetic Reynolds Number sufficient for direct generation of alternating current.

The force of electrical origin is always in a direction such that the fluid tends to travel at the same velocity as the field. The slip velocity (s) is defined as the difference between the field velocity (v_s) and the fluid velocity (v) normalized with respect to v_s . If v is greater than v_s , the force opposes the motion and the machine is a generator, converting mechanical energy to electrical energy. However, if there is to be an appreciable energy transfer relative to the stored magnetic energy, as is required for high efficiency, the induced magnetic field, due to the fluid currents, must be comparable to the applied magnetic field.

Previous studies on the potential of MHD induction machines for a-c generation have indicated that (1) there should be no material between the conducting fluid and magnet which will decrease the magnetic flux density in the fluid; and (2) the magnet characteristics must include high permeability, high saturation flux density, and low loss.

All of the configurations considered thus far have required (1) a channel to contain liquid metal at temperatures ($>1000^\circ\text{F}$) envisioned for central station application or for smaller, space vehicle power systems; and (2) thermal insulation to restrict heat loss from the fluid and to keep the magnet temperature sufficiently below the Curie point.

Accordingly, an analytical study was undertaken to determine the probable materials constraints on the efficiency of the a-c induction generator. A detailed description of the study has been prepared for publication as ANL-7148.¹

4.1.4.2 Analytical Approach and Results

Briefly, the approach used was to establish trends from the approximate slit channel solution of the problem, and then obtain numerical results from the exact solution.

Figure 4-8 shows typical results for a generator constructed of refractory material (conductivity = $\sim 2 \times 10^6$ mhos/meter and operating with potassium at 1600°F . The parameters displayed are defined as follows:

R_{Mf} = magnetic Reynolds Number based on fluid velocity

R_{Mw} = magnetic Reynolds Number in the wall

α = ratio of channel width to excitation wavelength

α_i = insulation thickness

α_w = wall thickness

κ = ratio of fluid to magnet permeability

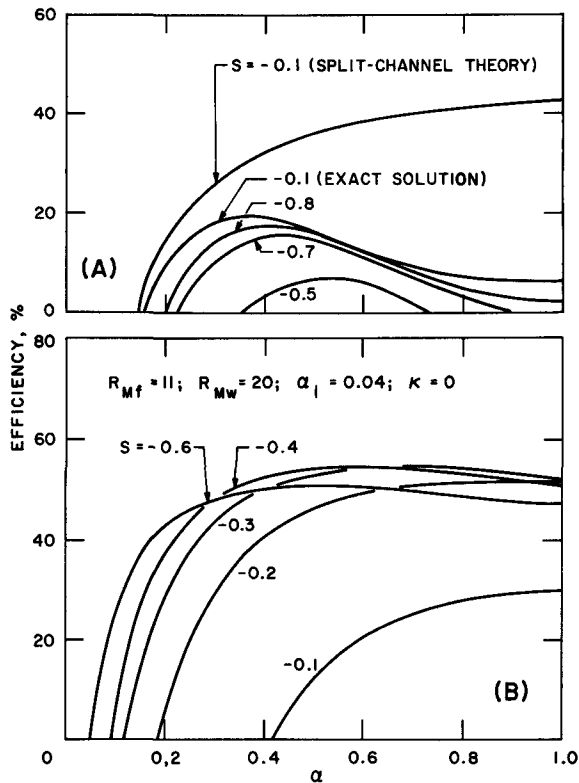


Fig. 4-8. Generator efficiency vs. α as a function of slip velocity (s) for refractory metal channel wall thickness of (A) 1/2 in. and (B) 1/8 in.

As can be seen, the efficiency for a given slip velocity (s) goes through a peak. This is in contrast with slit-channel theory, which predicts a steady rise and eventual leveling off at $1/1-s$ when the fluid completely dominates. In Fig. 4-8(A), the exact and slit-channel solutions for $s = 1.0$, for which case there is never a good correspondence, show the difference.

The peak is due to the interaction between the excitations on the two sides of the fluid. For moderate or large values of α , the power loss in the walls is essentially independent of α . However, as α increases, the field in the fluid drops off rapidly and the power density drops off faster than the volume increases. Initial increase in the fluid volume causes the performance to improve, but the eventual decrease in the fluid power density results in the drop in efficiency.

The efficiency curves cross for different sets of parameters. This does not mean that a degeneracy occurs, but only that the ratio of output power to input power is the same for both parameter sets, and that the slit-channel solution is no longer valid.

For $\alpha_w = 0.08$ (a 1/2-in. wall), the maximum generator efficiency of about 20% is not acceptable. It has improved to about 55% for $\alpha_w = 0.02$ (a 1/8-in. wall), but this is still too low since viscous and other losses are not included. Efficiencies calculated for a 1/16-in. coating ($\alpha_w = 0.01$) peaked at about 66% for $\alpha = 0.6$, $s = -0.3$, which is still too low, especially since the viscous velocity profile will decrease the efficiency. Finally, a 1/64-in. coating gave an efficiency of 76% at $\alpha = 0.3$, $s = -0.1$.

In summary, structural considerations have shown that a refractory metal channel at least $1/4$ -in. thick is required to contain the pressure of the liquid metal and to provide protection against corrosion and erosion. However, as evidenced by Fig. 4-8, a wall thickness less than $1/64$ in. is required in order to achieve an acceptable generator efficiency. These two conflicting requirements must be reconciled since successful resolution of the wall problem is essential to the ultimate success of the MHD induction generator.

The answer entails several avenues of research and development. These include development of suitable nonconducting wall materials, or methods of applying refractory metal coatings a few mills thick on an insulator which will transmit the stress to the field structure. Another possibility is to use a laminated wall of alternate sheets of refractory metal and insulation. In addition, a design study should be performed on an MHD induction generator coupled to a complete liquid metal power cycle. This study would include further investigation of wall construction, design of a field structure, and associated cooling at a temperature determined by system and materials consideration. Finally, an experimental program should be conducted concurrently, using small-scale MHD induction generators, to verify the theoretical analysis. In most cases, the models analyzed are crude approximations to the parent machine; hence, it is not known how well the predictions will correlate with actual performance.

REFERENCE

1. E. S. Pierson and W. D. Jackson, *Channel Wall Limitations in the MHD Induction Generator*, ANL-7148 (to be published).

Section 5

✓ FAST REACTOR SAFETY RESEARCH AND DEVELOPMENT5.1 Coolant Dynamics5.1.1 Analytical Model for Predicting Incipient Boiling Superheats in Liquid Metals

One objective of the fast reactor safety program is to develop analytical models and techniques for accurately predicting system dynamics during various hypothetical reactor accidents. Knowledge of the degree of liquid superheat required to initiate boiling is of particular importance in the safety analysis of liquid metal-cooled reactor concepts. Because of insufficient information, current methods of analyses usually assume zero liquid superheat.

Recent experiments performed elsewhere have shown that superheats ranging up to 700°F may be required to promote boiling in liquid metal systems. Some of the variables generally accepted as pertinent to the onset of boiling are: (1) thermophysical properties of the fluid; (2) surface conditions, i.e., roughness and cleanliness; (3) heat flux; (4) gas phase in the liquid; (5) system pressure; and (6) pressure-temperature history of the boiling surface. In any given liquid metal system, however, once the working fluid, materials (surface conditions) and cover gas (if any) have been determined, and the system operating conditions have been established, the remaining significant factor to be explored is the pressure-temperature history of the boiling surface.

Accordingly, an analytical model has been developed which utilizes this history to predict the superheat required to promote boiling in a liquid metal system. A detailed description of the analytical procedure and illustrative examples of its application have been prepared for publication as ANL-7184.¹

Briefly, the model examines the various conditions of wetting and nonwetting of surfaces, possibilities of entrapped gases, etc., and then correlates this information with the pressure-temperature history to determine the bubble radius at incipient boiling. This radius is then used in conjunction with the bubble equilibrium equation to calculate the degree of superheat required.

Model predictions of superheats for incipient boiling of sodium and potassium were found in good agreement with the sparse amount of experimental data reported in the literature. For example, Fig. 5-1(A) and (B) shows a comparison between predicted values and data due to Lewis² and Edwards and Hoffman.³ In both figures, the calculated curves for P_ℓ (subcooled) are the maximum system pressures used in the model.

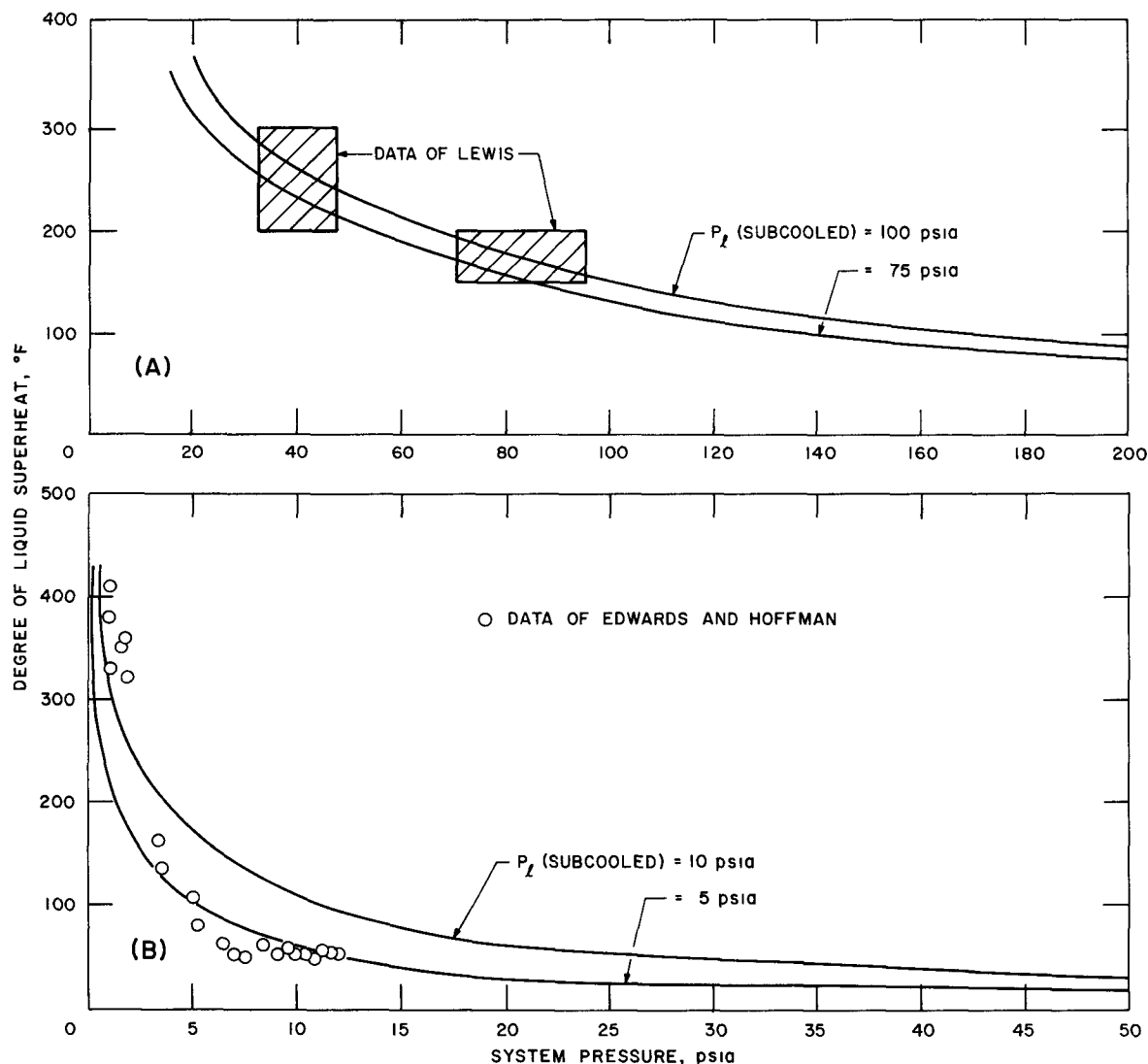


Fig. 5-1. Comparisons of model superheat predictions with experimental data

In summary, the good agreement between model predictions and available experimental data lends support to the contention that relatively high liquid superheats may be required for bubble nucleation in reactors cooled by either sodium or potassium. The model also shows that increasing the system pressure, while the liquid is subcooled, will reflect a corresponding increase in the degree of superheat required.

A series of tests are planned wherein parameters will be systematically varied to determine, quantitatively, their independent and combined effects on the liquid-metal superheat required to initiate boiling in simulated fast reactor environments. In addition to the pressure-time history, these parameters will include pressure, dissolved gas content, heat flux, and surface characteristics. An experimental facility for this test program has been designed and is under construction.

5.1.2 Sodium Expulsion Studies

During an accidental rapid power excursion in a fast reactor, the temperature of the fuel and cladding will increase rapidly, possibly causing boiling, generation of pressure, coolant expulsion, and, ultimately core meltdown. It is vital to the safety of fast reactors to know under what conditions these untoward effects occur and, when they do occur, what is their magnitude and significance.

To these ends, exploratory tests have been conducted with water, methanol, acetone, and ethylene bromide, to refine experimental techniques and to observe the physical response of the working fluid. In addition, an experiment has been designed to conduct similar tests with sodium.

The facility used for the nonmetallic fluid tests was described in ANL-7190.⁴ In operation, the test fluid was contained in a simulated coolant annulus formed by (1) an inner tube (fuel pin) of Type 304 stainless steel, which was heated rapidly (power transient) by the sudden discharge of storage batteries; and (2) an outer quartz pipe, to facilitate high-speed camera recording of the ensuing dynamics. The inside diameter of the annulus was 19 mm, the annular gaps used were 3.2 and 1.3 mm, and the heated length was 254 mm. Power inputs ranged from 2.5 to 13.7 kW, corresponding to volumetric energy generation rates of 2.5 to 13.7 kcal/(sec)(cm³) or 162 to 891 Btu/(sec)(in.³). Other variables included initial liquid temperatures from 20°C to saturation, inlet velocities from zero to 10 m/sec, and liquid column heights from zero to 2 m above the top of the heated length.

On the basis of the test data and film recordings, the following sequence of events was deduced: as heat energy is rapidly generated in the test section (simulated fuel pin), the surface temperature exceeds the boiling point of the adjacent fluid. Vapor bubbles are suddenly formed, causing a pressure pulse; this pulse is relieved by motion of the liquid away from the heated source. If the liquid is near its saturation temperature, the magnitude of the consequent pressure pulse is sufficient to completely expel the liquid from the annulus. If significantly subcooled, the liquid again is expelled; however, before a displacement of several centimeters occurs, the vapor recondenses, creates a partial vacuum, and pulls back the liquid, which contacts the hot surface and revaporizes. This cycle is repeated up to 15 or 20 times (depending upon system parameters), with a frequency of 40 to 100 cps, and terminates when the heated surface is cooled below the boiling temperature of the liquid.

A systematic study of parameters which affect the initial and secondary pressure pulses was made and the following preliminary conclusions were reached:

(1) As the initial liquid temperature is increased, the initial pressure pulses increase monotonically, while the larger secondary pulses at first increase, then decrease, finally not appearing for nearly saturated liquid.

(2) As the energy generation rate is increased, the pressures all increase monotonically.

(3) As the height of the liquid column is increased, the initial pressure pulses at first increase, then decrease slightly.

(4) As the annular gap is decreased, the pressure pulses increase.

(5) As the liquid velocity is increased, the pressure pulses change insignificantly.

(6) The magnitude of the initial pressure pulse increases with increased liquid density and decreased latent heat of vaporization.

An analytical model, devised in advance of the water tests, hypothesized pressure generation and expulsion by sudden thermal expansions. As a result of the tests, the model is being modified to include the effects of vaporization and condensation.

Similar parameters as were studied in the water tests will be evaluated in the sodium test facility. If necessary, the analytical model will be modified to include any new phenomena that are observed.

5.1.3 A Technique to Study Sodium-Air Reactions

The unique assembly shown in Fig. 5-2 is an outgrowth of the FARET Project. It was developed to determine if ejections of small quantities of sodium into a scaled-down air cell would provide reaction data which could be extrapolated to the FARET containment cell.⁵ This assembly marked the first phase of an effort to show that the design pressure of the containment cell would not (or would) be exceeded in the event of a sodium-air reaction following a maximum credible accident. The contention was that if small-scale experiments were successful in defining the physical nature of the reaction then larger, more costly, and more time-consuming experiments could be avoided.

The assembly illustrated employs a 0.38-caliber Teflon pellet fired from a revolver to effect ejection of ~2 gm sodium into a scaled-down Lucite air cell. Prior to ejection, the sodium is contained in a stainless steel capsule (1) which is open at the top and rests on an impact diaphragm of spring steel (2) inside the capsule barrel (3). The sodium is blanketed with argon (4) and can be heated to temperatures up to 1200°F by an external heater (5) which surrounds the barrel. An aluminum foil (6) seals the sodium atmosphere from the air cell (7) above the barrel.

The details of the sodium-air experiments are described in ANL-7120,⁶ and a film record (ANL-MP-730-11) is available upon request from the Argonne Film Library. The most significant observation made in these tests was that, for a given sodium-oxygen ratio, the peak pressure recorded was a function of the height-to-diameter ratio of the air cell.

Subsequent tests are in the planning stage. In these tests, the significant factors, e.g., air cell geometry, sodium temperature and velocity, etc., affecting peak pressure would be determined statistically, and their respective influences quantified.

5.1.4 Analytical-Experimental Studies of Critical Flow of Steam-Water Mixtures, Sodium, and Water

5.1.4.1 Objectives

Although analysis of postaccident behavior of a reactor requires a thorough understanding of void distributions in the coolant (which relates closely to the expulsion velocity), no data exist for critical velocities of liquid metals, and very little detailed information is available for steam-water mixtures. However, calculations reveal that critical flow might occur in the core, leading to voidage of the coolant channel, shock phenomena, and pressure buildup. Because shocks will cause subsonic velocities, the critical velocity or maximum critical flowrate will set the expulsion velocity.

Accordingly, the objectives of these combined studies are (1) to experimentally investigate the critical flow and velocity of sound through steam-water mixtures, sodium, and water, by measuring the critical flowrates, pressure profiles, and void distributions in simulated reactor coolant channels; and (2) to use these data to develop analytical techniques that can predict critical velocities, metastability, superheat, velocity ratios, and flow patterns in high-velocity, two-phase flows of the fluids of interest.

5.1.4.2 Experimental

Two experiments were initiated during the fiscal reporting period: (1) fluid behavior of critical steam-water mixtures in constant-area ducts; and (2) critical flow of sodium and water.

Steam-Water Mixtures. This series of tests involves detailed investigation of fluid behavior at the point of choking. It includes measurements of critical flowrate, critical pressure, quality, velocity ratio and metastability, axial pressure, and void profile. These measurements are made mainly in the low-quality region, i.e., voids of 0-95%, and at low pressures (15-400 psia).

The experimental facility has been constructed, circular (I.D. = 0.312 in.; L = 36 in.) and rectangular (1/8 x 1 x 36 in.) test sections have been installed, and several runs have been made in the quality range 0.1-10%. Measurements of critical flowrate, axial pressure profile, and void fraction at the point of choking are being analyzed.

Preliminary findings are: (1) that the test section geometry has no significant effect on the critical flowrate; (2) that the variation of critical flowrate with quality does not exhibit a maximum, as predicted by some available analytical models; (3) that the assumption of thermal equilibrium in the low-quality region is erroneous; and (4) that the velocity ratio at the point of choking is considerably less than predicted. These experiments are expected to be completed in early fiscal 1967.

Sodium vs. Water. These experiments are designed to identify any differences between critical flow of sodium and of water. They involve identical but independent loop tests with a number of long and short tubular ducts (I.D. = 1/16 in., 1/8 in.; L/D = 10-40), and fluid pressures in the range 1-15 psia. Overall measurements will be made of total flow, critical pressure, and stagnation properties.

The subatmospheric water loop has been assembled and is undergoing shakedown tests. Fabrication of the boiler, blowdown, and test sections for the sodium loop is scheduled for completion by early fiscal 1967.

5.1.4.3 Analytical

Analyses of the dynamic behavior of two-phase, one-component droplet flow, including critical flow and the velocity of sound, were completed.⁷ The results are summarized below.

Critical Flow. Based on the assumption of one-dimensional droplet flow, the equations of continuity and momentum for a differential element at the point of choking are:

$$\frac{\partial}{\partial y} (\bar{\rho}_g u_g + \bar{\rho}_l u_l) = 0 \quad (1)$$

$$\frac{\partial}{\partial y} (\bar{\rho}_g u_g^2 + \bar{\rho}_l u_l^2) + \frac{\partial P}{\partial y} = 0 \quad (2)$$

where

$\bar{\rho}_g$ = concentration of gas phase per unit volume of the mixture

$\bar{\rho}_l$ = concentration of liquid phase per unit volume of the mixture

u_g = average gas velocity

u_l = average liquid velocity

P = pressure

y = length of differential element

Consideration of relaxation phenomena that result from temperature and velocity lags between the phases in the approach region to critical flow leads to the following conditions:

$$\frac{\partial}{\partial P} \left(\frac{\bar{\rho}_l}{\rho_l} \right) = 0; \quad \frac{\partial}{\partial P} \left(\frac{\bar{\rho}_g}{\rho_g} \right) = 0; \quad \frac{\partial x}{\partial P} = 0; \quad \frac{\partial \rho_g}{\partial P} = \frac{\rho_g}{KP}$$

where

ρ_l = density of liquid phase

ρ_g = density of gas phase

x = quality (ratio of gas weight to total weight of mixture flowing)

K = isentropic coefficient for gas ($K = 1.32$ for water vapor)

Combining Eqs. (1) and (2) with the above conditions results in a solution for the critical flowrate, G :

$$G^2 = \frac{KP\bar{\rho}_g}{x^2} \quad (3)$$

At low pressures and high qualities, $\rho_g \approx \bar{\rho}_g$. In these cases, no information is required about the slip between the liquid and vapor phase, and Eq. (3) can be readily evaluated.

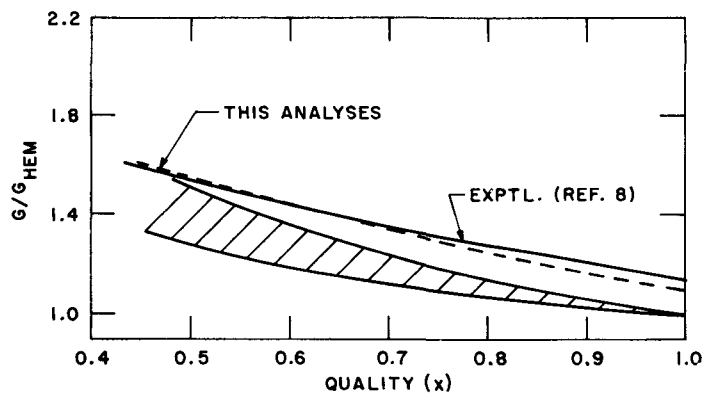


Fig. 5-3. Comparison between calculated and experimental critical flowrates for steam-water mixtures at 40 psia. Shaded band represents earlier model predictions.

As evidenced by Fig. 5-3, the calculated critical flowrates for steam-water mixtures are in excellent agreement with data taken in the high-quality region (dispersed flow).⁸ Also shown is the range of values predicted from previous models.⁸⁻¹³

With reference to the ordinate label, G_{HEM} is the homogeneous thermal equilibrium model critical flowrate.

Further comparison between values calculated from Eq. (3) and the most recent data available in the literature¹³ indicates that the theory is capable of predicting measured values to within $\pm 6\%$.

Velocity of Sound. A one-dimensional propagation velocity model was formulated on the assumption that the flow pattern is a homogeneous mist flow, initially at zero velocity. In the dispersed flow regime (high quality), the effect of mass transfer is negligible, and the momentum equation across the wave may be written:

$$dP = (\bar{\rho}_\ell du_\ell + \bar{\rho}_g du_g) a \quad (4)$$

where

a = pressure propagation velocity in the mixture

Furthermore, with the assumptions that the liquid phase is incompressible and the volume fraction occupied by the liquid droplets is negligible ($\bar{\rho}_g = \rho_g$), the continuity equation for the gas phase on both sides of the wave front takes the form:

$$\rho_g du_g = a d\rho_g \quad (5)$$

Equations (4) and (5) lead to the following general expression for the sonic velocity in a two-phase, one-component droplet mixture:

$$a^2 = \rho_g / \left[\frac{d\rho_g}{dP} \left(\bar{\rho}_g + \bar{\rho}_\ell \frac{du_\ell}{du_g} \right) \right] \quad (6)$$

Two extreme cases were investigated: (1) a system wherein disturbances occur in much shorter times than the relaxation times of the mixture (high frequencies), i.e., no heat and momentum transfer between the phases, resulting in

$$a_{NE}^2 = \frac{KP}{\bar{\rho}_g} \quad (7)$$

and (2) a system which remains in equilibrium throughout the disturbance (low frequencies), resulting in

$$a_{TDE}^2 = P / \left[\left(1 - \frac{P}{h_{fg} \rho_g} \right) (\bar{\rho}_g + \bar{\rho}_\ell) \right] \quad (8)$$

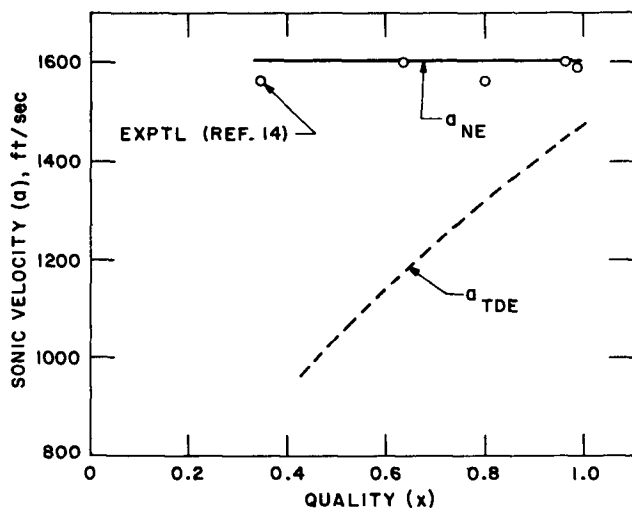


Fig. 5-4. Comparison between calculated and experimental values for velocity of sound in steam-water mixtures at 45 psia

The solutions for both cases are plotted in Fig. 5-4. For high vapor fraction by weight, Case (1) gives calculated propagation velocities independent of the mixture quality and equal to the velocity of sound in saturated vapor. This is in good agreement with an experimental study using small wave-growth times.¹⁴ On the other hand, Case (2) indicates that the moisture content can affect greatly the propagation velocity. In this case, the velocity decreases with decreasing mixture quality, resulting in considerably lower values than the propagation velocity obtained for the all-vapor case.

If the accepted explanation of single-phase flow choking is adopted, i.e., that the critical velocity is equivalent to the sonic velocity of the medium, it is easily shown that the sonic velocity obtained from Eq. (7) results in an expression for the critical flowrate which is identical to Eq. (3). This leads to the important conclusion that the two-phase critical flow phenomenon is associated with the velocity of sound as obtained when the two-phase mixture is subjected to a high-frequency disturbance.

A preliminary analytical investigation of the speed of sound in low-quality mixtures also was completed. Simplified models were formulated to show the effect of metastability and slip on the speed of sound. The results appear to bracket and predict the trends of available data in the literature.

However, an examination of the literature reveals that for low-quality, one-component mixtures, only the propagation velocity of compression waves has been investigated, no information exists for rarefaction waves. The latter appears more important in interpreting the critical flow phenomenon. Furthermore, thermodynamic considerations indicate that the speed of propagation of the two types of waves in one-component mixtures may be quite different, particularly in the low-frequency range. Accordingly, an experimental program will be implemented in late fiscal 1967 to obtain sufficient data to check the model predictions.

5.2 Reactor Control and Stability

5.2.1 A Single Fixed-Position Detector System for Continuously Monitoring Ten Decades of Neutron Flux

5.2.1.1 Problems of Conventional Systems

The requirement to continuously monitor the entire range of neutron flux in power reactors has long been recognized by control engineers to be a difficult task; particularly in fast sodium-cooled systems where gamma backgrounds exceeding 10^6 R/hr can be expected even at relatively low power.

In order to achieve full coverage, present monitoring systems conventionally use two or more types of neutron detectors installed in various locations relative to the core. However, adequate discrimination against gamma signals is still difficult over portions of the operating range.

5.2.1.2 A System of Promise

A neutron detection system designed to offset these problems has been assembled and performance tested in the Argonaut Reactor.¹⁵ It features a single fixed-position fission counter coupled to a "nonswitched" electronic system which continuously monitors up to ten decades of reactor power (exclusive of range-switching in the Campbell System). In contrast with conventional systems, calculations indicate that superior gamma discrimination is realized over the entire flux range. No attempt has been made to develop the special electronics required for installation in an operating power reactor. With improved electronics, however, it is believed that the counting system could easily monitor an additional half-decade of neutron flux.

The system is based upon principles established by others.¹⁶⁻²¹ For test purposes, a conventional counting technique was used to cover the source and low intermediate ranges, and a mean-square-voltage technique (Campbell System) was employed to monitor the intermediate and power ranges. Sufficient linear overlap of the two output signals was verified experimentally, thus demonstrating the continuous monitoring feature of the combined techniques. A mean chamber current measurement was included in the system; in a power reactor, it would be used to generate linear high-power-trip signals.

The only special component required was the preamplifier. System design criteria established that the unit be capable of producing (1) pulses suitable for counting at relatively high rates; and (2) detectable mean square voltage signals proportional to neutron flux at low power levels. Switching of preamplifiers, preamplifier internal characteristics, or detector excitation voltage was deemed unsafe practice for control system applications.

5.2.1.3 Test Procedure and Results

In operation, a standard fission counter operating at 300 volts provided the signal to a narrow-bandpass preamplifier. Output from the preamplifier was fed to a linear pulse amplifier, with a count-rate meter

output, and a true rms voltmeter connected in parallel. The mean chamber current signal was measured with a pico-ammeter.

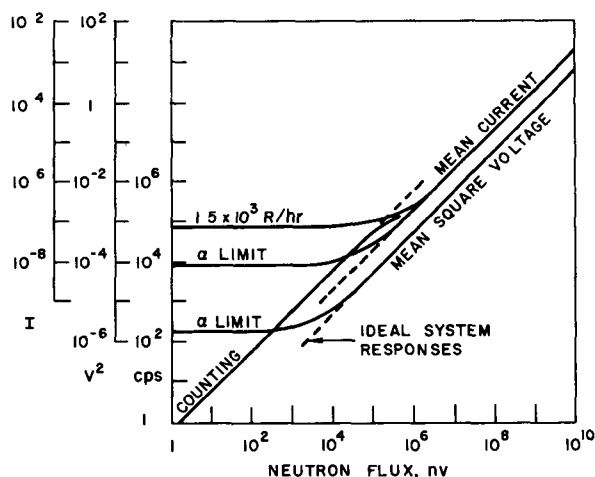


Fig 5-5 Responses of prototype monitoring system to neutron flux levels in the Argonaut reactor

Figure 5-5 shows the various responses of the experimental system to neutron flux prevailing in the Argonaut reactor. Only the mean current measurement was influenced by a gamma flux of $\sim 1.5 \times 10^3$ R/hr. With respect to the counting system, the upper limit was established by the particular electronics used, and the lower limit by the allowable statistical variation of the count-rate meter output. In the case of the statistical current fluctuation system, the upper range probably will be

determined by detector space charge effects, however, such effects were not perceptible over the range of neutron flux monitored by the test assembly.

The lowest flux level that can be measured will be determined either by the alpha output of the fissionable coating (as shown by this experiment) or by the gamma output. Calculations indicate a gamma flux of 10^5 R/hr would be required to produce a 10% error in a measured neutron flux of 10^5 nv.

In summary, the experimental system has monitored ten decades of neutron flux with a single fixed-position detector installed in the Argonaut reactor. No changes in the preamplifier characteristics or the detector excitation voltage were made or required throughout the experiment. The excellent gamma discrimination has not been completely verified. Hence, plans are underway to conduct a similar experiment in the EBR-II Facility. In addition to its large gamma background at low neutron flux levels, the EBR-II will provide an excellent means of evaluating response of the prototype system in a fast reactor operating environment.

5.2.2 Studies of Time- and Space-Dependent Reactor Dynamics

5.2.2.1 Objectives and Basic Approach

The objectives of these studies are: (1) to resolve the problem of analyzing the dynamical properties (e.g., stability, etc.) of reactor system variables which are a function of time and space (i.e., neutron flux, fuel temperature, and coolant flow); and (2) to establish control technology that will ensure the stability and controllability of large, fast power breeder reactors.

The basic approach to the problem consists of sequentially (1) deriving mathematical models to describe the nuclear and nonnuclear characteristics of the reactor system; (2) examining existing methods or developing new methods for studying spatially-dependent reactor dynamics; and (3) evaluating their suitability for stability analysis of space-dependent reactor dynamic systems.

Mathematical Model. The model for the neutron flux was the conventional multigroup diffusion equation coupled with delayed neutron equations. In order to more accurately describe the system (which is basically inhomogeneous and nonstationary in its material composition due to motion of the control rods), the nuclear parameters were assumed to be space-time varying and, possibly, nonlinear.

The model for the nonnuclear variables (e.g., temperatures) was derived from studies of representative local temperature distributions within a typical fuel element and its surrounding coolant channel. Reactor heat transfer and hydrodynamics equations were formulated by using the average temperature distributions.

Finally, the neutron kinetics equations were coupled with equations governing the nonnuclear variables to formulate the model for the complete reactor system.

Methods and Evaluations. Both nodal and modal methods were examined with respect to their suitability for studying spatially dependent reactor dynamics. The former involves dividing a large-size reactor into smaller regions or zones and approximating the dynamic behavior of each zone by a space-independent model (using the average or weighted average of the system variables in each zone) similar to that of a point model. These points or zones are coupled through their mutual properties (e.g., diffusion, etc.). A set of coupled nodal equations was derived for the reactor system. In addition, a study of several "weighting functions" (used to calculate the weighted average of the system variables) was conducted to find the best nodal approximation for various applications of the method (e.g., stability analysis, experimental measurements, etc.).

The modal method assumes the solution of the system variables to be a combination of the characteristic functions of the system. When this assumed solution is substituted into the system equations, and with suitable manipulations, the system can be reduced to a set of space-independent equations. The difficulty of this method is finding the characteristic functions of the reactor system. An attempt to develop a simpler method for application to general reactor systems was unsuccessful; however, the results that were obtained can be applied to reactor systems involving one or two space-dependent variables.

Although Lyapunov's second method has proved useful in stability analysis of systems involving linear and nonlinear ordinary differential equations, no generalized technique exists for finding Lyapunov functions for space-dependent dynamic systems. However, a technique for finding Lyapunov functions for a class of reactor dynamic systems was developed. First, a generalized Lyapunov function was developed for the linearized reactor system to provide conditions sufficient for stability with respect to the system parameters. Next a new Lyapunov function for the nonlinear system was constructed by adding nonlinear terms to the linear system function. This modified function is used to determine a region of stability and to assess the proper feedback function which will ensure system stability within the physical limits where the chosen mathematical model and assumptions are valid.

The mathematical model chosen for the analysis was rather general, but was kept as close to reality as possible. Since the effect of the control devices are embedded in the system parameters, the analysis based on this model should be more accurate, and consequently, more reliable. Treating the problem directly eliminates the need for defining reactivity, since the generation and destruction of neutrons are inherent in the system equations.

In this instance, the conventional modal method, using the characteristic function of a bare homogeneous reactor system, was found readily applicable in limited cases, and rather complex for most other systems. The nodal method has the advantage that the results are confined to a finite number of equations, but the restriction on system variation limits its range of applicability.

In summary, stability analysis of linear systems can be performed by either the nodal or modal method. In the case of nonlinear systems, however, similar analysis is best performed by constructing a Lyapunov function pertinent to the space-dependent reactor system under study. Moreover, it can be applied to other related system dynamics governed by partial differential equations (e.g., stability of reactor heat generation, structural, and containment shell problems).

5.2.3 Synthesis of Optimal Control System for Nuclear Reactors with Generalized Temperature Feedback

5.2.3.1 Synthesis Problem

Control objectives (and problems) vary from one type of reactor to another. In central station plants, for example, the objective might be to program the power output to follow a given time function determined by consumer demands. A similar situation might exist in a nuclear rocket, where the thrust is programmed to effect certain rocket maneuvers. Other problems are reflected by control objectives such as changing power levels in minimum time, or minimizing xenon buildup, hence, restart time after shutdown.

In all instances, the control inputs to the system are the reactivity and the coolant flow. Hence, the synthesis problem is to manipulate these variables in the form of a feedback system.

5.2.3.2 Analytical Approach

The mathematical model of the reactor consisted of the point kinetic equations with a single delayed neutron group. By generalizing the functional analysis approach, an open-loop-type solution was obtained. This solution was combined with an analysis of the reactor trajectories in the state plane (plot of prompt neutrons vs. delayed neutrons) to derive the closed loop control law. These results were then extended to include six groups of delayed neutrons. Under these conditions, the state plane is no longer adequate; hence, a multidimensional state space concept was applied. Finally, the reactor system was expanded to include a generalized temperature feedback, and the controller requirements were derived.

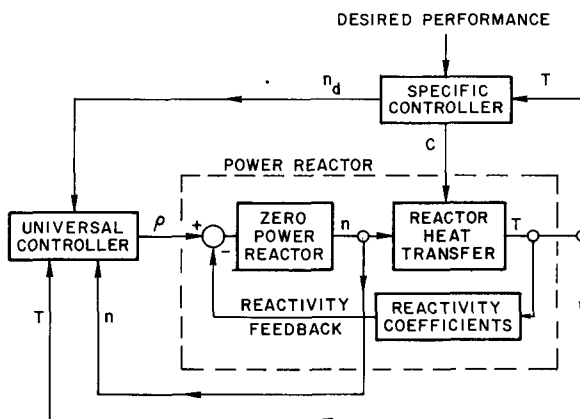


Fig. 5-6. Schematic of optimal control system for reactors with generalized temperature feedback

5.2.3.2 Mode of Operation

Two controllers are employed, as shown schematically in Fig. 5-6. Desired performance is achieved by the specific controller which controls reactor heat transfer (temperatures (T)) through the coolant flow (C), and determines the derived neutron density (n_d) input to the universal controller. Control reactivity (ρ) input from the latter forces the reactor to generate the specified neutron flux level (n).

The system is applicable to many types of reactors. In the final design of the universal controller, the "only" information required is the feedback effects on the reactivity, as given by the reactivity coefficients. These coefficients must be determined experimentally.

5.3 Fuel Meltdown Studies: Experimental Facilities

5.3.1 Large TREAT Loop

During the fiscal reporting period, installation of the out-of-pile portion of the loop was completed and pressure tested preparatory to filling with sodium; the in-pile test section was fabricated and partially instrumented to monitor temperatures and pressures; and the center of the TREAT core was modified to accommodate the test section. In March, 1966, the latter was delivered to the Reactor Physics Division for completion of instrumentation and physics calibrations consistent with the next phase of scheduled meltdown experiments in TREAT. These experiments will involve clusters of 7 to 17 EBR-II fuel elements and, ultimately, a modified, full-size subassembly containing a maximum of 37 elements of appropriate enrichment surrounded by 54 stainless steel dummy counterparts to complete the loading. A more detailed description of these experiments and analyses of hypothetical hazards attendant to their execution is in various stages of review by cognizant Argonne and Idaho personnel.

Significant aspects of the foregoing fiscal efforts are summarized in the following subsections.

5.3.1.1 Pressure Testing of Out-of-Pile Assemblage

This portion of the integrated loop (Fig. 5-7) was described in the previous annual report (ANL-7190, p. 181). In June, 1966, installation was completed and the entire assemblage was pressure tested with inert gas at room temperature and 180 psig. There were no leaks; however, one of the in-line expansion bellows assemblies was axially deformed to the extent that it had to be replaced. Fabricated of Type 304 stainless steel, this standard 3-ply (0.018 in. per ply), 5-convolution assembly was positioned in the 3-in. piping between the pump outlet and the bypass valve. Three identical assemblies were purchased: one for replacement of the defective unit, and two spares. Stiffeners were installed around the replacement unit to safeguard against similar deformation.

One of the spare bellows assemblies, identical to those employed in cross-over section (See Item 1, Fig. 5-7), was bench-tested to determine its pressure capability. During these tests, the assembly was compressed 1/4 in., or two-thirds the amount due to pipe expansion anticipated during heating from ambient to design temperature (1000°F). Figure 5-8 shows the appearance of the bellows after being pressurized (and held for 35 sec)

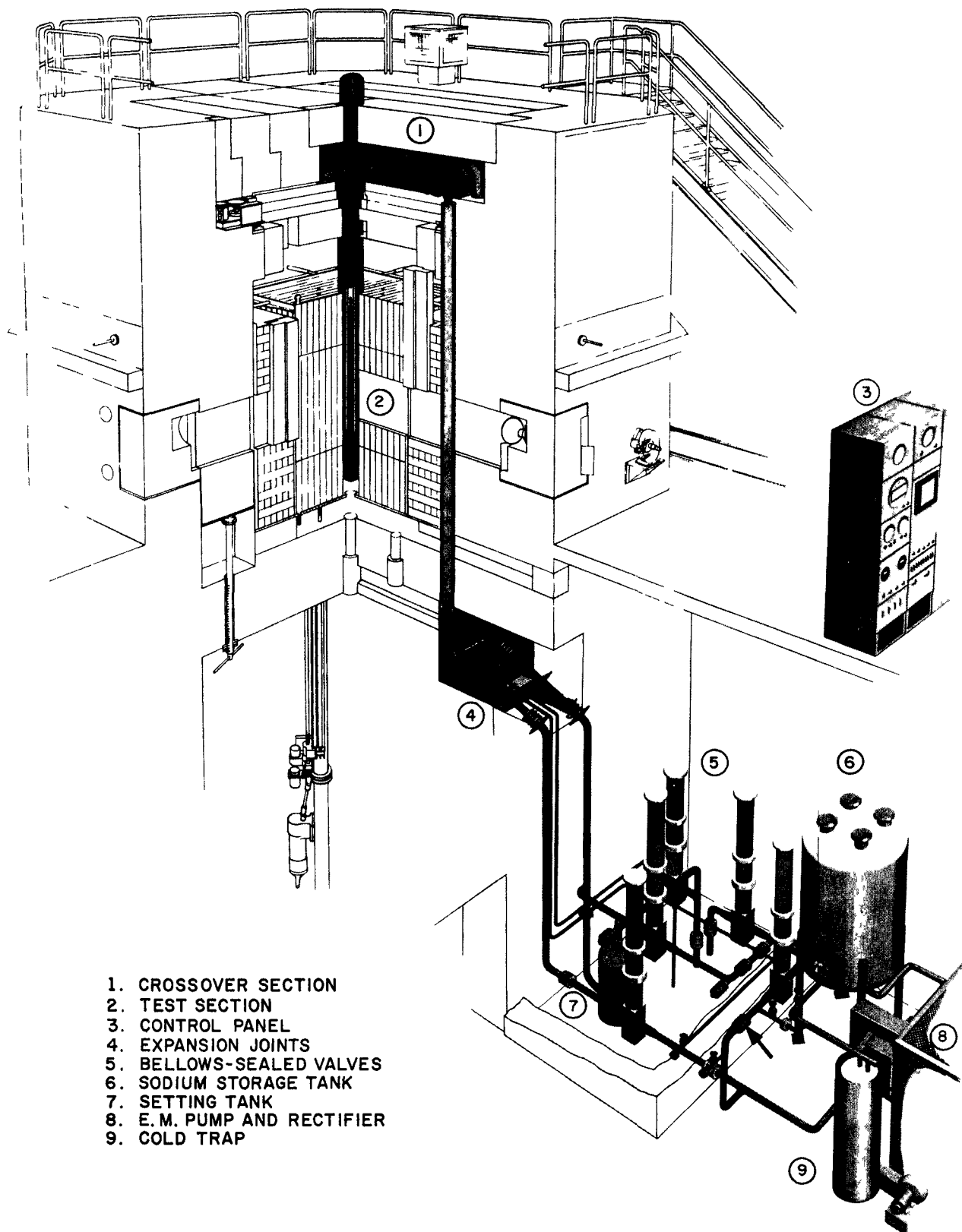


Fig. 5-7. Artist's concept of Large TREAT Sodium Loop. Arrow points to in-line pipe expansion bellows that was deformed.



Fig. 5-8. Appearance of Type 304 cross-over pipe expansion bellows after hydrostatic pressure tests up to and including 35 sec at 1180 psi.

Assembly consists of a $2\frac{1}{2}$ -in., Schedule 5 flow tube positioned concentrically within a 4-in., Schedule 80 pressure container. At the upper end, the flow tube is clamped between the flange faces of a 4-in. Conoseal pipe joint that interconnects the inlet and outlet header to the top of the pressure container. (Also see Fig. 5-7.) This header contains a short extension of the flow tube which is bellows-spring-loaded against the upper face of the parent flow tube to complete the coolant channel.

The lower portion of the test section is heated by six Chromolox heaters installed at 60-degree intervals around the pressure container. These heaters, are enclosed by a thin-walled stainless steel sheath which, in turn, is covered with thermal insulation. The entire assembly is positioned within a Zircaloy liner to protect adjacent TREAT fuel elements from mechanical damage and sodium spills. At the upper end, the liner is gasketed to a drip pan which underlies the cross-over riser and down-comer pipes leading to the equipment room.

at the maximum value of 1180 psi. Since the pressure-temperature rating for Type 304 stainless steel at 1000°F is 0.65 that at room temperature, the results of the loop pressure tests are comparable to long-term, 760-psi pressurization of the bellows at 1000°F. This exceeds by a factor of 1.5, the ~500 psi hypothesized for the maximum credible accident in the loop safety analyses.

5.3.1.2 Core Modifications

These modifications included (1) half-dummy elements to fill the voided region surrounding the core; (2) a Zircaloy liner to isolate the test section and contents from the TREAT fuel elements; and (3) installation of circuitry leading from sodium leak drip-grids positioned at sensitive loop areas.

5.3.1.3 Test Section

Figure 5-9 is a cutaway pictorial of the test section which will be positioned in the center of the TREAT core. Fabricated of Type 304 stainless steel, the assembly

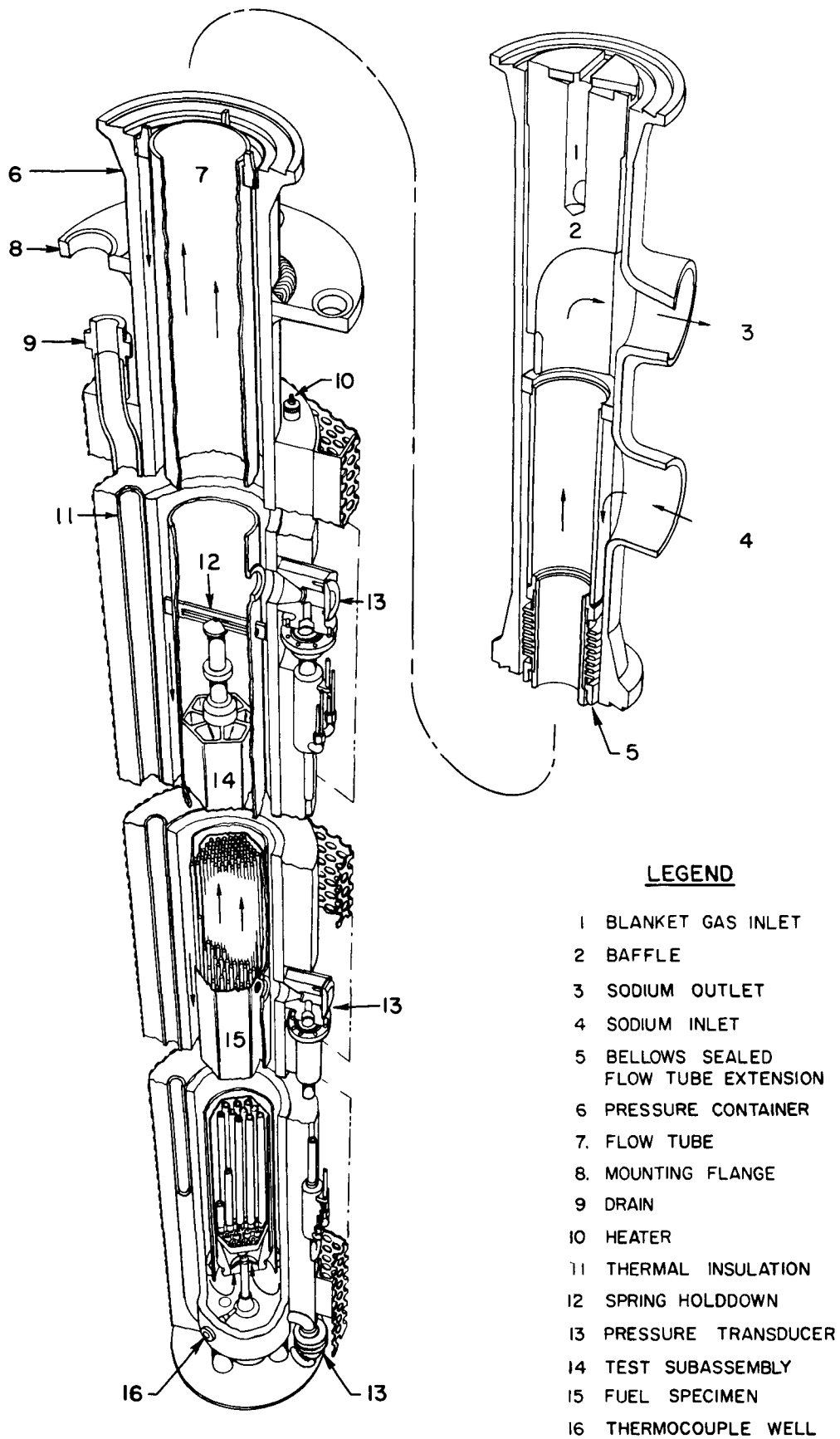


Fig. 5-9. Components of in-pile portion of Large TREAT loop

These pipes lead horizontally from the inlet and outlet headers to 90-degree elbows and then downward through cylindrical ducts cast in the biological concrete shielding. Horizontal sections of both riser and downcomer are flanged to facilitate removal of the test section upon completion of the experiment.

With reference to Fig. 5-9, sodium from the riser enters the header and flows downward through the annulus between the flow tube and the pressure container. At a level corresponding to the thermocouple well, the flow is diverted upward through the flow tube and experimental fuel cluster (in this instance, an EBR-II subassembly). The flow continues upward, past the bellows spring-flow tube extension, where it enters the downcomer line and returns to the out-of-pile portion.

Upon completion of the meltdown experiment, the sodium in the test section and interconnecting piping will be permitted to freeze. At that time, the shield blocks will be set aside and the test section disconnected and removed into a shielded cask. After a predetermined activity decay period, the drain line of the test section will be connected to a disposable container, and power lines attached to the heaters to melt the sodium. Upon completion of the draining operations (~ 42 lb or 0.75 ft³), the cask will be shipped to the Argonne site for subsequent removal and examination of the test assembly.

5.3.1.4 Safety Analysis Report

This report contains the results of detailed safety analyses of conditions that will prevail during normal experiments with reactivity additions (k_{ex}) of 2.0, maximum experiments with $k_{ex} = 2.3$ and, finally, the maximum credible accident hypothesized for a 2.8% reactivity addition, with a modified full-size EBR-II subassembly test specimen containing a maximum of 37 active fuel elements.

In all instances, CDC-3600 ARGUS Code calculations indicated that the loop is capable of sustaining the most severe conditions, with a considerable margin of safety. In operation, the code relates coolant and fuel temperatures during a transient; it also employs a second pressure pulse model which estimates temperatures and pressures that may result from a second contact between sodium and the molten fuel. To ensure more intimate contact and consequent higher heat transfer rates, the fuel was assumed to have ruptured into small fragments.

That a large factor of safety exists is evidenced by the calculated results (Table 5-1) and the fact that the steady-state design pressure of the test section is equal to 1990 psia.

Table 5-1. Calculated Maximum Coolant Temperatures and Pressures for the Large TREAT Loop

Conditions	Reactivity Addition, % k_{ex}	Total Energy Release, Btu	Maximum Coolant Temp., °C	Saturation Pressure Pulse, psia
Normal Experiment	2.0	650	1014	60
Maximum Experiment	2.3	850	1212	138
Maximum Credible Accident	2.8	1170	1490	~424

In summary, the Large TREAT Sodium Loop has been completed and checked out. The onset of scheduled meltdown experiments is pending final review of the hazards analysis report by cognizant Argonne, Idaho, and AEC personnel.

5.3.2 An In-Pile Loop to Study Fuel Failure Propagation

A study was made of an in-pile loop which would extend the scope of fuel failure experiments currently planned for the TREAT reactor. Unlike the TREAT experiments, the proposed tests would start from the full-power level, with system abnormalities permitted to develop gradually or rapidly as desired or encountered.

Typical experiments would include loss of cooling, fuel restart capability following such loss, catalytic failure propagation, and projection of failure to adjacent fuel. Initially, fuel samples would be installed in the loop and the reactor brought up to normal coolant flow, temperature, and power levels. This phase of the test would include checkout and calibration of instrumentation to measure significant operating parameters. Subsequently, the abnormal condition would be introduced and the consequent behavior of the parameters recorded. Finally, the fuel specimens would be removed, inspected, and the results correlated with conditions prevailing during the test.

The range of temperatures of interest and consequence imposes severe demands upon materials and instrumentation. For example, the current target operating temperature for large, sodium-cooled reactors is 1200°F. Hence, the loop will have to accommodate a coolant outlet temperature of this magnitude, with a power reject capability up to 1 MW. Provisions must be made for containment of still higher sodium temperatures which may be encountered on a transient basis or during possible

short-term, steady-state boiling. In addition, the loop must contain the consequences of abnormal conditions up to and including fuel meltdown. Hence, development of special materials and monitoring equipment will be required in support of the loop design effort.

The nature of the proposed tests necessitates their conduct in an operating reactor since realistic generation of heat cannot be reproduced by out-of-pile methods. A choice of reactor has not been made; consequently, a specific loop design does not exist. However, the basic components would consist of a special alloy re-entrant test section, a sodium-to-nitrogen heat exchanger, a continuously variable mechanical sodium pump, piping, tanks, and instrumentation. A survey of operating systems indicates that the loop complex envisioned is amenable to installation in reactors such as the BAWTR, GETR, SRE, or others.

The status of the study is as follows. Preliminary cost estimates of the basic loop installation have been prepared. Exploratory meetings and information exchanges have been conducted with cognizant management personnel to determine availability of reactors. This information has been compiled in a proposal for local and AEC review.

5.4 Containment

5.4.1 A New Concept of Primary Containment by Energy Absorption

Current provisions for containment of U.S. nuclear reactors vary according to the type of reactor, its location, magnitude of maximum credible accident hypothesized, and other considerations. In most systems, however, two distinct stages of confinement are employed. These stages are identified as primary and secondary containment, respectively.

This section summarizes the results of an analytical study conducted in support of a new primary containment concept which offers improvement in safety and substantial cost reductions over accepted systems. A more detailed account is reported elsewhere.²²⁻²⁵

5.4.1.1 Old vs. New Concept

Nuclear accidents are most commonly assumed to originate in the reactor cavity which is formed by the biological concrete shield walls (usually 4 to 6 ft thick). This cavity contains the reactor vessel, certain primary system piping and components, and some form of independent blast shield which surrounds the reactor vessel.

Quite often, the blast shield is comprised of four or more concentric steel cylinders with interim layers of crushable material. This configuration is based upon the following principles of containment. In the

event of a major nuclear accident, the first significant confining action is offered by the walls of the reactor vessel and of the cavity. Further attenuation of the burst effects is accomplished by sequential expansion of the blast shield cylinders and crushing of the intervening material.

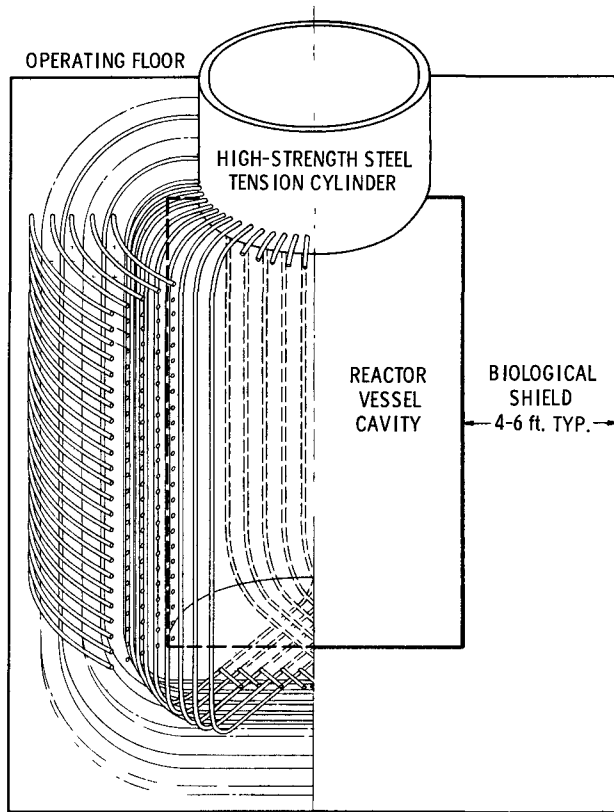


Fig. 5-10. Concept of primary containment by energy absorption. Sectioned half of concrete shield shows basket-like reinforcement formed by successive layers of vertical and horizontal strands of high-tensile steel positioned in sheaths. Sheaths are mounted on concentric wire mesh cylinders (not shown). Vertical strands terminate in top cylinder designed for internal pressure equal to tension applied by the strands.

There are three basic disadvantages to the blast shield concept. First, cost of material, fabrication, and erection of multiple steel cylinders and layers of crushable composition is substantial. Second, they are designed to satisfy semifictitious pressure-volume calculations which do not disclose the presence and magnitude of existing margins of safety. Finally, installation of the assembly between the reactor vessel and biological shield results in a larger reactor building.

In contrast, the proposed primary containment concept (Fig. 5-10):

(1) Effects substantial cost reductions by eliminating the need for an independent blast shield.

(2) Permits establishment of defineable safety margins by equating ascertainable quantities, i.e., the destructive components of the explosion, to the energy-absorption capability of material surrounding the reactor.

(3) Offers potential savings commensurate with diametral reduction (by several feet) of the secondary containment shell.

Economy is achieved by making the ever-present concrete biological shield an integral part of the primary containment structure and independent of the secondary containment. As shown in Fig. 5-10, this is done by reinforcing the concrete shield with several layers of commercially-available, unstressed strands of high-tensile steel to form an extremely efficient, energy-absorbing basket. The strands are placed in sheaths to prevent

bonding to the concrete; thus, tension applied at one point is manifested over the entire length, with negligible losses due to friction. Number, size, and spacing of the strands can be determined by the magnitude of the destructive components of the hypothetical accident.

These components (shock wave, fluid momentum, gas bubble, with their respective time parameters) are absorbed by the elasto-plastic deformation of the strands. In Fig. 5-11, the areas below the stress-strain curves show the strain energy-deformation properties of high-tensile strength steel strands and structural carbon steel reinforcement. Analysis of a high-strength steel basket, similar to that of Fig. 5-10, embedded in a 4-ft-thick biological shield wall showed that the destructive components of an equivalent 300-lb TNT explosion in the cavity could be absorbed by an elasto-plastic deformation of 6%. This value is based on the minimum spacing consistent with maximum strand diameter which would not fail the concrete in bearing. If the wall thickness were increased to 6 ft, the strand diameter and spacing could be modified to realize containment of a 500- to 1000-lb TNT detonation for the same percentage of deformation.

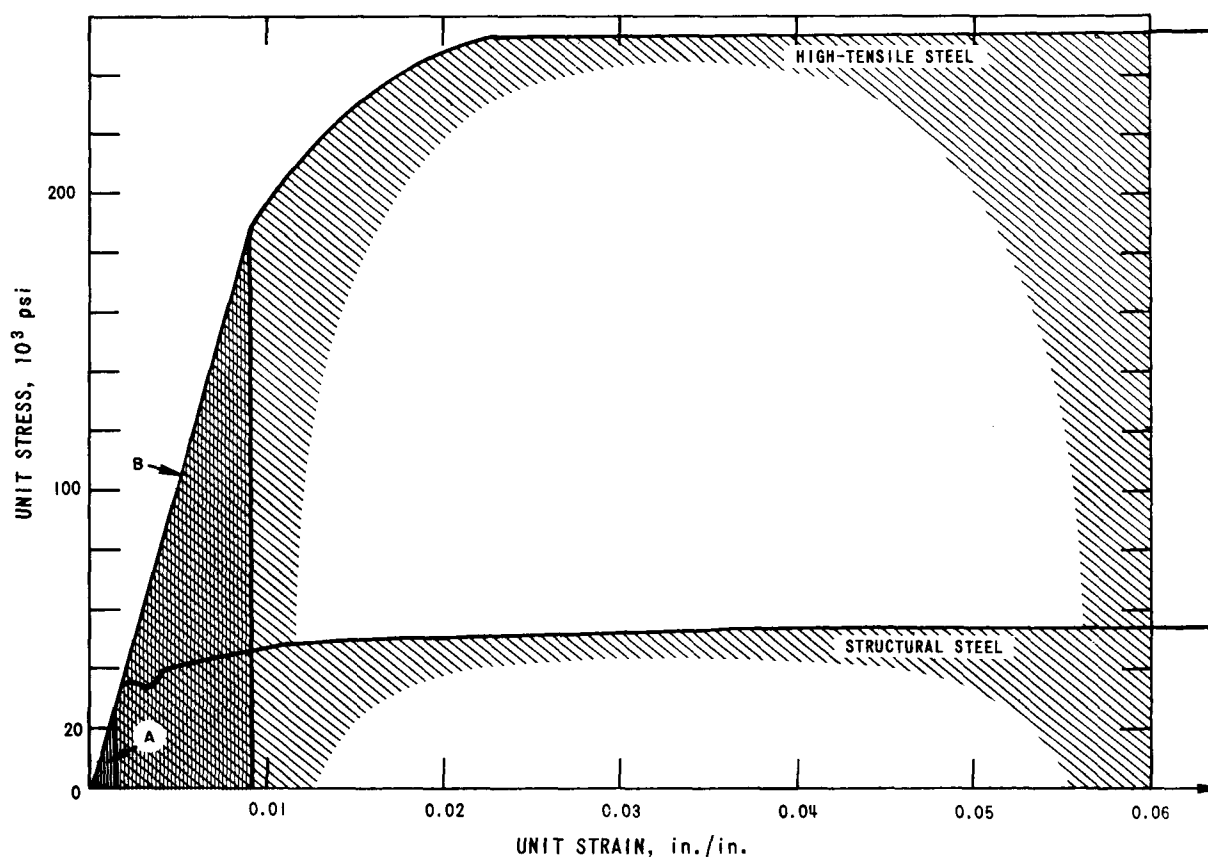


Fig. 5-11. Stress, strain, and strain-energy diagram for structural and high-tensile steels. Light cross-hatching beneath each curve signifies plastic strain energy for each steel. Denser triangles A and B indicate the corresponding elastic energy-absorbing properties.

5.4.1.2 Assessment of Safety Margins

A realistic assessment can be obtained by the individual and sequential treatment of the various destructive manifestations inherent in the nuclear incident. Briefly, the destructive component to be absorbed probably manifests itself into three subcomponents occurring over different times: shock wave, fluid momentum, and expanding gas bubble.

The shock wave proceeds extremely fast (10^{-6} to 10^{-4} sec) and probably causes rupture of the reactor vessel. Some energy is lost in rupturing the vessel and in crushing and accelerating certain reactor internals. The shock wave cannot effectively propagate past the vessel wall due to density differences in the wall and the surrounding material (usually inert gas or air). Therefore, the energy is converted into work, heat, and kinetic energy, imparting momentum both initially and on reflection as it passes through the materials. Conversion of the kinetic energy in the material momentum must be considered over longer time periods (10^{-4} to 10^{-2} sec). Finally, the expanding gas bubble contains about one-half the total destructive energy and its effects occur over a still larger period (10^{-2} to 1 sec).

5.4.1.3 Strain-Rate Properties of Strand Materials

The time elements associated with the destructive subcomponents emphasize the importance of strain-rate properties of the strand materials employed in this containment concept. To provide some insight into the magnitude of strain rate imposed on any strand, a fluid dynamics analysis was made of an idealized sodium reactor containment system having spherical symmetry.²⁴

For this analysis, the destructive component was assumed equivalent to the detonation of a bare charge of 376 lb of TNT. This charge, measuring 2 ft in diameter, was surrounded successively by 5 ft of water, 1 ft of argon, and a 6-ft-thick concrete biological shield embedded with non-prestressed, unbonded, high-strength-steel strands.

The hydrodynamical equations of motion, which constitute a set of nonlinear partial differential equations, were integrated numerically by the CDC-3600 computer. Propagation of shock discontinuities was treated by a common form of the artificial viscosity technique of von Neumann and Richtmeyer. General information on the mode of propagation and changes with time of the destructive component was obtained by monitoring the pressure at various critical locations in the system and by following the movement of the fluid-gas interfaces. Detailed information in the form of pressure-time and location-time plots is given in reference 24.

The rate of strain imposed on the steel strands is related to the pressure pulse acting on the inside face of the concrete shield. For the reactor system described above, the maximum strain rate on any steel strand was calculated to be 12.32 in./in./sec. This is classified in the extreme lower range of the moderate rate of strain (10^0 to 10^{-3} in./in./sec).

Klinger²⁵ has reported strain rates of $10^{-5} < \epsilon < 10$ for high-strength steel (SAE 4340) ranging from 120,000 psi ult (annealed condition), up to a nominal ultimate strength of 220,000 psi. A review of his results indicates, in general, that the strain-rate effect decreases markedly as the strength level of the steel is increased. In fact, the 220,000-psi steel showed either no change or slight loss (<3%) in strength with increasing strain rate. There was no noticeable effect on the total elongation at any strength level.

The new concept of primary containment is based upon the energy-absorbing capability of the embedded steel strands. This capability, in turn, is dependent upon the strength and elongation properties of the strands; and both properties are functions of the strain rate. Therefore, the modest strain rates imposed on the basket-containment concept, compared to the high strain rates reported by Klinger, render the concept entirely feasible. For example, since the strength and elongation properties of the 220,000-psi steel do not change appreciably at a strain rate of <10 in./in./sec, which is the region of relevance to the new concept (12.32 in./in./sec), corresponding properties obtained (by static tests) at a strain rate of 10^{-3} in./in./sec could be applied in the design of the spherical configuration analyzed.

REFERENCES

1. R. E. Holtz, *The Effect of the Pressure-Temperature History upon Incipient Boiling Superheats in Liquid Metals*, ANL-7184 (to be published).
2. J. P. Lewis, *Experimental Studies of Boiling of Sodium and Condensing of Potassium*. Presented orally at the Conference on Application of High Temperature Instrumentation to Liquid-Metal Experiments, Argonne National Laboratory, September 28-29, 1965.
3. J. A. Edwards and H. W. Hoffman, *Superheat with Boiling Alkali Metals*, Proceedings of the Conference on Application of High-Temperature Instrumentation to Liquid-Metal Experiments, Argonne National Laboratory, September 28-29, 1965, ANL-7100 (June, 1966), pp. 515-534.
4. L. J. Koch and M. R. Sims, *Reactor Engineering Division Annual Report: July 1, 1964 to June 30, 1965*, ANL-7190 (March, 1966), p. 176.
5. J. D. Geier (ed.), *Fast Reactor Test Facility*, ANL-7168 (March, 1966).
6. I. Charak and F. A. Smith, *Preliminary Evaluation of a Technique to Study Expulsion of Sodium into Air*, Proceedings of the Conference on Safety, Fuels, and Core Design in Large Fast Power Reactors, ANL-7120 (June, 1966), pp. 868-872.

7. H. K. Fauske, *Critical Flow and the Velocity of Sound in Two-Phase, One Component Droplet Flow*. Paper to be presented at the 16th Annual Conference of the C.I.C., Windsor, Ontario, Canada, October 17-19, 1966.
8. F. R. Zaloudek, *The Low Pressure Critical Discharge of Steam-Water Mixtures from Pipes*, HW-68934 rev. (March, 1961).
9. H. K. Fauske, *Critical Two-Phase Steam-Water Flows*, Proceedings of the 1961 Heat Transfer and Fluid Mechanics Institute (Stanford: Stanford University Press, 1961), p. 79.
10. S. Levy, *Prediction of Two-Phase Critical Flow Rate*, ASME Trans., Series C, J. Heat Transfer, 87, 53 (1965).
11. F. J. Moody, *Maximum Flow Rate of a Single Component, Two-Phase Mixture*, ASME Trans., Series C, J. Heat Transfer, 87, 134 (1965).
12. J. E. Cruver and R. W. Moulton, *Critical Flow of Liquid-Vapor Mixtures*. Paper presented at the 55th National Meeting of the AIChE, Houston, Texas, 1965.
13. W. J. Klingebiel, *Critical Flow Slip Ratios of Steam-Water Mixtures*, Ph.D. Thesis, University of Washington, 1964.
14. R. E. Collingham and J. C. Firey, *Velocity of Sound Measurements in Wet Steam*, I&EC Process Design and Developments, 2, No. 3, 197 (July, 1963).
15. G. F. Popper, W. C. Lipinski, and J. M. Harrer, *A Wide Range, Gamma-Compensated, Neutron Flux Detection System*, ANL-7224 (to be published).
16. D. A. Gwinn and W. M. Trenholme, *A Log N and Period Amplifier Utilizing Statistical Fluctuation Signals from a Neutron Detector*, IEEE Trans. in Nuclear Science, NS-10, No. 2, 1-9 (April, 1963).
17. R. A. DuBridge, *Mean Square Voltage Fluctuation Measurements with Neutron Sensitive Ion Chambers*, Trans. Am. Nucl. Soc., 6, No. 2, 306 (November, 1963).
18. E. P. Fowler and R. W. Levell, *The Use of Current Fluctuations from a Neutron Detector with Logarithmic Amplifiers as a Measure of Neutron Flux Levels*, AEEW-R375 (June, 1964).
19. R. A. DuBridge and W. K. Green, *A Full-Range In-Reactor-Core Neutron Monitoring System Employing Ion Chambers*, GEAP-4643 (June, 1964).
20. L. R. Boyd et al, *Reactor Control Systems Based on Counting and Campbell Techniques, Wide-Range Instrumentation Development Programs, Seventh Quarterly Progress Report, February - April, 1965*, GEAP-4862 (May, 1965).
21. R. A. DuBridge et al, *Reactor Control Systems Based on Counting and Campbell Techniques, Full Range Instrumentation Development Program, Final Progress Report*, GEAP-4900 (July, 1965).
22. S. H. Fistedis, *A New Reactor Containment Concept by Energy Absorption*, Nuclear Engineering and Design, 3, No. 2, 281-286 (February - March, 1966).

23. S. H. Fistedis, *Summary of Concept and Cost of Containment by Energy Absorption*, Trans. Am. Nucl. Soc., 9, No. 1, 306 (June, 1966).
24. N. C. Sorensen and S. H. Fistedis, *Hydrodynamic Analysis of Nuclear Containment by Energy Absorption*, ANL-7214 (to be published).
25. R. F. Klinger, *Effect of Rate of Strain on the Tensile Properties of SAE 4340 Steel*, WADC-TR-53-507 (AD-76276) (1955).

Section 6

STUDIES AND EVALUATIONS

✓
6.1 Feasibility Study of a Nuclear Steam Supply System Using a 10,000-MW Sodium-Cooled Fast Breeder Reactor6.1.1 Origin of Study

Consistent with an AEC Program, Oak Ridge National Laboratory has been assigned several tasks relating to development of nuclear heat sources for large-scale desalting plants. One task concerns the technical feasibility of nuclear steam supply systems capable of 10,000 MW thermal output. In early August, 1965, the part of this task relating to large sodium-cooled fast breeder reactors was delegated to Argonne in the form of a purchase order:

"Based on power-only conditions and using as a starting point the 1000 MWe reports on ceramic fueled reactors by Westinghouse, General Electric, Combustion Engineering, Allis-Chalmers, and Atomics International, the technical feasibility of extrapolating sodium-cooled fast reactors to 10,000 MWt will be studied. The emphasis will be placed on those aspects of nuclear steam supply system which may cause limitations on the extrapolation..."

In addition to allocating \$100,000 and a 6-month time limit for the study, the purchase order provided for selection of a subcontractor to make a feasibility determination of the primary pumps and the entire secondary system equipment up to and including the steam generators. Westinghouse Electric Corporation was selected and, owing to its established position, extended the scope to include considerations of size and availability of turbine-generator equipment.

A description of the conceptual 10,000-MW nuclear steam supply system evolved from this joint effort.¹ The significant design considerations, plant features, operating characteristics, and exploratory cost estimates are summarized in the following subsections.

6.1.2 Design Considerations

The approach used to determine system feasibility was to develop a conceptual design. This involved (1) establishment of general ground rules; (2) engineering choices of design criteria; (3) selection of certain system parameters and equipment based on experience; (4) brief thermal and neutronic studies in support of the most promising core geometry, system arrangement, etc; and finally, (5) evolution of a concept with some engineering description.

Of the general ground rules established, the most important was an assumption that the era of 10,000-MW reactors would be prefaced by a well-developed technology for nominal 1000-MW(e) sodium-cooled fast breeder reactor plants. Moreover, that these plants would be competitive for central station use in the U.S. before the 10,000-MW(t) plant is built. Also it was ruled that no new development would be conceived to solve a problem or to accomplish a segment of plant design.

Engineering choices of criteria were largely concerned with safety and fuel performance. With regard to safety, the sodium-voiding characteristics and the level of Doppler coefficient were evaluated with slightly more optimism than prevails in current projections to the nominal 1000-MW(e) fast breeder plant. Ideally, fuel material selection and temperature of operation should be made on reasonable performance expectations for known materials. However, application of this general criterion to the present study was difficult because of insufficient data on material behavior at the anticipated temperatures and neutron irradiations.

Accordingly, a conservative outlet sodium temperature of 1050°F was selected, together with a 720°F inlet temperature to lessen the burden on material performance. Free surface mechanical pumps and single-tube-wall-type steam generators are illustrative of the equipment selection. A carbide form of fuel was chosen because of its potential for high neutronic and thermal performance.

Based on brief thermal and neutronic investigations, an annular reactor geometry was selected. At the time of selection as well as at completion of the work, it was realized that other geometries (modular, double annular, pancake) also could meet feasibility requirements. A remote, nonvisual, fuel-handling scheme, as exemplified by the EBR-II and Fermi plants, was chosen after consideration of other refueling methods. A loop-type primary coolant system was selected over the large-tank-of-sodium concept because it afforded greater freedom in equipment selection and system arrangement.

These considerations reflected other decisions and supporting investigations before the reference concept became fixed. In all instances, equipment cost as well as the operation and maintenance costs were used as guides in effecting resolutions. Formal installed-cost estimates were limited to specific equipment and the fuel cycle.

6.1.3 Plant Description

For ease of description, the plant is divided into three islands: reactor, steam-generator, and turbine-generator. The bounds of each island are mainly defined by the walls of their respective buildings. (See items 11, 12, and 14, in Fig. 6-1.) Certain plant services and auxiliary systems are

located in separate structures. Summary design data and a simplified flow diagram for the overall plant are listed in Table 6-1 and shown in Fig. 6-2, respectively.

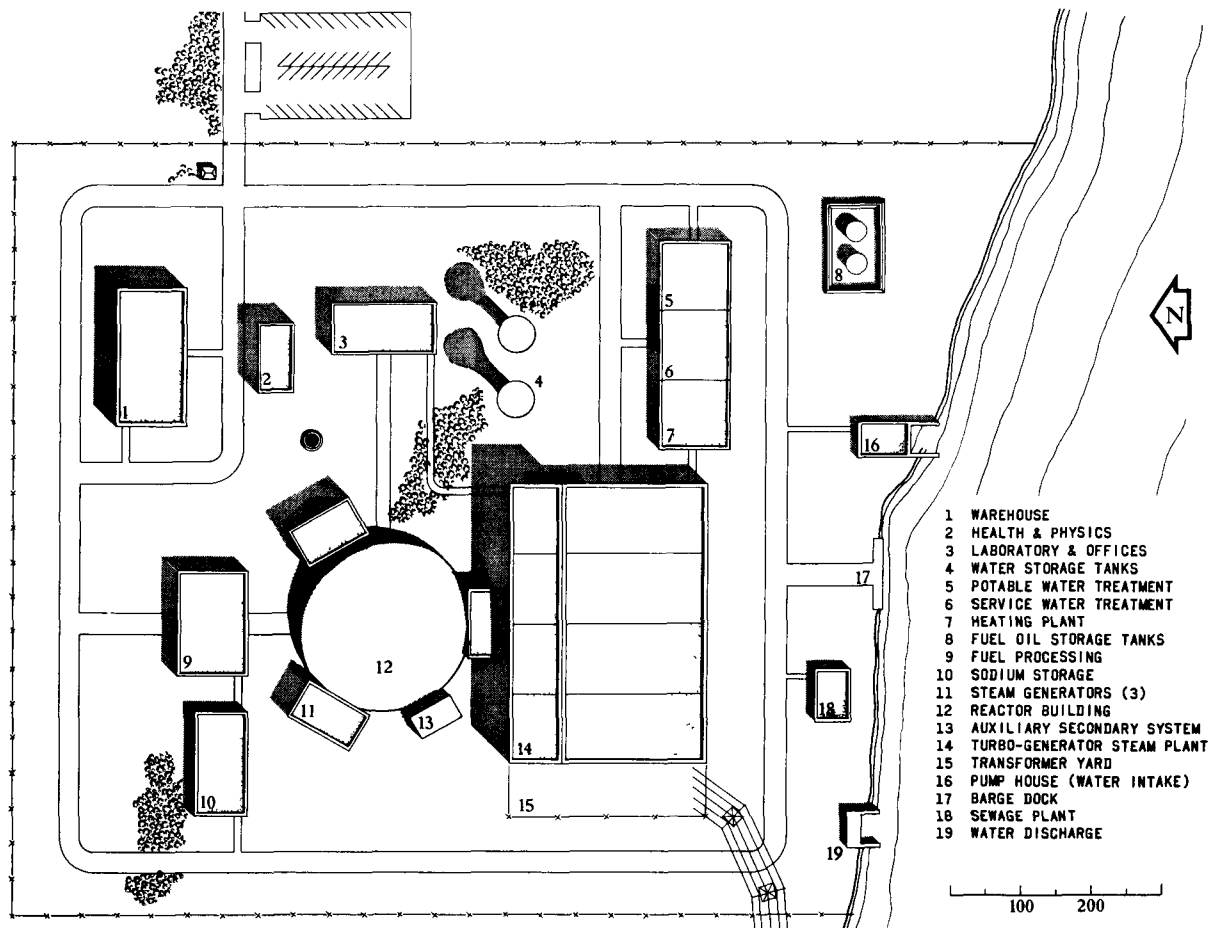


Fig. 6-1. Plan view of 10,000-MW(t), sodium-cooled, fast breeder reactor plant complex

Table 6-1. Summary Data for Very Large Fast Breeder Reactor Plant

Gross thermal output	10,000 MW	Core volume	16,700 liters
Net electrical output	3,880 MW	Reactor fissile Pu weight	10,500 kg
Sodium inlet temperature	720°F	Reactor breeding ratio	1.4
Sodium outlet temperature	1050°F	Fissile material doubling time	7 years
Steam pressure	2400 psia	Linear heat rate (avg.)	16 kW/ft
Steam temperature	900°F	Core burnup (avg.)	110,000 MWD/MT
Type of fuel in core	(U+Pu)C	Interval between refuelings	1/2 year
Core geometry	Annular	Equilibrium fuel cycle cost	1/4 mill/kWhr

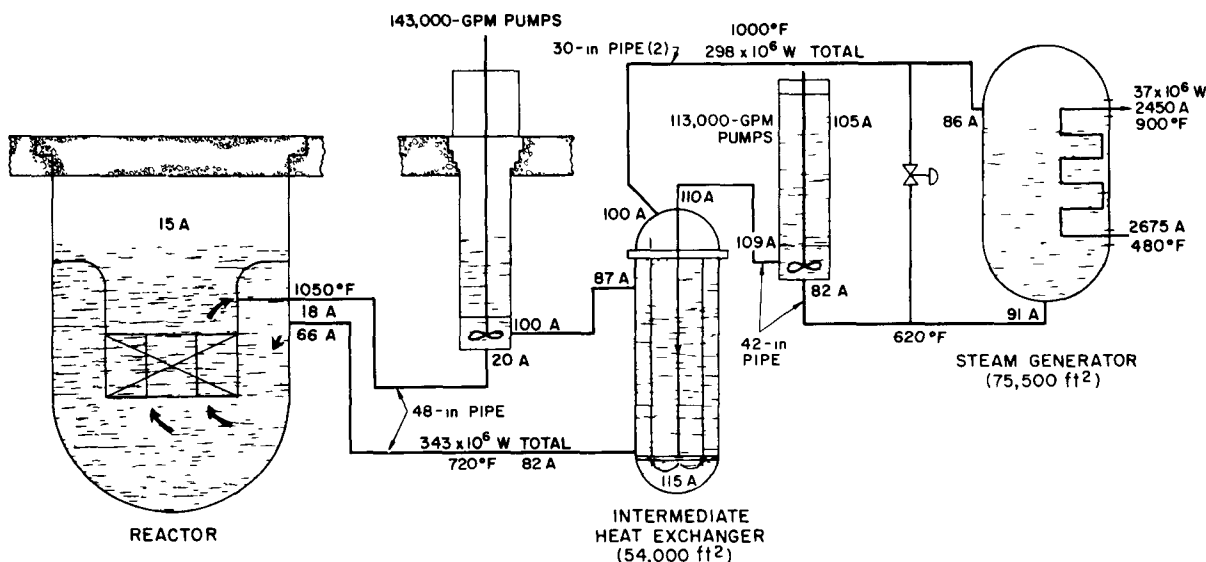


Fig. 6-2. Simplified flow diagram showing thermal and hydraulic characteristics of one of six primary-secondary loops comprising the 10,000-MW(t) system

6.1.3.1 Reactor Island

The core and integral axial blankets of the reactor contain 456 hexagonal subassemblies arranged in an annular ring four subassemblies thick to produce a core I.D. and O.D. of 19.9 and 24.6 ft, respectively. Each of the 331 elements per subassembly consists of a 106-in.-long, 0.275-in.-O.D., 0.015-in.-thick, Type 304 stainless steel tube containing a 43-in.-length of uranium-plutonium carbide between 16-in.-lengths of uranium carbide. The remaining 30-in.-length of the fuel element serves as a reservoir for released fission product gases. The hyperstoichiometric core and axial blanket carbides are vibratory compacted to 80% theoretical density within the cladding and utilize a helium thermal bond. Within the core region, control rods containing boron carbide are concentric with about one out of every five subassemblies.

The inner radial blanket is comprised of the two, single-subassembly-thick regions located adjacent to the internal and the external peripheries of the core. Each of the 234 radial blanket subassemblies adjacent to the core (102-internal inner radial blanket, 132-external inner radial blanket) contains 217 elements which have a clad O.D. of 0.385 in. and a 0.022-in. wall thickness. The outer radial blanket is comprised of 235 subassemblies (96-internal outer radial blanket, 138-external outer radial blanket), each containing 169 elements which have a 0.515-in. clad O.D., and a 0.025-in. wall thickness. Both the inner and outer radial blanket elements contain U-10 wt-% Zr pins and a measured amount of sodium to provide a thermal bond between the blanket pins and the Type 304 stainless steel cladding.

The annularly-shaped reactor is housed in a 40 ft O.D. by 64 ft high vessel. (See Fig. 6-3.) The volume inside the reactor annulus is used for wet fuel storage. Refueling of the reactor takes place twice a year during shutdown. On each occasion, approximately 25% of the core and 16% of the radial blanket subassemblies are replaced. Figure 6-4 shows the general scheme and equipment arrangement of the remote-controlled fuel-handling systems used to effect these replacements.

A brief description of the refueling concept is included because of its importance in considering plant availability. Following reactor shutdown, the control rod drive shafts are disengaged from their fully-inserted control subassemblies and lifted clear of the path inscribed by the Offset Handling Mechanism (OHM). This mechanism is similar to the one employed

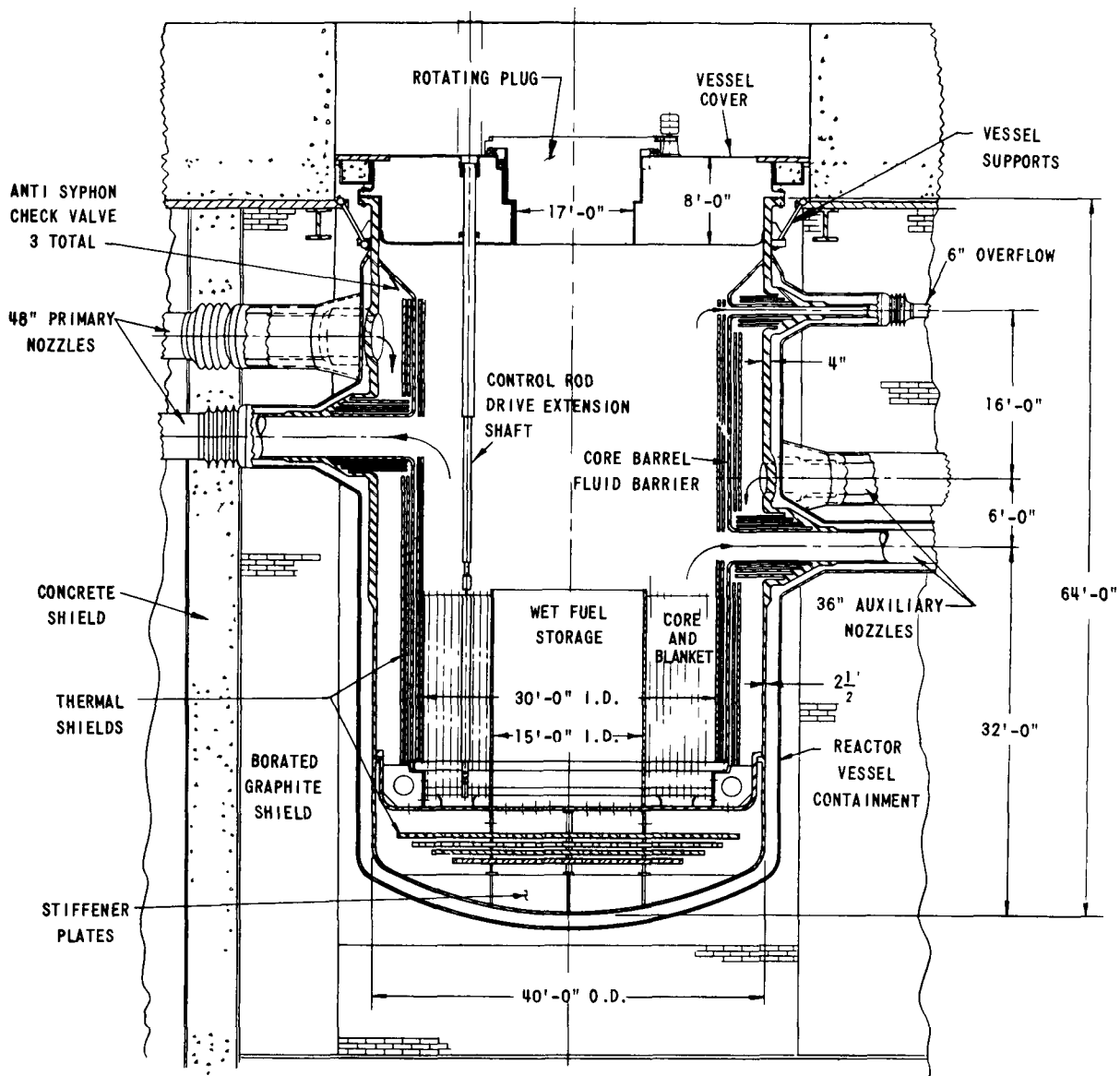


Fig. 6-3. Reactor vessel assembly

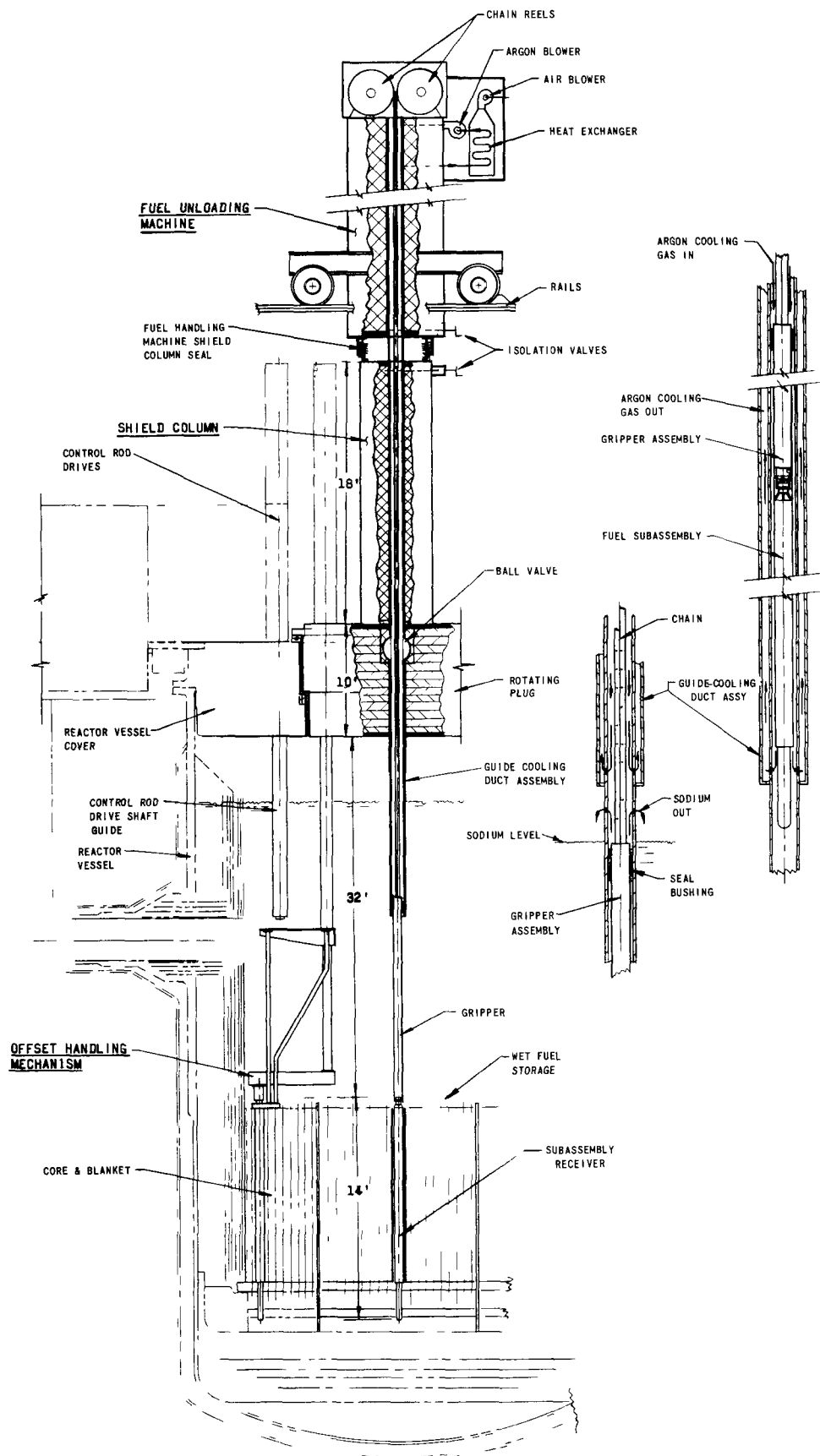


Fig. 6-4. Sectional views of fuel-handling system components

successfully in the Fermi Plant. Suspended from an eccentrically-located port in the top indexing plug, the OHM is used to exchange spent core and blanket subassemblies with fresh units stored in the central region of the reactor (Wet Fuel Storage). Upon resumption of reactor operation, and after a predetermined decay period, the OHM is used to remove each spent unit to the subassembly receiver in the storage lattice. At this point, the gripper of the Fuel Unloading Machine is lowered to engage and withdraw the subassembly into a shielded cask for transport to a processing plant. After completion of the unloading operation, the Unloading Machine is used in conjunction with the OHM to replenish the Wet Fuel Storage with fresh fuel and blanket subassemblies for the next recharging cycle.

The reactor vessel and six primary coolant loops are centrally located in the containment sphere. With reference to Figs. 6-2 and 6-5, sodium at 1050°F and near atmospheric pressure flows from the vessel into a U-leg expansion loop and to the primary pump (143,000 gpm capacity). The flow continues through the shell side of a vertical sodium-to-sodium intermediate heat exchanger and returns to the reactor via another U-leg expansion loop to complete the cycle.

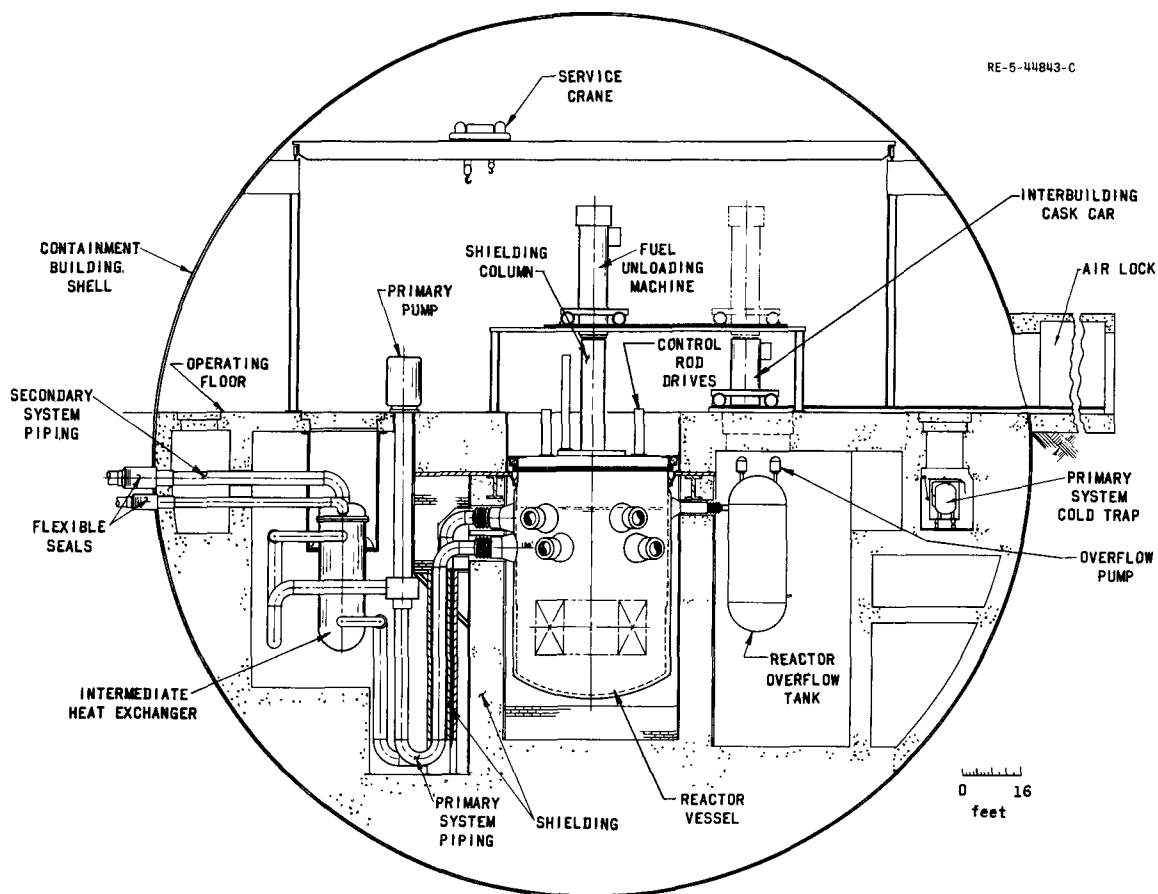


Fig. 6-5. Elevation view of primary system component arrangement within containment sphere

6.1.3.2 Steam-generator Island

The steam generators and secondary sodium pumps are housed in pairs in three buildings symmetrically arranged adjacent to the containment sphere. (See Fig. 6-6.) Each building also houses auxiliary equipment for two secondary loops. Each steam generator is of the once-through, vertical, shell-and-tube type and measures 14 ft dia. by 50 ft long. The once-through design was selected for its simplicity of construction and operation, low cost, compactness, and very low water retention in case of leakage. Materials of construction include Type 316 stainless steel for the shell, tube sheets, and internals. The tubes are of Incoloy-800, which is compatible with both sodium and water; they are bundled into six basic modules.

Again, with reference to Figs. 6-2 and 6-5, secondary sodium circulates from the tube side of the intermediate heat exchanger through two 30-in. pipes leading to the shell side of the steam generator. From the steam generator the flow returns through a single, 42-in. pipe and an axial flow pump (113,000 gpm capacity). The secondary system is designed so that the pumps and steam generators are hung by tie bars. This allows lateral motion due to pipe expansion and thus permits more direct piping runs.

6.1.3.3 Turbine-generator Island

Superheated steam at 2400 psia and 900°F from the steam generators flows to three tandem-compound-quadruple-flow turbine generators in the turbine-generator building. (See Fig. 6-6.) Throttle steam is used to reheat exhaust steam from the intermediate pressure cylinder to 660°F before entering the low-pressure cylinder. Feedwater is returned to the steam generator at 480°F. With seven stages of feedwater heating and $1\frac{1}{2}$ in. Hg backpressure, each generator provides a gross output of 1320 MW(e).

6.1.4 Safety

In developing the concept, major design features were scrutinized from a safety standpoint and no manifestly unsafe situations were tolerated. As with other aspects of this study, the 1000-MW(e) designs were taken as the departure point. However, in the present state of fast reactor technology, there are numerous unresolved safety questions associated with these designs. For example, a variety of viewpoints were expressed by the participating organizations on the problem of sodium voiding. For the purposes of the present study, in most cases, a middle ground was taken between the most conservative and the most optimistic of the 1000-MW(e) designs.

In general, safety problems are basically the same as those encountered in the design of a 1000-MW(e) plant. Certain design criteria were adopted: (1) a negative power coefficient was provided for stability during

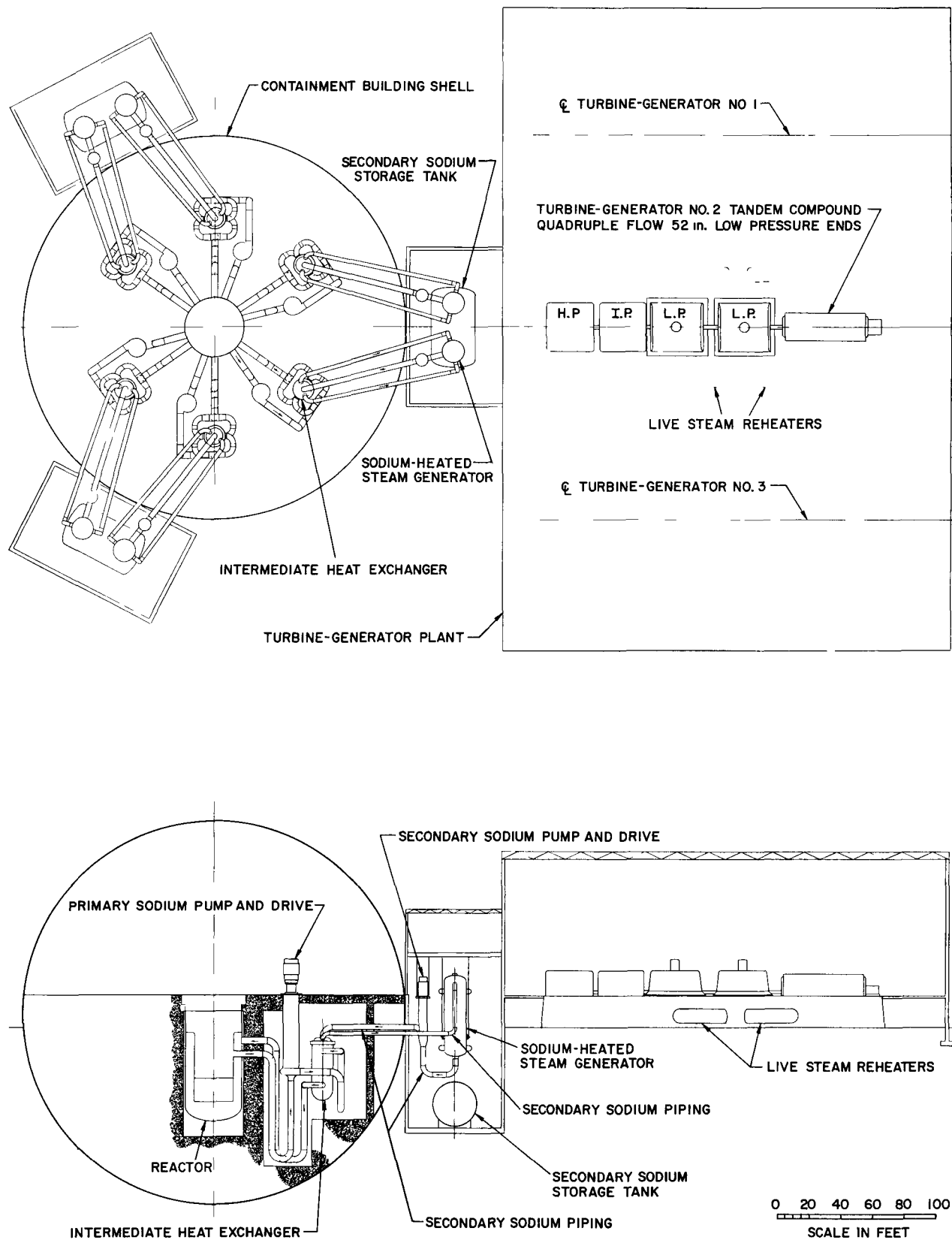


Fig. 6-6. Plan and elevation views of reactor, steam-generator, and turbine-generator islands

normal operation; (2) the design makes incredible the total loss of sodium from the reactor; and finally, (3) nominal containment of the reactor and primary loops is provided by a 240-ft-dia. spherical shell. No significant new safety problems were encountered in design other than those normally expected in the scale-up of plant size; and these problems will have solutions similar to those found in 1000-MW(e) designs.

6.1.5 Cost Factors

Although the main purpose of the study was to determine the technical feasibility of a 10,000-MW nuclear steam supply system, a significant objective concerned definition of certain "cost factors." These factors were: fuel cycle costs, capital cost of some pieces of equipment, and plant availability as affected by refueling time. In addition, technical feasibility in some respects cannot be separated from costs, and some cost guidance is required in design. This guidance, however, should not be interpreted as cost optimization; such an effort would be beyond the scope of the study.

Based on an annual plant factor of 90%, a 5% charge on working capital, and a fissile plutonium cost of \$10/g, the fuel cycle cost was estimated at 1/4 mill per kilowatt-hour. On an installed basis, the sodium-to-sodium heat exchanger, secondary sodium pumps and drives, secondary sodium piping, and steam generators were estimated at \$10 to \$12 per net electrical kilowatt. Plant availability, as limited by two partial refuelings per year, was 95.6%. If an additional shutdown time of 14 days a year is assumed for scheduled and unscheduled maintenance, a plant availability of 92% can be attained.

6.1.6 Conclusions

In the future, examinations of very large fast reactors may result in a more suitable selection of design conditions, those which give a lower energy cost. These examinations may modify, but probably will not change, the following conclusions:

(1) The 10,000-MW(t) sodium-cooled fast breeder reactor is feasible within the context of the ground rules of this study.

(2) In view of the estimated fuel cycle cost and doubling time, fuel performance for this concept is in line with other fast breeder studies using carbide fuel.

(3) Equipment sizes and duties are not excessive by comparison to the probable requirements for nominal 1000-MW(e) designs.

(4) Successful development of fast breeder plants of nominal 1000 MW(e) size will provide the technological base for very large fast breeders, with no significant additional R&D program required.

In summary, very large sodium-cooled fast breeder plants will come about by an evolutionary process, and nuclear power plants utilizing such reactors will be available when electrical systems can accommodate the output, provided the fast reactor research and development program achieves plants of 1000 MW(e) size in the 1980's.

REFERENCE

1. K. Hub et al, *Feasibility Study of Nuclear Steam Supply System Using 10,000 MW Sodium Cooled Breeder Reactor*, ANL-7183 (in press).

Section 7

PUBLICATIONS

7.1 Methods of Reporting

The status of various programmatic and basic research activities of the Reactor Engineering Division, and other Divisions at Argonne, is published in Laboratory Monthly Progress Reports. Ultimately, these chronologies are compiled to present a comprehensive description and evaluation of specific accomplishments in the form of ANL topical reports. These reports are distributed to all AEC sites and to preselected AEC-affiliated organizations and institutions which have an immediate interest in their contents.

In certain instances, the topical reports are supplemented by abridged articles or papers. These are prepared for publication in trade journals, or for oral presentation to professional and educational organizations which maintain an interest in the state of the art.

Finally, and not too infrequently, Staff personnel are solicited or volunteer to publicize their expertise. The nature of these publications may range from brief critiques of journal articles, to editing or writing handbook chapters and monographs. These activities, the latter in particular, entail several man-months' effort on the part of the author. In most cases, the work is performed in addition to his regularly assigned tasks.

7.2 Recap of Publications

The following recapitulation represents the literary output by Division Staff personnel during the fiscal reporting period. In order to conserve space, the publications are indexed to the major sections which comprise this report.

EXPERIMENTAL BREEDER REACTOR-II

H. O. Monson, *EBR-II Initial Operation - Highlights*, Paper No. Ref: 2/1, International Conference on Fast Breeder Reactors, London, England, May 17-19, 1966; sponsored by the British Nuclear Energy Society.

G. K. Whitham, F. J. Tebo, and F. D. McGinnis, *EBR-II Reactor Building Leak Testing*, Trans. Am. Nucl. Soc., 8 (Suppl.), 40-41 (July, 1965).

E. Hutter, *EBR-II Fuel Unloading Machine: Design and Performance Characteristics*, ANL-7201 (to be published).

ARGONNE ADVANCED RESEARCH REACTOR (AARR)

R. C. Skaardal, *AARR - A New Tool for Nuclear Research*, Teknisk Ukeblad, 112, No. 31, 675-679 (September, 1965).

EBWR - PLUTONIUM RECYCLE EXPERIMENT

N. Balai et al, Abstract: *Summary of the 1965 Partial Inspection of the EBWR Vessel: Cracking of Cladding*, Trans. Am. Nucl. Soc., 9, No. 1, 222 (June, 1966).

R. F. Jones et al, Abstract: *Reactor Vessel Surveillance Program for the Plutonium Recycle Experiment*, Trans. Am. Nucl. Soc., 9, No. 1, 222-223 (June, 1966).

C. R. Sutton et al, Abstract: *Examination and Evaluation of Experimental Boiling Water Reactor Pressure Vessel Cladding*, Trans. Am. Nucl. Soc., 9, No. 1, 222 (June, 1966).

ARGONNE NUCLEAR ROCKET PROGRAM

H. Halle, *Deformation Analysis of a Circular Coupled-Plate Structure*, ANL-7145 (March, 1966).

FAST REACTOR RESEARCH AND DEVELOPMENT

I. Charak and F. A. Smith, *Preliminary Evaluation of a Technique to Study Expulsion of Sodium into Air*, Proceedings of the Conference on Safety, Fuels, and Core Design in Large Fast Power Reactors, Argonne National Laboratory, October 11-14, 1965, ANL-7120 (June, 1966), pp. 868-872.

T. W. Eckels and A. Smaardyk, *Design, Performance, and Evaluation of Shielding Window for FARET Containment Cell*, ANL-7157 (July, 1966).

A. P. Grunwald, *Fuel-Handling Machine Design*, ANL-7159 (to be published).

FAST REACTOR RESEARCH AND DEVELOPMENT (Contd.)

E. Hutter, T. E. Sullivan, and G. D. Giorgis, *Design and Development of Prototype Control Rod Drive Mechanisms for the Fast Reactor Test Facility (FARET) - Terminal Report*, ANL-7158 (July, 1966).

A. H. Marchertas, *Stress Analysis of a Reactor Core Support Structure Consisting of Two Interconnected Multiregion Plates*, ANL-7162 (to be published).

P. J. Persiani, T. R. Bump, and W. J. Kann, *FARET Core-I Reference Design*, Proceedings of the Conference on Safety, Fuels, and Core Design in Large Fast Power Reactors, Argonne National Laboratory, October 11-14, 1965, ANL-7120 (June, 1966), pp. 766-775.

G. F. Popper, *Measuring Neutron Flux Distribution in Operating Reactors*, Power Reactor Technology, 9, No. 1 (Winter, 1965-1966).

G. F. Popper, W. C. Lipinski, and J. M. Harrer, Abstract: *Ten Decades of Continuous Neutron Flux Monitoring from a Single Fixed Position Detector*, Trans. Am. Nucl. Soc., 9, No. 1, 316-317 (June, 1966).

G. F. Popper and A. E. Knox, *FARET In-Core Instrument Development - Terminal Report*, ANL-7161 (July, 1966).

R. W. Seidensticker et al, *FARET Containment Structure Analysis and Design*, ANL-7154 (to be published).

R. W. Seidensticker et al, *FARET Reactor Vessel Design*, ANL-7163 (to be published).

D. Thompson, *Vapor Traps Protect Liquid-Metal Systems*, Power Reactor Technology, 8, No. 4, 259 (Fall, 1965).

HEAT TRANSFER AND FLUID FLOW RESEARCH

R. C. Brubaker et al, *The Boiling Liquid Metal Program at Argonne National Laboratory*, Proceedings of the Second Joint USAEC-EURATOM Two-Phase Flow Meeting, Germantown, Md., April 29-May 1, 1964, USAEC CONF-640507 (July, 1965), p. 3.1.1.

T. R. Bump, *Surface Temperatures of Infinite Plates Subjected to Sudden Environment Temperature Changes*, ASME Trans., Series C, J. Heat Transfer, 87, No. 4, 526 (November, 1965).

T. R. Bump, *Coolant Mixing in Fuel Subassemblies*, Trans. Am. Nucl. Soc., 9, No. 1 (1966).

H. K. Fauske, *Two-Phase, Two- and One-Component Critical Flow*, Proceedings of Symposium on Two-Phase Flow, University of Exeter, Exeter, England, June 21-22, 1965, Vol. 1, pp. SG 101-104.

HEAT TRANSFER AND FLUID FLOW RESEARCH (Contd.)

H. K. Fauske, *An Evaluation of Existing Models for Calculating Maximum Escape Rates of Reactor Coolant*. Paper presented at the 8th National Heat Transfer Conference, Los Angeles, Calif., August 8-11, 1965.

H. K. Fauske, *The Discharge of Saturated Water Through Tubes*, AIChE and ASME 7th National Heat Transfer Conference, Cleveland, Ohio, Chem. Eng. Prog. Symp., Series No. 59, 61, 210-216 (December, 1965).

H. K. Fauske, Review of: *Boiling Heat Transfer and Two-Phase Flow* by L. S. Tong (New York: John Wiley & Sons, Inc., 1965). Review to be published in Nuclear Science and Engineering.

H. K. Fauske, *What's New in Two-Phase Flow*, Power Reactor Technology, 9, No. 1 (Winter, 1965-1966).

H. K. Fauske, T. C. Min, and M. Petrick, *Effect of Flow Passages on Two-Phase Critical Flow*, Ind. Eng. Chem. Fundamentals, 5, No. 1, 50-55 (February, 1966).

H. K. Fauske, *Compressibility Affects Flow Instability and Burnout*, Power Reactor Technology, 9, No. 2 (Spring, 1966).

H. K. Fauske, Comments on: *Maximum Two-Phase Vessel Blowdown from Pipes* by F. J. Moody. (To be published in ASME Trans., J. Heat Transfer, 1966.)

H. Halle, Note to Editor: *Exact Solution of Elementary Transient Heat Conduction Problem Involving Temperature-Dependent Properties*, ASME Trans., Series C, J. Heat Transfer, 87, No. 3, 420 (August, 1965).

J. B. Heineman, *Forced Convection Boiling Sodium Studies at Low Pressure*, Proceedings of the Conference on Application of High Temperature Instrumentation to Liquid-Metal Experiments, Argonne National Laboratory, September 28-29, 1965, ANL-7100 (June, 1966), pp. 189-194.

R. E. Holtz, *A Liquid-Metal Heat Transfer Experiment*, ANL-7038 (June, 1965).

R. E. Holtz, Letter to Editor: *Investigation of Heat Transfer to Liquid Metals Flowing in Circular Tubes*, AIChE Journal, 11, No. 6, 1151-1153 (November, 1965).

R. E. Holtz, *The Effect of the Pressure-Temperature History upon Incipient Boiling Superheats in Liquid Metals*, ANL-7184 (May, 1966).

R. E. Holtz, *Heating Techniques for Liquid Metal Loops*, Proceedings of the Conference on Application of High Temperature Instrumentation to Liquid-Metal Experiments, Argonne National Laboratory, September 28-29, 1965, ANL-7100 (June, 1966), pp. 9-22.

A. A. Kudirka, R. J. Grosh, and P. W. McFadden, *Heat Transfer in Two-Phase Flow of Gas-Liquid Mixtures*, Ind. Eng. Chem. Fundamentals, 4, 339-344 (August, 1965).

HEAT TRANSFER AND FLUID FLOW RESEARCH (Contd.)

D. E. Lutz, *Turbine Controls Steam Pressure for a Nuclear Power Plant*, Power, 110, 59-61 (January, 1966).

M. Petrick, *Building-11 Two-Phase Flow Program*, Proceedings of the 2nd Joint USAEC-EURATOM Two-Phase Flow Meeting, Germantown, Md., April 29-May 1, 1964, USAEC CONF-640507 (July, 1965), p. 6.5.1.

R. P. Stein, *Fog Flow Models*, Proceedings of the 2nd Joint USAEC-EURATOM Two-Phase Flow Meeting, Germantown, Md., April 29-May 1, 1964, USAEC CONF-640507 (July, 1965), p. 6.1.1.

R. P. Stein, *Heat Transfer Coefficients in Liquid-Metal Cocurrent Flow of Double-Pipe Heat Exchangers*, AIChE and ASME 7th National Heat Transfer Conference, Cleveland, Ohio, Chem. Eng. Prog. Symp., Series No. 59, 61, 64-75 (December, 1965).

R. P. Stein, *The Graetz Problem in Cocurrent-Flow Double-Pipe Heat Exchangers*, *ibid.*, pp. 76-87.

R. P. Stein, *A Method for the Determination of Local Heat Fluxes in Liquid Metal Heat Exchangers*, Proceedings of the Conference on Application of High Temperature Instrumentation to Liquid Metal Experiments, Argonne National Laboratory, September 28-29, 1965, ANL-7100 (June, 1966), pp. 483-498.

R. P. Stein, *Mathematical and Practical Aspects of Heat Transfer in Double Pipe Heat Exchangers*, Proceedings of the Third International Heat Transfer Conference, Chicago, Ill., August 7-12, 1966, Vol. I, pp. 139-148.

R. P. Stein, *Liquid Metal Heat Transfer*, Advances in Heat Transfer, (eds.) T. F. Irvine and J. P. Hartnett (New York: Academic Press, 1966), Vol. III, pp. 101-173.

R. P. Stein, *Discussion of: Experiments on Turbulent Heat Transfer in an Asymmetrically Heated Rectangular Duct* by E. M. Sparrow, J. R. Lloyd, and C. W. Hixon, ASME Trans., Series C, J. Heat Transfer, 88, No. 2, 174 (1966).

R. Viskanta, *Heat Transfer in Couette Flow of a Radiating Fluid with Viscous Dissipation*, Developments in Mechanics, Proceedings of the 8th Midwestern Mechanics Conference, Case Inst. Tech., April 1-3, 1963 (eds.) S. Ostrach and R. H. Scanlon (Oxford: Pergamon Press, 1965), Vol. 2, Part 1, pp. 376-402.

MAGNETOHYDRODYNAMICS

M. Petrick, *Liquid-Metal MHD Topping Cycles*, Power Reactor Technology, 8, No. 4, 199 (Fall, 1965).

M. Petrick, *Why Liquid Metal MHD?* Paper presented at the Fourth Annual ANL-AMU Faculty-Student Conference, Argonne National Laboratory, August 26, 1965.

MAGNETOHYDRODYNAMICS (Contd.)

M. Petrick, *ANL-AMU Program*. Paper presented at Jet Propulsion Laboratory, Los Angeles, Calif., November 8, 1965.

M. Petrick, *Liquid Metal Magnetohydrodynamics - Its Potential and Status*. Paper presented at the University of Illinois, Urbana, Ill., January 6, 1966, and at the University of Windsor, Windsor, Ontario, March 25, 1966.

M. Petrick, *MHD Generators Operating with Two-Phase Liquid Metal Flows*, Seventh Symposium on Engineering Aspects of Magnetohydrodynamics, Princeton, N. J., March 30-April 1, 1966.

M. Petrick, *A Second-Round Look at Liquid Metal MHD*. Paper presented at the Technical Institute of Berlin, Berlin, Germany, June 30, 1966.

R. M. Singer, *A Study of Convective Magnetohydrodynamic Channel Flow*, ANL-6968 (March, 1965).

R. M. Singer, *Transient Magnetohydrodynamic Flow and Heat Transfer*, Z. Angew. Math. Phys. 16, No. 4, 483-494 (1965).

R. M. Singer, *Unsteady Convective Magnetohydrodynamic Channel Flow*, AIChE and ASME 7th National Heat Transfer Conference, Cleveland, Ohio, 1964. Chem. Eng. Prog. Symp. Series No. 59, 61, 36-49 (1965).

FAST REACTOR SAFETY RESEARCH AND DEVELOPMENT

T. R. Bump and W. R. Simmons, *Hold-down Requirements for Poison Control Rods*, Trans. Am. Nucl. Soc., 9, No. 1 (1966).

G. Cinelli, *An Extension of the Finite Hankel Transform and Applications*, Int. J. Eng. Sci., 3, 539-559 (1965).

G. Cinelli, *The Solution of Dynamic Beam Problems by Means of Finite Cis-Hyperbolic Transforms*, Shock and Vibration Bulletin, 35, Pt. 3, 81-88 (January, 1966).

G. Cinelli, *Thermo-elastic Vibrations of a Thick-Walled Elastic Sphere*, Paper presented at the 71st Meeting of the Acoustical Society of America, Boston, Mass., June 1-4, 1966 (to be published).

G. Cinelli, *Dynamic Vibrations of Thick Elastic Cylinders and Spheres*, Paper presented at the 5th National Congress of Applied Mechanics, University of Minnesota, Minneapolis, Minn., June 14-17, 1966 (to be published).

S. H. Fistedis, *Abstract: Pressure Testing of Thick Reinforced Concrete Cell*, Trans. Am. Soc. Civil Engrs., 130, 324-326 (December, 1965).

S. H. Fistedis, *A New Reactor Containment Concept by Energy Absorption*, Nuclear Engineering and Design, 3, No. 2, 281-286 (February-March, 1966).

FAST REACTOR SAFETY RESEARCH AND DEVELOPMENT (Contd.)

- S. H. Fistedis, *Summary of Concept and Cost of Containment by Energy Absorption*, Trans. Am. Nucl. Soc., 9, No. 1, 306 (June, 1966).
- H. Halle, *Deformation Analysis of a Circular Coupled Plate Structure*, ANL-7145 (to be published).
- C. Hsu and C. F. Chen, *The Determination of Root Loci Using Routh's Algorithm*, J. Franklin Institute, 281, No. 2, 114-121 (February, 1966).
- I. Kliger, *Synthesis of an Optimal Nuclear Control System*, Symposium on Neutron Dynamics and Control, University of Arizona, Tucson, Ariz., April 5-7, 1965 (to be published).
- I. Kliger, *Synthesis of Optimal Control System for Nuclear Reactors with Generalized Temperature Feedback*, Proceedings of the International Atomic Energy Agency Conference on Nuclear Electronics, Bombay, India, November 22-26, 1965 (to be published).
- I. Kliger, *An Automatic Control of a Nuclear Reactor for a Minimal Time Response*, Proceedings of the Third International Congress of the International Federation of Automatic Control, London, England, June 20-25, 1966 (to be published).
- R. M. Singer, *How Coolant Dynamics Affect Fast Reactor Safety*, Power Reactor Technology, 9, No. 1 (Winter, 1965-1966).
- R. Skaardal, *Operational Problems and Solutions*, Power Reactor Technology, 8, No. 4, 271 (Fall, 1965).
- F. A. Smith, *Hallam Operation in Retrospect*, Power Reactor Technology, 8, No. 4, 279 (Fall, 1965).
- H. C. Sorensen and S. H. Fistedis, *Hydrodynamic Analysis of Nuclear Containment by Energy Absorption*, ANL-7214 (to be published).
- E. S. Sowa and J. C. Heap, Abstract: *The Development of a Small Integral Loop for In-Pile Fuel Failure Studies in the Presence of Flowing Sodium*, Trans. Am. Nucl. Soc., 8, No. 2, 559 (November, 1965).
- E. J. Croke, *Ocean Technology and Nuclear Power*, Power Reactor Technology, 9, No. 1 (Winter, 1965-1966).
- K. A. Hub, *Reactors for Desalting*, Power Reactor Technology, 9, No. 2 (Spring, 1966).
- K. A. Hub et al, *Feasibility Study of Nuclear Steam Supply System Using 10,000 MW Sodium-Cooled Breeder Reactor*, ANL-7183 (in press).
- L. E. Link et al, *A Large Metal-Fueled Fast Reactor Study. Part II: Core Design and Fuel Cycle*, Proceedings of the Conference on Safety, Fuels, and Core Design in Large Fast Power Reactors, Argonne National Laboratory, October 11-14, 1965, ANL-7120 (June, 1966), pp. 94-103.

MISCELLANEOUS

R. E. Grench and H. C. Thacher (eds.), *Collected Algorithms 1960-1963 from the Communications of the Association for Computing Machinery*, ANL-7054 (July, 1965).

B. M. Hoglund, *UHTREX Operation Near*, Power Reactor Technology, 9, No. 1 (Winter, 1965-1966).

F. A. Smith, *Interpreting the French Liquid-Metal-Heated Steam Generator Progress*, Power Reactor Technology, 9, No. 2 (Spring, 1966).

C. R. Sutton, *Effect of Hydriding on Zircaloy Properties*, Power Reactor Technology, 8, No. 4, 245 (Fall, 1965).

M. W. Wambsganss, Jr., *Simulation of Reciprocating Gas Compressors with Automatic Reed Valves*. Paper presented to Midwestern Simulation Council Meeting, Battelle Memorial Institute, Columbus, Ohio, March 21-22, 1966.